IMPERIAL COLLEGE LONDON

Trapping, transport and polarisation of ultracold lithium

Aisha Kaushik

Thesis submitted in partial fulfillment of the
requirements for the degree of
Doctor of Philosophy

Quantum Optics and Laser Science Group
Department of Physics

September 2014

Declaration

Declaration of originality

I declare that all of the work presented in this thesis is my own. I confirm that where I have used the work of others, this is always clearly acknowledged and referenced appropriately.

Copyright declaration

Abstract

The aim of our experiment is to explore two methods of creating an ultracold dipolar gas which can subsequently be used to simulate quantum phenomena. The first method is to sympathetically cool polar molecules. In this case, the molecules are overlapped with ultracold lithium atoms, thus allowing the two clouds to thermalise through elastic collisions. The second method is to electrically polarise ultracold lithium atoms using an electric field of approximately 1 MV/cm. This involves placing the atoms between two high voltage electrodes.

This thesis describes and characterises the setup used to produce, trap and transport a cloud of lithium-7 atoms. The setup consists of a lithium oven, Zeeman slower, magneto-optical trap (MOT) and magnetic trap. Up to 2.3×10^8 atoms are loaded into the MOT with an initial temperature of 1.3 mK. By implementing a compressed MOT phase the temperature is reduced to 0.75 mK. Before transport, 23% of the MOT atoms are transferred into the magnetic trap, which has a lifetime of 1.53 ± 0.01 s in the MOT chamber. Using a motorised translation stage to move the magnetic trapping coils, atomic transport over a distance of 44 cm from the MOT chamber to the science chamber has been demonstrated. The transport efficiency is 41%. In the science chamber the lifetime of the magnetic trap has been measured as 18.5 ± 0.7 s. Experiments to optimise the absorption imaging system have also been carried out, highlighting the fact that a time and position dependent magnetic field is present after the trapping coils switch off. The feasibility of producing a 1 MV/cm electric field has been investigated. By using indium tin oxide coated glass electrodes in an adjustable electrode mount, an electric field of approximately 0.2 MV/cm has been generated. These electrodes were subsequently replaced with super-polished stainless steel electrodes which generated a field of 0.38 MV/cm.

Acknowledgements

Without the help and support of many people over the years, this thesis would not have been possible. First and foremost, I would like to thank my supervisor Mike Tarbutt for his encouragement, guidance and limitless patience. I have learnt a lot from his clear explanations and careful approach to physics. It has been a privilege to work for Ed Hinds as a member of CCM, as it has brought me into contact with many fantastic physicists. In particular, I would like to thank Sean Tokunaga for the many interesting pub discussions and for being a great post-doc, until he abandoned me. Thankfully I was able to work with another equally brilliant post-doc, Rich Hendricks, who has helped me through many lab problems, including the endless AOM saga. I would also like to thank Jon Dyne and Steve Maine in the CCM workshop, as the experiment would not be what it is today without them. Thanks to Val Gerulis for his help with all things electronic, and for being a quirky presence in the lab. I am also grateful to the rest of CCM as they have created a friendly working atmosphere that has made my PhD much more enjoyable. Thanks to both Lilian Wanjohi and Sanja Maricic for their administrative work and for organising the best parties.

A special thanks goes to Doug Plato for keeping me fed, watered, and (mostly) entertained throughout my PhD. I am especially grateful to him for introducing me to the wonderful city of Slough. I also want to give special thanks to Gao Ya for her unwavering support and friendship over the years. She never fails to make me laugh, even through the toughest times. Lastly but by no means least, I would like to thank my parents, and my brother, Aritz, for their constant support and guidance. It is to them that I dedicate this thesis.

Contents

List of Figures

List of Tables

Chapter 1

Introduction

1.1 Motivation and background

In order to provide context for the work described in this thesis, three important questions must be answered. These are, what are we trying to make? Why are we trying to make it, and how can it be made? To answer the first of these questions, section 1.1.1 starts by describing the overall aim of the project, which is to create an ultracold dipolar gas. In sections 1.1.2 and 1.1.3, the second question is addressed. In particular, by looking at some of the potential applications, we explain why dipolar gases are interesting systems to study. Finally in section 1.1.4, the third question is answered. Here we describe the many different production techniques that are currently being explored and discuss some of the experimental challenges that are faced.

1.1.1 What are we trying to make?

Since the first observation of Bose-Einstein condensation in 1995 [1–3], much experimental and theoretical research has been directed towards studying these quantum systems. The properties of these gases are determined by the interactions between the constituent particles. For the majority of Bose-Einstein condensates (BECs) these interactions are described by the van der Waals potential which is short range, isotropic and scales as $-C_6/r^6$, where C_6 is a dimensionless, species specific coefficient, and r is the atomic separation. To study the collision physics of such a gas, calculations are carried out in the centre of mass frame. This allows the interaction between two particles with masses m_1

and m_2 to be treated as the scattering of a single particle by the interaction potential, where the particle mass is now the reduced mass $\mu = m_1 m_2/(m_1 + m_2)$. Given that the interaction potential is spherically symmetric, the technique of partial wave analysis is usually adopted. This involves decomposing the wavefunction of the particle into its constituent angular momentum components, which are called partial waves. When the collision energy is low, as it is for an ultracold gas, only the zero angular momentum partial wave is significantly scattered by the interaction potential. This is because there is an angular momentum barrier for all other partial waves which prevents a close approach to the scattering centre. Therefore only s-wave scattering occurs, and as a result only the s-wave scattering length a_s, is required to describe the properties of an ultracold gas. Here we define ultracold as temperatures below 1 mK.

One particular property that depends upon the sign of the scattering length, is the stability of a BEC. When $a_s > 0$ the interactions are repulsive. However when $a_s < 0$ the interactions are attractive and this creates an unstable condensate that will eventually collapse if the atom number is increased above some critical value [4, 5]. In general the sign of the scattering length is fixed for a given atomic species in a particular spin state. However in the presence of a Feshbach resonance, the scattering length can be tuned by varying the size of an applied magnetic field. This has enabled researchers to study the collapse of a BEC in an highly controlled manner [6].

Given the important role that interactions play, much research effort has been directed towards producing ultracold gases that instead exhibit dipole-dipole interactions. As these interactions are long range, anisotropic and scale with distance as $1/r^3$, many of the properties of the gas should be distinctly different. The aim of our experiment is to produce one of these ultracold dipolar gases. In order to create such a gas, many different approaches are currently being explored. We plan to employ two different methods, which are discussed in more detail in section 1.2. No matter which approach is adopted, the chosen particle, whether it be an atom or a molecule, must have an appreciable magnetic or electric dipole moment. In order to compare different systems, it is useful to introduce the dimensionless parameter, ϵ_{dd}. This parameter characterises the strength of the dipolar interaction by comparing the effective dipole-dipole interaction length, a_{dd}, to the s-wave scattering length, a_s. It is normally written as [7]

$$\epsilon_{dd} \equiv \frac{a_{dd}}{a_s} = \frac{mC_{dd}}{12\pi\hbar^2 a_s}, \tag{1.1}$$

where m is the mass of the particle and C_{dd} is a coupling constant which varies depending on whether the particles have a magnetic or electric dipole moment. For systems with a magnetic moment μ, the coupling constant becomes $C_{dd} = \mu_0 \mu^2$, where μ_0 is the permeability of free space. For a system with an induced electric dipole moment, we instead have $C_{dd} = \alpha^2 E^2/\epsilon_0$. Here α is the electric polarisability of the atom, E is the applied electric field and ϵ_0 is the permittivity of free space. Finally for any species with a permanent electric dipole d_e, the coupling constant becomes $C_{dd} = d_e^2/\epsilon_0$. As might be expected, when $0 < \epsilon_{dd} < 1$, short range interactions are dominant, although some dipolar features can be observed. When $\epsilon_{dd} > 1$ dipole-dipole interactions dominate. Depending on the the size of this value, the potential applications will vary. This is discussed in more detail in the following sections.

1.1.2 Why are dipolar gases interesting?

Dipolar interactions are of interest to researchers for two main reasons. Firstly dipole-dipole interactions are predicted to change many of the properties of an ultracold gas. For example the critical temperature at which condensation occurs is expected to shift [8, 9], although this is only likely to be apparent for systems that are strongly dipolar. In addition to this, it is possible to tune the dipolar interaction using easily controlled experimental parameters. As only some of the properties and potential uses of dipolar gases are highlighted here, the reader is directed to references [7] and [10] for a more thorough discussion.

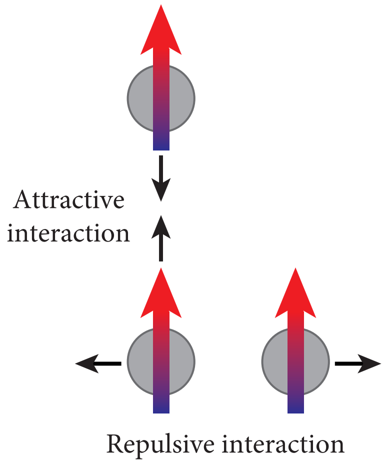

Figure 1.1: Anisotropy of the dipole-dipole interaction. Aligned dipoles positioned end to end produce an attractive interaction, whilst dipoles placed side by side experience a repulsive interaction.

One particular property that is affected by the presence of dipolar interactions is the stability of the BEC. As shown in figure 1.1, for aligned dipoles that are positioned end to end, an attractive force is produced that results in an unstable BEC. However when the aligned dipoles are positioned side by side, a repulsive force is produced which acts to stabilise the BEC. Therefore, in contrast to a non-polar BEC, the inherent anisotropy of the dipolar interaction allows the stability of the condensate to be varied by simply adjusting the aspect ratio of the trap [11, 12]. The ease with which the interaction can be manipulated also extends to the strength of the dipolar interaction. By using a rotating field to polarise the dipoles, it is possible, due to time-averaging, to reduce the effective strength of the dipole-dipole interaction, and even change its sign [13]. This has a clear advantage over non-polar BECs as these methods can be applied to all dipolar condensates.

In order to replicate the systems that are commonly encountered in condensed matter and solid state physics, BECs are often loaded into the periodic potential of an optical lattice. This trapping potential is formed by the periodic intensity variation that occurs when two or more laser beams interfere. As the potential can be altered by simply changing the intensity, or wavelength of the laser light, quantum phase transitions can be easily investigated. By using a non-polar BEC of rubidium-87 atoms, the superfluid to Mott insulator phase transition has already been experimentally observed [14]. However by making use of a dipolar BEC instead, the number of predicted phases increases to include the supersolid and checkerboard phases [15]. As these have not yet been observed, dipolar gases provide a unique opportunity to test theoretical predictions in a highly controlled environment.

1.1.3 Why are ultracold molecules interesting?

Although an ultracold dipolar gas can consist of either atoms or molecules, much interest currently surrounds molecular gases as they have a wide range of applications that go far beyond the study of quantum phase transitions [16]. Unlike atoms, molecules are generally difficult to cool. Therefore by developing techniques to reduce their temperature, many improvements are expected in a wide variety of research areas. Precision measurement is one area in which ultracold molecules are expected to play an increasingly important role. A common factor that limits the precision of these experiments is the interaction time. As a result, cooling and trapping techniques are employed wherever possible. For example, by using an ion trap to confine a single electron, its magnetic moment has been measured to 0.28 parts per trillion [17]. Therefore experiments that already utilise molecules can gain in precision by increasing the interaction time. This can be achieved by using cooled and trapped molecular samples.

A particular instance where molecules are currently favoured over atoms is for measurements of the electron electric dipole moment (EDM). This measurement is important as it provides a direct way of testing the extensions of the standard model. As many of these theories predict the electron EDM to have a small but potentially measurable value, by placing an upper limit on its size, these theories can be tested and if necessary discounted. In our laboratory a pulsed source of ytterbium monofluoride (YbF) molecules has previously been used to set the upper limit of the electron EDM at $|d_e| < 10.5 \times 10^{-28}\, e\,\mathrm{cm}$ [18]. The next generation of this experiment plans to use laser cooled YbF molecules and a molecular fountain to increase the interaction time and therefore the precision [19]. More recently a new upper limit of $|d_e| < 8.7 \times 10^{-29}\, e\,\mathrm{cm}$ has been placed on the electron EDM [20]. This was achieved by using a pulsed, cryogenic buffer gas source of thorium monoxide (ThO) molecules.

Another area in which cold molecules are expected to make a significant contribution is in the search for time variation of the fundamental constants. There are two principle methods by which this can be probed. The first is to compare spectroscopic data obtained in the laboratory with astronomical data. As the transition frequency is dependent on the fine structure constant, α, time variation of α would present itself as a frequency shift. As recently demonstrated for CH molecules [21], high resolution spectroscopy is required if stringent limits on time variation are to be found. The second method involves comparing highly accurate frequency measurements of two transitions that depend differently on α. From this comparison it is possible to place a limit on the yearly variation of fundamental constants [22, 23].

Cold chemistry can also benefit from the greater control that comes with reducing the temperature of molecules. It might be expected that chemical reaction rates would decrease as the temperature is lowered. However due to quantum effects, this is not necessarily the case. For example calculations have shown that atom exchange reactions, which lead to vibrational relaxation in $x + x_2$ collisions, where $x =$ Li, Na or K, can have a high rate

[24]. In order to fully explore the dynamics of these ultracold reactions, a high level of control is required. To achieve this, external fields can be used to manipulate the interaction potential, thus allowing the reaction dynamics, reaction rates and perhaps even the outcome of the chemical reaction to be controlled [25].

Finally cold polar molecules have also been highlighted as potential systems for quantum information processing [26, 27]. A particular advantage of these molecular schemes is that, due to their complex structure, there are many degrees of freedom in which a qubit could be encoded. For example, a qubit could be formed by the electric dipole moment of the molecule, which is either orientated along or against an external electric field [26]. Currently the major obstacle in realising any such scheme is producing large samples of polar molecules at sufficiently low temperatures.

1.1.4 How can an ultracold dipolar gas be made?

In order to create an ultracold dipolar gas, a variety of methods are currently being investigated. Depending on whether the constituent particles are atoms or molecules, different experimental challenges are faced. For instance, many atoms are easy to cool, but do not have a sizeable electric or magnetic dipole moment. Therefore either an electric dipole has to be induced by applying a very large DC electric field, or atoms possessing a large magnetic dipole moment have to be used.

Chromium is a particular example of an atom that has a relatively large magnetic moment of $\mu = 6\mu_B$, where μ_B is the Bohr magneton. In 2005 a sample of Chromium-52 was successfully cooled to form a BEC [28] and since then it has been used to explore the effects of dipolar interactions. Despite having a value of $\epsilon_{dd} = 0.16$, where ϵ_{dd} is given by equation (1.1), the effects of dipole-dipole interactions have been observed. In particular anisotropic expansion of the cloud has been witnessed [29], the collapse dynamics for different harmonic trap geometries have been investigated [30], and it has been shown that the potential well depth of a one dimensional optical lattice can affect the stability of the BEC [31]. More recently BECs of erbium-168 which has a magnetic moment of $\mu = 7\mu_B$ [32], and dysprosium-164 with a magnetic moment of $\mu = 10\mu_B$ [33] have also been demonstrated.

When it comes to molecules the experimental challenges are slightly different. In general heteronuclear molecules have a large permanent electric dipole moment that ranges from anywhere between 0.1 D to 10 D. This produces a value of $\epsilon_{dd} \gg 1$, which means that dipolar interactions are dominant. However due to their complex internal structure which consists of electronic, rotational and vibrational energy levels, molecules are difficult to cool. As a result many different cooling techniques, which can be categorised as either direct or indirect, are currently being investigated.

Direct cooling techniques involve taking pre-existing molecules and reducing their temperature. Stark deceleration, which uses a time varying inhomogeneous electric field to slow molecules, has been employed to cool a variety of species which include OH [34], NH_3 [35] and LiH [36]. In an analogous method, pulsed magnetic fields have been used to Zeeman decelerate oxygen molecules [37]. As these techniques produce molecules at mK temperatures, they can subsequently be confined in static electric traps [38], AC electric traps [39], or magnetic traps [40].

Buffer gas cooling is another well established technique that can be used to cool molecules [40, 41]. For this method to work the molecules of interest must be created within a buffer gas cell that is filled with low temperature helium. This is usually achieved by laser ablation of a suitable precursor target. As the molecules collide with the helium, thermal equilibrium is reached, and a cold source of molecules, with a temperature on the order of 1 K, is produced.

As the above mentioned techniques cannot cool molecules to the μK regime, additional cooling stages are required. One possible method that could be employed is sympathetic cooling. This involves overlapping a trapped sample of molecules with an ultracold sample of atoms, thus allowing the two species to reach thermal equilibrium via elastic collisions. Although this technique is often used to cool atoms [42–44], atomic ions [45] and molecular ions [46], sympathetic cooling of neutral molecules has not yet been demonstrated.

For the vast majority of molecules, due to their complex structure, laser cooling is not possible. This is because laser cooling relies on the repeated absorption and spontaneous emission of photons in order to produce a force that slows the particle down. In general tens of thousands of scattering events are required, so a closed cycling transition is necessary. As most molecules do not have such a transition, they are quickly pumped to states that no longer interact with the laser, thus making laser cooling impossible. However for a small subset of molecules [47], with the use of a modest number of repump frequencies, laser cooling to mK temperatures can be achieved. Experimentally this technique has been demonstrated for strontium monofluoride (SrF) [48], calcium monofluoride (CaF) [49] and yttrium oxide (YO) [50].

In contrast to direct methods, indirect cooling techniques involve constructing molecules from pre-cooled atoms. There are two distinct ways in which this can be done. The first, called photoassociation, is the process in which two colliding atoms absorb a photon to form an electronically excited molecule [51]. This newly formed molecule can then be transferred to the ground electronic state via spontaneous emission. The second method, which is called magnetoassociation, instead uses a Feshbach resonance to produce molecules [52]. A Feshbach resonance occurs when a bound molecular state is energetically close to the scattering state of two atoms. By adiabatically tuning an external magnetic field through this resonance, the colliding atoms are transferred to the bound molecular state.

As both techniques produce weakly bound molecules in highly excited vibrational states of the ground electronic potential, methods are required to transfer the population to deeply bound vibrational states. If this is not done, the newly formed molecules can undergo inelastic collisions and be lost from the trap. To coherently transfer the population to the vibrational ground state, stimulated Raman adiabatic passage (STIRAP) is often employed [53]. This technique uses two laser frequencies to couple the initial and final states together via an intermediate excited state. By using STIRAP, samples of KRb [54, 55] and Rb_2 [56] in the vibrational ground state have been produced. As these indirect cooling techniques rely on having pre-cooled atoms, in the past production has been limited to alkali metal dimers. However due to progress in laser cooling of species such as ytterbium [57], a number of experiments are currently focussed on producing molecules such as RbYb and CsYb.

1.2 Project aims

This section describes the techniques that we plan to employ in order to create an ultracold dipolar gas. For our experiment there are two possible ways in which this can be done. Either polar molecules can be sympathetically cooled using ultracold atoms, or the same ultracold atoms can be electrically polarised by using a high electric field, thus producing the desired dipolar interactions.

1.2.1 Sympathetic cooling of polar molecules

In order to create an ultracold dipolar gas, we plan to sympathetically cool polar molecules by using ultracold atoms. As mentioned in the previous section, the molecules must first undergo a preliminary cooling stage, such as Stark deceleration, helium buffer gas cooling, or laser cooling. Next, the molecules must be trapped and subsequently overlapped with an ultracold cloud of atoms. Provided elastic collisions occur, the two species will reach thermal equilibrium, and a cold cloud of polar molecules will be produced.

Although the basic idea is simple, it is challenging to realise experimentally. This is largely due to the occurrence of inelastic collisions, which produce a heating effect. These are particularly problematic if the molecule is not confined in its absolute ground state. This is because the collision can de-excite the molecule to an untrapped state, causing it to be lost. As a result the ratio of the elastic to inelastic collision cross section is an important parameter. A general rule of thumb is that this ratio must be greater than 100 for sympathetic cooling to be successful [58]. There is also a possibility that the two species will undergo a chemical reaction. Therefore the molecular and atomic species used in our experiment must be carefully selected. As the molecular trap can influence the type of collisions that occur, it must also be chosen with care.

To act as a refrigerant, lithium-7 atoms are a good choice as they can be evaporatively cooled to temperatures below $1\,\mu$K. In addition to this, their low mass results in a large angular momentum barrier, so that s-wave scattering dominates at relatively high temperatures [59]. As there is no orbital angular momentum in the collisions, the probability of an inelastic collision is greatly reduced.

In order to determine which kind of molecular trap is most suited for sympathetic cooling of ^{7}LiH molecules with ^{7}Li atoms, simulations have been carried out for three different kinds of trap [60]. In each simulation the atom cloud contained 10^{10} lithium atoms at a temperature of $50\,\mu$K. The first trap to be studied was a static electric trap. It works by creating a minimum in the electric field, thus confining only low-field seeking states. As the absolute ground state of a molecule is always high-field seeking, inelastic collisions will lead to trap loss. Therefore the inelastic collision rate has to be low if cooling is to be successful. These simulations indicated that sympathetic cooling in a static electric trap is likely to fail due to the small ratio of elastic to inelastic collision cross sections. It is worth noting that these simulations used collision cross sections that were calculated in zero electric field. As demonstrated in [61], the presence of an electric field can have a large effect on atom-molecule collisions. In particular it was found that the inelastic collision cross section for Rb + ND_3 was enhanced by the presence of the electric trapping field, implying that sympathetic cooling in a static electric trap is even more likely to fail.

Simulations were also carried out for molecules in an AC electric trap and a microwave trap [62]. As both of these confine the absolute ground state, inelastic collisions are suppressed. However in the AC trap, collisions can force the molecules into an unstable trajectory, causing them to be ejected. The losses produced by this mechanism are significant. After only 1 s of cooling, 94% of the molecules are lost, and after 10 s of cooling 99% are lost. As a result an AC electric trap is also unsuitable for sympathetic cooling. In the microwave trap on the other hand, there are no such losses, thus making sympathetic cooling achievable. In particular it was shown that after 10 s of cooling, the molecular temperature was reduced from 100 mK to 200 μK. On average, 30 collisions per molecule were required to reach this temperature.

In response to these findings, a prototype microwave trap has recently been constructed and characterised in our laboratory [63, 64]. It consists of two concave copper mirrors which are used to form a Fabry-Pérot cavity. The mirrors have a diameter of 90 mm, a radius of curvature of 73 mm and a separation of 35 mm. In order to form a standing wave, microwaves are injected into the cavity through a small hole in one of the mirrors. This allows high-field seeking molecules, and atoms, to be confined at the antinodes of the standing wave. To increase the quality factor of the cavity, which depends on the fractional power loss per round trip, the mirrors are internally cooled using liquid nitrogen. Typical trap depths for molecules are on the order of 1 K, whilst for lithium atoms the trap depth is 0.44 mK. Currently an ultra high vacuum compatible version is being built and tested. It has been designed so that ultracold lithium can be magnetically transported from a lithium MOT into the microwave trap and that is one of the goals of this work.

1.2.2 Atoms under high electric fields

The second way in which we can create an ultracold dipolar gas is by polarising the lithium atoms using a very high electric field. To achieve this, the atoms must first be positioned between two electrodes. By applying a high voltage to the electrodes, the resulting electric field will induce a dipole on each atom, thus producing the desired dipolar interactions. For lithium-7 trapped in the $F = 2$, $M_F = 2$ state, the scattering length is $a_s = -27.6a_0$, where a_0 is the Bohr radius [65]. By using equation (1.1) we find that an electric field of 1 MV/cm only produces a value of $\epsilon_{dd} = 0.16$. Comparing this to some of the values of ϵ_{dd} for other systems, as shown in table 1.1, this is no better than the value given for Chromium atoms. However if the lithium atoms are instead trapped in the $F = 1$, $M_F = -1$ state, then the scattering length is $a_s = 5.3a_0$, which produces a value of $\epsilon_{dd} = 0.82$ when an electric field of 1 MV/cm is used. Although this is slightly below the value required for dipolar interactions to dominate, they should still have a significant effect on the properties of the gas. To date a dipolar gas of this nature has not been experimentally realised.

Dipole type	C_{dd}	**Species & parameter values**	ϵ_{dd}
Magnetic	$\mu_0\mu^2$	^{7}Li, $\mu = \mu_B$, $a_s = -27.6a_0$ [65] ^{52}Cr, $\mu = 6\mu_B$, $a_s = 96a_0$ [66]	0.002 0.16
Induced electric	α^2E^2/ϵ_0	^{7}Li, $\alpha = 164\,\mathrm{au}$ [67], $E = 1\,\mathrm{MV/cm}$, $F = 2$, $M_F = 2$, $a_s = -27.6a_0$ $F = 1$, $M_F = -1$, $a_s = 5.3a_0$ [65]	0.16 0.82
Permanent electric	d_e^2/ϵ_0	Molecule, $d_e = 1\,\mathrm{D}$, $m = 50\,\mathrm{amu}$, $a_s = 100a_0$ [68]	47

Table 1.1: Comparison of ϵ_{dd} for different atomic and molecular systems. The atomic unit of electric polarisability is au= $e^2a_0^2/E_h$, where e is the charge of the electron, a_0 is the Bohr radius and E_h is the Hartree energy.

It is worth noting that producing an electric field of 1 MV/cm is by no means trivial. In order to achieve anything close to this value, great care must be taken to ensure that the electrodes have a smooth surface. As the size of the electric field is given by $E = V/d$, where V is the applied voltage and d is the electrode separation, it is important to keep d as small as possible. Therefore we plan to set $d = 0.5\,\mathrm{mm}$. To reach our desired field, the two electrodes will be held at $V = \pm 25\,\mathrm{kV}$ respectively. Although our ultimate aim is to generate an electric field of 1 MV/cm, provided the field is greater than 0.45 MV/cm, the value of ϵ_{dd} will be greater than 0.16. If a field of approximately 0.54 MV/cm can be reached, it should be possible to experimental verify the existence of a shape resonance that has been predicted for lithium atoms in the $F = 2$, $M_F = 2$ state [69]. This has interesting applications, as it allows the scattering length to be tuned from negative to positive. Therefore the unstable condensate that is usually formed by lithium atoms in the $F = 2$, $M_F = 2$ state could be stabilised by varying the size of an external electric field. This shows that even if we are unable to produce a field of 1 MV/cm, interesting properties can still be investigated.

1.3 Thesis overview

Although there are two possible ways in which we can create an ultracold dipolar gas, both techniques rely on having an ultracold source of lithium-7 atoms. This thesis describes the work that has been carried out to cool, trap and transport such a cloud. Broadly the setup consists of a lithium oven, Zeeman slower, magneto-optical trap (MOT) and magnetic trap. As we plan to electrically polarise the lithium atoms, a setup capable of producing fields of up to 1 MV/cm needs to be developed. Therefore this thesis also highlights the progress that has been made towards realising this goal.

This thesis has been divided into three main chapters. Chapter 2 begins with a brief outline of the relevant theory associated with laser cooling and trapping. This is followed by a description of the original setup that was used to cool, trap and transport lithium atoms. From initial transportation experiments it became clear that the setup suffered from a number of shortcomings. To overcome these problems, it was redesigned. This new setup, which is currently in use, is described in detail. Finally the results of characterisation experiments are presented. In particular the number of atoms trapped in the MOT, and the cloud temperature are measured, and subsequently optimised by varying parameters such as the laser beam power and detuning.

Chapter 3 describes the magnetic trap and transportation system that we use to move atoms from one vacuum chamber to another. Atomic transport is necessary because neither the microwave trap, nor the high field electrodes can be directly overlapped with atoms confined in the MOT. After the atoms have been transported, it is important that we are able to image them. Therefore the problems associated with imaging the atom cloud after release from the magnetic trap are highlighted. In order to determine the source of these problems line shape measurements were taken. These results, and their implications are discussed in detail. This is followed by a description of the method used to test and optimise the transport procedure.

Finally chapter 4 covers the progress that has been made towards generating high electric fields. First the processes which lead to electrical breakdown are described along with the techniques that are commonly employed to improve electrode performance. In order to electrically polarise the atoms, in addition to a high field, we require almost perfectly parallel electrodes. Achieving this through machining of the electrode surface is incredibly challenging. Therefore we have designed an adjustable electrode mount that allows the angle between the plates to be precisely varied. By using indium tin oxide (ITO) coated glass electrodes, interferometric techniques can be employed to ensure that the plates are parallel. Using this design, high voltage tests were performed. It was not possible to generate the high fields that we require, therefore super-polished stainless steel electrodes were also tested. As it is not possible to align these electrodes using interferometric techniques, the electrode mount has recently been redesigned by Devin Dunseith. An overview of this new design is given. The chapter concludes by describing the next steps that will be taken in order to create an ultracold dipolar gas.

Chapter 2

The lithium MOT

This chapter details the experimental setup used to cool and trap a large cloud of lithium-7 atoms. In section 2.1 a brief introduction to the theory of laser cooling is given, along with a description of the properties of magneto-optical traps. Section 2.2 describes the original experimental setup used and the problems associated with it. The new setup that has been built to overcome these problems is detailed in section 2.3, and the methods used to image the atoms are described in section 2.4. Finally the results of experiments to optimise the number of trapped atoms, compress the cloud and cool it further are reported in sections 2.5 and 2.6.

2.1 Laser cooling and trapping

Without the invention of the laser the field of atomic physics would not be what it is today. The start of modern day atomic physics experiments can be marked by the suggestion made in 1975 by Hänsch and Schawlow that laser light could exert a substantial force on atoms that could be used to cool them [70]. Around the same time it was suggested by Wineland and Dehmelt that laser cooling could also be applied to trapped ions [71]. Further development of this idea came a few years later when Ashkin suggested that lasers could be used not only to cool but also to trap atoms [72].

In 1982 came the first demonstration of deceleration of an atomic beam by laser light [73] and since then laser cooling has proved to be a hugely successful technique. As the range of laser wavelengths has increased, so too has the variety of species that have been successfully laser cooled [48, 57, 74, 75]. In addition to this laser cooling has a wide variety of applications in such things as tests of fundamental symmetries, investigations into quantum degenerate gases, and the development of time and frequency standards.

In order to understand how laser cooling and trapping works, it is necessary to first look at how light and atoms interact. To do this we will use a semiclassical approach, that is, the atom is treated as a quantum mechanical system and the light as a classical electric field. It should be noted that only a brief outline of important concepts is given here and for a more thorough explanation the reader is directed to [76] and the references therein.

To simplify the situation the atom is modelled as a two level system consisting of a ground state $|g\rangle$ with energy E_g and an excited state $|e\rangle$ with energy E_e such that $E_e - E_g = \hbar\omega_0$, where ω_0 is the angular frequency of the atomic transition. The light drives transitions between $|g\rangle$ and $|e\rangle$ with a strength governed by the electric dipole moment matrix element, $D = e\langle e|\underline{\epsilon} \cdot \underline{\hat{r}}|g\rangle$, where e is the charge of the electron, $\underline{\hat{r}}$ is the position operator and $\underline{\epsilon}$ is a unit vector defining the state of polarisation of the light. The wavelength of an atomic transition is much longer than the size of the atom, so the spatial variation of the electromagnetic field over the volume of the atom can usually be neglected. This is the dipole approximation and in this approximation the Rabi frequency Ω, which describes the oscillation frequency between the two states when the light is on resonance, is related to D by

$$\Omega = -\frac{DE_0}{\hbar} = -\frac{e\langle e|\underline{\epsilon} \cdot \underline{\hat{r}}|g\rangle E_0}{\hbar} \tag{2.1}$$

where E_0 is the amplitude of the electric field.

Once the atom is in the excited state it can undergo either stimulated or spontaneous emission. When the lifetime of the excited state is short, as it is for the lithium D2 line which has a lifetime of $\tau = 26.87\,\mathrm{ns}$, then the process of spontaneous emission becomes important. The optical Bloch equations give a complete description of the coherences and populations of the system, taking into account the damping term which arises due to spontaneous emission. Finding the steady state solution of the optical Bloch equations then yields an expression for the population of the excited state ρ_{ee} as [76]

$$\rho_{ee} = \frac{2\Omega^2/\Gamma^2}{2(1 + 2\Omega^2/\Gamma^2 + 4\delta^2/\Gamma^2)}, \tag{2.2}$$

where Γ is the decay rate of the transition, which is also known as the natural linewidth, and $\delta = \omega - \omega_0$ is the detuning of the laser light from the atomic resonance, where ω is the angular frequency of the light. By defining the saturation parameter s_0 as

$$s_0 = \frac{I}{I_{\text{sat}}} = \frac{2|\Omega|^2}{\Gamma^2}, \tag{2.3}$$

where I is the laser intensity, and I_{sat} is the saturation intensity, the equation for the excited state population can be rewritten in the more useful form,

$$\rho_{ee} = \frac{I/I_{\text{sat}}}{2(1 + I/I_{\text{sat}} + 4\delta^2/\Gamma^2)}. \tag{2.4}$$

Rearranging equation (2.3) to give $I_{\text{sat}} = I\,\Gamma^2/(2|\Omega|^2)$, makes it possible to find an expression for the saturation intensity. By using equation (2.1), along with the relations $I = (c\epsilon_0 E_0^2)/2$, and $\Gamma = (\omega^3 e^2 |\langle e|\underline{\epsilon} \cdot \underline{\hat{r}}|g\rangle|^2)/(3\pi\epsilon_0 \hbar c^3) = 1/\tau$ we find

$$I_{\text{sat}} = \frac{\pi h c}{3\lambda^3 \tau}. \tag{2.5}$$

The scattering rate R_{scatt}, is given by the population of the excited state multiplied by the decay rate of the transition,

$$\begin{aligned} R_{\text{scatt}} &= \Gamma \rho_{ee} && (2.6)\\ &= \frac{\Gamma}{2} \frac{s_0}{(1 + s_0 + 4\delta^2/\Gamma^2)}. && (2.7) \end{aligned}$$

2.1.1 The spontaneous force

The force used to laser cool atoms is produced by the repeated cycle of absorption and emission of photons that comes about when an atom is exposed to resonant laser light. Each time the atom absorbs a photon, it receives a small momentum kick of size $\Delta p = \hbar k$, in the direction of travel of the photon. Here k is the wavevector of the light and is related to the wavelength by $k = 2\pi/\lambda$. When the atom de-excites it will spontaneously emit a photon in some random direction and again will experience a momentum kick. Therefore laser cooling works because all absorbed photons come from a particular direction whereas spontaneously emitted photons are distributed isotropically, so averaging over many cycles there is a net force in the propagation direction of the incident laser beam. This can be used to oppose the motion of the atom and hence slow it down.

To find how much force is exerted by the light on the atom, we start with Newton's second law,

$$F = \frac{dp}{dt}, \tag{2.8}$$

where p is the momentum of the photon. The rate of change of momentum is equal to the momentum of a single photon multiplied by the rate at which photons are scattered. This means the force can be written as

$$F_{\text{spon}} = \hbar k R_{\text{scatt}}, \tag{2.9}$$

where F_{spon} is called the spontaneous force because it relies on the absorption and subsequent spontaneous emission of photons. Using equation (2.7) this becomes

$$F_{\text{spon}} = \hbar k \frac{\Gamma}{2} \frac{s_0}{(1 + s_0 + 4\delta^2/\Gamma^2)}. \tag{2.10}$$

As $I \to \infty$, the force limits to $F_{\max} = \hbar k \Gamma/2$. This happens because the rate of spontaneous emission for a two level atom tends to $\Gamma/2$ when the intensity of the light is high, as in the steady state the populations of the upper and lower states both approach a half. For lithium we find that the light will exert a maximum force of $1.8 \times 10^{-20}\,\text{N}$, which is equivalent to a deceleration of $1.6 \times 10^{6}\,\text{m/s}^2 \approx 160,000\,\text{g}$. In our experiment the lithium gas typically has a temperature in the region of $500\,^\circ\text{C}$ ($773\,\text{K}$), which means the atoms have a velocity of around $960\,\text{m/s}$. With this velocity we require a minimum distance of $0.29\,\text{m}$ to slow a lithium atom to rest, and require over $11,000$ scattering events.

2.1.2 Optical molasses

Now that we have an expression for the force exerted by light on an atom, it is instructive to look at the resultant force from two counter-propagating light beams of the same frequency. This configuration is called a one dimensional optical molasses and can readily be extended to three dimensions by the inclusion of two more counter-propagating beam pairs placed in orthogonal directions to the first.

To produce the frictional force which gives the optical molasses its name, the beams must have a frequency lower than that of the atomic transition ($\delta < 0$), in other words the beams must be red detuned. Here it is assumed that the total force acting on the atom is equal to the sum of the force from each of the two individual beams. Using equation (2.10) from the previous section, it is clear that for a stationary atom the net force will be zero. However if the atom is moving, then because of the Doppler shift $\Delta\omega$, an imbalance in the force is created.

Placing the one dimensional optical molasses along the horizontal x axis and starting with an atom travelling with velocity v in the positive x direction, the frequency of the light as seen by the atom will be shifted according to $\Delta\omega = k \cdot v$. This means the atom will see the counter-propagating beam as having a higher frequency and the co-propagating beam as having a lower frequency. As the beam is red detuned, it follows that the counter-propagating beam will be shifted closer to resonance and therefore the atom will absorb more photons from this beam. This will lead to a net force which will act to slow the atom down.

The Doppler shift introduces an additional term into the detuning giving $\delta_{\mathrm{om}} = \omega - \omega_0 \mp kv$, where the sign of kv depends on the relative motion between the atom and the light. The total force acting on the atom in a one dimensional optical molasses can then be written out as

$$\begin{aligned}
F_{\mathrm{om}} &= F_{\mathrm{spon}}(\omega - \omega_0 - kv) - F_{\mathrm{spon}}(\omega - \omega_0 + kv) && (2.11)\\
&\approx F_{\mathrm{spon}}(\omega - \omega_0) - kv \left.\frac{\partial F}{\partial \delta}\right|_{\omega-\omega_0} - \left[F_{\mathrm{spon}}(\omega - \omega_0) + kv \left.\frac{\partial F}{\partial \delta}\right|_{\omega-\omega_0} \right] && (2.12)\\
&\approx -2kv \left.\frac{\partial F}{\partial \delta}\right|_{\omega-\omega_0} && (2.13)
\end{aligned}$$

where we have carried out a Taylor expansion and assumed that the velocity and hence Doppler shift is small, thus allowing all terms of order v^3 and higher to be neglected. Note that the term proportional to v^2 vanishes. The force can now be written in the form $F_{\mathrm{om}} = -\alpha v$, where α is called the damping coefficient. By differentiating equation (2.10) with respect to δ, we end up with an expression for the force in an optical molasses,

$$F_{\mathrm{om}} = 8\hbar k^2 s_0 \frac{\delta/\Gamma}{[1 + s_0 + 4\delta^2/\Gamma^2]^2} v. \tag{2.14}$$

Figure 2.1 shows how the force in an optical molasses varies with velocity. The blue curve shows the total force given by equation (2.11), the red line is the linear approximation of equation (2.14) and the black dashed lines represent the force from each individual laser beam, as described by equation (2.10). Here we can see that the linear approximation is only valid at low velocities. In this region the force is proportional to the velocity of the atom, so faster atoms will experience a larger force. However as the velocity continues to increase the force begins to decline, as shown by the blue curve. At these higher velocities the Doppler shift is no longer small, and the light becomes increasingly detuned from the atomic transition, leading to a smaller force and ineffective slowing of the atom. The capture velocity of the optical molasses, defined as $v_c^{\mathrm{om}} = \delta/k$, indicates the velocity below which the linear approximation holds.

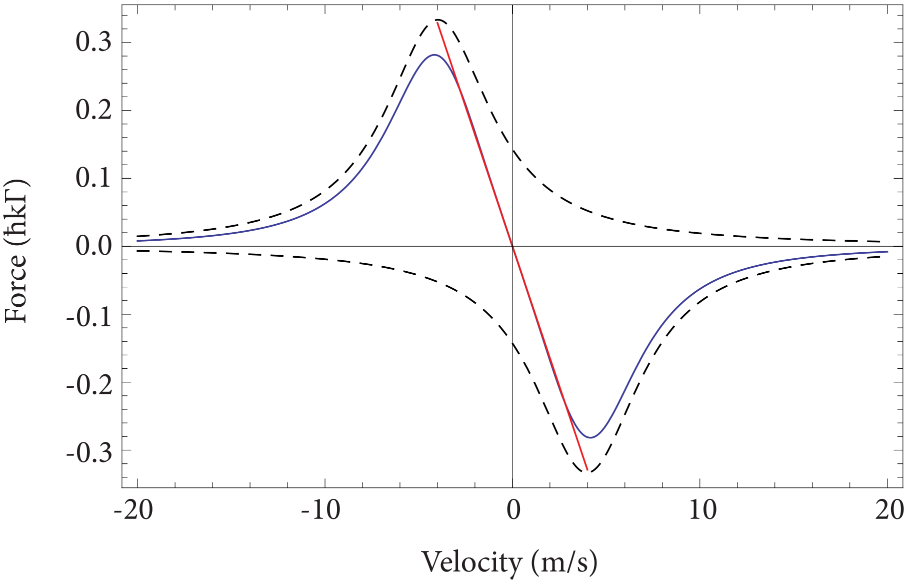

Figure 2.1: Velocity dependence of the force in a one dimensional optical molasses given a detuning $\delta = \Gamma$ and a saturation parameter $s_0 = 2$. The dashed black curves show the force from each of the two counter-propagating beams and the blue curve is the combined force from these two beams. The red line shows how the total force can be approximated by a damping force for low velocities.

It may seem as though an optical molasses alone would be enough to trap atoms, as naively we might expect the frictional force to cool the atoms to zero velocity, thus effectively trapping them within the confines of the optical molasses beams. This however would result in a cloud with zero temperature, which is clearly unphysical. The reason this does not happen is due to the fact that the frictional force is discontinuous in nature. This leads to the cloud reaching a non-zero temperature limit, the details of which are discussed in section 2.1.5, and means that an optical molasses produces a dissipative force which confines the atoms in velocity space. In other words an optical molasses can only be used to slow the atomic motion. In order to trap the atoms, an additional restoring force must be applied which acts whenever an atom moves too far away from a particular point in space.

2.1.3 The magneto-optical trap

By combining three pairs of orthogonal, counter-propagating light beams and a modest, inhomogeneous magnetic field, it is possible to form an atom trap. This trap configuration is called a magneto-optical trap, or MOT, and was first demonstrated by Raab *et al.* in 1987 using sodium atoms [77]. By using a three dimensional optical molasses the resultant damping force is able to slow the atomic motion, whilst the magnetic field is used to tune the atom-light interaction creating a position dependent restoring force. This results in atoms that are both cooled and trapped.

In a MOT, the restoring force used to trap atoms is created by having both a linearly varying magnetic field gradient and light with the correct polarisation. In order to generate the required spherical quadrupole field, which has a zero field point at its centre, a pair of anti-Helmholtz coils are used. Typical field gradients are in the region of $10 - 20\,\mathrm{G/cm}$, meaning that the magnetic field alone provides only a weak trapping force.

To understand the details of how a MOT works, we start with the situation depicted in figure 2.2. For simplicity we choose a system with only two energy levels, an $F = 0$ ground state and an $F' = 1$ excited state, where the prime is used to indicate the excited state. Here $F = I + J$, where F is the total angular momentum of the atom, I is the nuclear spin and J is the total electronic angular momentum. These particular states have been selected for clarity only, meaning that the following explanation can be readily extended to any other $F = N$ to $F' = N + 1$ pair of states.

A one dimensional optical molasses is formed along the horizontal x axis where both beams are circularly polarised. The polarisations have been chosen so that the beam travelling towards the left excites a σ^- transition, meaning $\Delta M_F = -1$, where M_F is the projection of the total angular momentum on the magnetic field axis. The beam travelling towards the right excites a σ^+ transition, so $\Delta M_F = +1$. As before both beams have the same frequency and are red detuned.

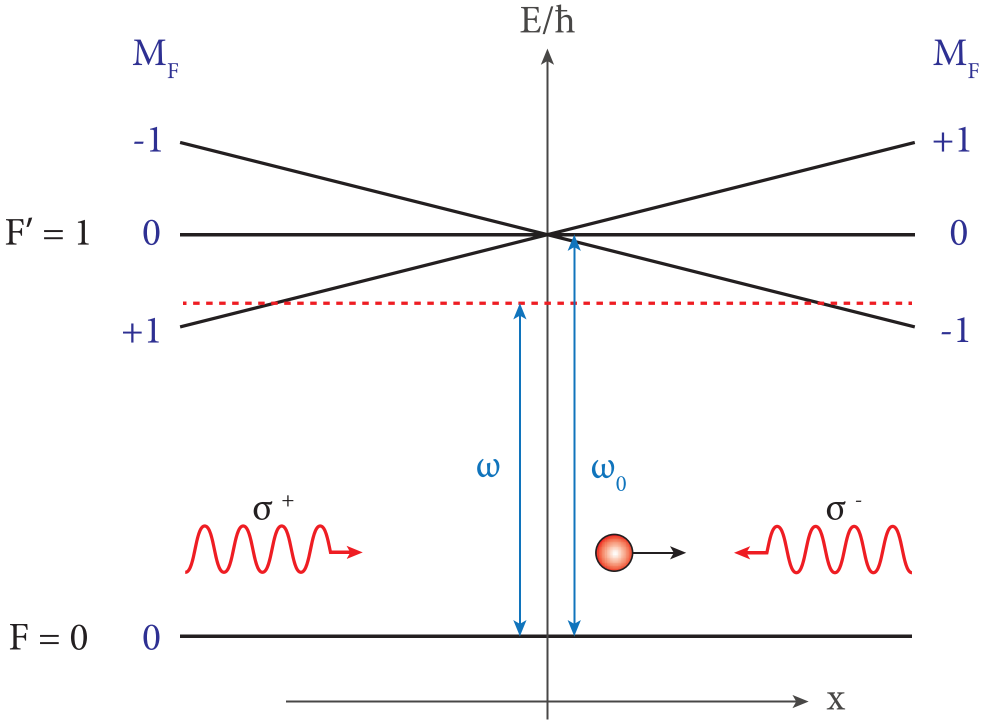

Figure 2.2: Illustrates the MOT trapping mechanism for an atom with an $F = 0$ ground state and an $F' = 1$ excited state. A linearly varying magnetic field produces a Zeeman shift of the excited states causing an atom moving to the right to experience a restoring force back to the centre of the trap.

Due to the Zeeman effect, the energy levels of the atom shift as it moves through the magnetic field. Consider what happens to an atom moving to the right. As the magnetic field increases the $M_F = -1$ state is shifted to lower energies, bringing it closer into resonance with the σ^- laser beam. This causes the atom to absorb more photons from this beam than the σ^+ beam, resulting in a force which pushes the atom back towards the zero field point at the centre of the trap. If however the atom is moving to the left, the opposite situation arises where the $M_F = +1$ state is brought closer into resonance with the σ^+ light and so again the atom will absorb more photons from the laser beam which opposes its motion, thus pushing the atom back towards the trap centre. In a MOT, this situation occurs along all three orthogonal axes and so provides a three dimensional restoring force that depends on the position of the atom.

Going back to equation (2.10) which describes the force exerted by a single laser beam on an atom, it is possible to include the effect of the magnetic field by introducing a Zeeman shift term into the detuning along with the Doppler shift term described in section 2.1.2. In the MOT the total detuning is given by $\delta_{\text{mot}} = \omega - \omega_0 \mp kv \pm \frac{\Delta\mu B(x)}{\hbar}$, where $B(x)$ is the magnetic field as a function of position and $\Delta\mu = (g_{F'}M_{F'} - g_F M_F)\mu_B$ is the effective magnetic moment of the transition in question. Here μ_B is the Bohr magneton and $g_{F'}$ and g_F are the Landé g-factors of the excited and ground states respectively.

Using a similar method as was used for the optical molasses, we can write down an approximation to the total force in the MOT along one axis. Here it is assumed that the Doppler shift and Zeeman shift are both small compared to the detuning, $\delta = \omega - \omega_0$. The total force can then be written in the form $F_{\text{mot}} = -\alpha v - \kappa x$, where κ is the spring constant and equals

$$\kappa = \frac{2\Delta\mu B'}{\hbar} \frac{\partial F}{\partial \delta}\bigg|_{\omega-\omega_0} \tag{2.15}$$

$$= \frac{\Delta\mu B'}{\hbar k}\alpha. \tag{2.16}$$

Here $B(x)$ has been replaced by using $B(x) = B'x$ where B' is the magnetic field gradient. Writing out fully the expression for the total force in the MOT we are left with

$$F_{\text{mot}} = -\alpha v - \kappa x \tag{2.17}$$

$$= 8\hbar k^2 s_0 \frac{\delta/\Gamma}{[1 + s_0 + 4\delta^2/\Gamma^2]^2}\left(v + \frac{\Delta\mu B'}{\hbar k}x\right). \tag{2.18}$$

Looking at the form of equation (2.17) we see that the atoms in a MOT undergo damped simple harmonic motion. This means there is a characteristic angular oscillation frequency, ω_{mot}, as well as a damping rate, Γ_{mot}, that describes the motion of atoms in the MOT. These are given by

$$\omega_{\text{mot}} = \sqrt{\frac{\kappa}{m}} \tag{2.19}$$

$$\Gamma_{\text{mot}} = \frac{\alpha}{m}, \tag{2.20}$$

where m is the mass of the atom. Using typical values for our lithium MOT, namely $\delta = -3.5\,\Gamma$, $s_0 = 2.2$, $B' \approx 15\,\text{G/cm}$ and cooling on the $F = 2$, $M_F = 2$ to $F' = 3$, $M_{F'} = 3$ transition which gives $\Delta\mu = \mu_B$, the oscillation frequency is then $\omega^{\text{Li}}_{\text{mot}} = 5.1\,\text{krad/s}$ and the damping rate is $\Gamma^{\text{Li}}_{\text{mot}} = 18.4\,\text{krad/s}$. As the damping rate is larger than the oscillation frequency, the system is overdamped. This is generally true for all MOTs.

Two additional parameters which are useful to define when characterising the MOT are the capture radius R_c and the capture velocity v_c, which is not to be confused with the capture velocity of the optical molasses, v^{om}_c described earlier. The capture radius is defined as the distance from the trap centre at which an atom at rest will be resonant with the MOT light. This is simply given by

$$R_c = \frac{\hbar\delta}{\Delta\mu B'}. \tag{2.21}$$

This quantity gives a measure of the trapping volume of the MOT such that if an atom enters this volume with a sufficiently low velocity it will remain trapped within the MOT. In the situation where the capture radius is larger than the radius of the MOT beams, the latter should be used instead. Employing the same values as used previously for our lithium MOT results in a capture radius of $R_c = 0.99\,\mathrm{cm}$, which is just slightly larger than our beam radius of 0.96 cm. Therefore the capture radius of our MOT is $R_c^{\mathrm{Li}} = 0.96\,\mathrm{cm}$.

The capture velocity is defined as the highest atomic velocity that can be slowed to $v = 0$ within the trapping region. An estimate is obtained by assuming the maximum acceleration, $a_{\max} = F_{\max}/m = \hbar k\Gamma/2m$ is continuously applied over a distance of R_c, and results in

$$v_c = \sqrt{\frac{\hbar k\Gamma R_c}{m}}. \tag{2.22}$$

Using the value of R_c^{Li} given above and the usual values we have in our MOT, this leads to a capture velocity of $v_c^{\mathrm{Li}} = 174\,\mathrm{m/s}$. This is an over-estimate of the actual capture velocity as the atom cannot be resonant with the light throughout the entire slowing process and the laser intensity is finite. In [78] the capture velocity of a lithium MOT was found to be approximately 35 m/s when using a MOT beam detuning of -2Γ (red detuned), whilst at a detuning -5Γ the capture velocity was about 50 m/s. As our setup is similar, it is reasonable to assume that the capture velocity for our lithium MOT lies somewhere within this range.

2.1.4 MOT density limit

In the MOT there are two distinct density regimes which occur depending on the total number of atoms, N, that are present. When N is small, typically less than 10^4, the cloud density is low, meaning that interatomic effects can be neglected and the cloud can be treated as a collection of N independent particles. In this situation the density distribution $n(x, y, z)$ for a cloud at temperature T, in a potential $U(x, y, z)$ is given by the Boltzmann distribution

$$n(x, y, z) = n_0 e^{-\frac{U(x,y,z)}{k_B T}} \tag{2.23}$$

where n_0 is the peak density of the cloud. As can be seen in equation (2.17) the potential is harmonic, which leads to

$$U(x, y, z) = \frac{1}{2}(\kappa_x x^2 + \kappa_y y^2 + \kappa_z z^2). \tag{2.24}$$

Clearly the density distribution of the cloud is Gaussian, with a width along each Cartesian axis given by

$$\sigma_i = \sqrt{\frac{k_B T}{\kappa_i}} \tag{2.25}$$

where $i = x, y, z$. Normalising the distribution to the total number of atoms then produces a value for the peak atomic density,

$$n_0 = \frac{N}{(\sqrt{2\pi})^3 \sigma_x \sigma_y \sigma_z} \tag{2.26}$$

$$= \frac{N}{2(\sqrt{2\pi}\sigma_z)^3}, \tag{2.27}$$

where we have assumed a typical MOT configuration so that the magnetic field gradient along the coil axis, that is the z axis, is twice that of either the x or y directions, meaning $\sigma_x/\sqrt{2} = \sigma_y/\sqrt{2} = \sigma_z$. In this regime the radius of the cloud depends only on the temperature so that for a fixed T, as the atom number increases, so too does the density. In the vast majority of MOTs however the atom number is well above this low density limit, and this results in the density reaching a peak value such that when more atoms are added only the radius of the cloud will increase.

This second density regime occurs when $N > 10^4$ and is called the multiple scattering regime. Here the atom cloud density is sufficiently high that a scattered photon has a significant chance of being reabsorbed by a second atom. This leads to an effective repulsive force between the two atoms and so sets a limit on the density that can be achieved in the MOT. In [79] this maximum density is calculated to be of the form

$$n_{\max} \sim \frac{\kappa}{I\sigma_L(\sigma_R - \sigma_L)}, \tag{2.28}$$

where I is the laser intensity, σ_L is the cross section for absorbing a photon from the laser field and σ_R is the cross section for absorbing a re-radiated photon. In general these two cross sections are different because the re-radiated photons don't necessarily have the same polarisation, or frequency as the incident laser photons. Using a two level model for the atom, the absorption cross section for the laser light can be calculated using [80]

$$\sigma_L = \frac{3\lambda^2}{2\pi}\frac{1}{1+s_0+4\delta^2/\Gamma^2}, \tag{2.29}$$

whilst the value of κ can be found from equation (2.16). Obtaining an expression for σ_R is more involved. However for caesium it has been calculated numerically in [79] and analytically in [80] and [81].

Upon entering the multiple scattering regime the density distribution observed in [80] was well approximated by a Gaussian, and was found to have a maximum density which was almost completely independent of atom number. This means that as more atoms are added to the MOT the size of the cloud grows with no further increase in the density. Our observations, which are described in section 2.5.2, align well with this observation. In general the maximum density limit in the MOT tends to be around 10^{11} atoms/cm^3 regardless of the alkali species used [78, 80, 82].

In order to overcome this density limit two principal methods have been developed. The first is the dark spontaneous force optical trap (dark-SPOT) developed by Ketterle *et al.* in 1992 which reported densities approaching 10^{12} atoms/cm^3 [83]. Here they describe two processes by which the density in the MOT is limited, the first is due to re-radiated photons as explained above, the second is due to collisions between ground and excited state atoms where part of the excitation energy is converted into kinetic energy, thus ejecting the atom from the trap [84]. The dark-SPOT aims to mitigate both of these effects by keeping the atoms mostly confined in a dark state. This reduces the number of scattered photons, thus lowering the probability of another atom absorbing a re-radiated photon. It also reduces the amount of time that the atoms spend in the excited state and so decreases the rate of trap loss due to collisions between ground and excited state atoms, therefore allowing the density limit to be overcome.

The dark-SPOT can either be implemented temporally or spatially. In the temporal case it involves initially loading the atoms into a normal MOT so as to maximise the atom number, then reducing the intensity of the repump light for some period of time, thus forming a dark trap and allowing the cloud density to increase. The spatial realisation, often called a dark spot MOT, is generally a better choice as it allows the dark trap to be continuously loaded. It requires blocking a central portion of the repump light, thereby creating a dark spot at the centre of the MOT. When an atom reaches this central region it will be pumped to the dark state. If the atom then moves away from the centre, both repump and trapping light will be present and so the atom will once again enter the cooling cycle. Provided this spot is centred on the magnetic field minimum then the coldest atoms will accumulate in the dark spot and as before, due to the reduction in scattered photons, there will be an increase in the density.

The second approach used to overcome the density limit is to implement a compressed MOT [85]. Here the aim is to alter the spring constant, κ, of the trap because in the multiple scattering regime, as can be seen by equation (2.28), the density of the MOT is proportional to κ. Equation (2.16) shows that the spring constant in turn is proportional to the magnetic field gradient. Therefore by increasing the field gradient there should be a corresponding increase in the cloud density. As observed by Höpe *et al.* in [86] however, as the magnetic field gradient is increased the number of atoms loaded into the MOT can decrease dramatically. This phenomenon is indicated by equations (2.21) and (2.22), which show that as the magnetic field gradient increases the capture radius and capture velocity of the MOT decrease. A higher field gradient means that the Zeeman shift at a particular position is larger, so the point at which an atom at rest will be resonant with the laser beam, i.e. the capture radius, is shifted closer to the trapping centre. This leads to a reduction in the capture velocity, which means hotter atoms can no longer be trapped. Therefore the total atom number in the MOT decreases.

Clearly to have a large atom number at high density a separation of the collection and compression processes should be employed. This requires a MOT with a low field gradient to be used initially in order to collect a large number of atoms, followed by a period of compression which is achieved by rapidly increasing the field gradient. In this situation sometimes it is also beneficial to increase the detuning of the trapping light so that the scattering rate is reduced. The compressed MOT has been implemented using lithium-6 in [87], where there was a slight increase in the density going from 2.4×10^{10} atoms/cm^3 to 3.4×10^{10} atoms/cm^3 after compression.

2.1.5 Doppler cooling limit

As mentioned in section 2.1.2 there is a finite, non-zero temperature limit to which the atoms in an optical molasses can be cooled. This temperature limit, known as the Doppler cooling limit, comes about because the force exerted by light is discontinuous. In previous sections the force that has been calculated is the *average* force exerted over many absorption and emission cycles. This means the actual force applied at any given time will fluctuate, and it is these variations in the force which produce heating that counteracts the cooling effect of the light, resulting in a non-zero temperature limit.

There are two different sources of fluctuations which go on to produce heating. The first comes from variations in the number of photons absorbed in a given time interval, whilst the second is due to fluctuations in the direction of spontaneously emitted photons. Both of these processes lead to a random walk of the momentum of the atom. In order to find the temperature limit that results from this, it is necessary to find an expression for the heating rate and to compare it to the cooling rate.

To start we again consider an atom in a one dimensional optical molasses. As before the average force exerted on the atom is given by equation (2.14) and results in the average velocity of the atom being reduced to zero. This means the atom is equally likely to absorb a photon from either of the two beams, with each photon absorption contributing a step of size $\hbar k$ to the random walk of the momentum. Each spontaneous emission will also contribute an $\hbar k$ sized step, again with an equal probability of a positive or negative step, provided the situation is purely one dimensional. This means that each scattering cycle represents two steps in the random walk.

Although the mean velocity of the atom is zero, the mean squared velocity is not. Consequently, the mean squared momentum, $\langle p^2 \rangle$, is also non-zero and by finding the rate of change of this quantity it is possible to determine the heating rate. To find an expression for $\langle p^2 \rangle$ first we need to know the number of random walk steps N_p, taken in a given time interval t. This is given by

$$N_{\mathrm{p}} = 2(2R_{\mathrm{scatt}})t, \tag{2.30}$$

where $2R_{\mathrm{scatt}}$ is the total *average* scattering rate. As before R_{scatt} is given by equation (2.7) and the factor two comes from the assumption that two laser beams scatter twice as many photons as a single beam. The factor of two outside the brackets comes about because each scattering event consists of both absorption and emission of a photon. Therefore after N_{p} steps, the mean squared momentum will have increased according to $\langle p^2\rangle = (\hbar k)^2 N_{\mathrm{p}} = 4(\hbar k)^2 R_{\mathrm{scatt}} t$. The rate of change of momentum squared can then be written as

$$\frac{d\langle p^2\rangle}{dt} = 4\hbar^2 k^2 R_{\mathrm{scatt}}. \tag{2.31}$$

Using $E = p^2/2m$, the heating rate for two beams in one dimension becomes,

$$\left(\frac{dE}{dt}\right)_{\mathrm{heat}} = \frac{1}{2m}\frac{d\langle p^2\rangle}{dt} \tag{2.32}$$

$$= 2\hbar^2 k^2 \frac{R_{\mathrm{scatt}}}{m} \tag{2.33}$$

$$= \frac{\hbar^2 k^2 \Gamma}{m}\frac{s_0}{1 + s_0 + 4\delta^2/\Gamma^2}. \tag{2.34}$$

The cooling rate on the other hand is equal to the rate at which the atom loses kinetic energy when subjected to the average light force. For the one dimensional optical molasses this is

$$\left(\frac{dE}{dt}\right)_{\mathrm{cool}} = \frac{d}{dt}\left(\frac{1}{2}mv_x^2\right) = mv_x\frac{dv_x}{dt} \tag{2.35}$$

$$= v_x F_{\mathrm{om}} \tag{2.36}$$

$$= -\alpha v_x^2. \tag{2.37}$$

The atom will reach equilibrium when $(dE/dt)_{\mathrm{heat}} + (dE/dt)_{\mathrm{cool}} = 0$. Using this and rearranging for v_x^2 results in

$$v_x^2 = \frac{\hbar\Gamma^2}{8m|\delta|}(1 + s_0 + 4\delta^2/\Gamma^2), \tag{2.38}$$

where v_x^2 represents either the mean square velocity of a cloud of atoms undergoing laser cooling, or for a single atom, the time average of the squared velocity. To relate this to a temperature we use the equipartition theorem, so for each degree of freedom we have

$$\frac{k_B T}{2} = \frac{mv_i^2}{2} \tag{2.39}$$

where k_B is the Boltzmann constant, and $i = x, y, z$. This results in an equation for the Doppler temperature,

$$T = \frac{\hbar\Gamma^2}{8k_B|\delta|}(1 + s_0 + 4\delta^2/\Gamma^2). \tag{2.40}$$

The minimum temperature is found for $s_0 \ll 1$ and $\delta = -\Gamma/2$, which gives the Doppler cooling limit

$$T_{\mathrm{D}} = \frac{\hbar\Gamma}{2k_B}. \tag{2.41}$$

For lithium with a natural linewidth of 5.92 MHz the Doppler cooling limit is 142 μK. However the majority of lithium laser cooling experiments quote cloud temperatures in the region of $\sim 300\,\mu$K. This is because most experiments have $s_0 > 1$.

Originally it was thought that the Doppler temperature was the lowest temperature that could be reached via laser cooling and early experiments seemed to confirm this as the limit [88, 89]. However later experiments revealed that with the more complex structure of real atoms came new cooling mechanisms, thus allowing even lower temperatures to be reached [90, 91]. As discussed in the following section, these sub-Doppler cooling mechanisms as they are known, have not been observed when laser cooling lithium.

2.1.6 Sub-Doppler cooling

Having discovered that atoms could in fact be cooled to temperatures below the Doppler limit, it became apparent that Doppler theory alone could not fully explain the process of laser cooling. In response to this, a description of the mechanisms associated with sub-Doppler cooling was put forward by Dalibard and Cohen-Tannoudji [92]. Their explanation incorporated two features of the real life system which are ignored in the Doppler theory treatment, that is they took into account the multi-level nature of real atoms as well as the fact that the total polarisation of the light field varies with position.

Taking a one dimensional optical molasses, there are two different sub-Doppler cooling mechanisms which can occur depending on whether the beams have opposite circular polarisations, denoted $\sigma^+ - \sigma^-$, or orthogonal linear polarisations, lin $\perp$ lin. Starting with the lin $\perp$ lin configuration, the total polarisation of the light field varies over a $\lambda/2$ length scale. As depicted in figure 2.3 the polarisation is initially σ^-, it then changes to linear, followed by σ^+ and finally turns linear again, orthogonal to the previous linear polarisation. After this the pattern repeats. This variation in the polarisation results in the atoms being pumped to different M_J sub-levels depending on their position within the light field. For example, atoms in the σ^- region will be pumped to the $M_J = -1/2$

ground state, whilst in the σ^+ region the atoms will instead be pumped to the $M_J = +1/2$ state.

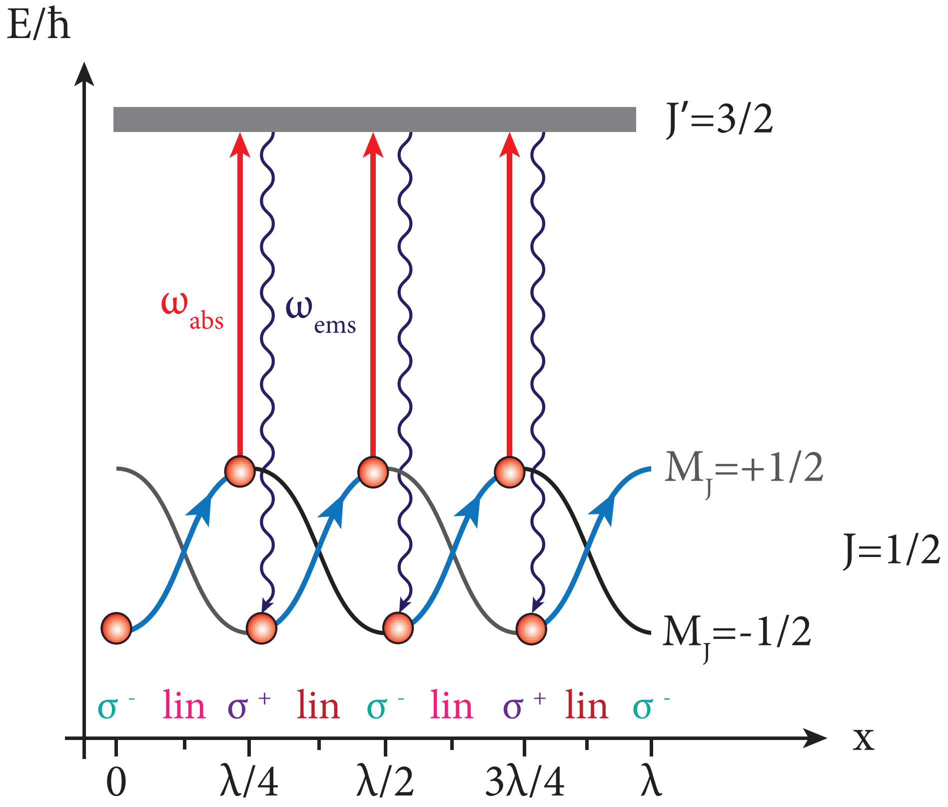

FIGURE 2.3: Diagram of the mechanism associated with Sisyphus cooling. The light standing wave has a polarisation gradient which produces a spatial modulation of the atomic energy levels. The atom loses energy by absorbing a photon at the top of the potential hill and emitting a photon which leaves it in a valley.

In addition to this there is also a modulation of the energy levels of the ground state. This is caused by the light shift, where the magnitude of the shift is dependent on the strength of the transition. In general the transition strength varies for different M_J sub-levels, meaning that the levels will be shifted by differing amounts. Additionally for any given M_J state the transition strength will vary with polarisation. Therefore the modulation of the energy levels occurs because of the polarisation gradient of the light field, and consequently is periodic on the same length scale.

In order for there to be cooling, the mean time taken to pump an atom from one sub-level to another, τ_p, must be comparable to the time it takes for the atom to travel a distance of approximately $\lambda/4$. To see this we consider an atom in the $M_J = -1/2$ state, starting at a position of σ^- polarisation, as shown in figure 2.3. If the atom moves through a distance of order $\lambda/4$ in the pumping time τ_p, then on average the atom will remain in the same M_J sub-level. Therefore as the atom travels to the right it will be able to climb a potential hill and reach the top before being optically pumped to the lower energy state, which is now the $M_J = +1/2$ state. As the atom continues moving to the right this process is repeated.

This sequence leads to cooling because each time the atom moves up a potential hill it converts some of its kinetic energy into potential energy. It then absorbs and emits a photon where the emitted photon has a higher energy. This means the atom has lost kinetic energy and has therefore been cooled. This cooling mechanism is known as Sisyphus cooling.

After each absorption-emission cycle the amount of energy lost by the atom is equal to the energy difference between the two ground state levels, that is the difference in their light shifts. Sisyphus cooling stops working when the energy lost in going from the top to the bottom of the potential hill is balanced by the recoil energy, which is the energy acquired by the atom when a photon is emitted. In this situation there is no net energy loss and so this imposes a temperature limit, T_{sis}, on the Sisyphus cooling mechanism. Provided the laser power is low, this limit becomes $T_{\text{sis}} \simeq T_{\text{R}} = E_r/k_B$, where T_{R} is the recoil temperature, or recoil limit, and $E_R = \hbar^2 k^2/2m$ is the recoil energy.

The cooling mechanism for the $\sigma^+ - \sigma^-$ configuration is slightly different. In this situation the polarisation of the light is linear everywhere, although the angle of polarisation rotates through 2π over a distance of λ. This means there is no spatial variation in the light shift of the energy levels, and so the Sisyphus effect just described does not occur. To understand how this mechanism works, first we consider a frame of reference that rotates with the linear polarisation such that the quantisation axis is always aligned with the oscillating electric field. This means that the laser can only drive π transitions.

Looking at figure 2.4 we see that when an atom is excited from $M_J = \pm 1$ it is equally likely to decay to $M_J = 0$ as to $M_J = \pm 1$, but when it is excited from $M_J = 0$ it is twice as likely to decay back to $M_J = 0$ than to the other two states. As a result, the $M_J = 0$ state will have a larger share of the population than the $M_J = \pm 1$ states, provided the cloud of atoms is stationary. This is the steady state distribution. For a moving atom the quantisation axis rotates and the atomic distribution is optically pumped to follow it. There is an intrinsic pumping time which leads to a lag between the current state of the system and the steady state distribution. This lag results in the $M_J = +1$ state having a

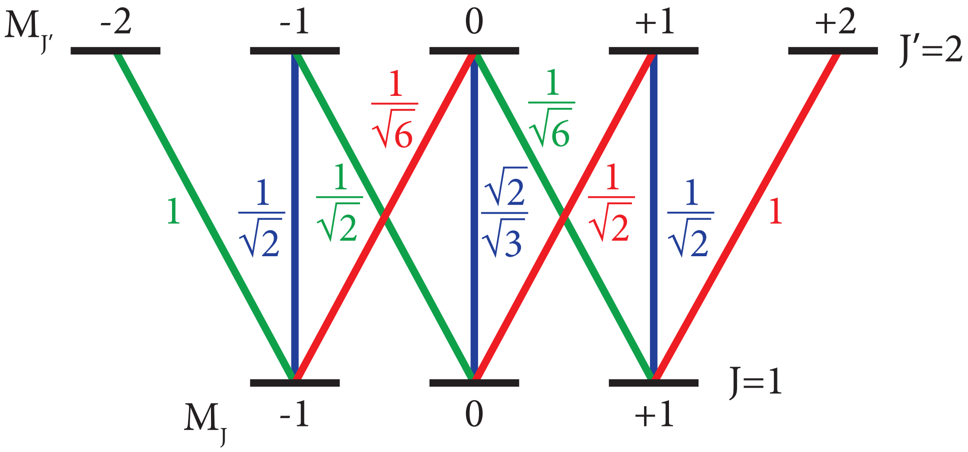

Figure 2.4: Clebsch-Gordan coefficients for a $J = 1$ ground state to $J' = 2$ excited state transition.

higher population than the $M_J = -1$ state for atoms propagating towards the laser beam with σ^+ polarisation [92]. Therefore these atoms will scatter more photons from the σ^+ beam as the transition strength is larger. For atoms travelling in the opposite direction the situation is reversed, so in both cases there exists a damping force which opposes the motion of the atoms and leads to cooling.

For the majority of alkali metals, including Na, Rb and Cs, sub-Doppler cooling mechanisms allow temperatures approaching the recoil limit to be reached. For lithium however no such cooling effect has been observed [78, 93]. This is due to the unresolved hyperfine structure of the excited state. For sub-Doppler cooling to be effective there must be a well defined variation in the populations of the ground state Zeeman sub-levels of the cooling transition. With an unresolved excited state the probability of an atom decaying to the lower hyperfine ground state is high, thus diluting the population in any given Zeeman sub-level and resulting in no additional cooling. Therefore for sub-Doppler cooling to work it is necessary for the cooling transition linewidth to be small compared to the excited state energy level spacing.

Even though it is possible to cool lithium to temperatures below the Doppler limit by employing, for example, evaporative cooling [2], or sympathetic cooling [94], some groups have devised alternative laser cooling schemes for lithium which allow lower temperatures to be reached. One such example can be found in [95], where lithium-7 has been cooled to temperatures as low as $60\,\mu$K using a Λ-enhanced gray molasses scheme on the D_1 line. An alternative approach is outlined in [87] where lithium-6 has been cooled on the narrow $2S_{1/2} \rightarrow 3P_{3/2}$ UV transition. Due to its narrow linewidth the Doppler limit of the transition is low, allowing the cloud to reach temperatures of approximately 59 μK. The relative disadvantage of this second scheme however is that lasers operating at 323 nm are required which is a wavelength where laser power is still relatively limited.

2.1.7 Properties of lithium

Although the first MOT was demonstrated in 1987 it wasn't until 1991 that the first lithium MOT was realised [93]. This was followed by the first lithium BEC in 1995 [2]. Since then lithium, although perhaps not one of the most commonly used alkali metals, has often been used in fermi gas experiments [96–98], as well as for the creation of Feshbach molecules [99, 100]. One of the advantages of using lithium to create a degenerate fermi gas stems from the fact that both a fermionic and bosonic isotope are naturally occurring. In order to reach quantum degeneracy using a bosonic species, evaporative cooling is usually employed. With fermions however, if they are in the same spin state then it is not possible to use this same technique as identical fermions do not undergo the necessary collisions which allow the cloud to rethermalise during the evaporative cooling process [101]. Therefore by using lithium it is possible to sympathetically cool the fermionic isotope by using the evaporatively cooled bosonic isotope, thus allowing the fermions to reach quantum degeneracy [43, 102].

Property	**Symbol**	**Value**
Natural abundance	^{7}Li (^{6}Li)	92.5 % (7.5 %)[76]
Enthalpy of vapourisation	ΔH_{vap}	147.1 kJ/mol [103]
Melting point	T_{M}	453.69 K (180.54° C) [103]
Boiling point	T_{B}	1614 K (1341° C)[103]
Atomic number	Z	3
Nuclear spin	I	3/2
Polarisability	α	164 au [67]

Table 2.1: General properties of lithium. The atomic unit of electric polarisability is au= $e^2a_0^2/E_h$, where e is the charge of the electron, a_0 is the Bohr radius and E_h is the Hartree energy.

Our reason for choosing lithium stems from its favourable properties for sympathetic cooling of molecules. For all of the experiments described throughout this thesis the bosonic isotope, lithium-7 has been used. Table 2.1 shows some general properties of lithium.

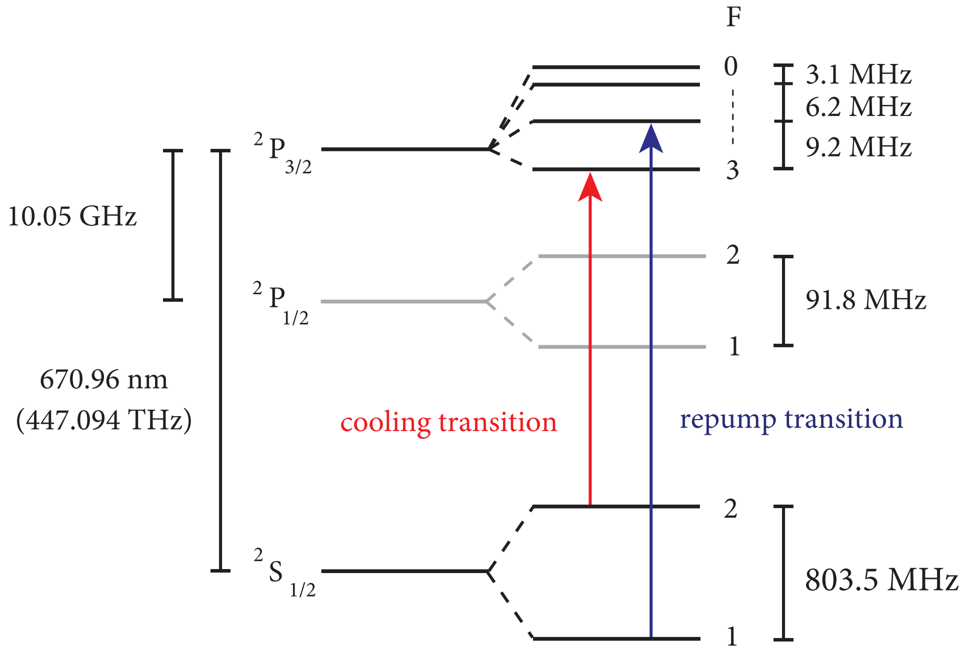

FIGURE 2.5: Energy level diagram for lithium-7 [104].

For the majority of laser cooling experiments, including this one, lithium is cooled on the D2 line. In figure 2.5 the energy level structure of lithium-7 is shown. In our experiment we cool on the $F = 2$ to $F' = 3$ transition as indicated by the red arrow. The natural linewidth of the D2 line is $\Gamma/(2\pi) = 5.92\,\text{MHz}$, which means the upper hyperfine states are partly unresolved. This results in an off resonant interaction which can excite atoms to the $F' = 2$ state, thus opening up a decay channel to the $F = 1$ ground state. Therefore, in order to maintain a closed cooling cycle we require an additional beam that is tuned to the $F = 1$ to $F' = 2$ transition. This pumps the atoms out of the lower hyperfine ground state and back into the main cooling cycle. It is indicated in the diagram by the blue arrow. In table 2.2 some useful values associated with the D2 line for lithium-7 are given.

2.2 Original experimental setup

This section briefly describes the original experimental setup used to produce an ultracold source of lithium atoms which could ultimately be utilised for sympathetic cooling of molecules, or for the investigation of atoms under high electric fields. As a number of major alterations have now been made to the setup, this section also highlights the

Property	**Symbol**	**Value**
Wavelength	λ	670.961 nm
Frequency	ν	446.8099 THz
Natural linewidth	$\Gamma/2\pi$	5.92 MHz
Excited state lifetime	τ	26.87 ns
Saturation intensity	I_{sat}	2.56 mW/cm^2
Absorption cross section	σ	215.0×10^{-15} m^2
Doppler cooling limit	T_{D}	142 μK
Doppler velocity	v_{D}	41.03 cm/s
Recoil temperature	T_{R}	6.061 μK
Recoil velocity	v_{R}	8.474 cm/s

Table 2.2: Properties of the D2 line for lithium-7. All values are taken from [76].

shortcomings of the original design and explains why changes were deemed necessary. For the full details of this setup, including characterisation of the equipment, see [105].

2.2.1 Setup description

In order to produce all of the beams required for the experiment a single diode laser system with built in tapered amplifier (Toptica TA100) was used. It operates at 671 nm and has a maximum output power of 500 mW. This laser is currently still in use and is locked, using polarisation spectroscopy [106], to the cross-over resonance which lies halfway between the two hyperfine levels of the ground state. The remainder of the optical setup has been completely replaced. Images of the atom cloud were taken with an AVT Marlin F-033B CCD camera by using fluorescence imaging.

Figure 2.6 shows a diagram of the original lithium MOT vacuum setup. Broadly speaking the experiment consists of a lithium oven, Zeeman slower and a single vacuum chamber, called the MOT chamber, where atoms were confined by using one of three pairs of trapping coils. In this chamber the atoms were initially loaded into a MOT and were then transferred to a magnetic trap so that they could be transported. Our initial work on magnetic transport of atoms was done using this setup, and this highlighted a number of difficulties that called for a complete redesign. The blue oval indicates the parts of the vacuum system which remain unchanged in the current setup.

In figure 2.7 (a) and (b) the lithium oven is shown in more detail. It consists of a T-piece orientated horizontally so that the trunk of the T is connected to the rest of the experiment. Granules of lithium are deposited into the bottom arm of the T-piece by

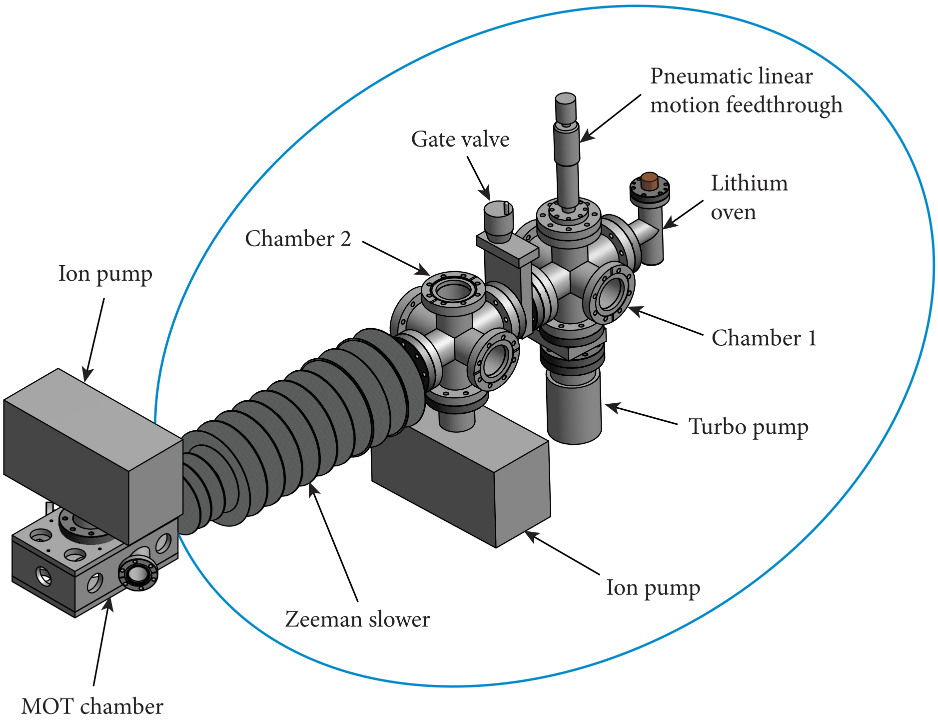

FIGURE 2.6: Diagram of the original lithium MOT vacuum setup. The blue oval indicates the parts of the vacuum system which remain the same in the current setup.

removing the top flange. Once sealed inside the lithium is heated to approximately 500 °C (773 K). A copper block has been inset into the top flange to improve heat conduction to the inner walls of the oven. To heat the oven two heater wires were used, each with a resistance of $\sim 26\,\Omega$. The first was wrapped around the bottom arm of the T-piece and was used to heat the lithium. The second was wrapped around the trunk and top arm of the T-piece, allowing these regions to be kept at a higher temperature whenever the oven was cooled. This was done to encourage the lithium to condense in the bottom arm. The current supplied to each heater wire was controlled by its own variac which was capable of producing a maximum of 120 V. In order to monitor the temperature, three type K thermocouples were attached to the top and bottom arms, as well as the trunk of the T-piece.

Lithium exits the oven through a small aperture of diameter 0.7 mm and length 2 mm to produce an effusive beam. To prevent large amounts of lithium from reaching the vacuum pumps and reducing their operational lifetime, a small copper cup was bolted to the outside of the oven flange. It has a total length of 74 mm, an aperture diameter of 8 mm and has been positioned so that it collects any atoms that exit the oven at an angle which prevents them from reaching the Zeeman slower.

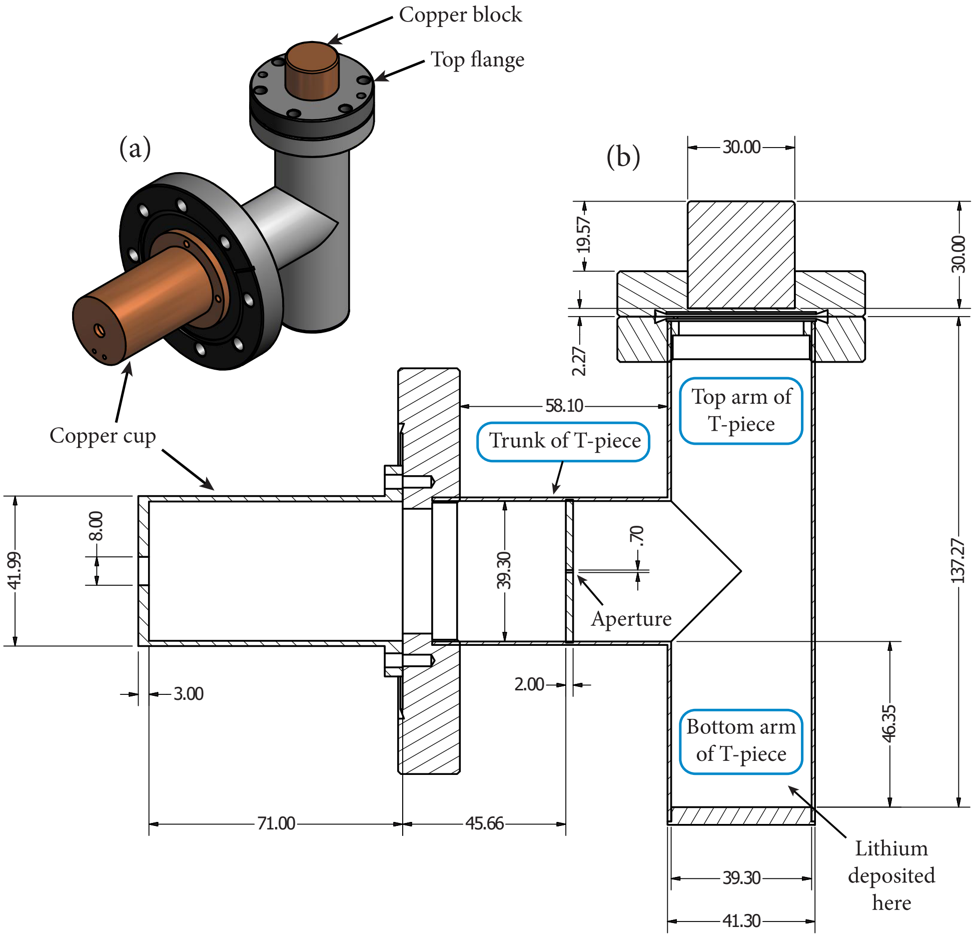

Figure 2.7: Diagram of the lithium oven. (a) Isometric view of the oven. (b) Cross-sectional view of the oven. Lithium exits through a 0.7 mm diameter aperture to produce an effusive beam. Excess lithium is collected by a copper cup which is attached to the oven flange. It has an 8 mm diameter aperture. All dimensions are given in millimetres.

Upon exiting the oven the atomic beam passes through a 6-way cross, referred to as chamber one. Two viewports are positioned perpendicular to the atomic beam in the horizontal direction to allow absorption measurements of the beam to be obtained. To block the atomic beam an aluminium flag is attached to the top flange and is lowered and raised by using a pneumatic, linear motion feedthrough. Chamber one is pumped by a 65 litres/second turbo pump (Leybold TurboVac TW 70H) which is backed by a diaphragm pump (Leybold DiVac 2.5VT). The pressure is monitored using a cold cathode gauge, and would typically reach 2×10^{-7} mbar when the oven temperature was approximately 500 °C.

A second 6-way cross (chamber two) is attached to the port opposite the oven chamber via an all-metal gate valve. This enables the oven and Zeeman slower sections to be sealed off from one another, allowing them to be opened independently if necessary. Between chambers one and two there is a small tube of length 100 mm and diameter 5 mm. This has been incorporated to allow for differential pumping, and by using a 53 litres/second ion pump (Varian Noble Diode VacIon Plus 55) it is possible to reach a pressure of approximately 2×10^{-8} mbar in chamber two. Like chamber one, the pressure is measured by using a cold cathode gauge.

Chamber two is then attached to the Zeeman slower which cools atoms on the $^2\mathrm{S}_{1/2}$, $F = 2$, $M_F = 2$ to $^2\mathrm{P}_{3/2}$, $F' = 3$, $M_{F'} = 3$ stretched state transition by utilising a decreasing magnetic field, which has a zero field point located approximately 0.47 m away from the slower entrance. It has a total length of 0.51 m and was designed to decelerate atoms from 900 m/s to 50 m/s. Upon exiting the Zeeman slower, the atoms enter the MOT chamber. This chamber is pumped by a second 53 litres/second ion pump which, due to the differential pumping tube of the Zeeman slower, allows pressures of approximately 1×10^{-9} mbar to be reached. Again a cold cathode gauge is used to measure the pressure.

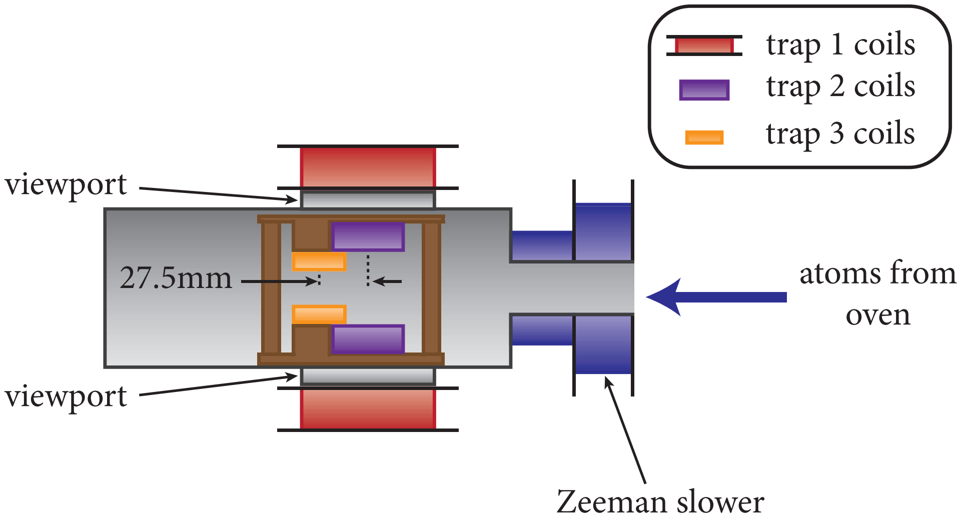

FIGURE 2.8: Cross-sectional view of the MOT chamber and the three sets of trapping coils used in the original setup. Trap one (red) was used to form a MOT, trap two (purple) was used as both a MOT and magnetic trap, and trap three (yellow) was used as a magnetic trap.

Figure 2.8 shows a cross-sectional view of the MOT chamber and indicates the position of the three pairs of coils that were used to trap atoms. The coils forming trap one, shown in red, were positioned outside of the vacuum chamber and could produce a maximum field gradient of 15 G/cm using a current of 20 A. Note that here all quoted field gradients are for the axial direction of the trapping coils. As this field gradient is relatively low, using these coils to form a magnetic trap would lead to a large, diffuse cloud making imaging more difficult. Therefore these coils were used only to form a MOT. Using trap one it was possible to collect a maximum of 2×10^{10} atoms in a cloud with a diameter of approximately 7 mm, giving a density of 1.1×10^{11} atoms/cm^3. The temperature of this cloud was measured to be 0.85 mK.

The coils forming trap two, shown in purple, were placed inside the vacuum chamber and positioned so that their centre was overlapped with the centre of trap one. As these coils were separated by only 37 mm they were able to produce a maximum field gradient of 40.2 G/cm using a current of only 3.75 A. Due to its positioning and higher field gradient, trap two was used as both a MOT and magnetic trap. The lifetime of the magnetic trap was measured to be approximately 1 second.

The final pair of trapping coils, trap three which are shown in yellow, were also placed inside the vacuum chamber. These coils were 25 mm apart and produced a maximum field gradient of 64.4 G/cm using a current of 5.35 A. As these coils did not overlap with the MOT beams, trap three could only be used as a magnetic trap. The lifetime of the trap was found to be quite short at approximately 100 ms. This was attributed to a local pressure increase due to outgassing from the coils.

2.2.2 Atomic transportation and design problems

In order to achieve the final experimental aims of sympathetic cooling of molecules, or the study of atoms under high electric fields, transportation of the atom cloud is required. To illustrate the reason for this, figure 2.9 shows a top view of the MOT chamber. The MOT beams along two orthogonal axes are depicted by the diagonal red lines and the position of the atom cloud is indicated by the black dot. The remaining MOT beam pair is not shown in the diagram, but would pass through the page and overlap with the atom cloud position. The Zeeman beam is represented by the horizontal red line.

To create a large trapping volume and therefore maximise the MOT atom number, beams with a large diameter ($\sim$2 cm for our MOT), must be able to pass unimpeded along three orthogonal axes. In addition to this, the Zeeman beam must be able to cross the intersection point of the MOT beams without being blocked. Therefore trying to directly overlap a microwave cavity with atoms in the MOT is impossible as the cavity mirrors will obstruct at least one of these beams. Additionally trying to design an electrode mount which preserves optical access whilst remaining rigid against large forces becomes unnecessarily challenging. For these reasons it is necessary to transport the atoms to a position away from the MOT where there are fewer optical access requirements.

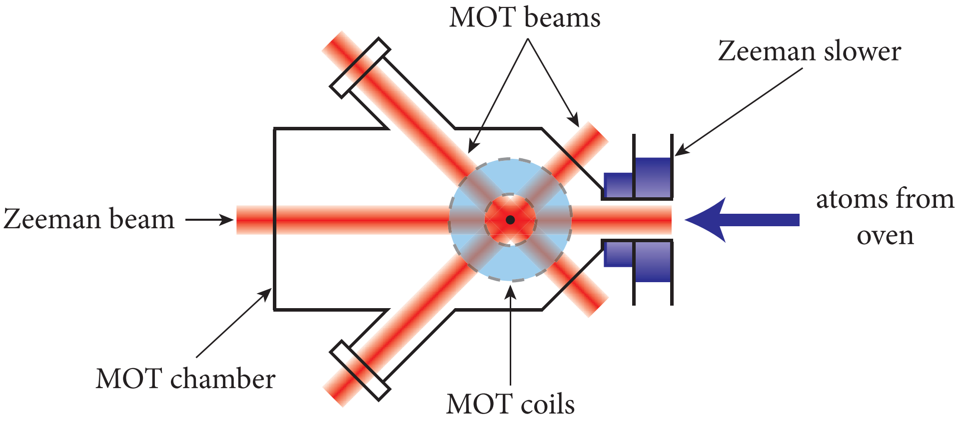

FIGURE 2.9: Top view of the MOT chamber along with the MOT and Zeeman laser beams. The atom cloud is indicated by the black dot and the light blue ring shows the position of the trap one coils.

In an attempt to meet this condition the atoms were transported from trap two to trap three, as trap three does not overlap with the MOT beams. By partially overlapping the coils of traps two and three, transportation of the cloud was demonstrated over a distance of 27.5 mm, with an efficiency of approximately 70%. This design of overlapping quadrupole traps is similar to that described in [107] where rubidium-87 atoms were transported through a 90 ° turn, covering a total distance of 33 cm.

Although transport experiments were successful, it became apparent that there were two particular problems with the setup. The first was that once the atoms had reached trap three there was no way to image them directly. This meant the atoms could only be imaged by moving them back to trap two. Clearly the ultimate aim of studying the atoms under high electric fields could not be realised with this setup, as it would not be possible to view the atoms once an electric field had been applied.

The second design problem was that trap three, although not overlapped with the MOT beams, did still overlap the Zeeman beam. This imposed a limit on how close together the trapping coils could be, which in turn restricted the maximum magnetic field gradient that could be produced. This is because the wire used to construct the coils had a polyester enamel coating that was rated to 200 °C, so the current, and hence magnetic field gradient, was limited by the amount of heat generated. This was problematic because having a cloud temperature of 0.85 mK and a maximum field gradient of 64.4 G/cm results in a minimum cloud diameter of 3.9 mm. As the electrodes will need to have a separation of around

0.5 mm in order to create the necessary electric field, clearly it is not possible to fit the entire cloud between the two electrodes. Overlapping the Zeeman beam also meant that designing a mount for the electrodes was not straightforward, as a rigid structure would not allow the Zeeman beam to pass through unimpeded. Similarly if the microwave cavity were to be overlapped with trap three, the Zeeman beam would end up being obscured.

A possible way to overcome these problems would be to incorporate additional overlapped quadrupole traps into the setup, thus allowing transport of the atoms to a position away from the MOT and Zeeman beams, where they could also be imaged. This however would require further in-vacuum components, which is not ideal as it would likely lead to outgassing, thus increasing the pressure in the chamber and reducing the lifetime of the magnetic trap. An alternative solution would be to position the overlapping coils outside of the chamber. This would solve all previous problems but would mean higher currents are required in order to produce a particular magnetic field gradient.

The main disadvantage of this design however is that to maximise the transport efficiency a complex optimisation procedure is required, as the trap depth during transport is dependent upon the way in which the current in adjacent coil pairs is ramped. So although this design is known to work, without careful optimisation there will always be some loss of atoms during the transport procedure. Therefore we decided to implement a more straightforward method of transport and opted for a complete redesign of the setup.

2.3 Current experimental setup

This section summarises the changes that have been made to the original experimental setup. First information about the new vacuum system is given, followed by details of the two pairs of trapping coils that have been constructed. Finally the new optical setup is described, along with the new control software used for the experiment.

2.3.1 Vacuum chamber setup

In figure 2.10 a diagram of the current vacuum system is shown. The oven and Zeeman slower sections remain unchanged, however a small alteration has been made to the way in which the oven is heated. Two band heaters have been incorporated into the design to replace some of the heater wire. The first has been placed around the trunk of the oven T-piece, the second is positioned around the bottom arm of the T-piece. One of the original heater wires is then used to heat the top arm of the oven. Each of these three heating units is controlled by its own variac, thus allowing for complete and independent temperature control of each section of the oven.

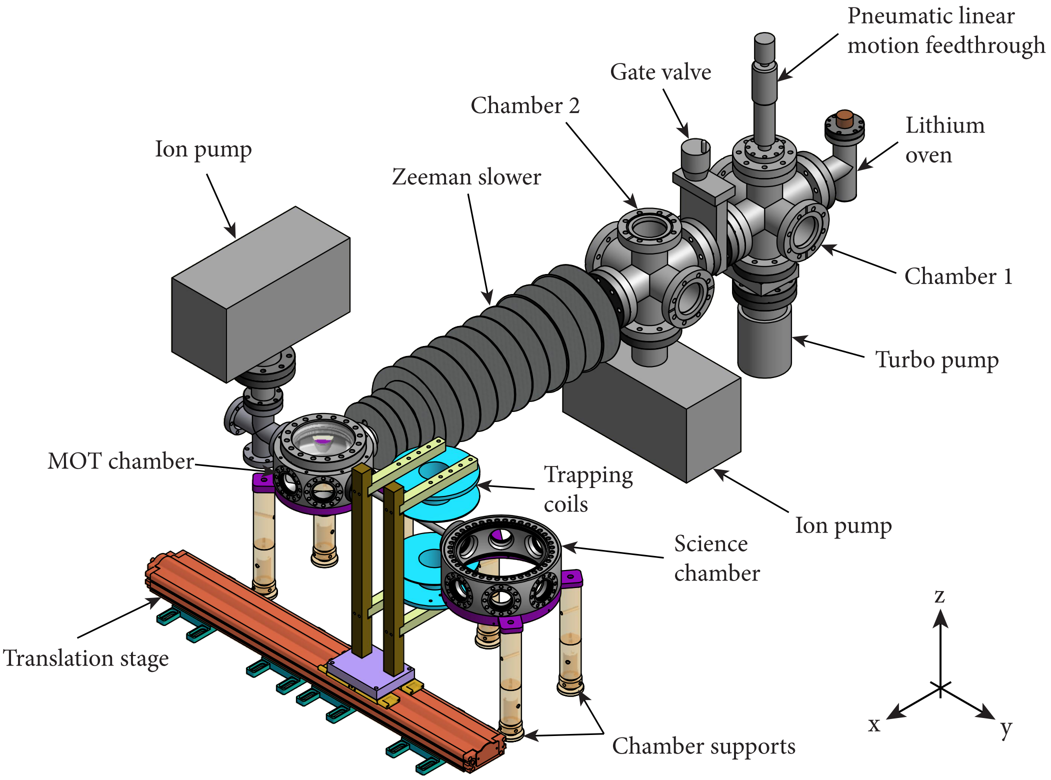

FIGURE 2.10: Diagram showing the current vacuum setup used for the lithium MOT experiment. The translation stage and moving coil setup is also depicted. In the bottom right hand corner the coordinate system used throughout this thesis is shown.

The original MOT chamber has now been replaced by a 6″ and an 8″ spherical octagon vacuum chamber, purchased from Kimball Physics (part numbers: MCF600-SphOct-F2C8 and MCF800-SphOct-G2C8 respectively). The former is referred to as the MOT chamber and the latter, the science chamber. They are connected together via a 250 mm long tube, which has an inner diameter of 9 mm. As before the MOT chamber is pumped by a 53 litres/second ion pump and the pressure routinely reaches 1×10^{-9} mbar. To ensure a low pressure is maintained within the science chamber, a SAES GP502F getter pump (with GP50-ST707 cartridge) is used. The pressure is monitored using a cold cathode gauge and is found to be below its measurement range. This sets an upper limit on the pressure of 1×10^{-9} mbar. In the bottom right hand corner of figure 2.10 the coordinate system that is adopted throughout this thesis is shown.

In order to trap the atoms, a single pair of water cooled coils are placed outside of the vacuum chamber. As these coils can run at high currents, they can be used to form either a MOT or magnetic trap. To overcome the optical access issues of the previous design, the sympathetic cooling and high electric field experiments are to be carried out in the science chamber. To transport the atoms to this chamber we have implemented a design similar to that described in [108] and [109]. In our setup the trapping coils are attached to a Parker 404XR motorised translation stage, which allows them to be physically moved from one chamber to the other. The atoms in the magnetic trap follow this motion, thus allowing transport over tens of centimetres to be easily realised. The main advantage of this design is that only one coil pair is required. This greatly simplifies the setup and removes the need to develop a complex current switching scheme in order to maximise the transport efficiency.

2.3.2 Water cooled trapping coils

If the atoms are to be placed, with minimal loss, between two electrodes which are $0.5\,\text{mm}$ apart then we require a cloud of a similar size. Two factors determine the cloud size, these are the temperature and the magnetic field gradient. Therefore, along with having a cold cloud, it is beneficial to have a magnetic trap with a high field gradient. As our trapping coils are placed outside the vacuum chamber, the minimum distance between the coils is set by the height of the biggest chamber. In our case this is the science chamber, which has a height of around $13\,\text{cm}$. This means the only way to create a high field gradient is by using a large current.

Taking a cloud with a temperature of $1\,\text{mK}$, where all of the atoms are in the $F = 2$, $M_F = 2$ state, we would need a magnetic field gradient of around $300\,\text{G/cm}$ to produce a cloud with a diameter of $1\,\text{mm}$. Given our coil separation, just under $26,700$ amp-turns are required to produce this field gradient in the axial direction. Using high currents means the coils will dissipate a large amount of heat, and so will need to be cooled. To meet this requirement we decided to construct coils using copper tubing so that they could be internally water cooled.

To determine the cooling power, P_c, of our water cooling system, we use the equation [110],

$$P_\text{c} = c_\text{H} R_\text{flow} \Delta T, \tag{2.42}$$

where $c_{\mathrm{H}} = 4.2\,\mathrm{J/(cm^3K)}$ is the specific heat capacity of water, R_{flow} is the measured volumetric flow rate in units of $\mathrm{cm^3/s}$ and ΔT is the allowable temperature rise in Kelvin. The power dissipated by the coil, P_{H}, is given by

$$P_{\mathrm{H}} = I^2 R, \tag{2.43}$$

where I is the coil current and R is the coil resistance. By comparing equations (2.42) and (2.43) we can establish a current limit and therefore determine the maximum magnetic field gradient that can be produced. It is important to note that this value relates to steady state operation, meaning that currents above the maximum can be used, provided they are only used briefly.

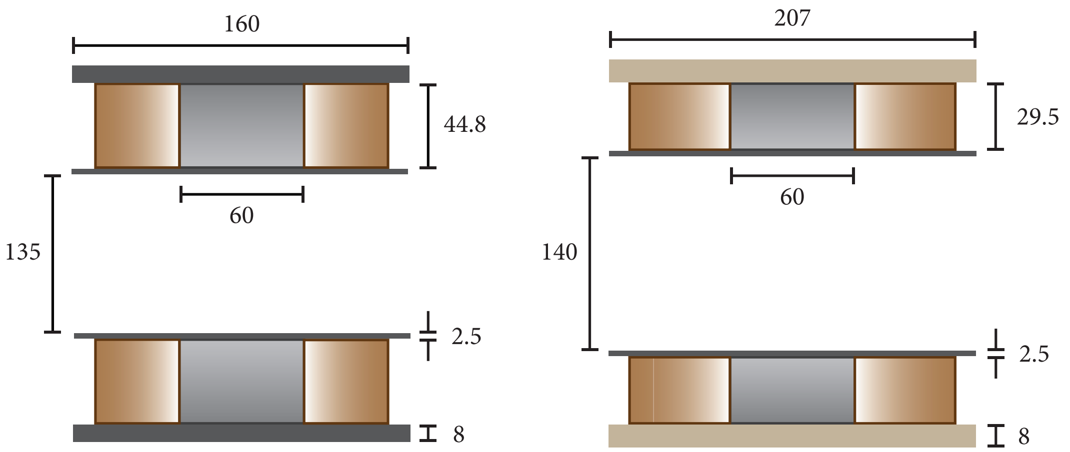
(a) Coil 1

(b) Coil 2


(c) Coil 1 wire

(d) Coil 2 wire

FIGURE 2.11: Dimensions of the two different coils used for experiments. Here (a) shows coil 1, (b) shows coil 2, (c) shows the wire used to construct coil 1 and (d) shows the wire used in coil 2. All dimensions are given in millimetres.

Experiments were carried out using two different coil pairs. The dimensions of coil 1 are shown in figure 2.11(a) and (c), whilst those of coil 2 are shown in (b) and (d). The characteristics of the two coils are described in table 2.3.

Figure 2.12 shows the power dissipated by coils 1 and 2 as the current is increased. Here the red and blue lines represent coil 1 and coil 2 respectively. Comparing the two curves,

Property	**Coil** 1	**Coil** 2
Total wire length	30.5 m	38 m
Number of turns	13	6
Number of layers	8	15
Coil resistance	120 mΩ	61 mΩ
Electrical insulation	MR8008 varnish	kapton tape
Coil former material	aluminium	aluminium & plastic
Water flow rate (pump off)	0.05 litres/minute	0.32 litres/minute
Water flow rate (pump on)	0.25 litres/minute	0.92 litres/minute

Table 2.3: Properties of coil 1 and coil 2.

which have been calculated using equation (2.43), we see that the power dissipated by coil 2 is a factor of two lower than that of coil 1 for any given current. This is due to the lower resistance of coil 2. As the cooling power of the water cooling system depends on the flow rate, a Flojet D131H5011AR diaphragm water pump was installed on the output side of the coils, thus allowing higher currents to be used. The two dash-dot lines represent the cooling power for coil 1, with the pump off (black line) and on (green line). The dashed lines depict the cooling power for coil 2, again with the pump off (black line) and on (green line). Note that these values were calculated using equation (2.42). The water flow rates are given in table 2.3, and a temperature rise of $\Delta T = 40\,\mathrm{K}$ is assumed. The current limit is set by the intersection point of these lines with the relevant curve. Therefore when the water pump is off, the current is limited to 24 A for coil 1 and 85 A for coil 2. When the pump is on, this increases to 54 A for coil 1 and 145 A for coil 2. This shows that coil 2, which has a higher water flow rate, can handle larger currents.

In order to produce high currents, each coil was powered by its own Agilent N8733A DC power supply, run in constant voltage mode. It has a maximum output of 220 A and 15 V. To control the current, a bank of five parallel field-effect transistors (FETs) were connected in series with each coil. Stabilisation of the current was achieved using a hall effect current sensor.

Figure 2.13 shows the variation of the magnetic field gradient with current for both coils. Again the red line represents coil 1 and the blue line represents coil 2. This shows that the magnetic field gradient of coil 1 is approximately 77% of the value produced by coil 2. The increase in the field gradient of coil 2 was achieved by reducing the height of the coil and increasing its diameter. The dotted gray lines show the maximum field gradient that can be generated by the two coils, given the highest current limits already discussed.

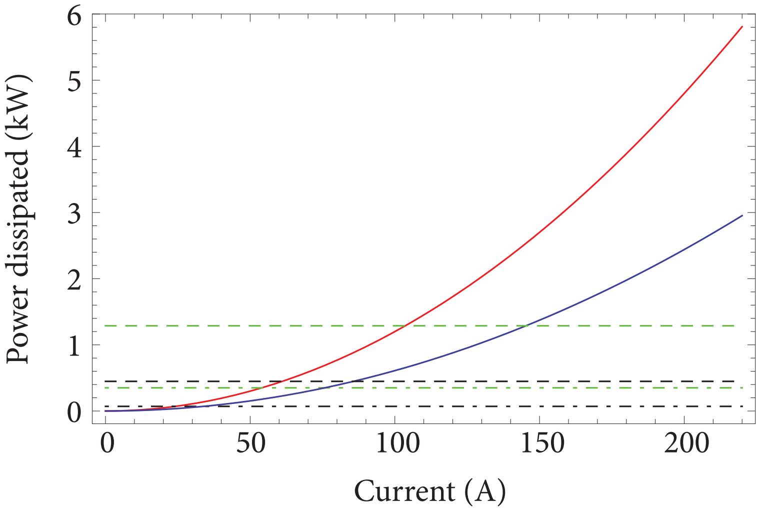

Figure 2.12: Graph showing the power dissipated by coil 1 (red line) and coil 2 (blue line). The dash-dot lines show the water cooling power for coil 1 with the water pump on (green line) and off (black line). The dashed lines show the water cooling power for coil 2 with the water pump on (green line) and off (black line).

These maximum gradients are 39 G/cm for coil 1, and 137 G/cm for coil 2. Taking a 1 mK cloud, these gradients produce a cloud diameter of 7.6 mm for coil 1 and a cloud diameter of 2.2 mm for coil 2. In both cases this is larger than our ideal cloud size of 0.5 mm. A possible way to decrease the cloud diameter is to reduce the temperature of the atoms. This would require lowering the temperature to 65 μK and 0.23 mK for coils 1 and 2 respectively. It is worth noting that even if coil 2 was run at 220 A, the resulting field gradient of 208 G/cm would not be large enough to produce a 0.5 mm wide cloud, assuming it has a temperature of 1 mK. Therefore the atoms need to be cooled to temperatures below 1 mK to ensure that a small cloud is created.

Ideally whenever an absorption image is taken, the atom cloud should always be released from the trap. This is because a non-zero magnetic field will cause the resonance frequency to shift, due to the Zeeman effect. As the magnetic field created by the coils is inhomogeneous, the size of the shift seen by each atom will depend on its position within the trap. This can cause problems if the Zeeman shift is large compared to the natural linewidth, as it leads to some of the atoms becoming invisible. To avoid this, the magnetic field must disappear quickly after the coils have been switched off, so that a field-free image can be obtained before the cloud has had time to expand significantly.

Figure 2.14 shows the decay of the magnetic field generated by a single coil after it has been switched off. In (a) the current of coil 1 was switched from 30 A to 0 A. To avoid

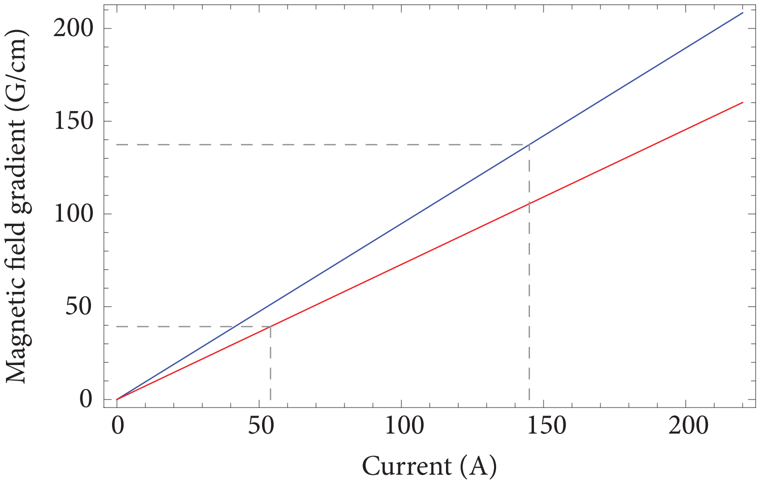

Figure 2.13: Magnetic field gradient versus current for both coils. The red line represents coil 1, the blue line represents coil 2. The gray dashed lines show the maximum field gradient that can be produced for each coil.

saturation, the magnetometer was positioned about 20 cm away from the coils. In (b) the current of coil 2 was switched from 5 A to 0 A. By moving the coils halfway along the connecting tube, it was possible to place the probe close to the zero field point, meaning that this measurement closely resembles the field at the atom cloud position. In both graphs the coils are switched off at $t = 0$, and a linear fit to the data, as described by the equation in the top right hand corner, is depicted by the red line. These results show that coil 1 has a very slow response time. In particular there is a delay of about 1 ms before the magnetic field begins to respond, and it takes around 14 ms for the field to disappear completely. This slow response is thought to be caused by the formation of eddy currents in the coil former and chamber, which create a magnetic field that opposes changes in the current. For coil 2 however, the field begins to respond after only 0.07 ms, and it takes 1.9 ms for the field to disappear completely. This improvement was obtained by using formers made out of plastic and aluminium.

As the overall performance of coil 2 is better, it has been used to obtain most of the results presented in this thesis. However for sections 2.5.1 and 2.5.2, coil 1 was used. The improved performance of coil 2 is due to its smaller height, larger diameter, the high water flow rate through the coil, and the plastic and aluminium former onto which the wire has been wound.

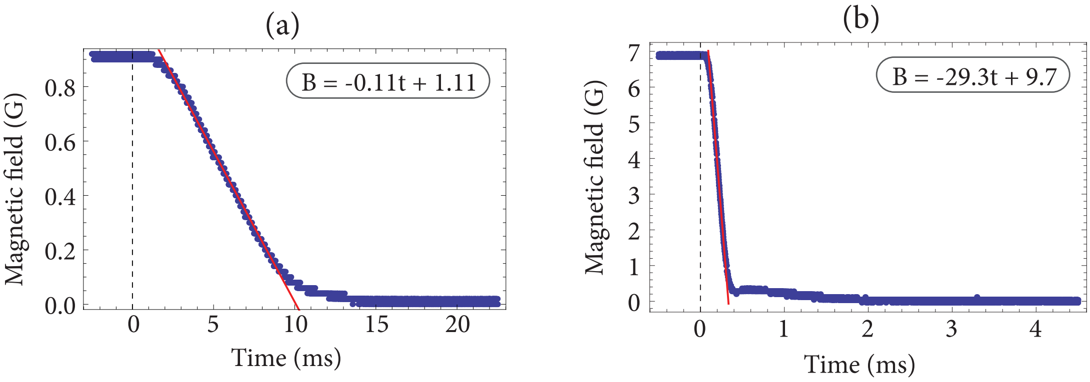

FIGURE 2.14: Magnetic field response after coils switch off. In (a) the current of coil 1 is switched from 30 A to 0 A. In (b) the current of coil 2 is switched from 5 A to 0 A. The coils are switched off at $t = 0$ in both cases.

2.3.3 Optical setup

In order to run the experiment, five separate laser frequencies are needed. These are shown in figure 2.15, along with their detunings from the relevant atomic transitions. Two of these frequencies are required for the MOT, where the first is used to address the main cooling transition and the second acts as a repump. In the diagram these are represented by the green and purple arrows respectively. In our MOT the main cooling beam, or MOT beam, is detuned to the red of the $F = 2$ to $F' = 3$ transition by 3.5 linewidths (20.72 MHz). The MOT repump beam is resonant with the $F = 1$ to $F' = 2$ transition.

The Zeeman slower also requires two laser frequencies. The first, called the Zeeman beam, is detuned by 401.75 MHz to the red of the $F = 2$ to $F' = 3$ transition and is depicted by the dark blue arrow. The second beam, called the Zeeman repump, has a detuning of 401.75 MHz to the red of the $F = 1$ to $F' = 2$ transition. It is represented by the red arrow. There are two main benefits in choosing to have such large frequency detunings. The first is that it minimises any interaction between the MOT atoms and the Zeeman beams. The second is that it places the Zeeman repump frequency at the cross-over resonance. As the laser is locked to this, no frequency shift is required, and this leads to a slight simplification of the optical setup. One further advantage, which comes from having red detuned beams, is that a smaller magnetic field is required at the start of the Zeeman slower. This is because the light and magnetic field work together to compensate the Doppler shift of the hot atoms that enter the Zeeman slower.

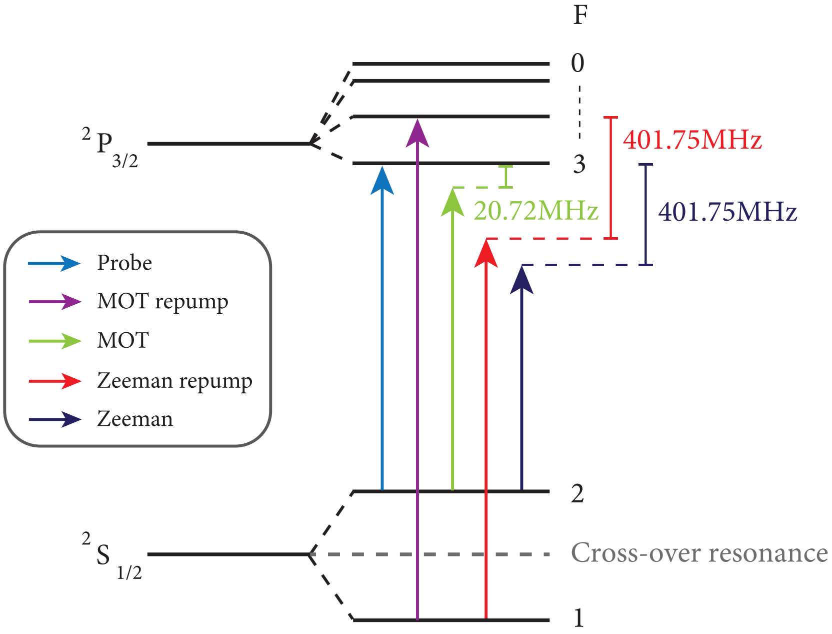

Figure 2.15: Diagram of the energy level structure of lithium along with the five different laser frequencies that are required by the experiment. The position of the cross-over resonance is also indicated.

The final laser beam frequency, which is represented by the light blue arrow, is resonant with the $F = 2$ to $F' = 3$ transition. It is used for taking absorption images of the atoms and is referred to as the probe beam. To generate each of the required frequency shifts, acousto-optic modulators (AOMs) are used. This design, as opposed to using a separate laser for each frequency, has the advantage that only one laser needs to be frequency stabilised.

In order to produce such large frequency shifts, we use 200 MHz AOMs in a double pass configuration. Originally Isomet 1250C AOMs, which have a bandwidth of 100 MHz, were used. However they were found to be very unreliable, as over time the single pass conversion efficiency would drop from approximately 70% to around 20%. This occurred even though the radio-frequency (RF) input power was always kept below the maximum rating given by the manufacturer. Clearly this was a major problem, especially given that for early experiments only 500 mW of laser power was available. This meant that if any AOM was not working properly then there would not be enough power for each of the required beams.

To drive the AOMs, Spectrum Microwave QBH-2832 RF amplifiers were used. These also caused problems as their output power would suddenly deteriorate, rendering them unusable. Initially this behaviour was thought to be caused by inadequate heat sinking, which allowed the amplifier to overheat. However even after improving the heat sinking, so that the amplifier temperature was well within the manufacturer's operating range, the issue still remained. So this, together with the AOM problems, resulted in beam powers that were completely unstable. As a result, both the AOMs and RF amplifiers were replaced. We opted for Gooch and Housego 3200-125 AOMs which have a bandwidth of 50 MHz, and Mini-Circuits ZHL-3010+ RF amplifiers. Since installing these there have been no further problems.

The biggest disadvantage of using only one laser is that the amount of available power is limited. To use this power efficiently, the light passing straight through the first AOM in the optical setup was used to form the other required beams. This meant that all of the beam powers were coupled together such that if one had more power, another would necessarily have less. It also made alignment of the whole optical setup very critical and difficult. It was a constant struggle to maintain sufficient power in all beams simultaneously and as there was no surplus power, the beams could not be spatially filtered. This was particularly problematic for the MOT, as we often found dark patches in the centre of the beams which led to distorted cloud shapes.

To overcome these problems an additional home-built tapered amplifier (TA) was incorporated into the optical setup and seeded using about 50 mW of power from the main laser. The design of the TA mount is similar to that described in [111]. It consists of an aluminium block, which houses the TA chip as well as two aspheric lenses that are used to focus the input beam and collimate the output beam. To power the TA, a Thorlabs LDC 220C current controller is used. Temperature stabilisation is achieved by using an AD590 temperature transducer, along with a Thorlabs TED 200C temperature controller, which is used to drive a thermoelectric cooler. By using approximately 50 mW of light to seed the TA, it is possible to obtain an extra 250 mW of frequency stabilised, laser power. This additional power allowed the MOT and Zeeman beams to be decoupled from one another, and allowed the MOT beams to be spatially filtered whilst still maintaining the same power as before.

Figure 2.16 shows the optical setup used to produce the probe and Zeeman beams. Starting at the laser, the beam first passes through a half-wave plate ($\lambda/2$) followed by a polarising beam cube (PBC). The beam reflected by the PBC is used to seed the TA (not shown). This beam passes through an optical isolator before being sent to the TA through a polarisation maintaining fibre. The beam power can be adjusted by rotating the half-wave plate. The straight-through beam of the PBC passes through a glass plate which picks off 17 mW of light for the polarisation spectroscopy setup. This is used to lock the laser and the full details of this setup can be found in section 2.3.1 of [105].

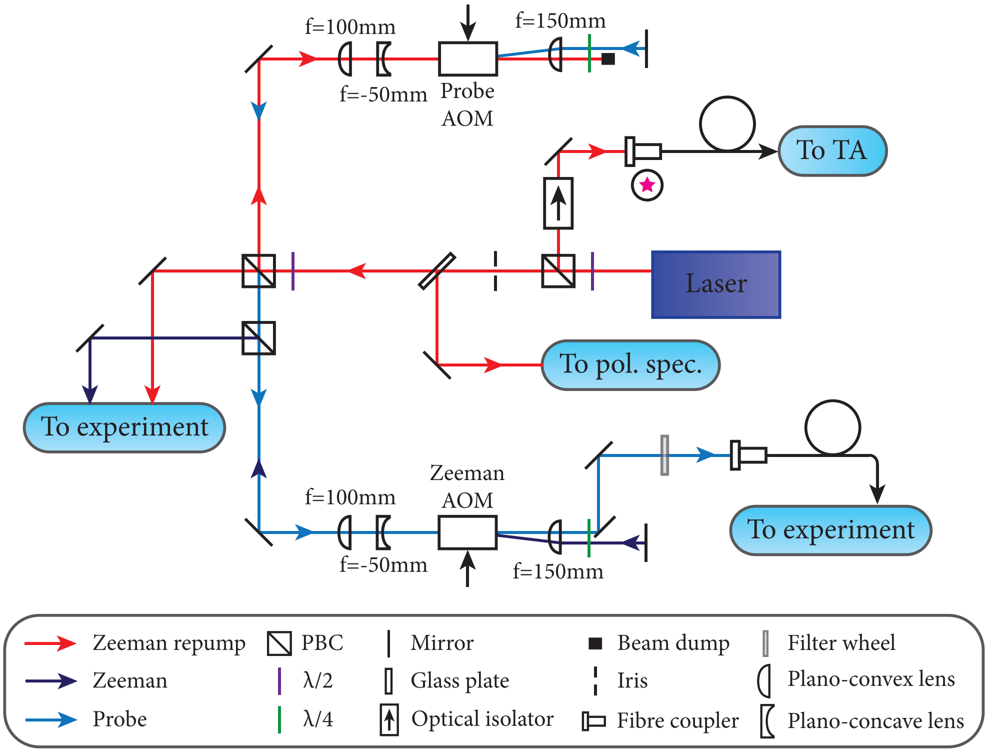

FIGURE 2.16: Optical setup used to produce the probe, Zeeman and Zeeman repump beams. The fibre coupler marked with a pink star is attached to the similarly labelled fibre coupler in figure 2.17.

Next the main beam passes through another half-wave plate and PBC. As the Zeeman repump light requires no frequency shift, the straight-through beam of the PBC can be used directly and is sent to the experiment. The light reflected at the PBC forms the Zeeman beam, which is sent through two double passed AOMs in order to produce a frequency shift of just over 800 MHz.

Following the path of this reflected beam, it first passes through an AOM called the probe AOM, where the assigned name refers to the beam that it controls. In order to maximise the diffraction efficiency, the beam diameter should be matched to the active aperture of the AOM, that is the region over which the performance specifications apply. For this reason we reduce the beam diameter by a factor of two to approximately 2 mm, by using a plano-convex and plano-concave lens, where the separation between them is approximately 50 mm.

After passing through the AOM the zeroth diffracted order, which experiences no frequency shift, is blocked. The first diffracted order however, is frequency shifted and exits the AOM at an angle which depends on the AOM frequency. Using a lens and plane mirror, the diffracted beam is perfectly retro-reflected, irrespective of diffraction angle. The quarter-wave plate ($\lambda/4$) that sits between the lens and mirror is used to rotate the polarisation angle of the retro-reflected beam by 90 °. This allows the incoming and frequency shifted beams to be separated from one another at the PBC. After being double passed through the probe AOM, the beam passes through the Zeeman AOM twice. Again the retro-reflected beam is split off at a second PBC, after which it is sent to the experiment. The zeroth order of the Zeeman AOM is used to form the probe beam. It is attenuated by a filter wheel and is then sent to the experiment through a polarisation maintaining fibre, which also acts as a spatial filter.

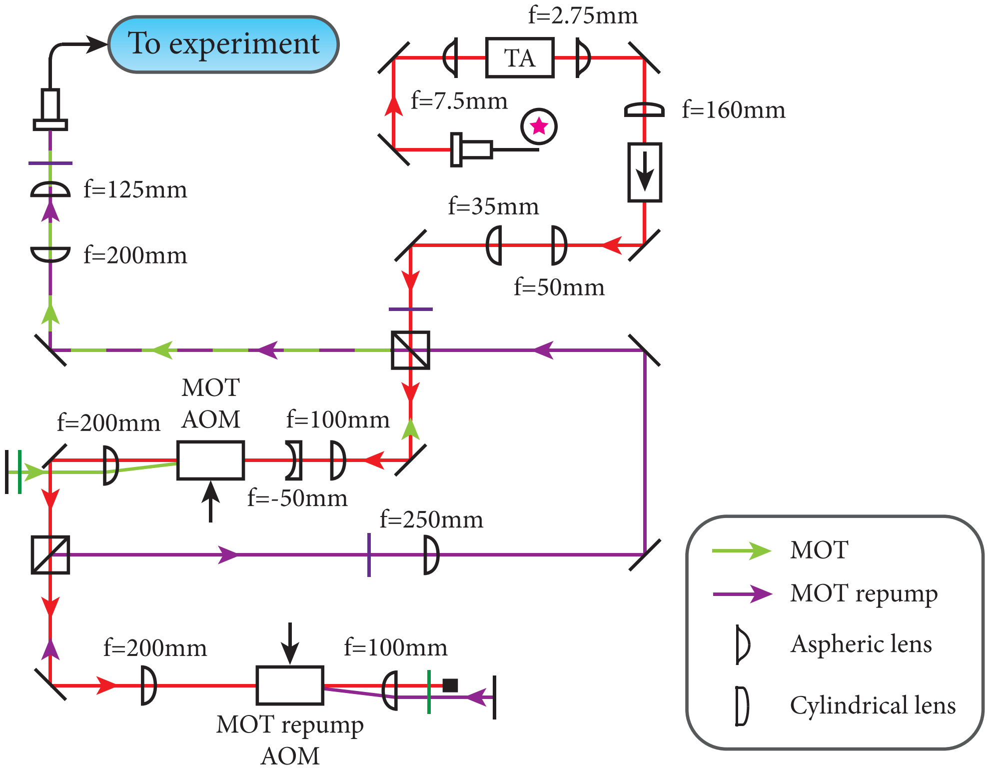

FIGURE 2.17: Optical setup used to produce the MOT and MOT repump beams. The fibre coupler marked with a pink star is attached to the similarly labelled fibre coupler in figure 2.16.

Figure 2.17 shows the optical setup used to produce the MOT beams. First, the beam from the fibre coupler is focussed into the TA by using an aspheric lens. Next the output from the TA is collimated using an aspheric and cylindrical lens, after which it passes through an optical isolator. To prevent back reflections which could damage the TA, the cylindrical lens is positioned at a slight angle. After this two plano-convex lenses are used to reduce the beam diameter to around 4 mm, and the beam is sent through a half-wave plate, PBC and into the MOT AOM. Again the first order diffracted beam is retro-reflected and split off at the PBC. Before being coupled into a polarisation maintaining fibre, the beam diameter is further reduced by a factor of 1.6, and is sent through a half-wave plate. This is used to align the polarisation of the light with the fibre axis, which helps to minimise any drift in the polarisation.

To form the MOT repump beam the zeroth order of the MOT AOM is utilised. It is sent to the MOT repump AOM where, as before, the first diffracted order is retro-reflected and subsequently picked off at the second PBC. It is then combined with the MOT beam at the first PBC, ready to be coupled into the fibre.

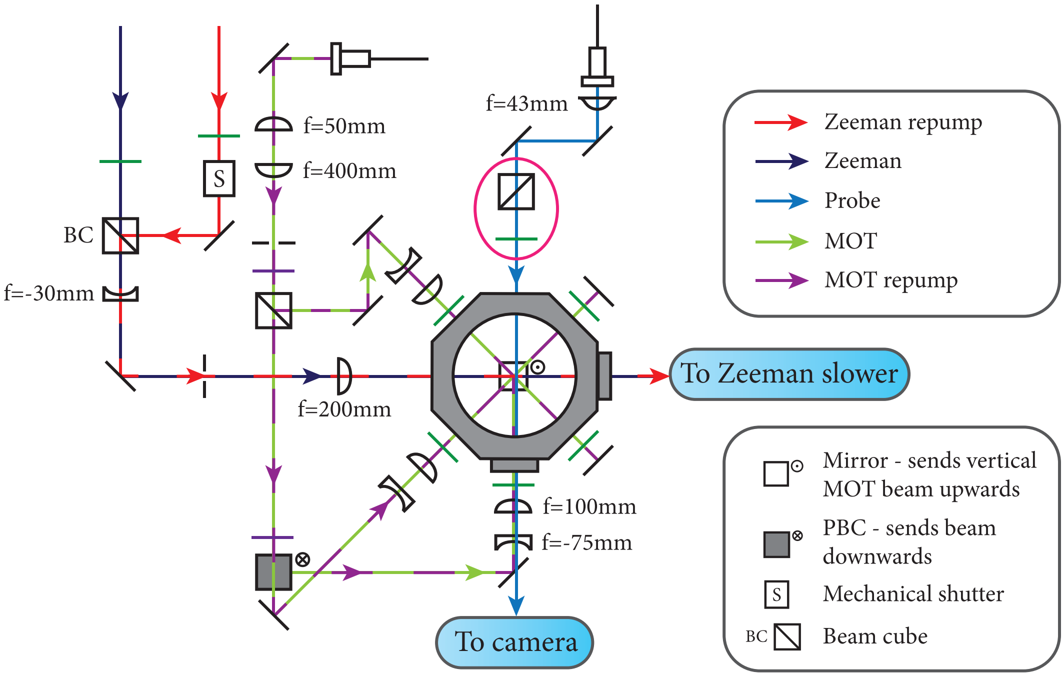

FIGURE 2.18: Optical setup used to send the MOT, Zeeman and both repump beams into the MOT chamber. The optics used to deliver the probe beam are also shown.

In figure 2.18 the optics used to deliver all beams to the MOT chamber are shown. We start by following the path of the two Zeeman beams. First each one is sent through a quarter-wave plate, after which the two beams are combined by using a regular beam cube (BC). As the Zeeman repump beam does not pass through an AOM, the only way to block it is by using a mechanical shutter. This is placed just before the BC. Next the combined Zeeman and Zeeman repump beam is expanded and focussed slightly, before being sent into the Zeeman slower via the MOT chamber.

The combined MOT beams exit the fibre coupler and are expanded. The first horizontal MOT beam is formed by splitting off light at the first PBC. This beam is circularly polarised by the quarter-wave plate, passes through the MOT chamber and is retro-reflected to form the counter-propagating MOT beam. As the retro-reflected beam has less power than the incoming beam, its intensity will be lower, provided the beam diameter is kept constant. This means the returning beam will produce a smaller trapping force. To mitigate this problem a plano-concave and plano-convex lens are used to slightly focus the incoming beam, thus increasing the intensity of the returning beam. This produces MOT beams with a $1/e^2$ radius of $0.96 \pm 0.06\,\mathrm{cm}$ at the trap centre on the first pass. The quarter-wave plate positioned before the retro-reflecting mirror is used to ensure the returning beam has the correct circular polarisation. To create the four remaining MOT beams a second PBC is used, and as before both the horizontal and vertical beams are focussed slightly before entering the MOT chamber. The power of each MOT beam pair is varied by rotation of the half-wave plates that are positioned in front of the two PBCs.

To expand the probe beam to a diameter of 9 mm and collimate it so that the change in size between the MOT region and the camera is $< 5\%$, we use a single anti-reflection coated aspheric lens on the bare output from the fibre. This is used instead of a fibre collimator as it was found to reduce abberations and fringing, whilst also producing a near gaussian spatial mode. After this the probe beam is sent straight to the experiment. It then passes through the connecting tube and science chamber (not pictured) before reaching the camera. A later addition to the setup is indicated by the pink oval. To properly define the polarisation of the probe beam, a PBC was introduced, along with a quarter-wave plate which is used to create circularly polarised light. The reasons for adding this to the setup and the results obtained by this alteration are discussed in section 3.2.

2.3.4 Control software

Computer control of the experimental hardware is obtained by using a National Instruments PXIe-1073 chassis with a PXI-6723 analogue output board, and PXI-6229 multi-DAQ board. To allow the user to vary experimental parameters easily, new software has been written in C# which provides various types of functionality. For immediate control of the hardware, a push button user interface has been developed. This allows all experimental parameters to be changed quickly and easily. To run a timed sequence of events, a secondary program was developed. It requires each experimental sequence to have a corresponding script, which contains information about all the necessary events. The program then compiles the chosen script, before sending instructions to the hardware controller about the changes that need to be implemented. A third program is used to alter particular values within a script before it is compiled. This allows a given parameter to be automatically scanned over a range of different values as chosen by the user.

2.4 Imaging the atoms

In this section the methods used to image the atoms are detailed. In particular the procedures used to obtain fluorescence and absorption images are described. As there are some problems associated with our absorption imaging setup, these are discussed and quantified where possible.

2.4.1 Fluorescence imaging

One way in which real-time measurements of the MOT atom number can be obtained is to use fluorescence imaging. This involves capturing some fraction of the light scattered by atoms in the MOT. If information about the spatial distribution is not required, then this can be done by using a single lens and a photodiode. Otherwise the cloud should be imaged onto a CCD camera, so that the size and distribution can be observed. Although fluorescence imaging is straightforward to implement, it can produce unreliable results if the atom cloud has entered the multiple scattering regime. This is because some of the emitted photons are re-scattered by a second atom, resulting in fewer photons reaching the detector in a given time interval. This leads to an underestimate of the atom number, which can be verified by comparison with absorption images.

In our setup we image the cloud onto a reverse-biased photodiode using a 75 mm focal length lens. To capture as much light as possible, the lens should be placed close to the atom cloud. Due to the positioning of various MOT optics, our collection lens, which has a diameter of 25 mm, has to sit approximately 180 ± 5 mm away from the atoms.

The output from the photodiode is connected to a 1 MΩ load resistor and the voltage drop across it is measured. To convert this voltage into an atom number, the light power emitted by the cloud has to be equated with the light power detected by the photodiode. The power emitted by the atom cloud, P_{a}, that reaches the photodiode is given by

$$P_{\mathrm{a}} = \eta \hbar \omega_0 N R_{\mathrm{scatt}}^{\mathrm{MOT}} \Omega_{\mathrm{L}}, \tag{2.44}$$

where η is the total transmission of all optical elements, ω_0 is the atomic resonance frequency, N is the total number of atoms in the MOT, $R_{\mathrm{scatt}}^{\mathrm{MOT}}$ is the MOT scattering rate and Ω_{L} is the fraction of the total solid angle captured by the lens. This is calculated by using $\Omega_{\mathrm{L}} \approx \frac{1}{4\pi}(\frac{\pi d_{\mathrm{lens}}^2}{4l^2}) = 1.2 \times 10^{-3}$, where d_{lens} is the lens diameter, and l is the distance between the cloud and lens. Here the $\frac{1}{4\pi}$ term denotes the full solid angle over which photons are emitted, and the term in brackets is the approximate solid angle of the lens. As the MOT viewports and the lens used in this setup are anti-reflection coated, losses are negligible which means that we can set $\eta = 1$.

The power detected by the photodiode, P_{pd}, is related to the measured voltage, V_{pd}, by

$$P_{\mathrm{pd}} = \frac{I_{\mathrm{pd}}}{\mathcal{R}} = \frac{V_{\mathrm{pd}}}{R_{\mathrm{L}}\mathcal{R}}, \tag{2.45}$$

where I_{pd} is the photocurrent, $\mathcal{R}$ is the responsivity of the detector, which is ~ 0.36 A/W at 670 nm for our particular detector (Thorlabs DET100A) and R_{L} is the load resistance. By equating these two powers and rearranging for N, an expression for the total atom number can be found,

$$N = \frac{V_{\mathrm{pd}}}{\eta \hbar \omega_0 \, \Omega_{\mathrm{L}} \, R_{\mathrm{L}} \, \mathcal{R} \, R_{\mathrm{scatt}}^{\mathrm{MOT}}}. \tag{2.46}$$

Before this equation can be used, a value for $R_{\mathrm{scatt}}^{\mathrm{MOT}}$ must be obtained. This is not straightforward to calculate because the scattering rate will vary not only with the internal state of the atom, but also with its position within the MOT. From equation (2.7) we see that the scattering rate for a two level atom is dependent on two uncertain parameters. These are the saturation parameter, s_0, and the detuning, δ. Therefore, to find an estimate of the total MOT scattering rate, we have to consider how each of these parameters varies over the entire atom cloud.

Referring back to equation (2.3), we find that the saturation parameter is dependent on the beam intensity, I, as well as the saturation intensity, I_{sat}. In turn, I_{sat} is proportional to the strength of the transition. As atoms in the MOT are in a mixture of Zeeman sub-levels, and are exposed to light of various polarisations, it is possible to excite a variety of transitions. This means the saturation intensity is not well defined. There are two ways to overcome this problem, either we can assume that all atoms scatter on the same transition, thus leading to a single value for I_{sat}, or alternatively, an average value can be calculated over all possible transitions. In [80], measurements of the fluorescent power scattered by a caesium MOT indicate that an average over all transitions yields a value for I_{sat} that is too small. This discrepancy is attributed to optical pumping between the Zeeman sub-levels, which results in an atom at any position being pumped towards the state that interacts most strongly with the light, thus producing a higher effective transition strength. In light of this, we choose to simplify the situation by assuming that all atoms scatter on the strongest transition, which means $I_{\mathrm{sat}} = 2.56\,\mathrm{mW/cm^2}$. This produces a value of $s_0 = 2.2$ for our MOT.

As mentioned in section 2.1.3, the MOT detuning can be described by $\delta_{\mathrm{mot}} = \omega - \omega_0 \mp kv \pm \frac{\Delta\mu B(x)}{\hbar}$, where for this experiment $\omega - \omega_0 = -3.5\,\Gamma$. Therefore the detuning depends on the Doppler shift, which is position dependent because of the variation in the velocity of the atom as it oscillates in the trap, and it depends on the Zeeman shift, which is position dependent because of the inhomogeneous magnetic field. The transition being excited also has an effect on the detuning through the $\Delta\mu$ term. This has some position dependence because the local polarisation affects the sign of the term.

To simplify the situation we only consider atoms that are moving towards the light beam. This is a reasonable assumption, as the Doppler shift causes atoms to interact most strongly with the beam that opposes their motion, and as atoms move away from the trap centre, the Zeeman shift will bring them into resonance with this counter-propagating beam. When an atom reaches the edge of the cloud its velocity will be small, thus producing a negligible Doppler shift. At this same position the Zeeman shift is maximised. Given that our atom cloud has a diameter of around 1 mm and the field gradient is approximately 15 G/cm, atoms at the cloud edge will be exposed to a 0.75 G magnetic field. This results in a Zeeman shift term of $\frac{\mu_B B(x)}{\hbar} \approx 1\,\mathrm{MHz}$. At the centre of the trap however, the atomic velocity is maximised and the magnetic field equals zero, resulting in no Zeeman shift. Assuming the atomic velocity is equal to the most probable velocity of the Maxwell-Boltzmann distribution means that $v = \sqrt{2k_BT/m}$. For a 1 mK cloud this results in a Doppler shift of $kv = 2.3\,\mathrm{MHz}$. As these two values represent the maximum

Zeeman and Doppler shifts present in the MOT, a reasonable estimate of the shift for all atoms can be obtained by taking the average. This produces a total MOT detuning of $\delta_{\mathrm{mot}} = -3.5\Gamma + 1.65\,\mathrm{MHz} = -19.07\,\mathrm{MHz}$.

Having found values for the saturation parameter and detuning in the MOT, it is now possible to calculate the scattering rate. By using equation (2.7) we find the MOT scattering rate to be $R_{\mathrm{scatt}}^{\mathrm{MOT}} = 9.2 \times 10^5$ photons/second. Substituting this into equation (2.46) shows the expected signal to be approximately $0.1\,\mathrm{nV}$ per atom. Typically we measure voltages of around $13\,\mathrm{mV}$ which equates to 1.1×10^8 atoms. It is worth noting that in this experiment fluorescence imaging is used only as an instantaneous diagnostic tool, and that none of the data presented in this thesis has been collected using this setup.

2.4.2 Absorption imaging

Absorption images are obtained by exposing the atom cloud to low intensity, resonant light. As the atoms scatter light out of the beam, a shadow is cast. By imaging this beam onto a CCD camera and measuring the loss of intensity, the atom number can be determined. The light intensity reaching the camera is given by the Beer-Lambert law,

$$I = I_0 e^{-\sigma \int n(x,y,z)dz} = I_0 e^{-OD}, \tag{2.47}$$

where I_0 is the initial light intensity, σ is the absorption cross section of the atoms, $n(x, y, z)$ is the number density of the cloud, and $OD = \sigma \int n(x, y, z)dz$ is referred to as the optical depth (OD). For this equation to be valid, the beam intensity must be low, meaning that $I \ll I_{\mathrm{sat}}$. This is required because at high intensity, stimulated emission starts to become an important process which increases the intensity of the light and offsets some of the absorption.

By integrating along one axis, the number density becomes the column density, which means $\int n(x, y, z)dz = N(x, y)/A_{\mathrm{col}}$, where $N(x, y)$ is the number of atoms in a particular column of the cloud and A_{col} is the area of this column. Using this it is possible to rearrange the above expression to give,

$$N(x, y) = \frac{A_{\mathrm{col}}}{\sigma} \ln\left(\frac{I_0}{I}\right). \tag{2.48}$$

We measure the absorption in each camera pixel, where the area A_{pixel} is related to A_{col} by $A_{\mathrm{col}} = A_{\mathrm{pixel}}/M^2$, where M is the magnification of the imaging system. In order to determine the total atom number, N, a summation over all pixel values must be carried out, which results in,

$$N = \frac{A_{\mathrm{pixel}}}{M^2 \sigma} \sum_{\mathrm{pixels}} \ln\left(\frac{I_0}{I}\right). \tag{2.49}$$

In order to form a single absorption image of the atoms, three separate photographs are taken. These are an image of the probe beam with atoms present, I_{atoms}, an image of the probe with no atoms present, I_{probe} and finally an image with no atoms or probe, I_{bkgd}, where this last image is used to remove background light from other sources. We then apply the following relation to each individual pixel to find the optical depth at every point in the image,

$$OD = \ln\left(\frac{I_0}{I}\right) = \ln\left(\frac{I_{\mathrm{probe}} - I_{\mathrm{bkgd}}}{I_{\mathrm{atoms}} - I_{\mathrm{bkgd}}}\right). \tag{2.50}$$

The final value that needs to be determined before the atom number can be calculated is the absorption cross section. For a two level atom, in the limit of low light intensity, equation (2.29) becomes,

$$\sigma = \frac{3\lambda^2}{2\pi} \frac{b}{1 + 4\delta^2/\Gamma^2}, \tag{2.51}$$

where b is the branching ratio of the transition being excited, and has a value between zero and one. Ideally the absorption cross section should be maximised to ensure that a large signal is obtained for short interaction times. This requires $b = 1$, which can only be obtained if all atoms are excited on the stretched state transition. Therefore atoms should be imaged using circularly polarised light, in a well defined magnetic field that lies parallel to the propagation direction of the light. Additionally, all atoms must start off in either the $F = 2$, $M_F = 2$, or $F = 2$, $M_F = -2$ state. In practice however, as we do not employ optical pumping, the MOT atoms will be in a mixture of Zeeman sub-levels. Also the magnetic field from the coils is usually kept on during imaging, meaning that the quantisation axis is not well defined unless a large bias field is applied. Therefore to obtain a reasonable estimate of the absorption cross section, b is averaged over all possible transitions from the $F = 2$ to $F' = 3$ state. A transition strength diagram for the D2 line of lithium can be found on page 285 of [76]. Using this and assuming an even population of all Zeeman sub-levels produces a value of $b = 7/15$.

For the majority of experiments described in this thesis, the atoms are imaged whilst still in the MOT. This can cause problems as the MOT beams will excite the atoms, thus reducing the overall absorption and producing an underestimate of the atom number. However, if the detuning of the light is large and the intensity is relatively low, then the excited state fraction will be small and atom number measurements should be reliable. In order to determine whether or not this effect is negligible, we compared images of the cloud with the MOT beams both on and off. As the difference in atom number was only 0.3%, we conclude that imaging the atoms with the MOT beams on does not greatly affect our atom number measurements.

To capture images of the cloud, initially an AVT Marlin F-033B CCD camera was used. It has a pixel size of $9\,\mu$m, and a sensor consisting of 656×494 pixels, which equates to a chip size of $7.48\,\text{mm} \times 6.15\,\text{mm}$. Its minimum exposure time is $32\,\mu$s and it produces an 8-bit image. The limited bit depth of this camera led to problems when imaging faint clouds, therefore it was replaced with an AVT Pike F-145B CCD camera, which produces 14-bit images. The Pike also offers better resolution with a pixel size of $6.45\,\mu$m and has a bigger sensor, consisting of 1388×1038 pixels, which equates to a size of $9.0\,\text{mm} \times 6.7\,\text{mm}$. Its minimum exposure time is slightly longer at $39\,\mu$s. All of the results presented in this thesis were obtained using absorption imaging. The results shown in sections 2.5.1 and 2.5.2, with the exception of figure 2.25, were obtained using the Marlin CCD camera. For all other results the Pike was used.

In our setup, due to the positioning of the MOT beams and coils, atoms in the MOT chamber can only be imaged by sending a probe beam along the transport axis. As we eventually want to obtain high quality images of the atoms in the science chamber, the camera has been positioned at this end of the experiment. This means however, that after passing through the MOT cloud, the probe beam has to travel a distance of 660 mm through the connecting tube and science chamber, before reaching the camera. As a result it is not possible to place a short focal length lens close to the atoms. A lens with a large diameter could be positioned close to the camera, provided it has a long enough focal length, however this does not allow a large solid angle to be collected, as the connecting tube acts as an aperture. Therefore we use no lens in our imaging system. This setup is not ideal as it can lead to imaging problems.

The first effect that needs to be taken into account is atomic lensing. Although the cloud is relatively diffuse, its density can be sufficiently high that it acts like a lens, causing the probe light to refract. The size of this lensing effect will depend upon the density of the cloud, its radius, and its refractive index, which will vary with detuning from the atomic resonance. We can determine how significant this effect is by calculating the focal length of the atomic lens given typical cloud parameters. To do this we first have to know how the refractive index of the cloud varies with detuning. For a two level atom, assuming a low intensity probe beam, the complex index of refraction, n_{ref}, is given by [112]

$$n_{\text{ref}} = 1 + \frac{\sigma_0 n \lambda}{4\pi}\left(\frac{i}{1+\delta^2} - \frac{\delta}{1+\delta^2}\right), \tag{2.52}$$

where $\sigma_0 = 3\lambda^2/2\pi$ is the resonant absorption cross section, n is the density of the cloud and $\delta = 2(\omega - \omega_0)/\Gamma$ is the detuning in half linewidths. Taking the real part of equation (2.52) gives the refractive index, whilst the imaginary part represents absorption through the cloud. By setting the density equal to the maximum achievable in a MOT, namely 10^{11} atoms/cm^3, and assuming it is constant across the cloud, we find the maximum refractive index occurs at a detuning of $-\Gamma/2$ and has a value of $\text{Re}(n_{\text{ref}}^{\text{max}}) = 1.00057$. If the light is detuned to the other side of the atomic resonance, the refractive index decreases by an equal and opposite amount from the zero detuning value, reaching a minimum of $\text{Re}(n_{\text{ref}}^{\text{min}}) = 0.99943$ at a detuning of $+\Gamma/2$. This changes the direction in which light is refracted, effectively turning the atoms from a converging lens into a diverging lens. So other than a change of sign, this has no effect on the focal length, and means that either of these two extremal values can be used.

Taking our value for $\text{Re}(n_{\text{ref}}^{\text{max}})$, and assuming the cloud is a sphere of radius r_{cloud}, we can calculate the effective focal length, f_{eff}, of the atomic lens by using [113]

$$f_{\text{eff}} = \frac{\text{Re}(n_{\text{ref}})\, r_{\text{cloud}}}{2(\text{Re}(n_{\text{ref}}) - 1)}, \tag{2.53}$$

where f_{eff} is measured from the cloud centre. For a 1 mm cloud diameter, the effective focal length is 440 mm, which is about 220 mm shorter than the distance between the atom cloud and camera. Therefore in the worst case scenario, light emerging from the cloud will focus before reaching the camera, making the cloud appear smaller than it really is. With decreasing cloud width, this lensing effect will become even more significant. In section 2.5.2, measurements show that our cloud has a maximum density of 9×10^9 atoms/cm^3, which means lensing effects should be greatly reduced. In addition to this we use a near resonant probe beam which should further minimise the effect.

With no imaging optics, and a camera positioned well away from the atoms, it is important to consider how much diffraction the cloud will produce, and the effect that this has on the apparent size of the cloud. In order to determine the diffraction regime, we can calculate the Fresnel number, F, [114]

$$F = \frac{r^2_{\text{cloud}}}{l\lambda}, \tag{2.54}$$

where l is the distance between the cloud and camera. When $F \geq 1$, Fresnel diffraction applies. In this regime calculating the amount of diffraction to expect becomes rather involved, however when $F \gg 1$ diffraction effects should be small and can therefore be neglected. For $F \ll 1$, the Fraunhoffer description of diffraction is accurate. In this regime, because our cloud has a Gaussian spatial profile, its diffraction pattern will also have a Gaussian shape.

Given our experimental parameters we calculate a Fresnel number of $F \approx 2$. This means we are in the intermediate regime and will therefore expect to see some minor diffraction effects. This could pose problems for the smallest clouds and we should bear this in mind in subsequent sections. Once the atoms have been transported to the science chamber, the situation improves drastically as l is then far smaller and also an imaging system can easily be set up to collect the diffracted light.

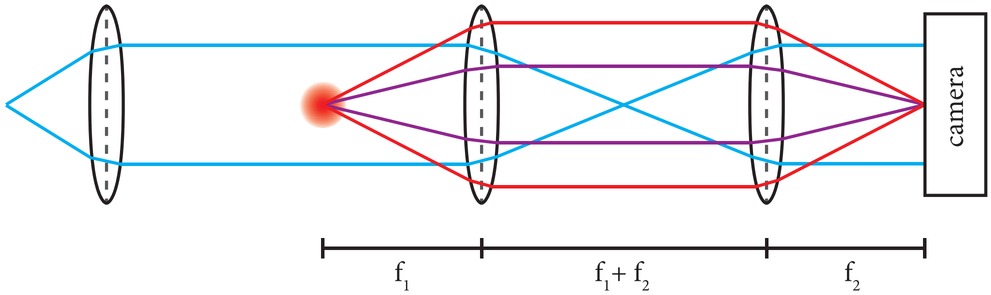

FIGURE 2.19: Ideal optical imaging setup that will be installed to image atoms in the science chamber. The blue lines represent the probe beam. The red circle depicts the atom cloud. After passing the cloud, light will diffract, this is shown by the purple lines. A $4f$ lens configuration can be used to collect this light. The red lines represent fluorescent light from the atoms.

The required imaging setup, which has not yet been installed, is shown in figure 2.19. A lens with a focal length, f_1, is placed one focal length away from the atoms. This simultaneously collimates the diffracted light, which is shown in purple, and focusses the unscattered light from the probe beam, which is depicted by the blue lines. Then a second lens, with focal length f_2, is positioned a distance $f_1 + f_2$ away from the first lens. This $4f$ configuration has the effect of focussing the diffracted light and re-collimating the unscattered probe beam. The camera is then placed at the focal plane of this second lens. To adjust the magnification of the image, the ratio of the focal lengths can be changed. It is worth noting that this configuration will also collect fluorescent light from the atoms, as shown by the red lines. This contribution to the signal can only be neglected when a small solid angle is captured.

2.5 Characterisation of the MOT

This section describes the experiments carried out to characterise the MOT. Measurements of the loading rate are first discussed, followed by a description of experiments aiming to maximise the number of atoms in the MOT. Finally the results of experiments designed to cool and compress the cloud are detailed.

2.5.1 MOT loading rate

The atom number in the MOT, N, is determined by the balance between the rate at which atoms are captured, and the rate at which they are lost. This can be described by the differential equation,

$$\frac{dN}{dt} = L - \frac{N}{\tau} - \beta \int n^2(r)dV, \tag{2.55}$$

where L is the loading rate in atoms/second, τ is the trap lifetime and the term $\beta \int n^2(r)dV$ describes losses due to two-body collisions between trapped atoms. In our MOT, the loading rate is predominantly determined by the flux of atoms from the Zeeman slower, which in turn depends on the atom flux from the oven. As the trap lifetime is determined by collisions with background gases, it is important to maintain a low pressure in the MOT chamber in order to maximise the atom number.

Two-body losses start to become significant as the density of the MOT increases. In practise we can verify that two-body losses are negligible by measuring the decay curve of the MOT, if this deviates from an exponential decay for early times when the density is still high, then two-body losses cannot be ignored. For lithium-7 the value of β has been measured and is found to be small compared to the loss rate from collisions with background atoms [115]. Therefore we can solve equation (2.55), neglecting the two-body loss term. This gives,

$$N(t) = L\tau(1 - e^{-t/\tau}), \tag{2.56}$$

where we have taken the atom number to be zero at time $t = 0$. As $t \to \infty$, the atom number limits to $N_{\text{max}} = L\tau$. By fitting equation (2.56) to our loading curve, a value for the capture rate and lifetime of the MOT can be extracted.

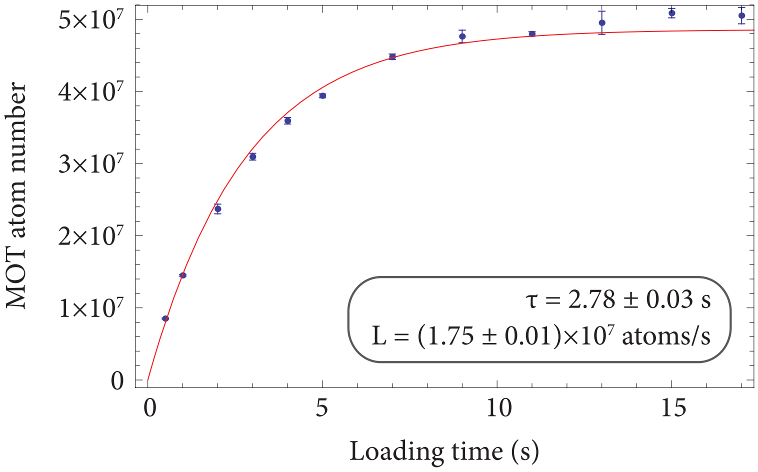

FIGURE 2.20: Measurements of the atom number in the MOT after various load times. A fit to the data is depicted by the red line. From this values for the capture rate, L, and MOT lifetime τ have been obtained.

Figure 2.20 shows the measured atom number in the MOT as a function of loading time. Equation (2.56) has been fitted to the data, producing a value of $\tau = 2.78 \pm 0.03\,\text{s}$, and $L = (1.75 \pm 0.01) \times 10^7$ atoms/second. This fit is shown by the red line. It takes approximately 10 s to load the MOT fully, at which point the atom number saturates at approximately 5×10^7. For all subsequent experiments we load the MOT for 10 seconds to ensure a large atom number is obtained.

2.5.2 Atom number optimisation

The MOT atom number is dependent on a variety of different parameters which include the MOT beam power and detuning, the magnetic field gradient and the oven temperature. Therefore by varying each of these parameters in turn it is possible to maximise the atom number.

Figure 2.21 shows the measured change in the atom number as the power of the MOT, MOT repump, Zeeman and Zeeman repump beams were changed. For each measurement the power of the relevant beam was scanned by varying the RF power to the AOM, whilst the other beam powers were kept constant and at their maximum values. As the Zeeman repump light does not pass through an AOM, its power was changed by using neutral density (ND) filters. The beam detunings were kept constant for all measurements and a magnetic field gradient of 14.6 G/cm was maintained throughout. As repeat measurements were taken, in each graph the data points represent the mean atom number, and the standard error of the mean has been used as the error bar.

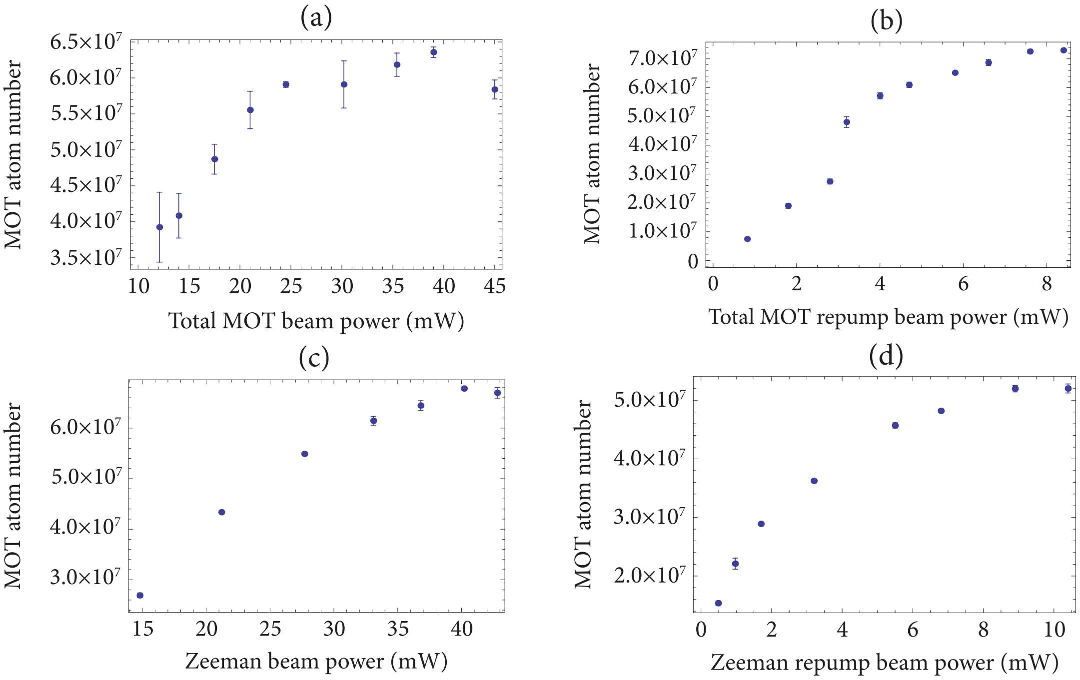

Figure 2.21: Experimental results showing the variation in atom number with the power of the (a) MOT beams, (b) MOT repump beams, (c) Zeeman beam, (d) Zeeman repump beam.

Each of the four graphs appears to have a similar shape where the atom number increases with beam power and eventually shows signs of saturation. Unsurprisingly, the highest atom number of 7.3×10^7 was produced by using the maximum beam powers of 46 mW, 8.4 mW, 38.1 mW and 11.4 mW for the MOT, MOT repump, Zeeman and Zeeman repump beams respectively. Looking at figure 2.21(a) saturation starts to become apparent for MOT powers above 25 mW. This corresponds to 8.3 mW per MOT beam, which results in an intensity just above I_{sat} in each beam. Further increasing the power does not increase the trapping force because the scattering rate saturates. This is equivalent to maximising the capture velocity of the MOT and so necessarily leads to saturation of the atom number. In figure 2.21(b) the atom number starts to saturate for MOT repump powers above 7.5 mW. As the repump light is used to form a closed cycling transition, saturation of the atom number indicates that atoms which have decayed to the $F = 1$ ground state are being pumped back into the main cooling cycle effectively. In figure 2.21(c) the atom number starts to level off as the Zeeman beam power approaches the relatively high value of 40 mW. It is important to have a high power Zeeman beam so that a large decelerating force can be applied, thus resulting in atoms with a lower average velocity upon exit from the Zeeman slower. Clearly this will lead to an increase in the number of atoms trapped in the MOT. A high beam power also makes the Zeeman slower less sensitive to small inaccuracies in the magnetic field profile of the slower. As before the atom number begins to plateau as the optical transition saturates, and all atoms with an initial velocity that can be captured by the Zeeman slower experience a reduction in their velocity that allows them to be loaded into the MOT. Figure 2.21(d) shows that saturation starts to occur for a Zeeman repump power of about 9 mW. Like the MOT repump, the Zeeman repump is used to maintain a closed transition at the zero field point of the Zeeman slower. Therefore saturation again indicates that atoms are being pumped back into the cooling cycle effectively.

Figure 2.22 shows the dependence of the atom number on the detuning of the MOT, MOT repump, and Zeeman beams. To vary the beam detuning, the AOM frequency was shifted. Therefore it was not possible to change the detuning of the Zeeman repump beam, as it does not pass through an AOM. For each measurement, the beam powers were kept at the optimal values mentioned above, each beam detuning was varied independently and again the magnetic field gradient was kept constant at 14.6 G/cm. In each graph a negative value denotes light that is red detuned from the relevant atomic transition.

In figure 2.22(a) the atom number peaks strongly as the MOT beam detuning reaches a value of $-4.2\,\Gamma$ from the $F = 2$ to $F' = 3$ transition. As the frequency is brought closer to resonance the atom number decreases. From equation (2.21) we can see that smaller detunings lead to a reduction in the capture radius. This in turn reduces the capture velocity of the MOT and results in fewer trapped atoms. When the detuning is larger than $-4.2\,\Gamma$, the capture radius exceeds the MOT beam radius. Therefore increasing the detuning no longer increases the capture radius. As large detunings reduce the average scattering rate, the force applied to the atoms is lower. Eventually the force becomes insufficient to slow the atoms that exit the Zeeman slower, meaning that they are no longer captured by the MOT. This produces a drastic drop in the atom number.

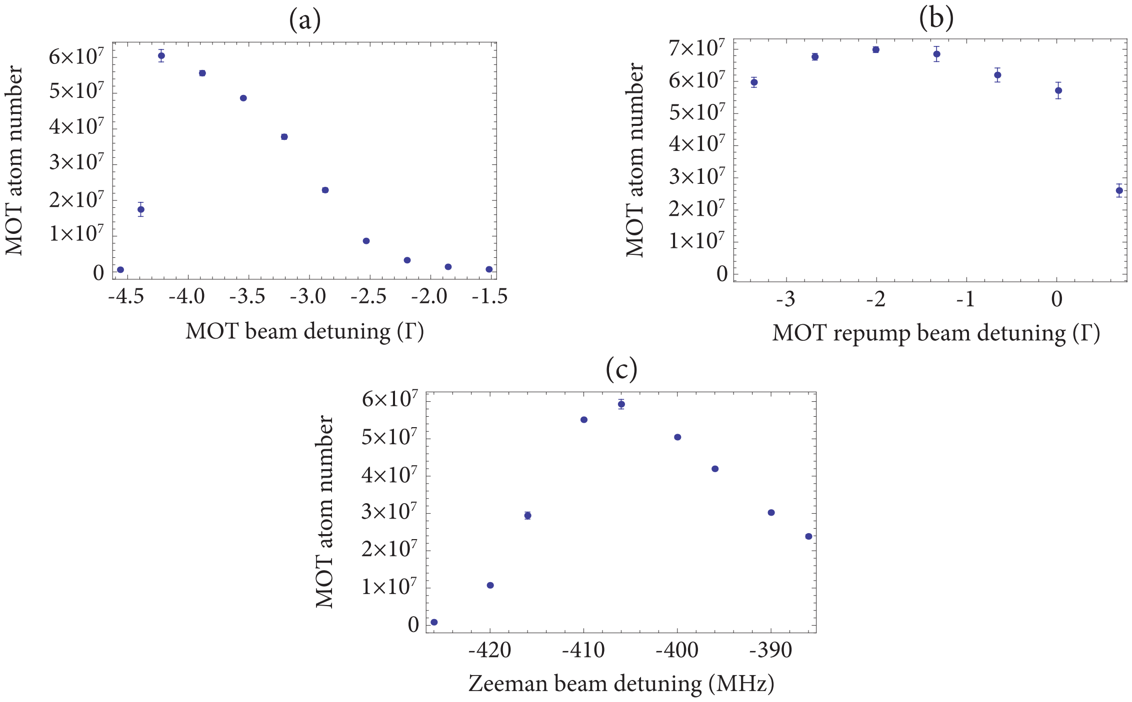

FIGURE 2.22: Experimental results showing the variation in atom number with the detuning of the (a) MOT beam, (b) MOT repump beam, (c) Zeeman beam.

The dependence of the atom number on the MOT repump beam detuning is shown in figure 2.22(b). The atom number is maximised for a detuning of $-2\,\Gamma$ from the $F = 1$ to $F' = 2$ transition, although the overall variation in atom number is small. As atoms are mainly cycling on the $F = 2$ to $F' = 3$ transition, the MOT repump light provides only a weak trapping force in the MOT and so the atom number does not depend strongly on this detuning. However when the repump light is blue detuned it heats the atoms causing a reduction in atom number.

The atom number as a function of the Zeeman beam frequency is shown in figure 2.22(c). Here the detuning is plotted in MHz from the $F = 2$ to $F' = 3$ field-free transition frequency for a stationary atom. The Zeeman slower has been designed to use light with a frequency of -401 MHz. This means atoms at the zero field point of the slower must have a velocity of 269.6 m/s in order to be resonant with the light. As these results show a peak in the atom number at a frequency of -406 MHz, atoms at the zero field point must instead have a velocity of 272 m/s. This discrepancy is most likely caused by the fact that the measured field profile in the Zeeman slower is smaller than the field expected from simulations [105]. This means the Zeeman shift to the atomic energy levels is smaller, so the light must have a larger red detuning in order to interact with the atoms. The reduction in atom number as the frequency is moved away from the peak value is most likely caused by inefficient slowing as the light is detuned from the atomic resonance.

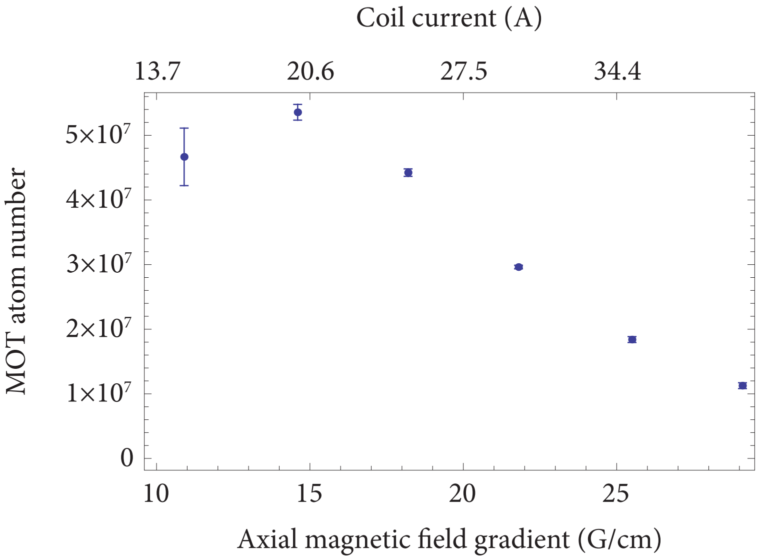

FIGURE 2.23: Experimental results showing the variation in atom number with axial magnetic field gradient.

The variation in atom number with magnetic field gradient is presented in figure 2.23 and shows a clear peak at a gradient of 14.6 G/cm. For larger field gradients, the steep drop off in atom number can be attributed to the reduction in the capture radius, which leads to a smaller capture velocity. For a given MOT beam intensity, there will be a particular MOT beam detuning and magnetic field gradient that maximise the atom number. As the field gradient rises, the detuning that optimises the atom number will also increase [116]. This is because a particular capture radius can only be maintained if both the field gradient and detuning rise together. As the detuning was not scanned at each of the field gradients tested, it is possible that our optimal parameter values represent a local maximum, and that a higher atom number could be attained by using a different combination of magnetic field gradient and MOT beam detuning.

Having optimised the MOT parameters to capture the largest number of atoms from the Zeeman slower, we proceeded to investigate the effect of oven temperature on the atom number. To measure the atomic flux exiting the oven, a 17 μW probe beam with a diameter of 6 mm and a height of 2 mm was sent through chamber one, perpendicular to the atomic beam. For reference see figures 2.7 and 2.10. This probe beam was positioned approximately 130 mm away from the oven aperture, and its frequency was scanned over a 0.8 GHz range about the $F = 2$ to $F' = 3$ transition frequency. The resulting absorption was detected using an amplified photodiode and the measurements were compared to the absorption signal predicted by theory.

In order to estimate how much absorption to expect, we must determine the average number of photons an atom will scatter as it passes through the probe beam. As there is no repump light present, atoms starting out in $F = 2$ will eventually be pumped to $F = 1$, due to the partially unresolved structure of the excited state. Therefore it is necessary to use a three-level model, where level 1 represents the $F = 2$ state, level 2 represents all hyperfine levels of the ${}^2P_{3/2}$ state, and level 3 represents the $F = 1$ ground state. We assume that all atoms start off in level 1 and through interaction with the probe beam are driven to level 2 at a rate given by

$$R_{LI} = \frac{\Gamma}{2} \frac{s_0}{(1 + 4\delta^2/\Gamma^2)}, \tag{2.57}$$

where R_{LI} is the scattering rate from equation (2.7) re-written in the limit of low light intensity and Γ is the spontaneous decay rate of level 2. From level 2 atoms will either decay to level 1 with a rate $b\,\Gamma$, or to level 3 with rate $(1 - b)\Gamma$, where as before b is the branching ratio and in this case has a value of approximately 2/3.

By solving the rate equations we find the number of atoms in level 2 as a function of time, $N_2(t)$. Then by integrating $\Gamma N_2(t)$ over the laser interaction time, τ, an expression for the number of photons emitted by an atom, n_p, is obtained [117],

$$n_p = \frac{R_{LI}\,\Gamma}{R_+ - R_-} \left(\frac{e^{-R_+\tau} - 1}{R_+} - \frac{e^{-R_-\tau} - 1}{R_-} \right), \tag{2.58}$$

where

$$R_\pm = R_{LI} + \Gamma/2 \pm \sqrt{R_{LI}^2 + b\,R_{LI}\,\Gamma + \Gamma^2/4}\,. \tag{2.59}$$

As the atomic beam is diverging, not all atoms will be moving perpendicular to the probe beam. Therefore the detuning of the light will not only depend on the laser frequency but also on the Doppler shift, $\Delta\omega = kv\sin\theta$. Here v is the velocity of the atom, and θ is the angle between the atomic velocity vector and the central axis of the atomic beam, which according to figure 2.10 is labeled as the x axis. To obtain an accurate estimate of the average number of photons scattered per atom, we can integrate equation (2.58) over the atomic velocity distribution and the range of angles that allow an atom to intersect the probe beam.

To determine the flux of atoms from the oven, we start with the Clausius-Clayperon equation which relates the lithium vapour pressure to the temperature [118],

$$P(T) = 101325 \exp\left[\frac{\Delta H_{\text{vap}}}{\overline{R}}\left(\frac{1}{T} - \frac{1}{T_{\text{B}}}\right)\right], \tag{2.60}$$

where P is the pressure in Pascal, ΔH_{vap} is the enthalpy of vapourisation, $\overline{R} = 8.31\,\text{J/Kmol}$ is the universal gas constant and T_{B} is the boiling point of lithium. The values of ΔH_{vap} and T_{B} can both be found in table 2.1. Using the ideal gas law, $P = nk_BT$, equation (2.60) can be re-written to describe the variation in number density as a function of temperature,

$$n(T) = \frac{101325}{k_BT} \exp\left[\frac{\Delta H_{\text{vap}}}{\overline{R}}\left(\frac{1}{T} - \frac{1}{T_{\text{B}}}\right)\right]. \tag{2.61}$$

We operate the oven in the effusive flow regime where the mean free path is much larger than the radius of the oven aperture. In this regime we can calculate the number of atoms that escape from the oven by using the kinetic theory of gases. The number of atoms dN, that strike a surface area element dS of the exit aperture, during a time interval dt, given atoms that have a velocity between v and $v + dv$ and a solid angle in the range $d\omega$ is

$$\begin{aligned} dN &= nv_xf(v)dv\,dS\,dt\frac{d\omega}{4\pi} && (2.62)\\ &= nv\cos\theta f(v)dv\,dS\,dt\sin\theta\frac{d\theta\,d\phi}{4\pi}. && (2.63)\end{aligned}$$

Here $v_x = v\cos\theta$ is the x component of the atomic velocity, θ is the angle between the atomic velocity vector and the x axis, and $f(v)dv$ describes the normalised velocity distribution of the atoms, which is just a Maxwell-Boltzmann distribution,

$$f(v)dv = \left(\frac{m}{2\pi k_BT}\right)^{3/2} 4\pi v^2 e^{-mv^2/2k_BT}dv. \tag{2.64}$$

Integrating equation (2.63) over all possible velocities, the full solid angle and the total area of the oven aperture, we obtain an expression for the total number of atoms that exit the oven per second,

$$\Phi = \frac{n\overline{v}A}{4\kappa} \tag{2.65}$$

$$= \frac{2r}{3l}n\overline{v}A, \tag{2.66}$$

where Φ is the atomic flux, $\overline{v} = \sqrt{8k_BT/\pi m}$ is the mean atomic velocity, A is the area of the aperture and $\kappa = 3l/8r$ is a correction factor that arises because our oven aperture is a tube with radius r and length l, where $l \gg r$, rather than a hole of negligible length [119]. Combining this with equation (2.61) we arrive at an expression for the number of atoms that exit the oven per second as a function of temperature. This leads to an estimated flux of 4.3×10^{15} atoms/second for our experiment when using an oven temperature of 500 °C.

The copper cup aperture at the oven exit ensures that only atoms with small θ can escape, and we can assume a $\cos\theta$ angular distribution for the atomic beam. By integrating $n_p\Phi$ over the atomic velocity distribution and a suitable solid angle we can then determine a value for the total number of photons scattered at any given temperature. By comparing this to the number of photons in the probe beam, we can estimate how much absorption to expect.

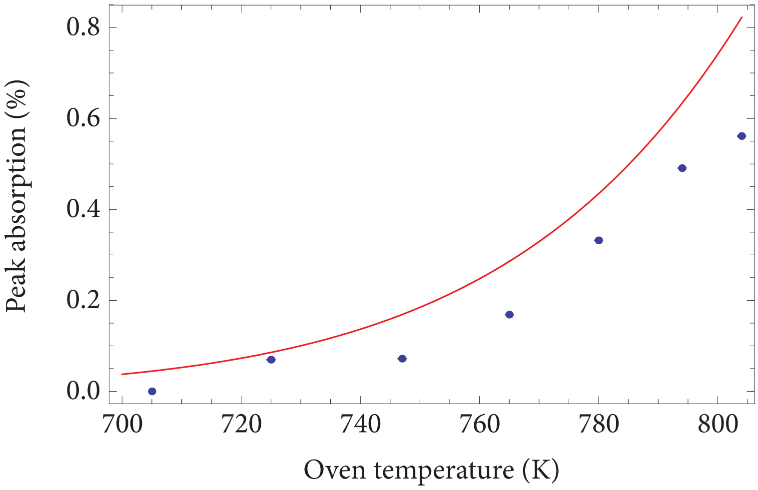

Figure 2.24: Measured peak absorption from the effusive lithium oven as oven temperature is varied. The red curve shows the theoretically expected variation in peak absorption as a function of temperature.

Figure 2.24 compares the expected amount of absorption, shown by the red curve, with experimental data. The peak absorption was determined by fitting a Gaussian to the absorption dip recorded by the photodiode, and extracting the peak height from the fit.

As expected the amount of absorption increases with temperature, due to the presence of more atoms. There is some disagreement between theory and experiment as we measure a smaller amount of absorption at each oven temperature. This discrepancy is most likely caused by an over-estimate of the temperature of atoms inside the oven. This could arise if, for example, the thermocouple used to measure the temperature was sitting too close to the band heater. By reducing the temperature assigned to each data point by only 10 K, we are able to obtain good agreement between theory and experiment.

In figure 2.25(a) the variation in MOT atom number with oven temperature is shown. These data were obtained by taking absorption images of the cloud after a loading time of 13 s. The initial rise in atom number with temperature can be attributed to the increase in atomic flux from the oven. We would expect this trend to continue with increasing temperature, however at 780 K the atom number clearly peaks at a value of around 2.3×10^8. Referring back to equation (2.56) we see that the number of atoms in the MOT depends on both the loading rate and the lifetime of the trap. As the oven temperature and atomic flux increase, the loading rate also increases, which leads to more atoms in the MOT. The peak in the data indicates that as the oven temperature rises, the lifetime of the trap falls. At some point the decrease in the lifetime is sufficiently large that, despite the increasing flux, the atom number in the MOT begins to drop.

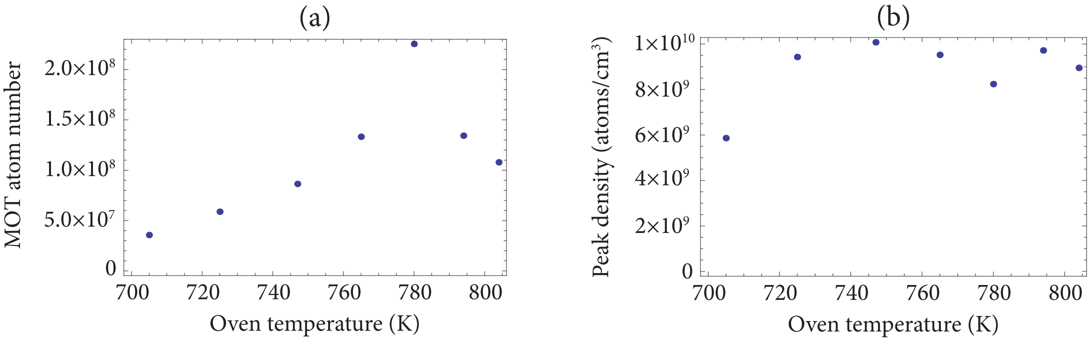

FIGURE 2.25: In (a) the measured atom number in the MOT is shown as the oven temperature is varied. In (b) the peak atomic density is shown as the oven temperature is varied.

Figure 2.25(b) shows the variation in the peak cloud density with oven temperature. This was determined by using the data in (a), measurements of the cloud size and equation (2.26). Here we can see that as the temperature rises above 705 K there is a small increase in the density, though for higher temperatures it appears to saturate at a value of around 9×10^9 atoms/cm^3. Although this is an order of magnitude smaller than the density limit found for other MOTs, it indicates that our atom cloud has entered the multiple scattering regime and is therefore density limited. To increase the density beyond this limit, one of the methods described in section 2.1.4 must be employed.

From these experiments we have found the parameters that lead to the largest number of atoms in the MOT. In particular the atom number is maximised for beam powers of 46 mW, 8.4 mW, 38.1 mW and 11.4 mW for the MOT, MOT repump, Zeeman and Zeeman repump beams respectively. The biggest atom numbers were found for detunings of $-4.2\,\Gamma$ for the MOT beam, $-2\,\Gamma$ for the MOT repump and -406 MHz for the Zeeman beam. In addition to this the largest atom numbers were found when using a magnetic field gradient of 14.6 G/cm and an oven temperature of 780 K. The largest atom number was found to be 2.3×10^8. For the rest of the experiments described in this thesis these optimal MOT parameters have been used, with the exception of the MOT beam detuning which is normally kept at $-3.5\,\Gamma$.

2.5.3 MOT temperature

In order to measure the temperature of atoms in the MOT we utilise the ballistic expansion technique. This method involves releasing the atoms from the trap by switching off the MOT beams and magnetic field. The atoms are left to expand freely for some period of time and are then imaged. Using an identically prepared cloud, this process is repeated so that a series of images showing the cloud at various stages of its expansion can be obtained. Then by measuring the cloud width as a function of time, it is possible to infer the temperature of the atoms. To see how this is possible we first have to determine how the atomic density distribution varies with time once the cloud has been released from the trap.

For simplicity, and because we only ever look at the expansion of the cloud along one axis at a time, we will derive an expression for the density distribution along the x axis as a function of time. This expression can be applied to any of the three cartesian axes, and can be easily extended to the three dimensional case if required. Referring back to section 2.1.4, we know that the density distribution of atoms in the MOT along the x axis can be described by the Boltzmann distribution,

$$n(x_0) = n_0 \exp\left[-\frac{U(x_0)}{k_B T}\right] \tag{2.67}$$

$$= n_0 \exp\left[-\frac{x_0^2}{2\sigma_0^2}\right], \tag{2.68}$$

where x_0 denotes the initial position of an atom and $\sigma_0 = \sqrt{k_B T/\kappa_x}$ is the initial standard deviation of the cloud.

The velocity of atoms in the MOT can be described by the Maxwell-Boltzmann distribution,

$$P(v_x)dv_x = A \exp\left[-\frac{m v_x^2}{2k_B T}\right] dv_x, \tag{2.69}$$

where $P(v_x)dv_x$ is the probability that an atom has a velocity between v_x and $v_x + dv_x$, and A is the normalisation constant. This can be re-written in terms of the initial position of the atom by using $v_x = x - x_0/t$, where x represents the atom's final position. This produces,

$$P(x_0, t)dx_0 = A \exp\left[-\frac{m(x - x_0)^2}{2k_B T t^2}\right] dx_0, \tag{2.70}$$

where the $1/t$ factor has been absorbed into the normalisation constant A. This expression describes the probability that an atom having an initial position x_0 ends up at a final position x.

As the density distribution at time t depends on both the spatial and velocity distributions of the cloud, we multiply (2.68) and (2.70) together and integrate over all possible initial positions,

$$n(x, t) = \int_{-\infty}^{\infty} n(x_0) P(x_0, t) dx_0 \tag{2.71}$$

$$= B \int_{-\infty}^{\infty} \exp\left[-\frac{x_0^2}{2\sigma_0^2}\right] \exp\left[-\frac{m(x - x_0)^2}{2k_B T t^2}\right] dx_0 \tag{2.72}$$

$$= B \exp\left[-\frac{x^2}{2\sigma_0^2 + 2k_B T t^2/m}\right]. \tag{2.73}$$

The exact form of B can be found through normalisation. This shows that the final density distribution along one axis has a Gaussian form with a standard deviation, or width of,

$$\sigma = \sqrt{\sigma_0^2 + \frac{k_B T t^2}{m}}. \tag{2.74}$$

To measure the temperature of our atom cloud we fit a two dimensional Gaussian to each absorption image. The fit is deemed adequate because the uncertainties on the fitting parameters are much smaller than the variation between successive shots. From the fit we extract values for the widths along the x and z axes, as shown in figure 2.10. In the following discussion these axes are referred to as the radial and vertical directions respectively. The width measurements are then plotted against time. With the initial width σ_0, and temperature T, left as floating parameters, we perform a weighted fit of the data to the model of equation (2.74). From this a value for the cloud temperature can be extracted.

Figure 2.26 shows the expansion of the cloud after release from the MOT, where the optimal MOT parameters found in the previous section have been used. The data shown here was obtained using coil 2, which switches of quickly enough that the residual magnetic trapping force has a negligible effect on the free expansion of the cloud. In the figure, the vertical cloud widths are represented by the red data points, and the radial widths are shown by the blue points. As repeat measurements were taken, each data point represents the mean value of σ, and the standard error of the mean has been used for each error bar. The error bars are larger at longer times because the signal from the expanded cloud is smaller, thus producing a less reliable fit.

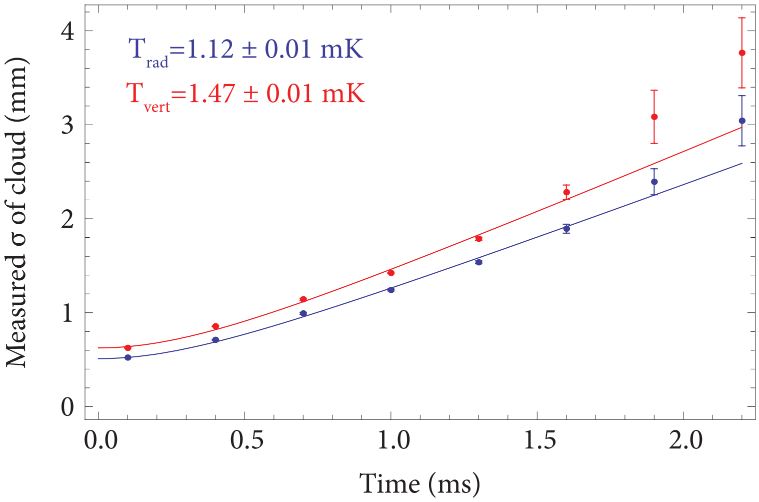

Figure 2.26: Ballistic expansion temperature measurement of the MOT cloud. The red data points represent width measurements in the vertical direction, whilst the blue points represent the width in the radial direction. Fits to the data are shown by the solid lines and from these temperature values are extracted.

Normally we would expect the vertical cloud width to be smaller than the radial width, as the vertical magnetic field gradient is higher. However these results show that our cloud has a smaller radial width. This could be caused by an imbalance in the MOT beam intensity, as this will alter the trapping force along the two axes, thus changing the aspect ratio of the cloud. From our fit to the data, we find the temperature of the cloud to be 1.47 ± 0.01 mK in the vertical direction, and 1.12 ± 0.01 mK in the radial direction. This discrepancy could be caused by small diffraction effects that make smaller clouds appear larger. If this is the case, the data at longer times should be more reliable, as diffraction effects become smaller with increasing cloud size. At shorter release times, although both width measurements will be affected, diffraction effects will be larger in the radial direction as the cloud is smaller along this axis. This would lead to the blue data points being higher than they should be, thus producing a larger underestimate of the temperature in the radial direction. Using equation (2.40) along with our MOT beam parameters, we find the temperature predicted by Doppler theory to be 0.5 mK, which does not agree well with our results. However, other lithium experiments which use similar powers and beam detunings measure temperatures in the 1 mK range [78]. This suggests that a simple two level model cannot be used to accurately describe the temperature of atoms in the MOT.

2.6 Cooling and compressing the cloud

In order to achieve our final experimental aims, ultimately we require a small, dense atom cloud. This means we have to simultaneously maximise the atom number and minimise the cloud width. As we have already found the parameters that produce the highest atom number, we now concentrate on finding a way to compress the cloud. In general there are two options available, either we can implement a compressed MOT (CMOT) phase by briefly increasing the magnetic field gradient with the MOT light still on, or we can alter the beam powers and detunings in order to decrease the cloud temperature. In an attempt to produce the smallest possible cloud, we have combined these two methods. For all the experiments detailed here coil 2 was used.

As we eventually want to have a large number of atoms in a magnetic trap with a steep field gradient, we began by looking at how variations in the CMOT phase affect the efficiency of transfer into the magnetic trap. Figure 2.27 shows the timing sequence used for these experiments. First atoms were loaded into the MOT. At this point the magnetic field gradient was equal to 14.6 G/cm and the MOT beams, which are shown in purple, were on and had their usual power and detuning. To take an absorption image of the MOT atoms, the probe beam, which is shown in yellow, was pulsed on. Next the coil current was either linearly ramped (blue), or instantaneously switched (pink) to produce a new magnetic field gradient given by y. This phase, where we have a MOT with increased magnetic field gradient, is called the CMOT, and it lasted for some period of time, x. By switching off the MOT beams the atoms were transferred into the magnetic trap, and were held there for 50 ms. After this the CMOT was reformed by switching on the MOT beams, and the field gradient was again switched or linearly ramped back to the original value. The cloud was then left for 20 ms to allow it to equilibrate before being imaged. Finally the percentage of retained atoms was calculated using the two cloud images obtained. By only imaging the atoms whilst in the MOT, as opposed to imaging after release from the magnetic trap, we are able to ensure that the imaging conditions remain the same. This is important as changes in the magnetic field could lead to some atoms becoming invisible.

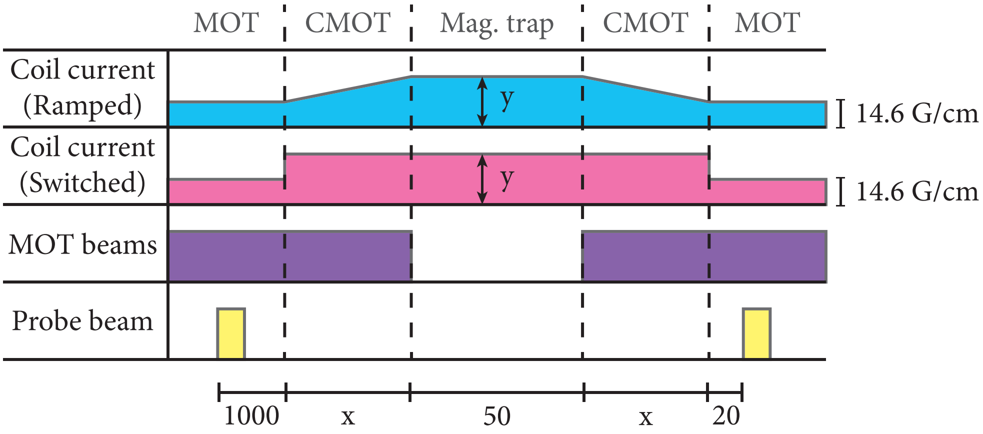

FIGURE 2.27: Timing sequence used to optimise CMOT phase. Depending on the experiment being carried out, either the coil current is ramped (blue), or switched (pink) to a higher current, thus producing a CMOT. The length of the CMOT stage is given by x. The magnetic field gradient in the MOT is 14.6 G/cm, this is increased to some value, y, during the CMOT stage. The timing sequence for the MOT beams (purple) and probe beam (yellow) is also shown. All times are given in milliseconds.

Figure 2.28 shows how the percentage of atoms retained changes with the final axial magnetic field gradient used during the CMOT phase. This value is represented by y in figure 2.27. For the black, blue and red data points the magnetic field was linearly ramped over $x = 25$ ms, 50 ms and 100 ms respectively, whilst for the green data points the magnetic field was instantaneously switched such that $x = 25$ ms. We can see that for field gradients below 50 G/cm there is little difference between the various data sets, and that higher gradients lead to an increase in the percentage of atoms retained. This is expected as the trap depth increases with magnetic field gradient, thus allowing hotter atoms to be captured. We would expect the atomic percentage to keep rising until the trap depth is large enough to capture the entire atomic velocity distribution, at which point it should saturate. Given that only three of the eight ground state M_F sub-levels can be magnetically trapped, we would expect to retain a maximum of $3/8 \approx 38\%$ of the atoms.

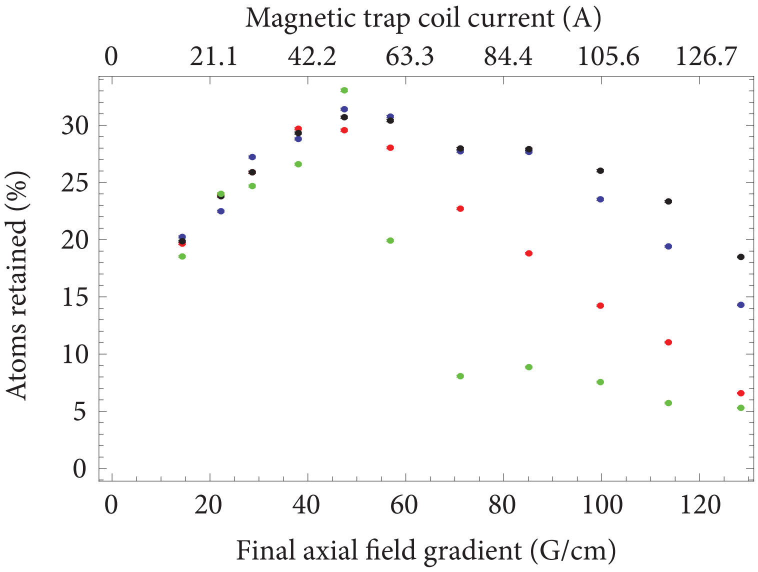

FIGURE 2.28: Percentage of atoms retained after transfer to and from the magnetic trap via the CMOT phase as the final axial field gradient used during the CMOT phase is varied. The black, blue and red data points use a linear ramp of the field over $x = 25$ ms, $x = 50$ ms and $x = 100$ ms respectively. For the green data points the field is rapidly switched such that $x = 25$ ms.

These results however, show a clear peak of around 30% at a gradient of 47.4 G/cm for all data sets. As the magnetic field gradient is increased above this point the atom percentage begins to fall, with longer ramp times producing a bigger drop. This suggests that shorter ramp times are better, and perhaps indicates that by rapidly switching the field, the highest percentage of atoms can be retained. However this is not the case, as the green points show the largest percentage drop of all four data sets. This can potentially be explained by considering how losses from the CMOT change as the cloud density varies.

We know from section 2.5.1 that two-body collisions between atoms in the MOT can lead to losses from the trap, and that this effect becomes significant when the cloud density is high. Therefore the reduction in atom percentage at large field gradients could be caused by an increase in the two-body loss rate due to the high density of the cloud. This effect could also explain why longer field ramps produce a smaller atom percentage, as the atoms spend more time at high density, thus allowing more collisions to occur. When the current is switched rather than ramped, the atoms spend even more time at high density, thus producing an even greater loss of atoms. This suggests that the largest percentage of atoms could be retained by switching the current immediately before transfer to the magnetic trap. However temperature measurements have shown that this induces a breathing mode, which causes the cloud width to initially decrease upon release from the CMOT. Therefore, if reliable temperature measurements are to be obtained a linear ramp of the magnetic field should be employed. To achieve a good balance between having a large atom number and a small cloud, for all subsequent measurements we ramp the field gradient to a value of 60 G/cm over 65 ms. From now on this will be referred to as the CMOT field ramp.

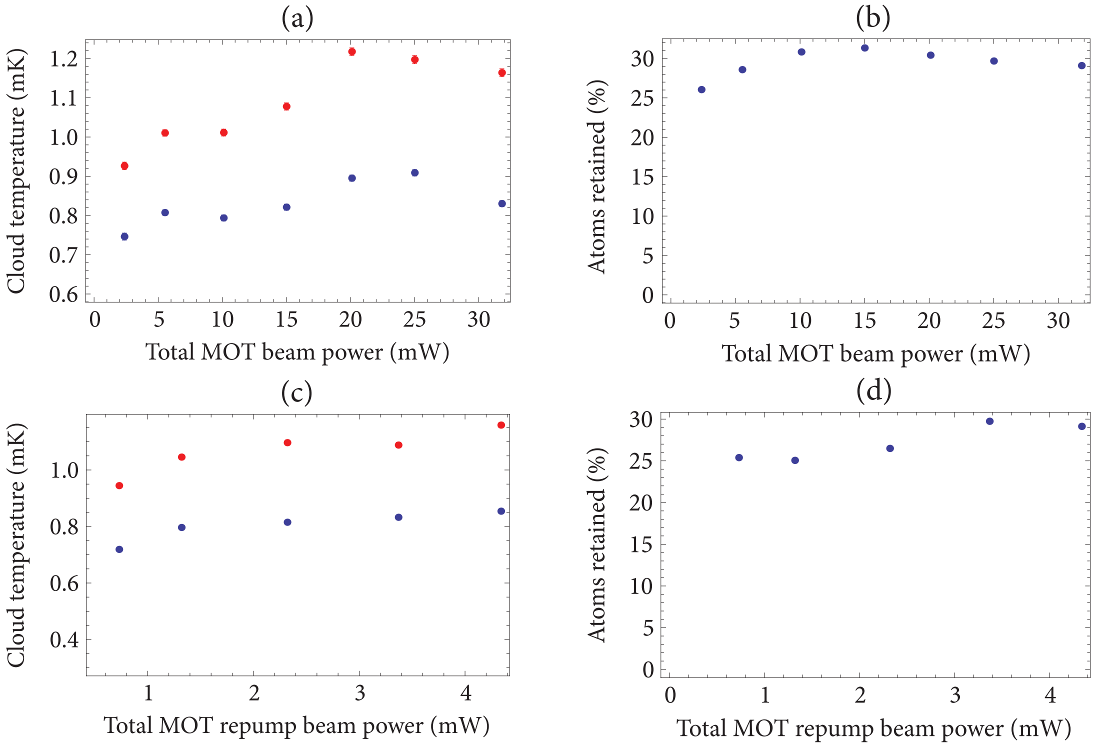

FIGURE 2.29: Experimental results showing the variation of the (a) temperature with MOT beam power, (b) percentage of atoms retained with MOT beam power, (c) temperature with MOT repump power, (d) percentage of atoms retained with MOT repump power, during the CMOT phase. In (a) and (c) the blue and red points represent temperature measurements in the radial and vertical directions respectively.

Having found the optimal field gradient to use during the CMOT phase, we then moved on to finding the beam powers and detunings that minimise the cloud temperature. Figure 2.29(a) shows how changing the power of the MOT beams during the CMOT stage affects the temperature of the cloud. Here the blue and red data points represent temperature measurements in the radial and vertical directions respectively. As before the radial direction corresponds to the x axis in figure 2.10, whilst the vertical direction corresponds to the z axis. For each measurement we employed the CMOT field ramp, whilst simultaneously ramping down the total MOT beam power to the various values given in the figure, over a period of 65 ms. All other beam powers and detunings were kept constant and the temperature was determined via ballistic expansion measurements. Here the error bars represent the error on the temperature fit. The figure clearly shows that lower MOT beam powers lead to a corresponding reduction in the cloud temperature, which is in agreement with simple Doppler theory.

To ensure that lower temperatures are not accompanied by a large loss of atoms, the atom percentage retained after transfer to and from the magnetic trap was also measured. These results were obtained using the same procedure as depicted in figure 2.27. As shown in figure 2.29(b) for beam powers below 10 mW, the atom percentage is reduced by approximately 5%.

In figure 2.29(c) the temperature variation with MOT repump power is shown, whilst figure 2.29(d) shows the change in atom percentage with MOT repump power. These results indicate that a small reduction in the temperature can be achieved by using a low MOT repump power, however this is accompanied by a small loss of atoms from the trap. From this we conclude that the optimal powers to use during the CMOT phase are 2.5 mW for the MOT beam, and 0.7 mW for the MOT repump beam, as this produces a lower cloud temperature without a large reduction in the percentage of atoms retained.

Figure 2.30(a) shows the variation in temperature as the detuning of the MOT beam is linearly ramped from an initial value of $-3.5\,\Gamma$ to a variety of different values over the 65 ms CMOT phase. Again the blue and red points represent temperature measurements in the radial and vertical directions respectively. As before the usual CMOT field ramp was utilised. By altering the frequency of the beam, its power will also change. Therefore to isolate the effects of detuning on the cloud temperature, the MOT and MOT repump beam powers were ramped down during the CMOT phase to 11.7 mW and 4.26 mW respectively, as this was the highest power that could be reached for every frequency in the tested range. This means there is likely to be an additional cooling effect because of the drop in power, however overall trends in the data should not be affected. All other beam powers and detunings were kept constant at the usual MOT values throughout the

CMOT phase. As expected the data shows a large drop in temperature as the frequency is shifted closer to resonance. From Doppler theory, provided $s_0 \ll 1$, we would expect the minimum temperature to lie at a detuning of $-\Gamma/2$, however our data does not cover this range. This is because, as can be seen in figure 2.30(b), for detunings below $-3.5\,\Gamma$ there is a drastic loss of atoms, making it impossible to measure the temperature at detunings much smaller than $-1\,\Gamma$. This loss of atoms could be caused by an increase in the rate of two-body losses, as smaller detunings will compress the cloud leading to a higher density.

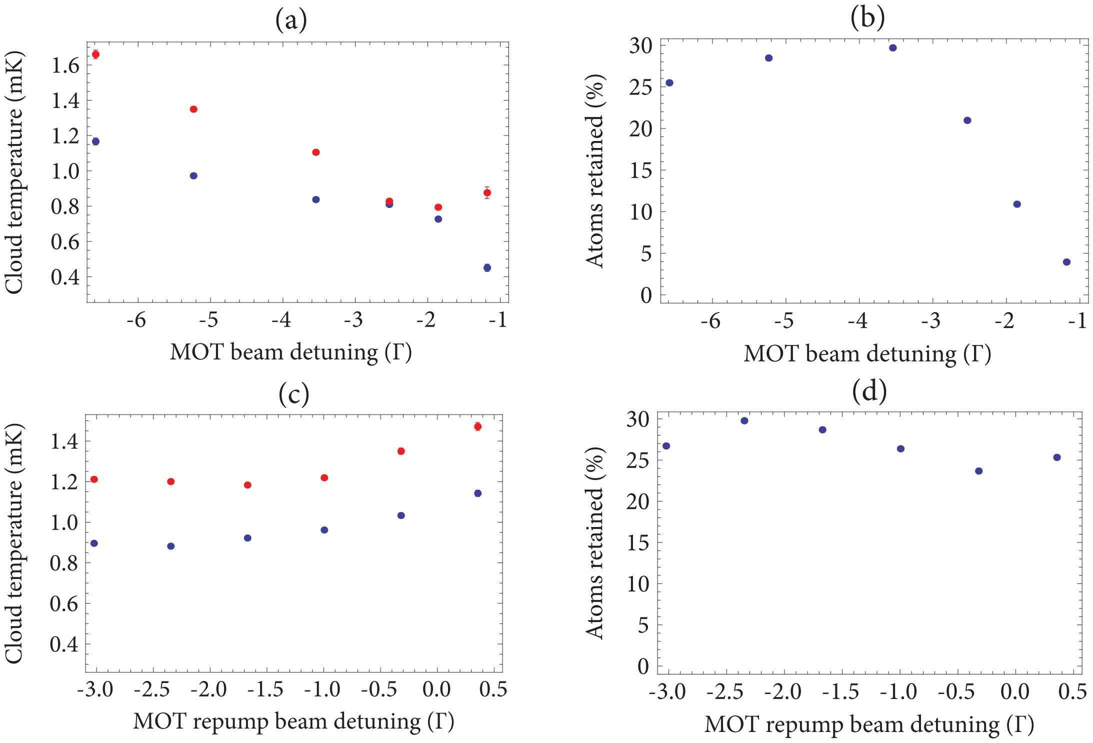

FIGURE 2.30: Experimental results showing the variation of the (a) temperature with MOT beam detuning during the CMOT phase, (b) percentage of atoms retained with MOT beam detuning during the CMOT phase, (c) temperature with MOT repump detuning during MOT loading and CMOT phase, (d) percentage of atoms retained with MOT repump detuning during MOT loading and CMOT phase. In (a) and (c) the blue and red points represent temperature measurements in the radial and vertical directions respectively.

The variation in temperature with MOT repump detuning is shown in figure 2.30(c). For these measurements the detuning was set to various values at the beginning of the MOT loading sequence, and was kept constant throughout the CMOT phase. As shown in section 2.5.2, the MOT atom number only changes slightly with MOT repump detuning. Therefore it makes sense to optimise the detuning to produce the lowest possible temperature. To ensure a constant beam power at each of the tested frequencies, the MOT repump power was kept at 3.5 mW throughout the MOT loading and CMOT phases.

This data set shows that a small decrease in temperature can be obtained by increasing the red detuning of the light. According to figure 2.30(d), there is a slight increase in the percentage of atoms retained for larger detunings. From these results we conclude that, in order to produce the lowest possible temperature we should use a MOT repump detuning of $-2.3\,\Gamma$ throughout the MOT loading phase. The MOT beam detuning on the other hand should be kept constant at $-3.5\,\Gamma$ as lower detunings lead to a large loss of atoms from the trap.

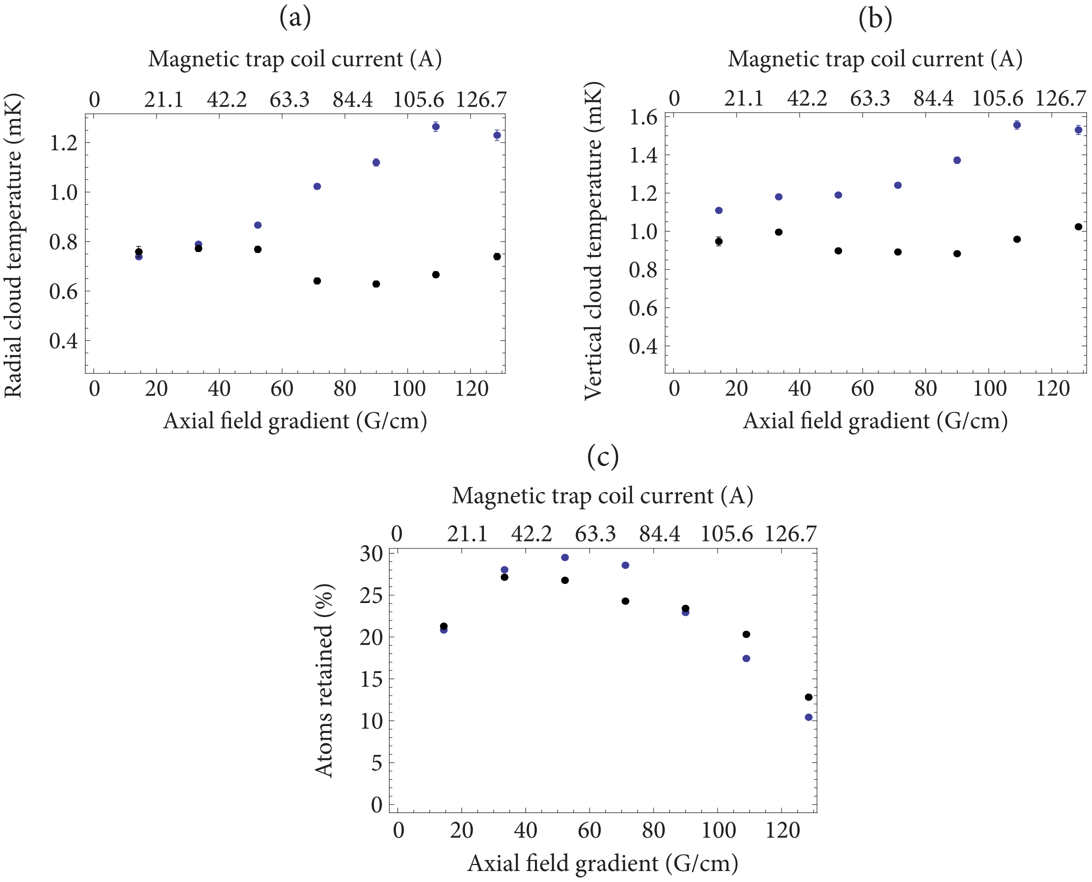

FIGURE 2.31: Experimental results showing the variation of (a) radial temperature, (b) vertical temperature, (c) percentage of atoms retained, with axial magnetic field gradient during the CMOT phase. The blue data points were obtained using a linear field ramp over 65 ms. The black data points use the same field ramp, along with a reduction in the MOT and MOT repump powers during the CMOT phase, and a switch of the MOT repump detuning at the start of the the MOT loading phase.

Finally we investigated how changes in the magnetic field gradient affect the temperature of the cloud. In figure 2.31(a) the radial temperature is shown, whilst figure 2.31(b) shows the vertical temperature. In both figures the blue data points were obtained by ramping the magnetic field to various values over 65 ms. To obtain the black data points, the same field ramp was used along with a reduction of the MOT and MOT repump beam powers to

2.5 mW and 0.7 mW respectively over a 65 ms time scale. Additionally the MOT repump detuning was kept at $-2.3\,\Gamma$ throughout the MOT loading sequence.

From the blue data we see that larger magnetic field gradients during the CMOT phase lead to higher temperatures. By increasing the field gradient, energy is transferred to the atoms, causing their temperature to rise. In general we would expect the MOT beams to re-cool the atoms on a time scale given by the MOT damping rate. For our experiment this is on the order of 0.3 ms. Therefore we do not expect to see any significant change in the temperature with magnetic field gradient. However these results could be explained by an increase in density at high field gradients. As shown in figure 2.31(c), the atom percentage drops with increasing magnetic field gradient. If this is due to an increase in two-body collisions, then atoms at the centre of the cloud will be preferentially lost, as they have the highest density. As these atoms also have the lowest temperature, this would result in an increase in temperature with magnetic field gradient.

Looking at the black data we see that the temperature of the cloud is reduced by ~ 0.5 mK at high field gradients, and only varies slightly across the entire range of gradients tested. As the beam power during the CMOT phase is lower for these measurements, the cloud density will not be as high, meaning that fewer of the low temperature atoms will be lost. Looking at figure 2.31(c), we see that for the highest field gradients more atoms are retained. This could occur if two-body losses have been reduced.

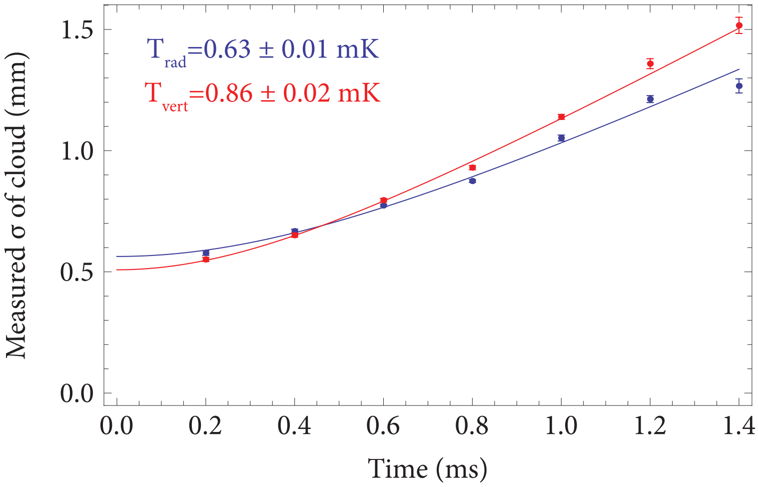

FIGURE 2.32: Ballistic expansion temperature measurement of the atoms released from the CMOT, using the optimal cooling parameters. The red data points represent width measurements in the vertical direction, whilst the blue points represent the width in the radial direction. Fits to the data are shown by the solid lines.

In figure 2.32 a measurement of the final cloud temperature given our optimal cooling parameters is shown. To maintain a large atom number we linearly ramp the field to 60 G/cm over 65 ms. At the same time we ramp the MOT and MOT repump powers to 2.5 mW and 0.7 mW respectively, so as to reduce the temperature. In addition to this the MOT repump detuning is kept at $-2.3\,\Gamma$ throughout the MOT loading sequence. Fits to the data produce a radial temperature of 0.63 ± 0.01 mK, and a vertical temperature of 0.86 ± 0.02 mK. Comparing this to the temperatures quoted in section 2.5.3 there has been a reduction of 0.49 mK and 0.61 mK in the radial and vertical directions respectively. Given our magnetic field gradient, this leads to a minimum cloud size of around 4 mm in the magnetic trap, which is eight times larger than our ideal cloud size of 0.5 mm. In the long term this will be problematic as it means only a small fraction of atoms can be placed between the high field electrodes. However by cooling further, via evaporative cooling for instance, it should be possible to reduce the size of the cloud. For now we want to maintain a high atom number to make characterisation of the atomic transport easier, therefore we have made no further attempts to reduce the cloud size.

2.7 Chapter summary

In order to maximise the number of atoms trapped in the MOT we have carried out experiments to measure how this varies with beam power, beam detuning, magnetic field gradient and oven temperature. This has allowed us to trap up to 2.3×10^8 atoms with an initial temperature of ~ 1.3 mK and a density of approximately 9×10^9 atoms/cm^3. As we eventually want our atomic sample to be cold and dense, we have implemented and optimised a CMOT stage. By varying the duration of this stage, the magnetic field gradient applied, the beam powers and detunings, we are now able to reduce the cloud temperature to ~ 0.75 mK, and can recapture $\sim 28\%$ of the atoms in the MOT after having spent 50 ms in the magnetic trap. This should be sufficient to allow us to characterise the transportation setup, although for further experiments it will be beneficial to have a colder cloud with a higher density.

Chapter 3

Magnetic trapping and transport

As the sympathetic cooling, and high electric field experiments will be carried out in the science chamber, it is necessary to transport the atoms. In order to do this they must first be transferred from the MOT to the magnetic trap. This chapter begins, in section 3.1, with a brief introduction to the theory of magnetic trapping and the associated mechanisms by which atoms are lost from the trap. The loss rate due to collisions with background particles is measured and the effect of the oven temperature on this loss rate is also studied. As the atoms will eventually have to be imaged in the science chamber, section 3.2 describes the problems associated with imaging the atom cloud after release from the magnetic trap. The source of these problems is identified through measurements of the atomic line shape. Finally section 3.3 discusses the transportation method used to move atoms from the MOT chamber to the science chamber. The optimisation procedure is described, and measurements of the magnetic trap lifetime in the science chamber are presented.

3.1 Magnetic trapping

In this section a brief overview of the theory of magnetic trapping is given. The main loss mechanisms from the magnetic trap are described and the loss rate due to collisions with background particles is measured. In addition to this the variation in the magnetic trap lifetime with oven temperature is investigated.

3.1.1 Theory of magnetic trapping

When an atom with a permanent magnetic moment is subjected to a static magnetic field, an interaction occurs that shifts the atomic energy levels and lifts degeneracy. This is known as the Zeeman shift. If the applied magnetic field is inhomogeneous, the atom will experience a force that causes it to move to a position where the interaction energy is minimised. It is this phenomenon which allows atoms to be trapped by a magnetic field.

If the applied magnetic field is low, the shift of the atomic energy level is given by

$$E = g_F M_F \mu_B B, \tag{3.1}$$

where g_F is the Landé g-factor, M_F is the projection of the total angular momentum onto the magnetic field axis, μ_B is the Bohr magneton and B is the applied magnetic field. The direction of this shift determines whether or not an atom can be trapped. If the energy level is shifted towards higher energies with increasing B the state is low-field seeking, as the energy is minimised at low magnetic fields. Conversely if the energy level is shifted downwards the state is high-field seeking. With the use of DC fields only relative minima can be produced [120], meaning that only low-field seeking states can be magnetically trapped. For lithium only three of the eight Zeeman sub-levels of the $^2S_{1/2}$ ground state are low-field seeking. These are the $M_F = 2$ and $M_F = 1$ levels of the $F = 2$ state for which $g_F = 1/2$, and the $M_F = -1$ level of the $F = 1$ state for which $g_F = -1/2$. Atoms in the $M_F = 2$ state experience the full trapping force and are more tightly confined than atoms in the $M_F = 1$ and $M_F = -1$ states. Assuming an equal population of all Zeeman sub-levels in the MOT, we can expect to transfer at most $3/8 \approx 38\%$ of the atoms to the magnetic trap.

Although a number of different geometries have been used to magnetically confine atoms, for our experiment we use the simplest configuration which is a quadrupole field. It is produced by a pair of anti-Helmholtz coils which means that, as long as high currents can be used, both the MOT and magnetic trap can be formed by the same coil pair. As well as this the trap is easy to construct, provides good optical access, and due to the linear field gradient close to the trapping centre, the atom cloud is tightly confined. The main disadvantage of this design is that atoms close to the zero field point can be lost from the trap, as they are able to make transitions to untrapped states.

As an atom moves through the trap, the local magnetic field vector will change. If the atom is to remain in a particular M_F sub-level, the adiabaticity condition must be met. This can be written as [112]

$$\frac{d\theta}{dt} < \omega_L = \frac{g_F M_F \mu_B |\mathbf{B}|}{\hbar}, \tag{3.2}$$

where θ is the angle between the magnetic moment and the magnetic field vector and ω_L is the Larmor frequency. This condition simply states that an atom will remain trapped if its magnetic moment precesses around the magnetic field vector faster than the rate at which the field direction changes. Close to the zero field point this condition is not met, meaning that transitions to untrapped states are possible. These are known as Majorana transitions.

To estimate the size of the low field region where Majorana transitions can occur, we consider an atom with velocity v and mass m moving in a circular orbit of radius ρ around the zero field point. The angular velocity of the atom is $\omega_{\text{vel}} = v/\rho$, which means the rate of change of the magnetic field direction can be written as $d\theta/dt = v/\rho$. Inserting this into equation (3.2) and setting the two sides equal to each other, we find the approximate radius, ρ_0, of the "hole" through which atoms can be lost,

$$\rho_0 \approx \sqrt{\frac{v\hbar}{g_F M_F \mu_B B'}}\,. \tag{3.3}$$

Here we have used $B = B'\rho_0$. The loss rate Γ_M is then given by the flux of atoms through this region and is found to scale as [121]

$$\Gamma_M \propto \frac{\hbar}{m}\left(\frac{g_F M_F \mu_B B'}{k_B T}\right)^2. \tag{3.4}$$

The proportionality constant has been determined for both rubidium [121–123] and sodium [124], however no such measurement has been carried out for lithium. Therefore in order to estimate whether Majorana transitions are significant, we insert the typical parameters for our magnetic trap into equation (3.3). Given our maximum field gradient of 60 G/cm and a temperature of $\sim$0.75 mK, which equates to a speed of $v = \sqrt{2k_BT/m} = 1.3\,\text{m/s}$, the radius of the hole is $5\,\mu$m for atoms in the $F = 2$, $M_F = 2$ state. Compared to our cloud radius of 2 mm, this is negligibly small, which indicates that Majorana losses are insignificant. However if at some later stage a colder cloud is required, they may become problematic as cold atoms are tightly confined to the trapping centre and as such spend more time in the low field region. If this becomes an issue a variety of different trap geometries could be incorporated into the setup. These include the time-averaged orbiting potential (TOP) trap [121], or the Ioffe-Pritchard trap [125].

3.1.2 Lifetime of the trap

In order to transport atoms to the science chamber, it is necessary to have a long magnetic trap lifetime. Just like the MOT, atoms in the magnetic trap are predominantly lost by colliding with background gas particles. This leads to an exponential decay of the atom number which can be written as,

$$N(t) = N_0 e^{-t/\tau}, \tag{3.5}$$

where $N(t)$ describes the number of atoms as a function of time, N_0 is the initial atom number and τ is the lifetime of the trap.

To estimate the trap lifetime we have to determine the number of collisions that occur between background gas particles and an atom as it moves through the vacuum chamber. This depends on three parameters which are the number density, n_{bg}, and velocity, v_{bg}, of the background gas, as well as the collision cross section between the background gas and the lithium atoms, σ_{Li}. Consider an atom as it moves through the chamber. In a time t it will sweep out a volume of size $\sigma_{\mathrm{Li}} v_{\mathrm{bg}} t$. If this same volume is occupied by a background gas atom, a collision will occur. Therefore the total number of collisions N_{coll}, will be equal to the number of atoms in this volume. This is given by $N_{\mathrm{coll}} = n_{\mathrm{bg}} \sigma_{\mathrm{Li}} v_{\mathrm{bg}} t = R_{\mathrm{coll}} t$, where $R_{\mathrm{coll}} = 1/\tau$ is the collision rate and τ is the trap lifetime. Using the ideal gas equation, $n = P/(k_B T)$, and the fact that the mean velocity of the Maxwell-Boltzmann distribution is $v = 2\sqrt{2k_B T/(\pi m)}$, the lifetime can be written as

$$\tau = \frac{1}{n_{\mathrm{bg}} \sigma_{\mathrm{Li}} v_{\mathrm{bg}}} = \frac{1}{\sigma_{\mathrm{Li}} P} \sqrt{\frac{\pi m k_B T}{8}} \,. \tag{3.6}$$

Although the exact composition of the background gas is unknown, we can obtain a rough estimate of the expected lifetime by using the value found in [119] for the collision cross section between lithium and helium, $\sigma_{\mathrm{Li}} = 1.06 \times 10^{-18}\,\mathrm{m}^2$. Given our measured

MOT chamber pressure of 1.7×10^{-9} mbar, and assuming the background atoms are at a temperature of 20 °C, we expect the magnetic trap lifetime to be $\tau \approx 18$ s.

In order to determine the actual lifetime of the magnetic trap we measure how the atom number decays as a function of time. The results of this measurement are shown in figure 3.1. To obtain this data set the atoms were first imaged in the MOT after a loading time of 10 s. Then they were cooled and compressed using the CMOT phase, which involved ramping the field gradient to 60 G/cm whilst simultaneously reducing the power in the MOT and MOT repump beams over a 65 ms time period. Next the atoms were loaded into the magnetic trap and were held there for various lengths of time. After this the CMOT was reformed by switching on the MOT beams, and all parameters were ramped back to the usual MOT values. Finally the atoms were left to equilibrate for 20 ms before being imaged. The percentage plotted in the figure is calculated by comparing the atom number of the reformed MOT with the initial atom number. For this data set an oven temperature of around 793 K was used.

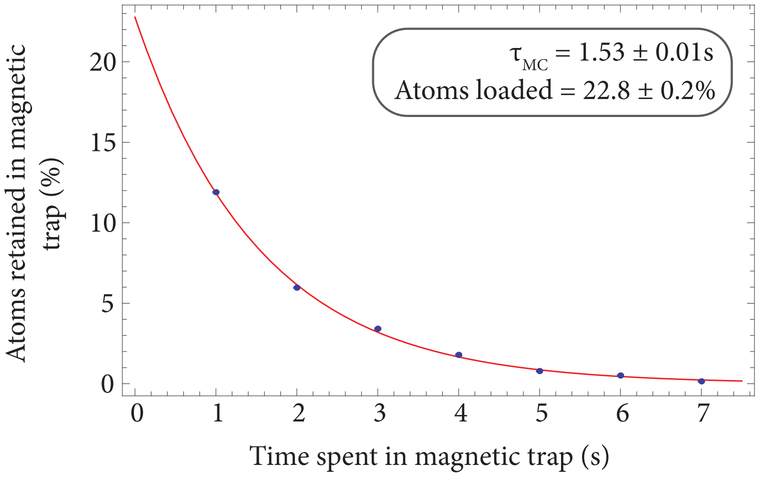

FIGURE 3.1: Measured loss of atoms from the magnetic trap with time. The red line is an exponential fit to the data. From this the lifetime and percentage of atoms loaded into the trap are extracted.

An exponential fit to the data is shown by the red line. From this we find the magnetic trap lifetime in the MOT chamber to be $\tau_{\mathrm{MC}} = 1.53 \pm 0.01$ s, which is an order of magnitude smaller than the theoretically predicted value. This discrepancy is most likely due to the background pressure in the MOT being substantially different to the pressure measured at the gauge. This is because the gauge is attached to the MOT chamber via two four-way crosses and it is close to the ion pump. In this position it is likely to measure a lower pressure than in the actual MOT region. From our measured lifetime we expect the pressure in the MOT chamber to be around 2.7×10^{-8} mbar.

Figure 3.1 also shows that the atomic percentage at time $t = 0$ has a value of $22.8 \pm 0.2\,\%$. This represents the percentage of atoms that are successfully loaded into the magnetic trap. For these measurements atoms are only recaptured if they remain within the recapture volume of the MOT. The radius of this volume is equal to the MOT beam radius, which is 0.96 cm. By finding the magnitude of the magnetic field at this position, the effective trap depth is found to be just under 4 mK in the axial direction. Using this value and assuming that the cloud has an average temperature of 0.75 mK, it is possible to predict the percentage of retained atoms by finding the fraction of the Maxwell-Boltzmann distribution that has a velocity below the trap depth. Atoms in the $F = 2$, $M_F = 2$ state will see the full trap depth and as such we expect to retain 82% of them. Atoms in the $F = 2$, $M_F = 1$ and $F = 1$, $M_F = -1$ states however see only half of the total trap depth, which means 52% of these atoms will be retained. Assuming an equal population of all Zeeman sub-levels, in total we expect to load around 23% of the MOT atoms into the magnetic trap. This agrees well with our results.

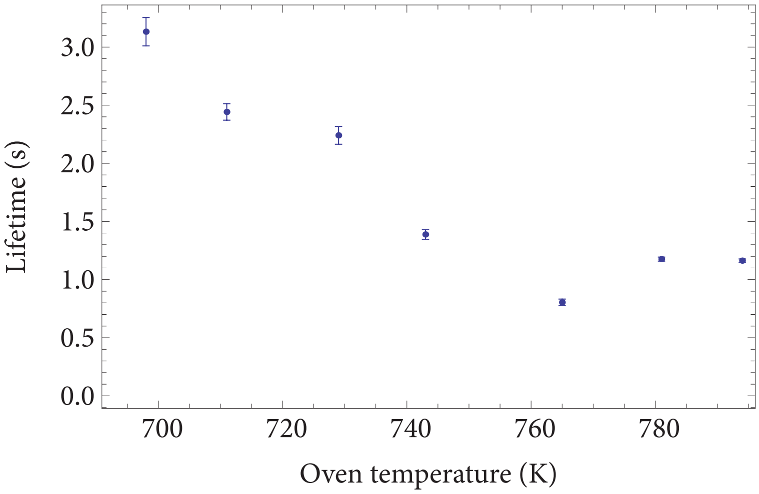

Figure 3.2: Lifetime of the magnetic trap as the oven temperature is varied.

In figure 3.2 the effect of oven temperature on the lifetime of the magnetic trap is shown. The procedure used to measure the lifetime again involved loading the atoms into the magnetic trap for varying amounts of time, before recapturing them in the MOT. However for this set of data no CMOT stage was used. Although this affects the percentage of atoms loaded into the trap, it should not affect the lifetime measurement itself. The error bars on each data point come from the errors on the exponential fit. The fitting errors are smaller at higher temperatures because this gives more atoms. This figure clearly shows that higher oven temperatures lead to a lower trap lifetime. This is because after repeated cycling of the temperature, the oven developed a small leak. By increasing the oven temperature, the leak worsens leading to an increase in the background pressure and a corresponding decrease in the magnetic trap lifetime. Ultimately this requires fixing, however for now the trap lifetime is sufficient to allow the transport procedure to be tested. Therefore to benefit from the increase in atom number that comes with higher temperatures, the cloud must be transported quickly to the science chamber where the background pressure should be lower.

3.2 Imaging the released cloud

Before testing the atomic transportation setup it is important to make sure that we are able to obtain reliable images of the atom cloud upon release from the magnetic trap. This is required because ultimately atoms will have to be imaged in the science chamber. A number of factors can affect the images obtained, including the presence of repump light, the length of the probe beam pulse, the polarisation of the probe beam and stray magnetic fields that persist after the coils have been switched off. In this section we investigate the effects of each of these factors and find the conditions that maximise the measured optical depth of the cloud.

3.2.1 Duration of the probe beam pulse

In figure 3.3 measurements of the peak optical depth are shown as the probe beam pulse duration is varied. These data sets were obtained by releasing the atoms from the usual CMOT and leaving them to expand for 0.7 ms, after which they were imaged. For the blue data points the MOT repump light was flashed on during imaging, whilst for the red data points no repump light was used.

Both data sets show a clear reduction in the peak optical depth as the probe beam pulse duration increases. To understand this trend we have to consider the effect of the probe light on the speed of the atoms being imaged. When an atom absorbs a photon from the probe beam, it will receive a momentum kick in the propagation direction of the light. This changes the velocity of the atom and creates a Doppler shift. If the atom is initially

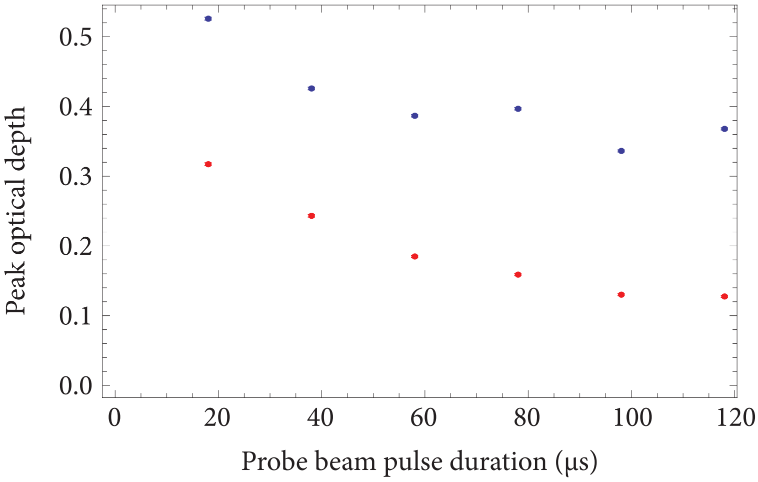

FIGURE 3.3: Measured peak optical depth as the probe beam pulse duration is varied. For the blue data points the MOT repump light was flashed on during imaging, whilst the red data points used no repump light.

resonant with the probe beam then, as the number of scattered photons goes up, the detuning of the light will increase. This means that the average scattering rate will be lower for longer interaction times. As a result we expect to measure a smaller peak optical depth as the probe beam pulse duration increases. If this effect is not taken into account then long probe beam pulses will produce an underestimate of the total atom number.

For sufficiently long interaction times the atom will be shifted out of resonance with the probe beam. To produce a Doppler shift of half a linewidth, the velocity of our lithium atoms must increase by 2 m/s. This requires 23 photons to be scattered. Given our probe beam has a detuning of approximately 0.6 MHz, it should take around 100 μs to scatter 23 photons. Therefore it is best to use a pulse duration of less than 100 μs.

By comparing the blue and red data points we find that a higher optical depth is obtained when the repump light is used. This is because the repump excites atoms out of the $F = 1$ state, thus allowing them to be imaged. Assuming an equal population of all Zeeman sublevels, we would expect the red data points to be 38% lower than the blue data points. This is in good agreement with our results where, for short pulses, the red data points are around 40% lower. As the pulse duration increases, the two data sets appear to diverge slightly. When the repump light is used to image the cloud, all of the atoms are visible, so the decrease in signal is caused only by the increasing Doppler shift, as already discussed. However when no repump light is used, atoms can decay to the $F = 1$ state where they no longer interact with the probe beam. As the interaction time increases more atoms will decay to this dark state, thus producing an additional loss of signal that increases with time. This is the most likely cause of the divergence of the two data sets.

As fewer atoms are present in the magnetic trap, it is beneficial to have as large an optical depth as possible. These results indicate that the optical depth can be maximised by utilising a short probe beam pulse. The shortest pulse we are able to produce is 58 μs. Therefore we expect to see a 26% reduction in the peak optical depth due to this Doppler shift effect. These results also highlight the fact that it is best to turn on the repump light when imaging the cloud, so as to obtain the most accurate measurement of the atom number. It is worth noting that about a third of the atoms in the magnetic trap will be in the $F = 1$ state, so without any repump light the signal from the magnetic trap will be reduced by approximately 33%.

3.2.2 Cancelling stray fields and controlling the polarisation

Next we consider the effect of the probe beam polarisation on the measured optical depth. From equation (2.51) we know that the absorption cross section depends on the branching ratio, and that to maximise the interaction all atoms must cycle on the stretched state transition. Therefore the polarisation of the light has to be chosen to excite either a σ^+ or σ^- transition. As atoms in the magnetic trap only reside in the positive M_F sub-levels of the $F = 2$ state, light that excites a σ^+ transition is required in order to maximise the interaction. To achieve this experimentally, a small uniform magnetic field must be applied parallel to the propagation direction of the probe beam, and circularly polarised light of the correct handedness must be used. By maximising the absorption cross section, each atom will scatter more photons, thus producing a higher peak optical depth and an improved signal.

In order to create a magnetic field pointing along the y direction as defined in figure 2.10, a pair of Helmholtz coils was installed. The first coil was wound around the MOT chamber flange through which the probe beam enters and the second was placed around the flange leading to the connecting tube. This should produce a roughly uniform field at the atom cloud position. To make sure that only a small field is required, stray magnetic fields should be cancelled. At the MOT position, in addition to the Earth's magnetic field, stray fields are also generated by the ion pump and pressure gauge which both contain permanent magnets. To cancel these fields two additional pairs of Helmholtz coils were positioned around the MOT chamber in perpendicular directions. The first pair, which cancels fields in the z direction, were wound around the top and bottom flanges of the MOT chamber. The second pair, which are used to cancel stray fields in the x direction, were positioned around the Zeeman beam viewport and the flange that connects to the Zeeman slower. Once atoms have been transported to the science chamber this process of stray field cancellation will have to be repeated if good quality absorption images are to be obtained.

Ideally the correct cancellation field to apply would be determined by measuring the background field at the atom cloud position using a magnetometer. As no such measurements were made during the assembly of the chamber, a different approach must be used. For magnetically trapped atoms, the cloud position is determined by the location of the zero field point. If no background fields exist, the position of the cloud centre will remain constant as the magnetic field gradient is increased. However if stray fields are present, the cloud centre will shift. Assuming a constant background field, the size of the shift will depend on the gradient of the trap. In particular for high field gradients the shift in position will be small. Therefore by measuring the cloud position as the trap gradient and cancellation fields are varied, it is possible to determine when the stray field has been nulled, as the cloud position will remain constant at all field gradients.

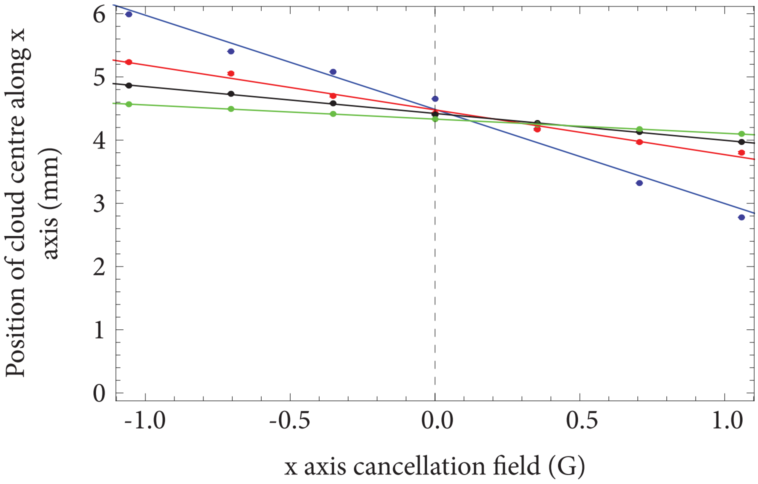

Figure 3.4: Position of the cloud along the x axis as the x axis cancellation field is varied. The red, black and green data points show the position of magnetically trapped atoms when using a field gradient of 33 G/cm, 57 G/cm, and 99 G/cm respectively. The blue data points show the position of atoms in the MOT. A linear fit to each data set is represented by the appropriately coloured solid line.

Figure 3.4 shows the variation in the x position of the atom cloud as the x axis cancellation field is changed. The red, black and green data points were obtained by loading atoms into the magnetic trap, where the field gradient used was 33 G/cm, 57 G/cm and 99 G/cm respectively. In each case the atoms were held in the magnetic trap for 0.1 s, and imaged 0.2 ms after release. The blue data points show the position of the MOT atoms as the cancellation field is varied. As the MOT position is influenced by both the magnetic field and the MOT beam powers, this data set cannot be used to cancel the stray field. However, it shows how well overlapped the MOT is with the centre of the magnetic trap. The solid lines are a linear fit to each of the data sets and the values given for the x axis cancellation field are calculated from the coil dimensions and current used. Here a magnetic field pointing away from the Zeeman slower is represented by a positive cancellation field value, and lower values for the cloud centre position represent atoms that are shifted towards the Zeeman slower.

The intersection points of the three magnetic trap fits vary slightly, so we take the average of the three intersection points as the best estimate of the required cancellation field, and use the spread of values as the uncertainty. This produces a value of $+0.32 \pm 0.12$ G for the x direction. The data also shows that the MOT is not completely centred on the magnetic trap, as the blue fit does not overlap with this mean intersection point. To determine the final cancellation field to use, this procedure was applied to the z direction and was subsequently iterated over. From this the final field values were found to be $+0.37$ G in the x direction and -0.49 G in the z direction. Note that a negative value in the z direction corresponds to a magnetic field that points downwards and that this shifts the cloud centre in the same direction.

Having cancelled the background field, the next step was to control the polarisation of the probe beam. The pink oval in figure 2.18 shows the additions that were made to the setup at this point. By introducing a PBC and quarter-wave plate into the probe beam path, the polarisation could now be varied through rotation of the wave plate. Prior to this the probe beam polarisation was not well defined.

Figure 3.5 shows the variation in the peak optical depth of the cloud as the quarter-wave plate is rotated. These data sets were taken by imaging the atoms 0.7 ms after release from the CMOT. For each measurement a field of around 1 G was applied parallel to the probe beam, and the cancellation fields were used. The blue data in the figure was obtained by flashing on the MOT repump light during the image, whilst the red points used no repump light. The solid lines are fits to the data of the form $a + b\cos(c\theta + \phi)$, where a, b, c and ϕ are left as floating parameters and θ is the angle of the wave plate. This fitting function is used because there is a periodic variation in the peak optical depth as the wave plate is rotated. The period of the fit is expected to be close to $90\,^{\circ}$, as this is the angle required to go from one orientation of circular polarisation to the other.

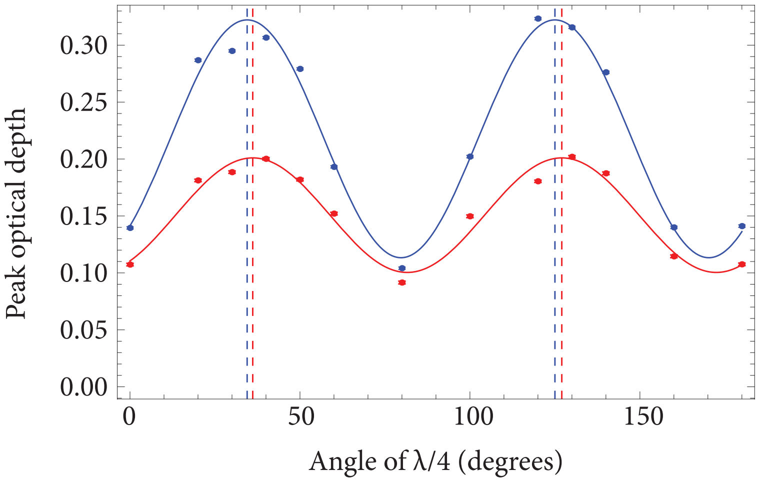

FIGURE 3.5: Variation of the peak optical depth of atoms released from the CMOT as the probe beam polarisation is changed. The blue data used the MOT repump light during imaging, whilst the red data used no repump light. The blue and red solid lines are fits to the data, and the dashed lines mark the peaks of these two fits.

Looking at the blue data points there are two clear peaks at angles of $34.5 \pm 0.5\,^{\circ}$ and $125.0 \pm 0.5\,^{\circ}$. These positions are indicated by the blue dashed lines. For the red data, again two peaks occur, this time at $36.1 \pm 0.5\,^{\circ}$ and $127.0 \pm 0.5\,^{\circ}$. These positions are depicted by the red dashed lines. As the approximate position of the wave plate's fast axis is known, we can predict the angles at which circularly polarised light is produced. We find these angles to be $39\,^{\circ}$ and $129\,^{\circ}$ for the two states of circular polarisation, thus showing that the peaks in the data correspond to having circularly polarised light.

If all atoms in the $F = 2$ state occupy either the $M_F = 2$ or $M_F = -2$ sub-level, then it is clear that circularly polarised light of the correct handedness will produce an increase in the optical depth. However when atoms are distributed evenly amongst all M_F sub-levels, which is close to the situation in the MOT, then the average transition strength is the same for all polarisations. Therefore the optical depth should remain constant. If optical pumping is taken into consideration, then some variation in the optical depth with polarisation is expected. In particular when the light is circularly polarised, after the first few photon scatters, the atoms will be pumped towards the sub-level with the largest transition strength. When the light is linearly polarised, the population of each

Zeeman sub-level will remain unchanged. Therefore when the light is circularly polarised the optical depth should be higher. This effect can perhaps explain the variation in the red curve as the angle of the wave plate is changed. Optical pumping could also explain the large difference between the blue and red curves when the probe beam is circularly polarised. With the repump light on, atoms in the $F = 1$ state are likely to be transferred to the $F = 2$ state, where they will be pumped towards the sub-level with the largest transition strength, thus producing an increase in the observed optical depth. However, optical pumping cannot explain why there is almost no difference between the two curves when the light is linearly polarised. We would expect the repump light to make visible atoms that occupy the $F = 1$ state, therefore the difference between the two curves should be at least $3/8$, assuming all Zeeman sub-levels are equally populated. This clearly does not agree with our data. In addition to this we have found that different results are obtained when the experiment is repeated using atoms released from the magnetic trap. This can be seen in figure 3.6. Therefore we conclude that some other process is taking place. As we shall see in section 3.2.6, when the cloud is imaged 0.7 ms after release from the CMOT, a large magnetic field is present which shifts the resonance frequency. Additionally the line shape changes with polarisation, as shown in figure 3.15 of section 3.2.7. This effect is the most likely cause of the variation in optical depth that we see in figure 3.5.

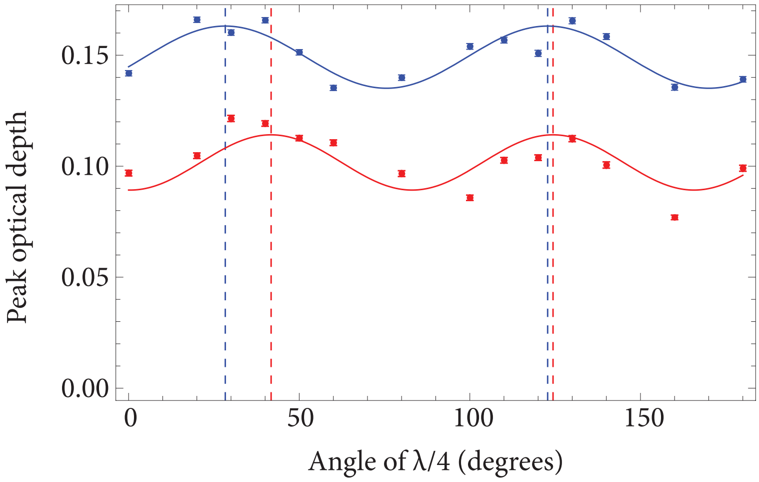

FIGURE 3.6: Variation in the peak optical depth of atoms released from the magnetic trap as the probe beam polarisation is changed. The blue data used the MOT repump light during imaging, whilst the red data used no repump light. The blue and red solid lines are fits to the data, and the dashed lines mark the peaks of these two fits.

Figure 3.6 shows the variation in peak optical depth with polarisation for atoms released from the magnetic trap. In this case the atoms were loaded into the magnetic trap via the usual CMOT phase. They were then held for 0.2 s, before being imaged 0.2 ms after release from the trap. Again a 1 G field was applied parallel to the probe beam, along with the cancellation fields. As before the blue data was obtained by using the MOT repump light during imaging, whilst the red data used no repump light. Both data sets show two clear peaks at roughly the same positions as that of the CMOT data. The biggest difference here is that the red data is consistently around 32% lower than the blue data. This is roughly what we expect to see due to the anticipated population distribution of the ground state. Due to optical pumping, we expect circularly polarised light to produce the highest optical depth. This agrees well with our results.

3.2.3 Imaging atoms released from the trap

For the majority of experiments discussed so far, atoms have been recaptured in the MOT. The main reason for using this method is that it provides a reliable measure of the percentage of retained atoms, as the cloud is always imaged under the same conditions. However as we eventually want to image atoms in the science chamber, it is important that we are able to obtain reliable images of the cloud after release from the magnetic trap. To check this, a series of cloud images was taken after release from the CMOT and for each image the atom number was calculated.

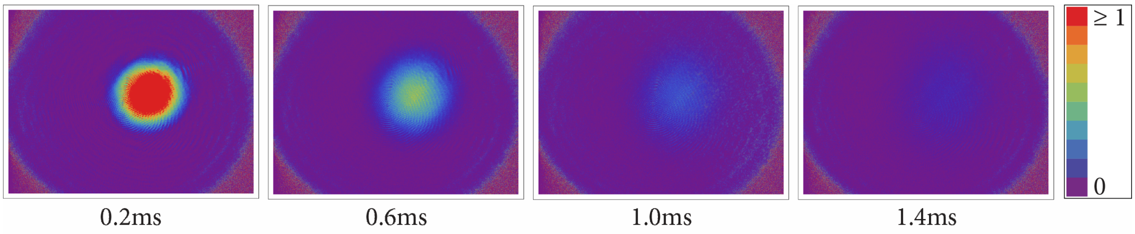

Figure 3.7: A selection of false colour images of the atom cloud taken at various times after release from the CMOT. The colour index on the right hand side shows that an optical depth of one or more is coloured red.

Figure 3.7 shows a selection of false colour images of the expanding cloud. From this the spatial distribution of the optical depth can be seen. The large circle that appears in each image is created by the circular aperture of the connecting tube, whilst the small circle is the atom cloud. In order to enhance the visibility of the cloud at long release times, the image colours have been scaled so that an optical depth greater than one is shown as red. This means that the image taken at 0.2 ms actually has a much greater peak optical depth than that of the other pictures. From these images we can see that the peak optical depth quickly drops below one, although there is no great increase in the width of the cloud. This suggests that the observed atom number is not constant.

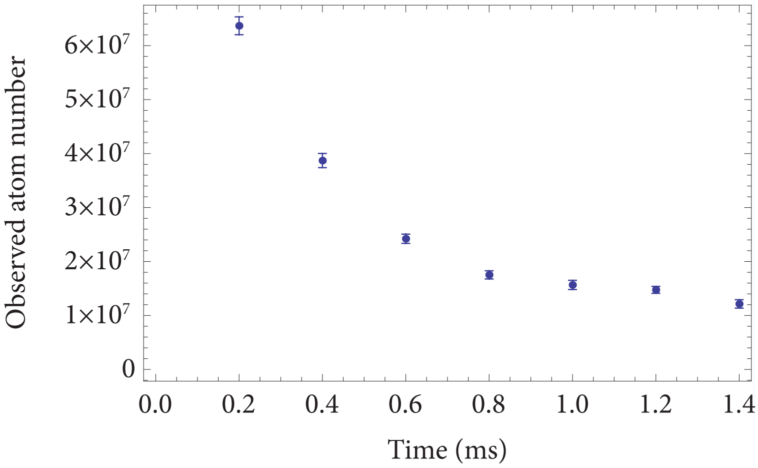

FIGURE 3.8: Measurements of the atom number at various times after the cloud has been released from the CMOT.

From these images the atom number was calculated. The results are shown in figure 3.8. This data set shows a clear reduction in the observed atom number with time. In particular a large drop in the atom number is seen initially. Following this the atom number levels off at around 20% of the original value. From the images it appears that the cloud has not expanded sufficiently for atoms to escape from the field of view of the camera, therefore atoms must be disappearing from the image for some other reason. This could be caused by stray fields that persist after the coils have been switched off, as this can shift the resonance position thus making some atoms invisible to the probe beam. In order to determine if this is the case, line shape measurements were taken.

3.2.4 Predicting the line shape

Before carrying out line shape measurements it is important to know what we expect to see. In particular it is useful to know how a magnetic field might affect the measured line shape, as this will allow us to determine whether or not stray fields are causing the atoms to disappear from our images. As a full calculation of the anticipated absorption signal is rather involved, we adopt a simplified approach. For this we require only two pieces of information. These are the frequency shift of each of the allowed transitions and the transition strength in an arbitrary magnetic field.

We start by looking at the Zeeman shift of the atomic energy levels as the magnetic field is varied. Since the hyperfine and Zeeman splittings are much smaller than the fine structure splitting of the $2P$ excited state over the range of magnetic fields that we are interested in, we can consider each fine structure state separately. The total Hamiltonian, $\hat{H}_{\text{tot}}$, for an alkali atom in a magnetic field is given by

$$\hat{H}_{\text{tot}} = A\underline{\hat{I}} \cdot \underline{\hat{J}} + \mu_B(g_L\underline{\hat{L}} + g_S\underline{\hat{S}}) \cdot \underline{B} + \mu_N g_I \underline{\hat{I}} \cdot \underline{B}, \tag{3.7}$$

where A is the hyperfine coupling constant, $\underline{\hat{I}}$ is the nuclear spin operator, $\underline{\hat{J}}$ is the total electronic angular momentum operator, $\underline{\hat{L}}$ is the electronic orbital angular momentum operator, $\underline{\hat{S}}$ is the electron spin operator, $\underline{B}$ is the applied magnetic field, μ_N is the nuclear magneton, and $g_L = 1$, $g_S \simeq 2$ and g_I are Landé g-factors. The first term in equation (3.7) describes the hyperfine interaction, which will be referred to as $\hat{H}_{\text{hfs}}$. It occurs because of the coupling between the nuclear spin and the total electronic angular momentum. The second and third terms describe the Zeeman interaction, $\hat{H}_Z$. As $\mu_N \ll \mu_B$, we are able to ignore the third term.

Considering either the high or low magnetic field cases in isolation is relatively straightforward as time independent perturbation theory can be used. A good explanation of the method can be found in [126]. For the intermediate regime however, a different method must be adopted. Instead we write down a matrix representation of $\hat{H}_{\text{tot}}$, and find the energy eigenvalues and eigenstates through diagonalisation. To construct the matrix we must first choose a basis. For convenience we use the field free basis, which are the eigenstates of $\hat{H}_{\text{hfs}}$. These states are written as $|I, J, F, M_F\rangle$. The eigenvalues of the hyperfine interaction can be calculated using [76],

$$E_{\text{hfs}} = \frac{1}{2}hA_1K + hA_2\frac{3/2K(K+1) - 2I(I+1)J(J+1)}{2I(2I-1)2J(2J-1)}, \tag{3.8}$$

where $K = F(F+1) - I(I+1) - J(J+1)$ and A_1 and A_2 are experimentally determined parameters that vary depending on the state being considered. For lithium these constants are $A_1 = 401.752\,\text{MHz}$ and $A_2 = 0$ for the $^2S_{1/2}$ state, and $A_1 = -3.055\,\text{MHz}$ and $A_2 = -0.221\,\text{MHz}$ for the $^2P_{3/2}$ state [76]. From this we can construct a matrix representation of $\hat{H}_{\text{hfs}}$.

Next we consider $\hat{H}_Z$. Taking the external magnetic field to be in the z direction means that $\hat{H}_Z = \mu_B(\hat{L}_z + 2\hat{S}_z)B$. By defining g_J as

$$g_J = 1 + \frac{J(J+1) + S(S+1) - L(L+1)}{2J(J+1)}, \tag{3.9}$$

we can rewrite the Zeeman interaction Hamiltonian as $\hat{H}_Z = \mu_B g_J \hat{J}_z B$. The eigenstates of the Zeeman interaction are given by $|I, J, M_I, M_J\rangle$ and the eigenvalues are $E_Z = \mu_B g_J M_J B$. As the states $|I, J, F, M_F\rangle$ are not simultaneous eigenstates of $\hat{H}_Z$, the Zeeman interaction is not diagonal in our chosen basis. Therefore to find the matrix representation of $\hat{H}_Z$ we have to express the $|I, J, F, M_F\rangle$ states in terms of the $|I, J, M_I, M_J\rangle$ eigenstates. For this we make use of the following transformation

$$|I, J, F, M_F\rangle = \sum_{M_I}\sum_{M_J} C|I, M_I\rangle|J, M_J\rangle, \tag{3.10}$$

where C are the Clebsch Gordan coefficients, and the summations are carried out over all possible M_I and M_J values. The only non-zero terms in the summation occur when the condition $M_F = M_I + M_J$ is fulfilled. Using this it is possible to write down a matrix for $\hat{H}_Z$ and by adding this to $\hat{H}_{\text{hfs}}$, we are finally able to construct $\hat{H}_{\text{tot}}$. By diagonalising this final matrix we find the energy eigenstates and eigenvalues in an arbitrary magnetic field. The result of the diagonalisation procedure in the case of the ground state where $J = 1/2$ is [127],

$$E = -\frac{\Delta E_{\text{hfs}}}{2(2I+1)} \pm \frac{\Delta E_{\text{hfs}}}{2}\sqrt{1 + \frac{2M_F}{I+1/2}x + x^2}, \tag{3.11}$$

where ΔE_{hfs} is the separation between the states $F = I + 1/2$ and $F = I - 1/2$ in zero magnetic field and $x = \mu_B g_J B/\Delta E_{\text{hfs}}$. This expression is known as the Breit-Rabi formula. For the ${}^2P_{3/2}$ excited state there is no closed-form expression and so the matrix is diagonalised numerically.

Figure 3.9 shows how the energy levels of the ${}^2S_{1/2}$ and ${}^2P_{3/2}$ states shift as the magnetic field is increased. Using this we can calculate the frequency shift of each transition.

Next we have to determine how the transition strength varies with magnetic field. From section 2.1, we know that the strength of the transition between a ground state $|g\rangle$ and excited state $|e\rangle$ is described by the dipole matrix element, $D = e\langle e|\underline{\epsilon} \cdot \underline{\hat{r}}|g\rangle$, where $\underline{\epsilon}$ is a unit vector defining the polarisation of the light. As the radial part of the dipole matrix

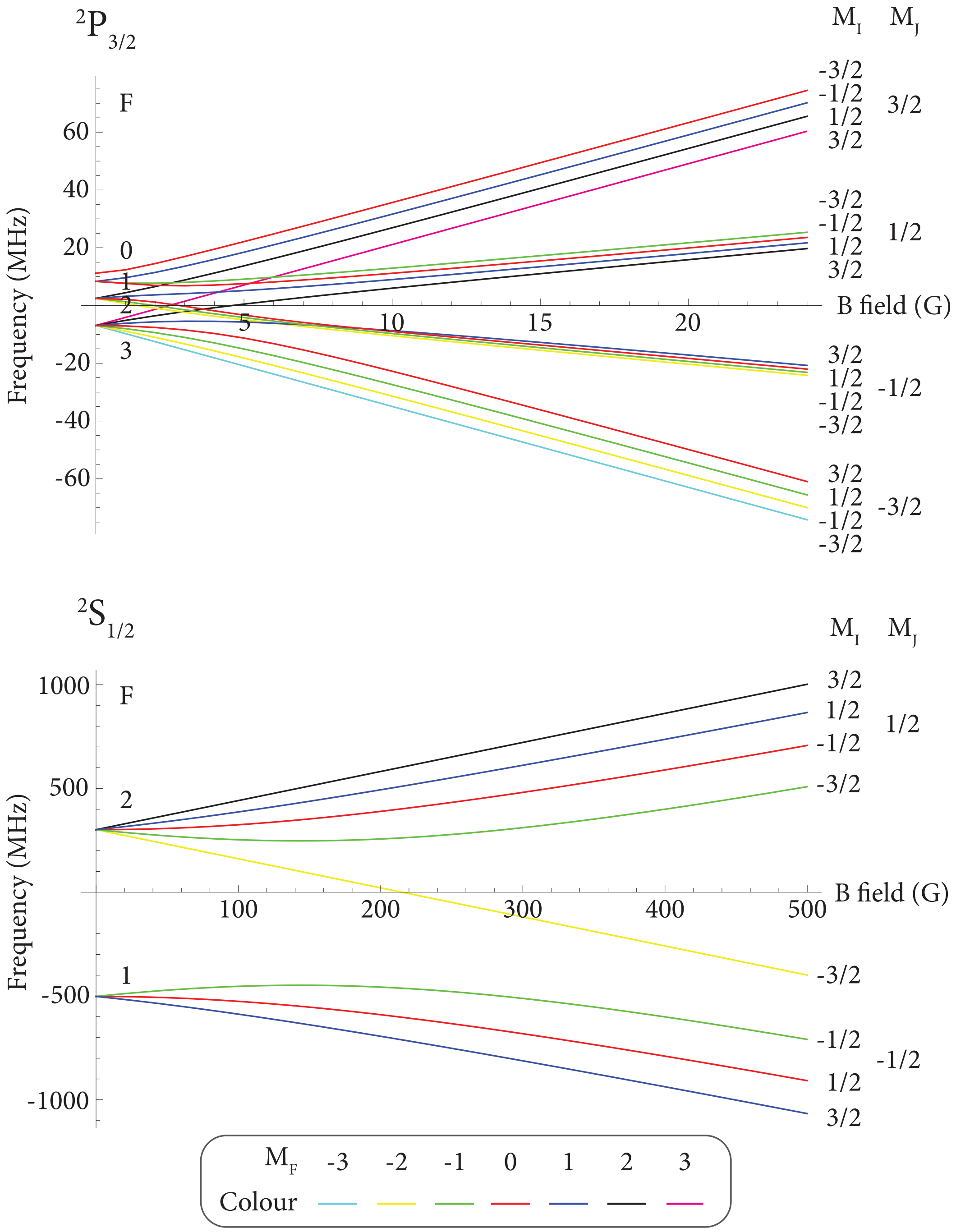

FIGURE 3.9: Energy level diagram for the $^2S_{1/2}$ and $^2P_{3/2}$ states as a function of magnetic field. The colour of each Zeeman sub-level corresponds to its M_F quantum number.

element is the same for all states of interest, it can be ignored. Applying this to the current situation we replace $|g\rangle$ and $|e\rangle$ with $|f_g, m_g\rangle$ and $|f_e, m_e\rangle$ respectively, where these are used to represent the ground and excited states in the presence of an external magnetic field. These are then expanded on the basis of field free states, which are labelled $|F_g, M_g\rangle$ and $|F_e, M_e\rangle$ for the ground and excited states respectively. We call the desired quantity the transition matrix element and write it as

$$\langle f_e, m_e|\underline{\epsilon}\cdot\hat{\underline{r}}|f_g, m_g\rangle = \sum_{F_e,M_e}\langle f_e, m_e|F_e, M_e\rangle\langle F_e, M_e|\underline{\epsilon}\cdot\hat{\underline{r}}\sum_{F_g,M_g}|F_g, M_g\rangle\langle F_g, M_g|f_g, m_g\rangle \tag{3.12}$$

$$= \sum_{F_e,M_e}\sum_{F_g,M_g}\langle f_e, m_e|F_e, M_e\rangle\langle F_g, M_g|f_g, m_g\rangle\langle F_e, M_e|\underline{\epsilon}\cdot\hat{\underline{r}}|F_g, M_g\rangle. \tag{3.13}$$

The first and second terms on the last line are obtained by using the eigenstates that were calculated previously, whilst the last term is obtained from standard angular momentum algebra.

Having finally calculated the transition matrix element up to some constant of proportionality, we are now able to predict the expected shape of the spectrum for any given magnetic field. First we assume that each transition has a Lorentzian line shape, where the amplitude is set by the square of the transition matrix element, the line centre is set by the frequency shift of the transition and the width is set equal to the natural linewidth. The square of the transition matrix element is used because the absorption cross section is proportional to the line strength which is defined as the square of the dipole matrix element. Each transition excited by a particular polarisation of light is represented in this same manner and is assumed to have an equal share of the population. The contributions from the various transitions are then added together to form the predicted spectrum for a given magnetic field. It is important to note that this does not predict the measured optical depth of the cloud, and so cannot be used as a fit to our data. However if changes in the spectrum are being caused by a magnetic field, we can expect the overall shape of our data to follow the trends shown in the calculation. Therefore it provides a useful tool to determine whether or not stray fields are affecting our results.

Figure 3.10 shows an example of the predicted spectrum when a magnetic field of 0.01 G is present. The zero frequency position has been chosen to coincide with the frequency of the $F = 2$ to $F' = 3$ transition, and for all other line shape plots this is used as our reference point. As this same line shape is calculated whether σ^+, σ^- or π transitions are being excited, we expect our measured spectra to have this overall shape in all situations.

If a magnetic field is present the predicted line shape varies dramatically depending on the type of transition that is being excited. Figure 3.11 shows an example of this, where

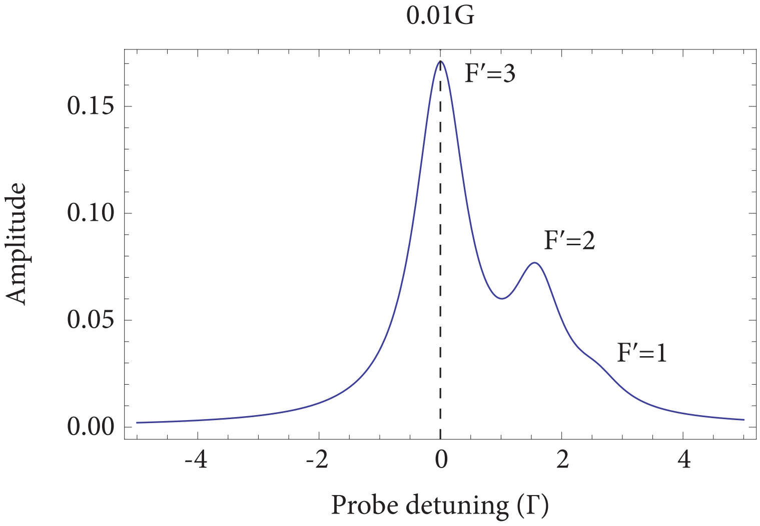

FIGURE 3.10: Theoretical line shape for a 0.01 G magnetic field. The peaks that correspond to the $F = 2$ to $F' = 3, 2, 1$ transitions are labelled.

a magnetic field of 5 G has been used. The blue, red and black lines show the line shape predicted for σ^+, π and σ^- transitions respectively. Therefore, not only are we able to determine the approximate size of any stray fields that are present, we can also ascertain in which direction the field is pointing by seeing which transitions are excited. In the following sections these results are compared to our measured data.

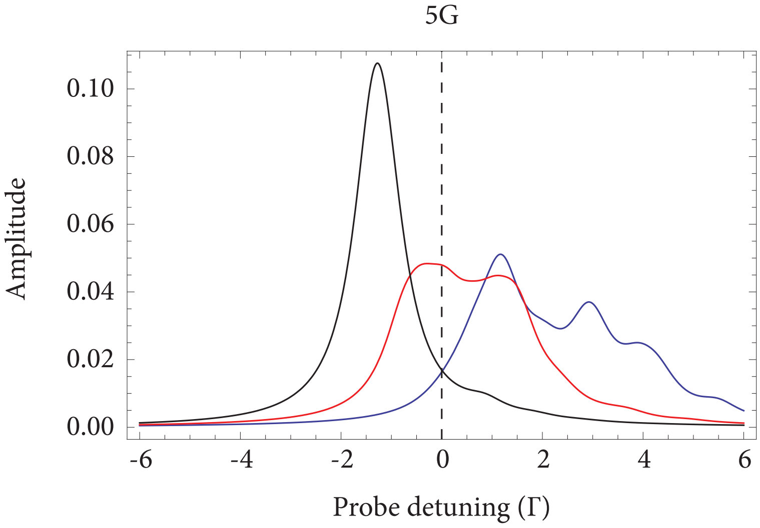

FIGURE 3.11: Theoretical line shape for a 5 G magnetic field. The blue, red and black curves show the line shapes for σ^+, π and σ^- transitions respectively.

3.2.5 Line shape for atoms released from the MOT

The first line shape measurements were carried out using atoms trapped in, and released from, the MOT. The results, which are presented in the left hand column of figure 3.12, show the variation in the peak optical depth of the cloud as the frequency of the probe beam is scanned. All data points were obtained by utilising a probe beam that was linearly polarised along the x direction as defined in figure 2.10, and by imaging the cloud using MOT repump light. No cancellation fields were applied during these measurements and as always a negative frequency value represents light that is red detuned.

The right hand column of figure 3.12 shows the theoretical spectra that best represent our measurements. As a fit to the data cannot be performed, this is determined by identifying the applied magnetic field value that most accurately produces the frequency separation of the various peaks. It was found that the data did not agree well with theory if only one type of transition was excited. However the results were fairly well reproduced by combining the plots for σ^+ and σ^- transitions. Therefore all of the theoretical plots show an equal combination of these two transitions. As our data was obtained using light that was polarised along the x direction, we conclude that the largest components of the magnetic field must lie either parallel to the probe beam, that is in the y direction, or in the z direction.

Figure 3.12(a) shows the spectrum from atoms in the MOT. Two partially overlapped peaks can be seen in the data. Here the larger peak corresponds to the $F = 2$ to $F' = 3$ transition, whilst the smaller peak is due to the $F = 2$ to $F' = 2$ transition. By fitting two Lorentzians to the data, the separation between the peaks is found to be $1.6\,\Gamma = 9.5\,\mathrm{MHz}$. This is in good agreement with theory, which says the field free separation should be 9.2 MHz. The peak widths are found to be $1.4\,\Gamma = 8.3\,\mathrm{MHz}$ for the larger peak and $2.2\,\Gamma = 13\,\mathrm{MHz}$ for the smaller peak. The lines have been broadened beyond the natural linewidth. For the $F = 2$ to $F' = 2$ transition, this is expected because the $F = 2$ to $F' = 1$ transition forms a shoulder. Additionally some Zeeman broadening is likely to occur. Comparing this to figure 3.12(b) which shows the predicted line shape for a 1 G magnetic field, there appears to be reasonable agreement, although the peak widths, and relative peak heights aren't precisely reproduced in the theoretical plot. Note that the zero frequency position of figure 3.12(a) has been chosen to coincide with the $F = 2$ to

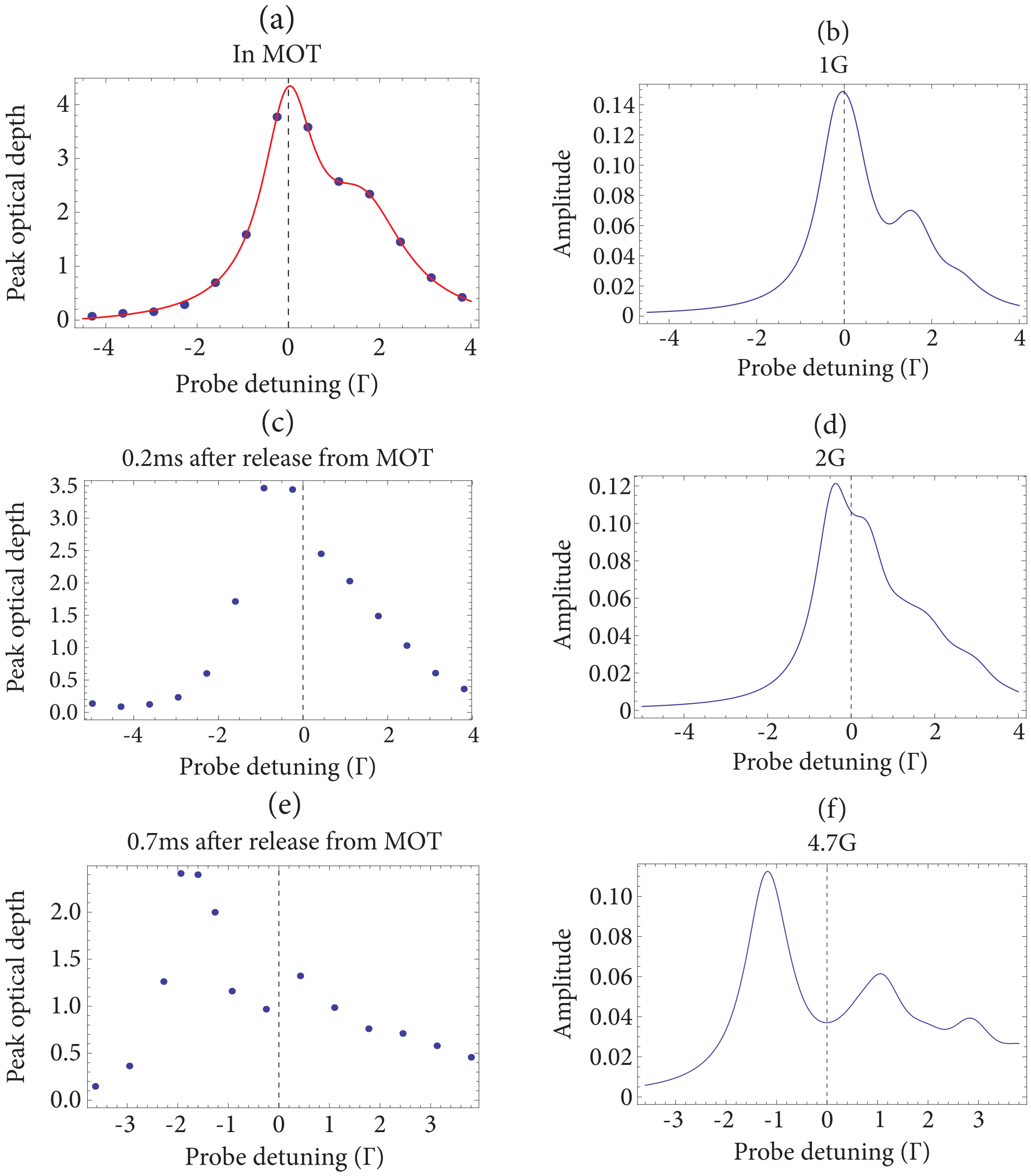

FIGURE 3.12: Comparison between line shape measurements and theoretical spectra. Measurements are presented in the the left hand column where (a) was taken using atoms trapped in the MOT, (c) was taken 0.2 ms after release from the MOT, and (e) was taken 0.7 ms after release. The red curve in (a) represents a double Lorentzian fit to the data. The right hand column shows theoretical line shapes for magnetic field values of (b) 1 G, (d) 2 G, and (f) 4.7 G.

$F' = 3$ transition. We use this as our reference point for all subsequent measurements as it should be close to the field free resonance position.

Figures 3.12(c) and (e) show the measured spectra 0.2 ms and 0.7 ms after release from the MOT. From figure 3.12(c) we can see that the spectrum has changed slightly. In particular the large peak has shifted towards the red by just under a linewidth, and the smaller peak is less well defined. In figure 3.12(e) the line shape appears to have changed significantly. Two clear peaks, which have a separation of just over $2\,\Gamma$, are visible and the larger peak is now located at approximately $-1.7\,\Gamma$. Figures 3.12(d) and (f), show the theoretical curves for an applied magnetic field of 2 G and 4.7 G respectively, as these are the theoretical spectra that best match the measured ones.

These measurements clearly show that there is a time dependent shift of the line shape. As the data agrees well with the theoretical spectra, we conclude that these changes are generated by a time varying magnetic field, that is uniform over the size of the cloud. This indicates that measurements of the atom number for release times greater than 0.7 ms are unreliable as the resonance frequency has shifted significantly, meaning that some atoms will become invisible.

3.2.6 Line shape for atoms released from the CMOT

In order to further investigate the results of section 3.2.3, line shape measurements were also carried out using atoms released from the CMOT. As before measurements were performed at various times after release, and by comparison with theory a magnetic field value was assigned to each line shape. The variation of this magnetic field with time is shown in figure 3.13. The relatively large error bars reflect the fact that the measured spectra does not follow the theoretical curve exactly, thus making it difficult to precisely estimate the magnitude of the magnetic field. These results show that after release from the trap the atoms are subjected to a magnetic field that increases with time. At longer times this field begins to saturate. When releasing atoms from the MOT we found that after 0.7 ms a field of approximately 4.7 G was present. Here the field reaches a value of about 10 G after 0.6 ms, thus indicating that the coil current used prior to switch off affects the size of the magnetic field that is produced.

To determine the cause of this increasing magnetic field the coils were moved half way between the MOT and science chambers. By placing a magnetometer close to the small tube that connects the two chambers, the z component of the magnetic field close to the atoms was measured. The reason for measuring only the z component of the field is discussed in the following section. The results are shown in figure 3.14. For negative times both coils were run at the usual CMOT current. They were then switched off simultaneously at time $t = 0$. The large magnetic field spike, which has a magnitude

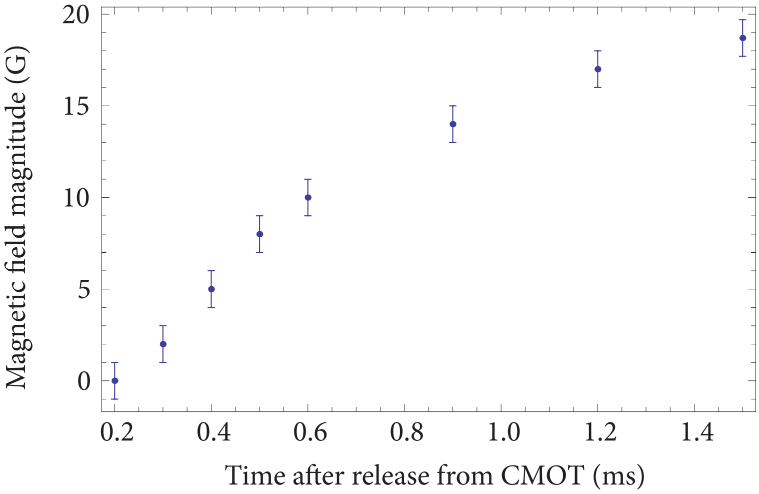

FIGURE 3.13: Variation in the magnitude of the induced magnetic field with time after release from the CMOT.

of 5.5 G and occurs at approximately 0.3 ms, results from a slight difference between the rate at which the current in the two coils dissipates. This means the coil currents are not completely balanced during the switch off, thus producing a relatively large transient field. After this the magnetic field drops to around -1 G and slowly decays away.

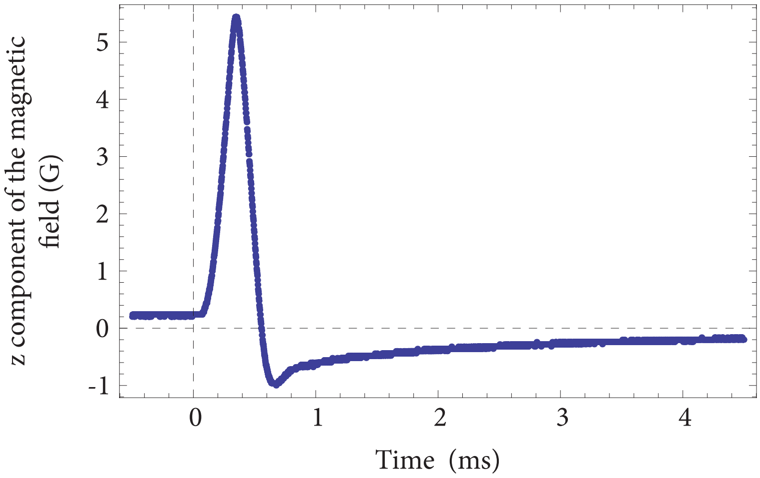

FIGURE 3.14: z component of the magnetic field measured close to the trap centre, after both coils have been simultaneously switched off.

Clearly these results are not consistent with the increasing magnetic field shown in figure 3.13. This suggests that the field measured halfway along the connecting tube is not representative of the field at the MOT position. To verify this position dependence, additional line shape measurements were performed at various points along the transport. Despite being taken at the same time after release, each spectrum was different, thus confirming the presence of a time and position dependent magnetic field. This field is most likely caused by the formation of eddy currents in the chamber which persist after the coils have been switched off. The magnetic field generated by these eddy currents will decay away slowly, and the size of the field will depend on the environment that surrounds the coils. This suggests that the largest fields will be produced in the vicinity of the two chambers, and that imaging problems will also occur in the science chamber. To determine the extent of the problem, line shape measurements should be carried out in the science chamber, once a suitable imaging system has been installed. Alternatively, when the chamber is opened up to install the microwave trap or high field electrodes, the magnetic field could be measured directly. As there is no simple way of removing this induced field, the transportation setup was tested by using the MOT recapture method.

3.2.7 Variation of the line shape with probe beam polarisation

From the results of section 3.2.5 we found that the induced magnetic field has to lie parallel to the probe beam, that is in the y direction or perpendicular to it, in the z direction. From these data sets alone it was not possible to determine the exact orientation of the magnetic field. However different transitions will be excited in these two situations if other polarisations of light are used. Therefore it is possible to distinguish between these two cases by measuring the line shape for different probe beam polarisations. Table 3.1 summarises the different transitions that occur for the two possible magnetic field orientations. As before the y and z directions are defined in figure 2.10.

Quantisation axis orientation	**Probe polarisation**	**Transition excited**
y	Linear	σ^+, σ^-
y	Right hand circular	σ^+
y	Left hand circular	σ^-
z	Linear along z axis	π
z	Linear along x axis	σ^+, σ^-
z	Circular	σ^+, σ^-, π

Table 3.1: Summary of the transitions that occur given two orientations of quantisation axis, and various polarisations of light. The probe propagates along y and z is the vertical direction.

Figure 3.15 shows the measured line shape for various probe beam polarisations. In each case the spectrum was taken 0.6 ms after the atoms were released from the CMOT. In figure 3.15(a) the probe beam is polarised along the x axis, whilst in figure 3.15(b) the probe is polarised along the z axis. Figures 3.15(c) and (d) show the line shapes for the two orientations of circular polarisation.

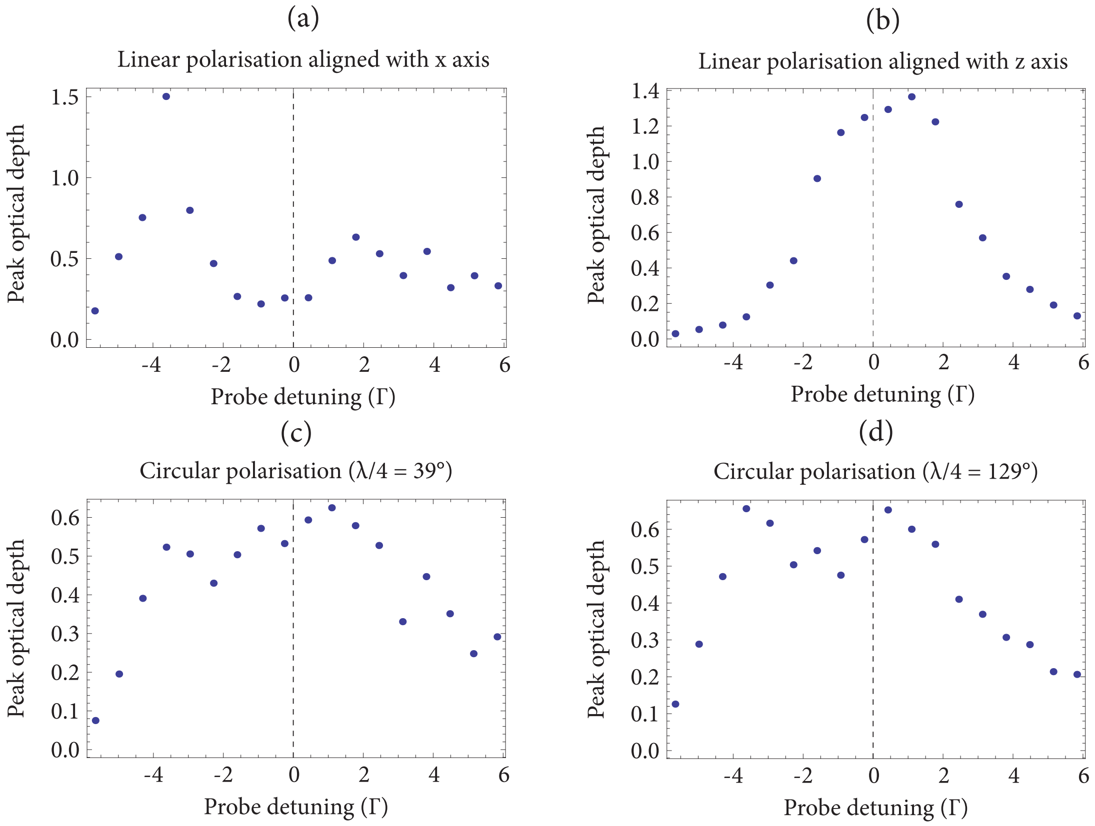

FIGURE 3.15: Line shape measurements taken 0.6 ms after atoms were released from the CMOT, where the probe beam polarisation was (a) linear, aligned the x axis, (b) linear, aligned the z axis, (c) circular with $\lambda/4 = 39\,°$, (d) circular with $\lambda/4 = 129\,°$.

Figure 3.16 shows the theoretical line shapes assuming a 10 G field is present. Here the blue, red and black curves represent the spectra for σ^+, π and σ^- transitions respectively. Comparing this to the data we find that figure 3.15(a) has a similar shape to the blue and black curves added together, whilst figure 3.15(b) is similar to the red curve. This indicates that the magnetic field must be aligned with the z axis. According to table 3.1 this should result in identical spectra for the two states of circular polarisation and we do indeed see nearly identical spectra in figures 3.15(c) and (d). Therefore we conclude that the magnetic field is predominantly in the z direction.

3.3 Transporting the atoms

As the induced magnetic field discussed above makes it difficult to reliably image the released atom cloud, the transport setup was tested by returning the atoms to the MOT

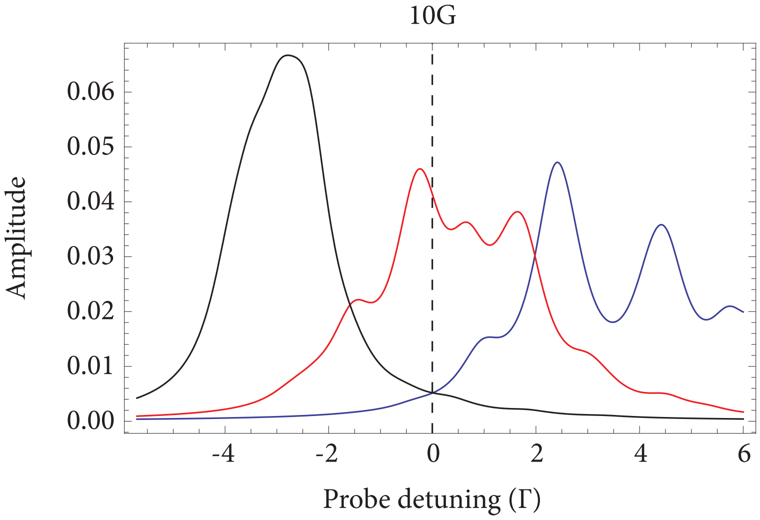

FIGURE 3.16: Theoretical line shape in a 10 G magnetic field. The blue, red and black curves show the line shapes for σ^+, π and σ^- transitions respectively.

chamber and imaging them in the recaptured MOT. This section describes the results of initial transportation experiments and details the method used to improve the transport efficiency. Having successfully transported the atoms to and from the science chamber, the lifetime of the magnetic trap in the science chamber was also measured.

3.3.1 First transport attempts

In order to transport atoms from the MOT chamber to the science chamber the trapping coils are attached to a Parker 404XR translation stage. It has a total track length of 600 mm and uses an SMB60 servo motor to drive a ballscrew mechanism. One revolution of the ballscrew moves the coils a distance of 20 mm. The translation stage has a maximum velocity of 1.08 m/s and a maximum acceleration of 20 m/s^2. It also has a bi-directional reproducibility of $\pm 3\,\mu$m, and an absolute positioning accuracy of 40 μm. To control the motor, a ViX500IE servo drive is used. Code describing the required move sequence is uploaded to the drive and executed upon receipt of a TTL pulse. The acceleration, deceleration and velocity of the stage can be varied by the user. Depending on the values chosen for these three parameters, the motion profile will either have a triangular or trapezoidal shape, as shown in figure 3.17 by the blue and red lines respectively. For the triangular motion profile, the stage goes through a period of constant acceleration, followed by a period of constant deceleration. The trapezoidal profile has an additional period of constant velocity in between the acceleration and deceleration phases.

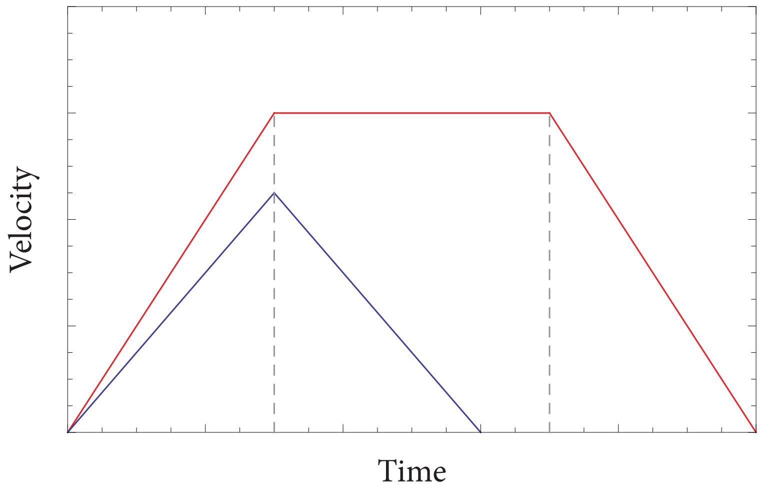

FIGURE 3.17: Translation stage motion profiles. The blue line shows the triangular motion profile and the red line shows the trapezoidal motion profile.

During the transport procedure it is important to maintain a deep trap so that the maximum number of atoms can be retained. However as the trap accelerates, the atoms gain energy. This leads to a reduction of the effective trap depth on one side, which can be modelled as a tilting of the trap. Therefore during any period of acceleration, the trap depth will decrease. To ensure that this reduction is small, the transport acceleration should always be much lower than the trap acceleration. By using $F = -dU/dx = ma$, where U is equal to the energy from equation (3.1), the trap acceleration, a_{trap} can be determined,

$$a_{\mathrm{trap}} = \frac{g_F M_F \mu_B B'}{m} . \tag{3.14}$$

For our magnetic trap this produces a maximum value of $a^{z}_{\mathrm{trap}} = 479\,\mathrm{m/s^2}$ in the z direction, and $a^{x,y}_{\mathrm{trap}} = 239\,\mathrm{m/s^2}$ in the x and y directions. To transport the cloud to the science chamber in just over 1 s, we use an acceleration of only $a_{\mathrm{trans}} = 2\,\mathrm{m/s^2}$. As $a_{\mathrm{trans}} \ll a^{x,y}_{\mathrm{trap}}$, the reduction in trap depth is negligibly small, meaning that no atoms should be lost during transport.

Initially the translation stage was aligned to the connecting tube by ensuring that the coils were roughly centred on both the MOT and science chambers. To test the efficacy of this alignment procedure, the percentage of retained atoms was measured as the transport distance was increased. Figure 3.18 shows the results of these measurements. To obtain this data set, the MOT atoms were first imaged and then loaded into the magnetic trap via the usual CMOT phase. After holding the atoms for 10 ms, the cloud was transported using a velocity of 0.5 m/s and an acceleration of $2\,\mathrm{m/s^2}$. Two seconds after loading the magnetic trap, the atoms were transported back to the MOT chamber, and the CMOT was reformed. Finally all parameters were ramped back to the usual MOT values and the cloud was imaged again. Given the acceleration used here, it takes 0.25 s for the translation stage to reach a velocity of 0.5 m/s. In this time the coils travel 62.5 mm, which means for transport distances less than 125 mm, the motion profile is triangular. For each of the transport distances tested, the atoms spent in total 3.335 s in the magnetic trap.

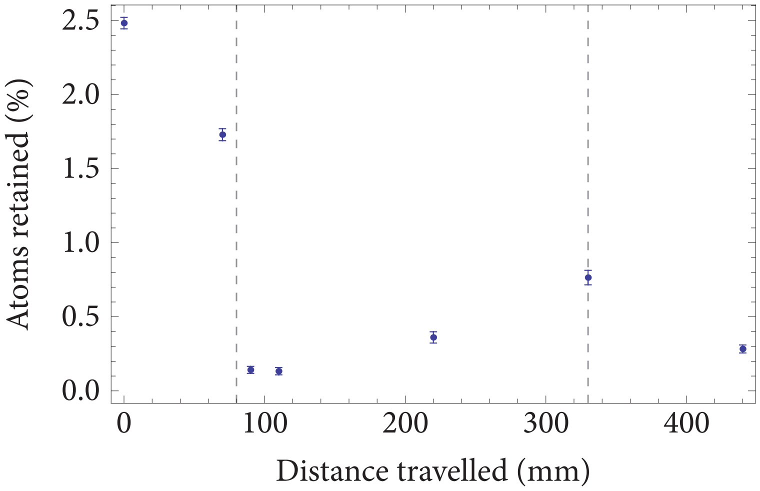

Figure 3.18: Preliminary transportation results showing recaptured atomic percentage as transport distance is varied. The gray dashed lines show the approximate positions of the two ends of the connecting tube.

The vertical axis in figure 3.18 is the fraction of atoms originally in the MOT that are finally recaptured back in the MOT. Therefore it includes all the loss processes, including the loss in transferring to the magnetic trap and the losses due to background collisions. The data shows that if the atoms are left at the MOT position for 3.335 s, around 2.5% of the MOT atoms are retained. Comparing this with figure 3.1, we find good agreement with the expected loss due to the lifetime of the trap. When the atoms are moved a distance of 70 mm, a small drop in the atomic percentage is seen. This is followed by a massive drop at a distance of around 100 mm. The dashed lines in the figure show the approximate positions of the two ends of the connecting tube. Therefore this large drop in atomic percentage is almost certainly due to the atoms colliding with the chamber wall. Upon further transport of the cloud, the atomic percentage begins to rise. This might seem strange, however it can be explained if the background pressure in the connecting tube is lower than in the MOT chamber. As the atoms spend differing amounts of time at each transport position, losses occur not only because of the transport procedure itself, but also through collisions with background gases. Therefore if the cloud is held at a position where the pressure is lower, fewer atoms will be lost. This results in a relative increase in the atomic percentage as the cloud moves from the higher pressure region to the lower pressure region. As a large percentage of atoms are lost at the entrance of the connecting tube, it is necessary to alter the alignment of the translation stage to improve the transport efficiency. From this data set alone it is not possible to calculate the absolute transport efficiency as the atoms are not immediately transported back to the MOT chamber after reaching the science chamber.

3.3.2 Optimising the transport

There are three possible explanations as to why atoms are lost at the entrance of the connecting tube. The first possibility is that the cloud is too large to fit through. The second is that the cloud is not well aligned with the centre of the tube, and the third is that stray magnetic fields, particularly at the welds of the connecting tube, perturb the atoms as they are transported. According to the temperature measurements of section 2.6, we expect the magnetically trapped cloud to have a $1/e^2$ diameter of 4 mm in the z direction, and about 8 mm in the x and y directions. Comparing this to the 9 mm inner diameter of the tube, most of the atoms should be able to pass through unimpeded, provided the cloud is perfectly centred. Therefore we attribute the loss of atoms either to stray magnetic fields, or to poor alignment of the cloud. In order to optimise the position of the cloud along the x axis, the magnetically trapped atoms were imaged at transport distances of 70 mm and 220 mm. As the outline of the connecting tube can be seen in the absorption images, it was possible to manoeuvre the translation stage so that the cloud was well centred at these two positions.

Figure 3.19 shows the position of the cloud at a variety of transport distances after realignment of the translation stage. To obtain these data sets the atoms were loaded into the magnetic trap as usual, transported some distance, and then imaged whilst still in the trap. The red dashed lines in both figures represent the approximate positions of the centre of the connecting tube. In figure 3.19(a) the x position of the cloud is shown. Here higher numbers correspond to a position that is further away from the Zeeman slower. Looking at the data we see that within the first 100 mm of transport the cloud position oscillates by about 0.5 mm. Upon entering the tube the cloud slowly drifts, covering a distance of 1.5 mm. Then after exiting the tube the cloud jumps back to its initial x position. This erratic behaviour is most likely caused by stray magnetic fields pushing the cloud as it travels through the connecting tube. To produce a shift of 0.5 mm given the 30 G/cm field gradient in the x direction, a 1.5 G stray field is required. Despite these fluctuations in position, overall the cloud is reasonably well centred. However we are likely to see some loss of atoms at the two ends of the tube as the cloud is displaced by more than 0.5 mm from the tube centre, thus providing an opportunity for the atoms to collide with the tube walls.

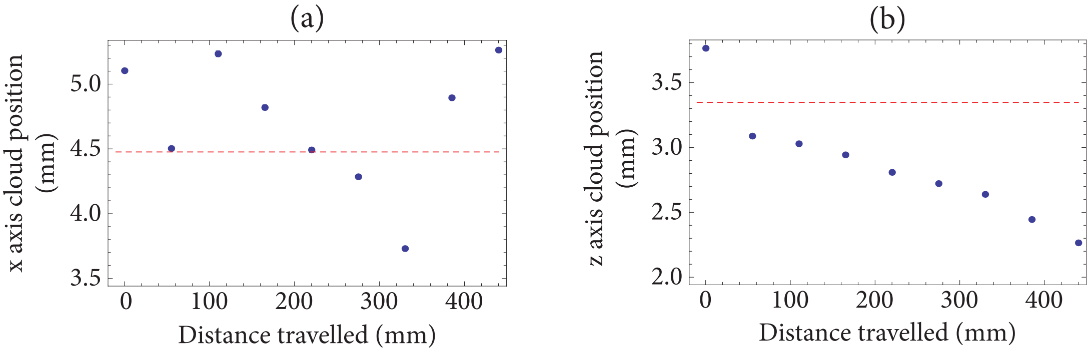

FIGURE 3.19: Cloud position during transport, after alignment of the translation stage, (a) shows the x axis cloud position whilst (b) shows the z axis cloud position. The red dashed lines indicate the approximate position of the tube centre.

Figure 3.19(b) shows the position of the atoms along the z axis. In contrast to the x axis data, the cloud position does not fluctuate erratically, thus indicating that there are no sizable stray fields orientated in this direction. Looking at the data in more detail we see an initial drop of 0.7 mm in the position. This represents a downwards shift of the cloud. As the atoms are transported further they continue to drop, ending up around 1.1 mm below the tube centre. Given a constant current, the z axis cloud position is fixed relative to the coils. Therefore the downwards drift of the cloud indicates that there is a relative tilt between the coils and the connecting tube. In order to keep the cloud vertically centred throughout the transport, this tilt must be removed. Unfortunately this is not straightforward to achieve. When considered in isolation this tilt is not necessarily a problem as the cloud has a maximum displacement of about 1 mm from the tube centre and a predicted width of 4 mm. However when coupled with the deviations in the x direction, it may lead to an increase in the number of atoms that are lost.

In an attempt to improve the transfer efficiency further, atoms were transported to and from the science chamber using unbalanced coil currents. In particular the bottom coil current was varied to shift the position of the cloud in the z direction. This was kept constant throughout the transport. By measuring the percentage of atoms recaptured in the MOT, the optimal cloud position was determined. Figure 3.20 shows the results of these measurements. The gray dashed line represents the coil current that is normally used, and higher currents correspond to an upwards shift of the cloud. This data set was obtained by loading the MOT atoms into the magnetic trap via the CMOT phase. The unbalanced trap was formed by ramping the bottom coil current to different values during the CMOT phase. It is worth noting that this procedure leads to small changes in the trap gradient. As shown in figure 2.28, this can affect the number of atoms that are loaded into the magnetic trap. However as the change in the gradient is less than ± 5 G/cm, the variation in atom number should be small. Looking at the results of figure 3.20, we see a peak of 1.8% is reached when the current is set equal to 63.4 A. Therefore by using unbalanced coils we are able to increase the transport efficiency slightly.

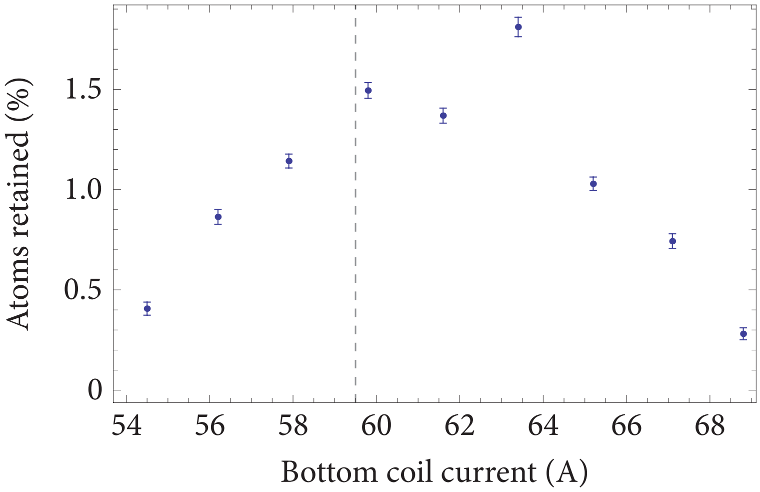

FIGURE 3.20: Variation in the percentage of atoms retained after transport to and from the science chamber as the bottom coil current is varied. The gray dashed line indicates the current that is normally used. The top coil also uses this current.

Having optimised the position of the cloud in both the x and z directions, the recaptured percentage was again measured as the transport distance was increased. In figure 3.21 these results are represented by the red data points. The blue points show the original transport data taken from figure 3.18 and the dashed gray lines represent the approximate positions of the ends of the tube. As expected the two data sets initially overlap when no transport occurs. For all subsequent points however the red data shows an increased atomic percentage. This indicates that the realignment procedure has been successful, although there is still a large loss of atoms at the entrance of the connecting tube. Further improvements to the transport efficiency could be obtained by eliminating the fluctuations of the x axis cloud position, or by reducing the size of the atom cloud through further cooling, using a technique such as evaporative cooling.

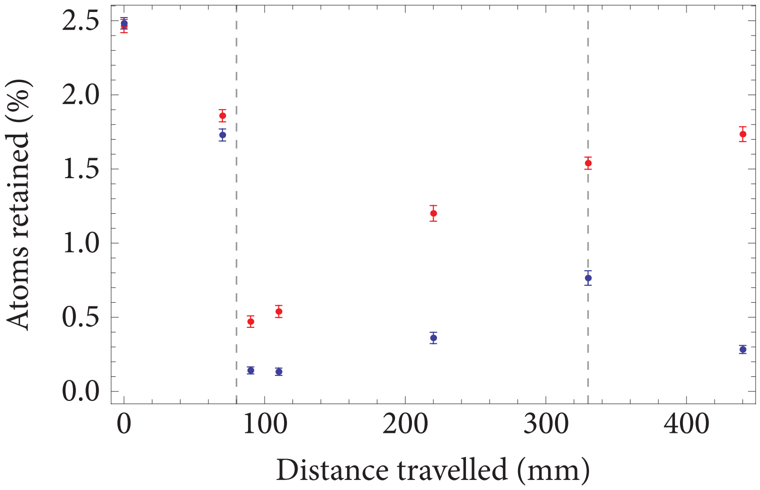

FIGURE 3.21: Transportation results showing recaptured atomic percentage as the transport distance is varied. The blue points repeat the preliminary transport data shown in figure 3.18. The red points show the results after aligning the cloud with the connecting tube. The gray dashed lines show the approximate positions of the two ends of the tube.

3.3.3 Lifetime in the science chamber

Having reduced some of the losses during transport, it became possible to measure the lifetime of the magnetic trap in the science chamber. In order to do this, atoms were loaded into the unbalanced magnetic trap via the CMOT phase. They were then transported to the science chamber and held there for varying amounts of time. Upon return to the MOT chamber, the atoms were recaptured in the MOT. The results of these measurements are shown in figure 3.22. The red line represents an exponential fit to the data. From this we find the lifetime of the magnetic trap in the science chamber to be $\tau_{\mathrm{SC}} = 18.5 \pm 0.7\,\mathrm{s}$, which corresponds to a background pressure of around 2.2×10^{-9} mbar. This trap lifetime is ten times longer than the lifetime in the MOT chamber.

The maximum percentage of 2.36% represents the maximum number of MOT atoms that are successfully returned to the MOT chamber when an acceleration of $2\,\mathrm{m/s^2}$ and a velocity of $0.5\,\mathrm{m/s}$ are used. Using this value it is possible to estimate the transport efficiency, η, of our system. In order to obtain a reliable value, the losses from background gas collisions must be taken into account. This loss rate is dependent on the local background pressure, which in turn varies with position. To simplify the situation we assume that the

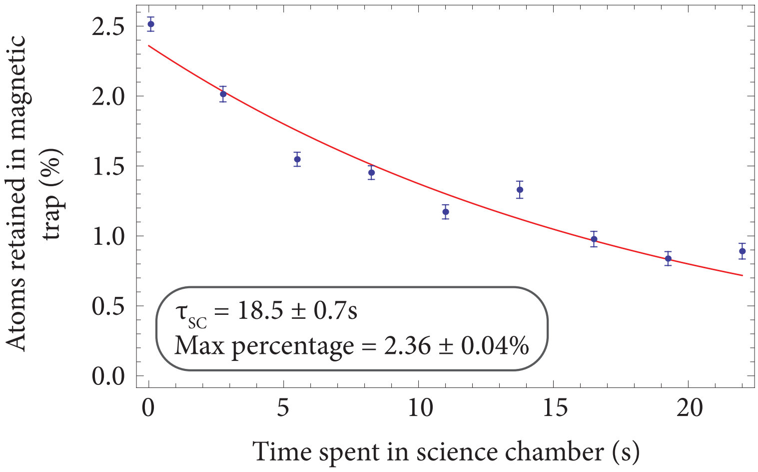

Figure 3.22: Measurement of the magnetic trap lifetime in the science chamber. The red line represents an exponential fit to the data.

lifetime of the trap is $\tau_{\mathrm{MC}} = 1.53\,\mathrm{s}$ for the first 80 mm of the transport, and is $\tau_{\mathrm{SC}} = 18.5\,\mathrm{s}$ for the remaining 360 mm. To travel these two distances of 80 mm and 360 mm, it takes 0.285 s and 0.845 s respectively. Therefore we estimate that 20% of the atoms are lost due to background collisions. We also know that 22.8% of the atoms are transferred from the MOT to the magnetic trap. The remaining losses are then due to the transport procedure itself. This produces a value of around $\eta = 41\%$ for the transport efficiency of our system. When compared to other experiments this value is quite low. For example, by utilising a similar setup, rubidium atoms have been transported with an efficiency of 100% [108]. Given the transport efficiency of our system, 7% of the MOT atoms are successfully transported to the science chamber, giving an absolute atom number in the science chamber of about 1.7×10^7.

3.4 Chapter summary

Before testing the transportation setup, the lifetime of the magnetic trap in the MOT chamber was measured to ensure that a detectable signal would be produced after transport. From these measurements the magnetic trap lifetime in the MOT chamber was found to be $\tau_{\mathrm{MC}} = 1.53 \pm 0.01\,\mathrm{s}$. This rather short lifetime resulted from a small leak in the oven chamber which worsened with increasing temperature. As the lifetime was deemed sufficient to test the transportation system, experiments were carried out to determine whether reliable images could be obtained after the cloud was released from the trap. This highlighted the fact that atoms were disappearing from the images. To investigate this problem, line shape measurements were performed at a variety of times, using atoms released from both the MOT and CMOT. By comparing these results to the predicted spectra, it was found that a time and position dependent magnetic field was present. This was attributed to eddy currents that persist in the chamber after the coils switch off. As it was not possible to remove this magnetic field, the transportation system was tested using the MOT recapture method.

Preliminary transportation experiments produced a low transfer efficiency, which was thought to be caused by poor alignment of the atom cloud with the connecting tube. Therefore the cloud position was optimised, resulting in a final transport efficiency of $\eta = 41\%$. This enabled lifetime measurements to be carried out in the science chamber, producing a value of $\tau_{\mathrm{SC}} = 18.5 \pm 0.7\,\mathrm{s}$. Although transportation has been demonstrated it should be possible to further improve the efficiency by reducing the cloud temperature or reducing the fluctuations of the cloud position. We find that about 7% of the MOT atoms, that is approximately 1.7×10^7 atoms, are successfully transported to the science chamber, so it should now be possible to directly image the cloud here by installing a suitable imaging system. Once this has been achieved the microwave trap, or high field electrodes can be incorporated into the setup and tested.

Chapter 4

Towards atoms in high electric fields

The aim of our experiment is to produce an ultracold dipolar gas. To create such a gas we plan to electrically polarise the lithium atoms by using a very large electric field. This means that the atoms must be placed between two high voltage electrodes which will have a separation of approximately 0.5 mm. In order to produce substantial dipolar interactions, electric fields of up to 1 MV/cm are required. This chapter describes the setup that has been developed to produce these large electric fields. Section 4.1 gives a brief overview of the process that leads to emission of electrons from a low temperature metallic surface. The mechanisms which lead to electrical breakdown are also discussed, along with the surface conditioning techniques that are commonly used to improve electrode performance. Section 4.2 discusses the design constraints that the electrode mount must satisfy. In particular the electrodes must be almost perfectly parallel, and they must be able to withstand large forces. With this in mind, an electrode mount design is presented. This mirror mount based design utilises glass electrodes that are coated with indium tin oxide (ITO), thus allowing interferometric techniques to be used to measure the angle between the electrodes. In section 4.3 this design is tested. In particular the angle between the plates and their separation is determined using optical methods, and the results of high voltage tests are presented. The ITO coated electrodes produced a relatively low electric field so they were replaced with super-polished stainless steel electrodes, which are described in section 4.4. The results of high voltage tests are also presented in this section. As these metal electrodes cannot be aligned using interferometric techniques, a different alignment procedure is required. Therefore the electrode mount has recently been redesigned by Devin Dunseith. A brief overview of this new design is given in section 4.5.

4.1 Producing high electric fields

In order to produce high electric fields, it is important to understand the processes that lead to electrical breakdown of the electrodes. Here breakdown is characterised by a large, persistent current flow between the plates. This section starts by describing the mechanism which leads to electron emission, and therefore current flow, from a low temperature metallic surface. From this theoretical description we find that it should be possible to generate very large electric fields before any measurable current is produced. However, this does not agree with the results of the numerous experiments that utilise broad area electrodes. In practice, currents often flow between the plates at much lower electric fields. Therefore this section also describes the mechanisms which lead to enhanced current flow between the electrodes. This section concludes with an overview of the surface preparation and surface conditioning techniques that have been developed in order to increase the electric field at breakdown.

4.1.1 Electric field limits

Classically, electrons are emitted from a metallic surface when their kinetic energy exceeds the binding potential of the metal. For this to occur in the absence of an applied field, the temperature of the metal must be increased. This process, which is known as thermionic emission, becomes significant for temperatures over $1000\,\mathrm{K}$. If an electric field is applied, electron emission can also occur from low temperature metallic surfaces. In this case emission is caused by quantum mechanical tunnelling of the electrons and is known as cold field emission. For our room temperature electrodes this second process is important, as it limits the maximum field that can be sustained.

An expression describing the current density produced during cold field emission was first derived by Fowler and Nordheim in 1928 [128]. Here they use the Sommerfeld free-electron model to represent the metal, and assume a temperature of $T = 0\,\mathrm{K}$. Initially when no electric field is applied, the atoms see a finite potential barrier at the surface of the metal.

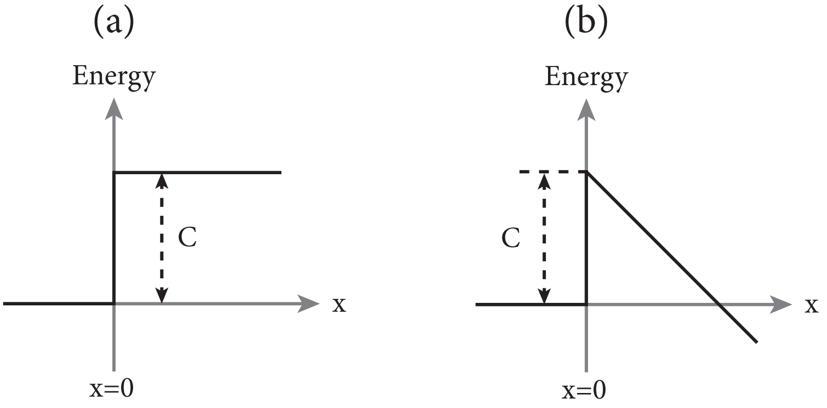

FIGURE 4.1: Potential barrier at the surface of a metal. In (a) the potential is modelled as a step function with height C. In (b) the potential has been modified by the presence of an electric field.

As shown in figure 4.1(a), this is modelled as a step function at $x = 0$, where the barrier height, C, is dependent on the strength of the Coulomb interaction between the electron and the positive ions close to the surface. As shown in figure 4.1(b), when an electric field with magnitude E is applied perpendicular to the surface, the potential is altered, thus allowing electrons to tunnel through the barrier. To find the probability of transmitting an electron with kinetic energy W, the wave equations,

$$\frac{d^2\psi}{dx^2} + \kappa^2(W - C + Ex)\psi = 0 \qquad (x > 0) \tag{4.1}$$

$$\frac{d^2\psi}{dx^2} + \kappa^2 W\psi = 0 \qquad (x < 0), \tag{4.2}$$

must be solved subject to the conditions that ψ, which represents the electronic wavefunction, and $d\psi/dx$ are continuous at $x = 0$, and that for $x > 0$, ψ represents a stream of particles moving to the right only. Here κ is a constant given by $\kappa = 8\pi^2 m_e/h^2$, where m_e is the mass of an electron. For the full details of this calculation see [128].

Having found an expression for the transmission probability, the authors then write down an equation, taken from [129], that describes the number of electrons, $N(W)$, with kinetic energy W that are incident on the surface per unit area per unit time. The current density, J, is then found by multiplying together $N(W)$, the transmission probability and the charge of an electron, e, and integrating over all possible energies. This results in,

$$J = \frac{e}{2\pi h}\frac{\mu^{1/2}}{(\chi + \mu)\chi^{1/2}}E^2 e^{-4\kappa\chi^{3/2}/3E}, \tag{4.3}$$

where $\chi = C - \mu$ is the work function of the metal and μ is the chemical potential. Strictly speaking this formula only applies when the metal temperature is zero, however it is still a valid approximation provided $\mu \gg k_B T$. Given that μ is typically between $5 - 10\,\mathrm{eV}$ for most metals, this condition is easily met for room temperature electrodes. Therefore we are able to use this equation to model the field emission from the circular stainless steel electrodes that are used in later experiments. These electrodes have a diameter of 25.4 mm, and should have a work function that lies somewhere between 4.7 eV and 5.6 eV [130]. Taking the average value of the work function we find that an electric field of 1 MV/cm produces a negligibly small current, whilst a $1\,\mu$A current is generated for an electric field of around 13 MV/cm. These values do not agree well with experimental data, as it is common to observe currents of $\sim 1\,\mu$A for fields of ~ 100 kV/cm. This indicates that additional processes lead to increased current flow between the electrodes, thus making fields above 100 kV/cm hard to obtain experimentally.

4.1.2 Breakdown mechanisms

Upon application of a sizeable voltage to a pair of electrodes, experiments have shown that there is often a measurable current flow between the two plates. As the voltage is increased, the current becomes unstable and is superimposed with spikes. These spikes are known as micro-discharges. Eventually at some critical voltage, a large and persistent current will suddenly flow between the electrodes. At this point electrical breakdown is said to have occurred. The event appears as an initial spark, followed by the formation of a glowing arc between the two electrodes. It is important to avoid electrical breakdown because it is an irreversible process that often has catastrophic effects and causes the subsequent performance of the electrodes to deteriorate. Therefore it is useful to understand the processes which lead to breakdown so that it can be avoided, and higher electric fields can be generated.

In general breakdown is initiated by the presence of ionisable material within the electrode gap. Due to the high vacuum typically attained in atomic physics experiments, residual gas plays no part in the breakdown process. Instead the primary causes of breakdown are mechanisms which lead to vaporisation of the electrode material itself. There are two such processes, the first of which is cathode initiated breakdown. Here micro-protrusions on the surface of the cathode enhance the local electric field, resulting in a larger field emission current and resistive heating of the protrusion. At some critical current density, this resistive heating causes the micro-protrusion to vaporise, thus initiating electrical breakdown. Using a point-to-plane electrode geometry it was found that a current density of 10^8 A/cm^2 was required for cathode initiated breakdown to occur [131]. The second mechanism is anode initiated breakdown. For a short, dull cathode protrusion that is thermally coupled to the cathode surface, the likelihood of vaporisation due to resistive heating is reduced. In this case the electron beam emitted by the protrusion can have a large enough power density that anode material is instead vaporised. This again initiates electrical breakdown.

Many experiments have been carried out in order to gain insight into the factors which affect the size of pre-breakdown currents, and the onset of full electrical breakdown. In particular it was found that the current flow between electrodes in a point-to-plane geometry was well described by equation (4.3) [131], whilst for broad area electrodes, the current flow was larger than expected [132]. This increase in current was attributed to the local field enhancement at micro-protrusions on the cathode surface. In order to bring these results in line with equation (4.3), a new electric field $E_\beta = \beta E$ was introduced. Here β is the field enhancement factor and E is the average field between the plates, which is given by,

$$E = \frac{V}{d}, \tag{4.4}$$

where V is the applied voltage and d is the distance between the electrodes. Theoretical analysis has predicted that the size of β compared to some critical value, β_0, will determine whether cathode or anode initiated breakdown is dominant [133]. These authors show that the size of β_0 depends on whether a pulsed or DC voltage is applied. For pulsed voltages β_0 is smaller, and this results in a higher probability of cathode initiated breakdown. However for DC voltages, anode initiated breakdown should be prevalent. The experimental results presented in [134] confirm these predictions.

In addition to this the variation in the size of the breakdown field with gap spacing has also been investigated in [132]. Their results show that, whilst E_β is independent of gap spacing, β rises as the gap length is increased. Therefore if a high average field is to be generated a small gap spacing should be employed. Also as both anode and cathode initiated breakdown are caused by the presence of micro-protrusions, it is important to ensure that the electrode surface is as smooth as possible. As a result, a number of different surface treatments and electrode conditioning techniques have been investigated over the years. A brief overview of them is given in the next section.

4.1.3 Electrode surface preparation and conditioning techniques

As the electrode surface has a major effect on the average field that can be obtained prior to breakdown, a wide range of surface preparation and surface conditioning techniques have been developed and tested. Most experiments use solid metal electrodes, thus allowing various polishing techniques to be employed. These include electro-polishing, which removes surface protrusions via chemical etching, and machine polishing, which utilises various grades of abrasive paste and polishing cloths to produce a smooth surface. Ultimately the surface finish depends on the exact details of the applied technique, and because of this neither of the above processes has been shown to consistently produce superior results. However experiments confirm that polished plates support higher voltages before breakdown than non-polished plates [135], thus highlighting the importance of having a smooth electrode surface. It is worth noting that polishing techniques cannot be applied to the ITO coated glass electrodes as this would remove the thin film coating. Therefore the surface finish will be dictated by the surface quality of the glass substrate, and the process used to apply the ITO coating.

Even if the electrode surface has been carefully prepared, micro-protrusions, adsorbed gas, and loosely adhering micro-particles are still likely to be present. Therefore to further improve the performance of the electrodes, additional in situ conditioning techniques are often employed. The most commonly used technique is called current conditioning [136]. This is done at high vacuum and involves increasing the voltage of the electrodes incrementally until micro-discharges occur. The voltage is then held constant to allow these to dissipate. After this the voltage is increased and the process is repeated. This leads to improved performance of the electrodes because micro-protrusions and loosely adhering micro-particles are removed from the surface of the plates.

Another commonly used technique is gas conditioning [137, 138]. In this case a high voltage of $> 20\,\mathrm{kV}$ is applied to the electrodes, so that a field emission current of a few microamps is produced. Next a gas such as argon, krypton or helium is introduced into the vacuum chamber via a leak valve, to produce a background pressure of anywhere between $10^{-6}\,\mathrm{mbar}$ and $10^{-3}\,\mathrm{mbar}$. At this gas pressure ions form close to the micro-protrusions on the cathode surface, where field emission is highest. These ions are accelerated back towards the emitter, blunting the protrusion and reducing field emission. In addition to this, gas conditioning also results in ion implantation [139]. This again reduces field emission as the work function of the metal increases.

A similar technique, known as glow-discharge conditioning, also uses ions to remove micro-protrusions. In this case the pressure in the chamber is increased to somewhere between 10^{-3} mbar and 10^{-2} mbar. Then by applying a low voltage to the electrodes, a 50 Hz, AC glow discharge is struck between the plates. Typically treatment lasts for up to an hour, as running for longer times can degrade the performance of the electrodes. Investigations have shown that the effectiveness of this technique is dependent on the gas species used, with nitrogen producing the best results [140].

By using various combinations of these surface preparation and conditioning techniques many experiments have shown that the performance of metal electrodes can be improved. For example by baking the setup and then using current conditioning, polished plane-parallel stainless steel electrodes, with a diameter of 7 mm and a gap spacing of 0.5 mm have been shown to support an average breakdown field of $E = 1.4\,\mathrm{MV/cm}$ [141]. A number of other experiments have reached lower field values by using broad area electrodes made from other metals. For example tungsten plates with a gap spacing of 0.254 mm were measured to have an average breakdown field of $E = 0.816\,\mathrm{MV/cm}$ [132], copper electrodes with a separation of 0.5 mm had an average breakdown field of $E = 0.36\,\mathrm{MV/cm}$ [142], whilst titanium plates at a gap spacing of 0.42 mm had a breakdown field of $E = 1.3\,\mathrm{MV/cm}$ [141]. This shows that by using metal electrodes it should be possible to reach the high electric fields that we ultimately require.

A breakdown study for ITO coated glass electrodes has shown that they can also generate high electric fields without the use of surface conditioning techniques. In this case the field at breakdown was found to be approximately $E = 1\,\mathrm{MV/cm}$ [143]. However it is worth noting that these ITO electrodes were formed by first depositing a single strip of ITO onto a glass substrate. This was then split into two, thus forming two planar electrodes with a gap spacing of $10\,\mu$m. As this geometry is significantly different to that of our ITO electrodes, these results are not necessarily a good indicator of the maximum electric field that will be produced in our setup.

4.2 Designing the electrode mount

Given our final aim is to study atoms under high electric fields, some care has to be taken when designing the electrode mount so that it is fit for purpose. In particular it is important to think about the forces that will act on both the electrodes and the atoms when large electric fields are applied. This section begins by discussing the effects of these forces, and the implications that this has on the design of the electrode mount. Having found that the plates will be subjected to large forces, and that the electrodes need to be very parallel, an electrode mount design is presented. To allow the angle between the electrodes to be varied, the design has been based on a mirror mount. In addition to this ITO coated glass electrodes are utilised, so that interferometric techniques can be used to accurately measure the angle between the electrodes.

4.2.1 Design constraints

Before designing a mount for the high field electrodes, it is important to consider the size of the attractive force between the plates. This force is due to the opposite charge of the electrodes, and when high voltages are used it can be substantial in size. Therefore the electrode mount must be designed to withstand this. To calculate the size of this force we start with two parallel plates that each have an area A, are separated by a distance d and have opposite total charges of Q and $-Q$. Here the force is labelled as F_{elec} and the electric field as E. The electric field at the negatively charged plate due to the positively charged plate is simply $E_+ = \sigma/2\epsilon_0$, where $\sigma = Q/A$ is the surface charge density. The force is then given by,

$$F_{\mathrm{elec}} = -QE_+ = -\frac{Q^2}{2\epsilon_0 A}. \tag{4.5}$$

By using $Q = VC$, and $C = \epsilon_0 A/d$, where V is the potential difference between the plates, and C is the capacitance, this can be re-written as

$$F_{\mathrm{elec}} = -\frac{1}{2}\epsilon_0 A E^2. \tag{4.6}$$

The ITO coated glass electrodes which are used in later experiments, have an area of $10.08\,\mathrm{cm}^2$. Substituting this into the above equation and setting $E = 1\,\mathrm{MV/cm}$, results in a force of $45\,\mathrm{N}$ acting on each plate. Therefore the electrode mount will have to be designed to withstand large forces, and will also have to hold the electrodes securely in place.

Next we have to consider the forces that act on the atoms themselves. Due to the DC Stark shift, any inhomogeneity in the electric field will produce a force that pushes the atoms to a position where the interaction energy is minimised. Therefore atoms in the $^2S_{1/2}$ ground state will be attracted to high field regions, as this state is high-field seeking. To produce a perfectly uniform electric field everywhere, the electrodes must be infinitely large and perfectly parallel. In reality neither of these conditions will be satisfied, so we must determine the effect that this has on the atoms. This in turn will influence the design of the electrode mount.

The finite size of the electrodes leads to an inhomogeneous electric field at the plate edges. To ensure that the field is uniform over the extent of the atom cloud, the plates need to be much larger than the cloud. As the axial field gradient of the magnetic trap is higher than the radial gradient, the cloud is smaller in the z direction. Therefore to retain the largest number of atoms between the plates, the electrodes should lie in the $x-y$ plane so that the gap between them is in the z direction. This means that we have to compare the width of the cloud in the x and y directions to the width and length of the electrodes in order to determine whether fringe fields at the plate edges are likely to have an effect. If we take a cloud that has been cooled to the Doppler temperature and assume that the maximum radial field gradient of approximately 69 G/cm can be applied, the cloud will have a diameter of around 0.6 mm in the x and y directions. Therefore, it should be possible to position the cloud between the electrodes with no loss of atoms, provided the temperature can be further reduced from its current value of 0.75 mK.

In order to determine whether the electric field is uniform over the size of the atom cloud, the fringe field at the plate edges must be calculated. To do this, we consider two semi-infinite electrodes, which extend from $x = -\infty$ to $x = 0$. The plates are held at a potential of $\pm V_0$ and have a separation in the z direction of d. As the equation for the electric field is derived in a number of textbooks, for example [144] and [145], the details of the calculation are not repeated here. The final expression for the electric field is

$$E(u,v) = \frac{2V_0}{d}\frac{1}{\sqrt{1+e^{2u}+2e^{u}\cos(v)}}, \tag{4.7}$$

where u and v are related to x and z by $x = d(1 + u + e^u \cos(v))/2\pi$ and $z = d(v + e^u \sin(v))/2\pi$. Using this equation the electric field at the edge of the electrodes can be calculated.

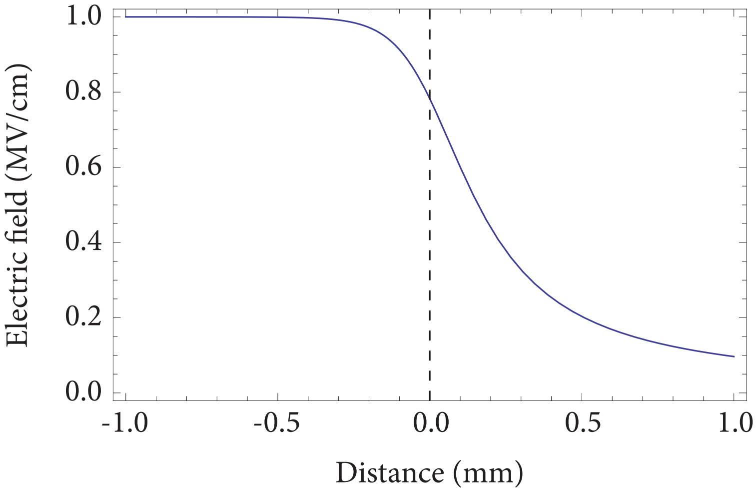

FIGURE 4.2: Electric field along the centreline of a semi-infinite capacitor. The capacitor plate edges are positioned at $x = 0$.

Figure 4.2 shows the variation in the electric field along the centreline of the capacitor as the edge of the electrode is approached. Here the applied voltage is $\pm V_0 = \pm 25\,\mathrm{kV}$, and the electrode separation is $d = 0.5\,\mathrm{mm}$. This shows that by moving only 1 mm away from the edge of the electrode, the electric field is essentially uniform and has the expected value of 1 MV/cm. As the ITO coated electrodes have a width of 24 mm and a length of 42 mm, the cloud, with its radial diameter of 0.6 mm, can be easily positioned many millimetres away from the plate edges. Therefore the electric field over the extent of the cloud will be uniform and fringe fields can be neglected.

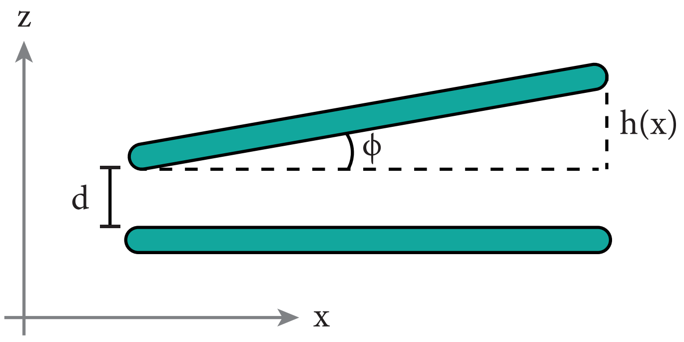

FIGURE 4.3: A pair of electrodes where one is tilted along the x direction only. The angle between the plates is ϕ, the gap spacing is d, and the displacement of the top plate is $h(x)$.

Finally we consider the force that acts upon the atoms if the electrodes are not completely parallel. Consider two plates that are separated along z and tilted along x only, as show in figure 4.3. The angle between the two plates is labelled ϕ, and the vertical displacement of the top plate is $h(x)$. The tilt between the plates produces an electric field gradient and a force along x. The size of this force is given by $F = -dE_S/dx$. Here the Stark shift of the atomic energy levels is $E_S = \frac{1}{2}\alpha E(x)^2$, where $E(x)$ is the electric field, and α is the polarisability of the atom. The value of α for the ${}^2S_{1/2}$ ground state of lithium can be found in table 2.1. For atoms to remain trapped, the magnetic trapping force must be larger than the force produced by the electric field. This condition can be written as

$$g_F M_F \mu_B \frac{dB}{dx} > \alpha E \frac{dE}{dx}. \tag{4.8}$$

Although we are only considering the x direction here, this condition must be satisfied along all three cartesian axes. In addition to this, because the atom cloud has a finite temperature, a minimum trap depth must be maintained, otherwise atoms will be lost. As the force from the electric field gradient produces an acceleration, the trap is effectively tilted, which reduces the magnetic field gradient on one side. By calculating the magnetic field gradient as the angle ϕ is varied, we can place an upper limit on ϕ.

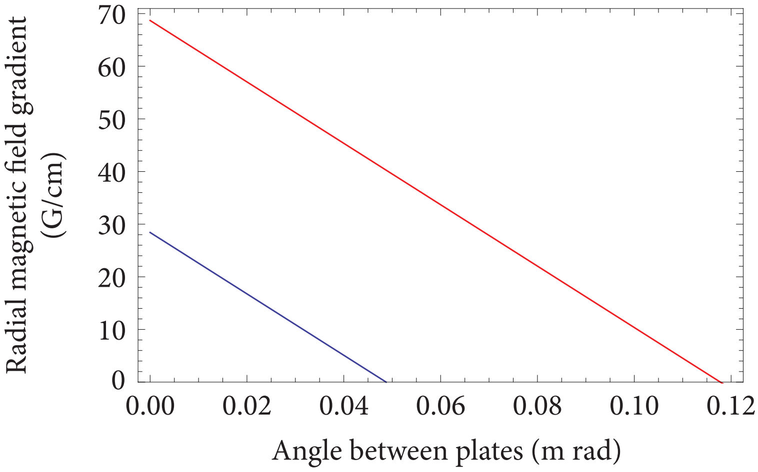

FIGURE 4.4: Variation in the radial magnetic field gradient as the angle between the electrodes is increased. The blue line represents a trap with a magnetic field gradient of 28.4 G/cm, the red line represents a trap with a gradient of 69 G/cm. In both cases a 1 MV/cm electric field is applied.

Figure 4.4 shows the variation in the radial magnetic field gradient as the angle ϕ is varied. The blue line represents a trap with a magnetic field gradient of 28.4 G/cm, whilst the red line represents a trap with a gradient of 69 G/cm. In both cases an electric field of

$E = V/d = 1\,\mathrm{MV/cm}$ is applied. For the blue line we see that the field gradient drops as the angle is increased, eventually reaching zero at an angle of 0.049 mrad. The red line shows that by utilising the maximum field gradient that our coils can produce, a larger angle between the plates can be tolerated. This is because the magnetic trapping force is larger. In particular the field gradient drops to zero when ϕ reaches a value of 0.118 mrad. It is worth noting that a reduction of the electric field will also relax the constraint on ϕ. From this we conclude that the angle between the plates must be well below 0.1 mrad if the atoms are to remain trapped. For plates with a width of 24 mm this means that the displacement, $h(x)$ in figure 4.3 must be less than $2.4\,\mu$m. In practice achieving such a high degree of parallelism through machining of the electrode surface is challenging. Therefore it is necessary to design an electrode mount that allows fine adjustments of ϕ to be made. In addition to this the mount must also be able to withstand large forces so that the parallelism of the plates can be maintained.

4.2.2 Final design

As the angle between the electrodes needs to be smaller than 0.1 mrad, it is necessary to have an accurate method of determining how parallel the plates are. Once atoms have been positioned between the electrodes, they can be used to verify whether the plates are tilted, as the atoms are drawn to regions of high electric field. However, unless the position of the plates can be adjusted whilst under vacuum, this method of alignment will be slow and cumbersome. Therefore it is important to ensure that the plates are parallel before placing them under vacuum. By using interferometric techniques the parallelism of the plates can be measured to a high level of accuracy. For this reason we have chosen to use glass electrodes, as they can be used as a Fabry-Pérot interferometer. To make the glass electrically conductive, a transparent, 150 nm thick coating of ITO has been applied. These plates were bought pre-coated from Torr Scientific. They are made from float glass and have dimensions of 42 mm × 24 mm × 3 mm. To reduce field enhancement from sharp protrusions at the plate edges, all edges have been rounded with a 0.5 mm radius, whilst all corners have been rounded using a 1 mm radius. As the ITO coating covers all but the two shortest sides, electrical contact can be made by simply pressing high voltage probes onto the back surface of the plate.

To allow the plates to be tilted we have based the electrode mount design on a typical mirror mount. As shown in figure 4.5, the mount is separated into two pieces. The inner surface of the bottom piece is shown in (a), whilst the inner surface of the top piece is shown in (b). In (c) a cross-sectional view of the top mount is depicted. Each mount has dimensions of 95 mm × 80 mm × 15.5 mm and both parts are machined out of polyether ether ketone (PEEK). To provide optical access to the plates so that they can be used as an interferometer, a hole with dimensions of 32 mm × 15 mm has been cut into the centre of each mount. As can be seen in (c) the glass electrode sits within a 1 mm deep recess, and protrudes from the surface of the mount. To hold the electrode in place, vacuum compatible glue is used. Once both electrodes are in position, as shown in (b), the two mounts are placed face to face. Four 1/4 inch diameter, 100 threads per inch, ball-tipped stainless steel screws (Thorlabs F25US100) are then inserted into the holes that contain a horizontal blue line. To hold the mounts together two stainless steel springs (RS components part number: 0821419) are inserted into the holes containing a purple vertical line. By turning just three of the screws the separation and tilt between the electrodes can be adjusted. The fourth screw is used to add extra support once the angle between the plates has been optimised.

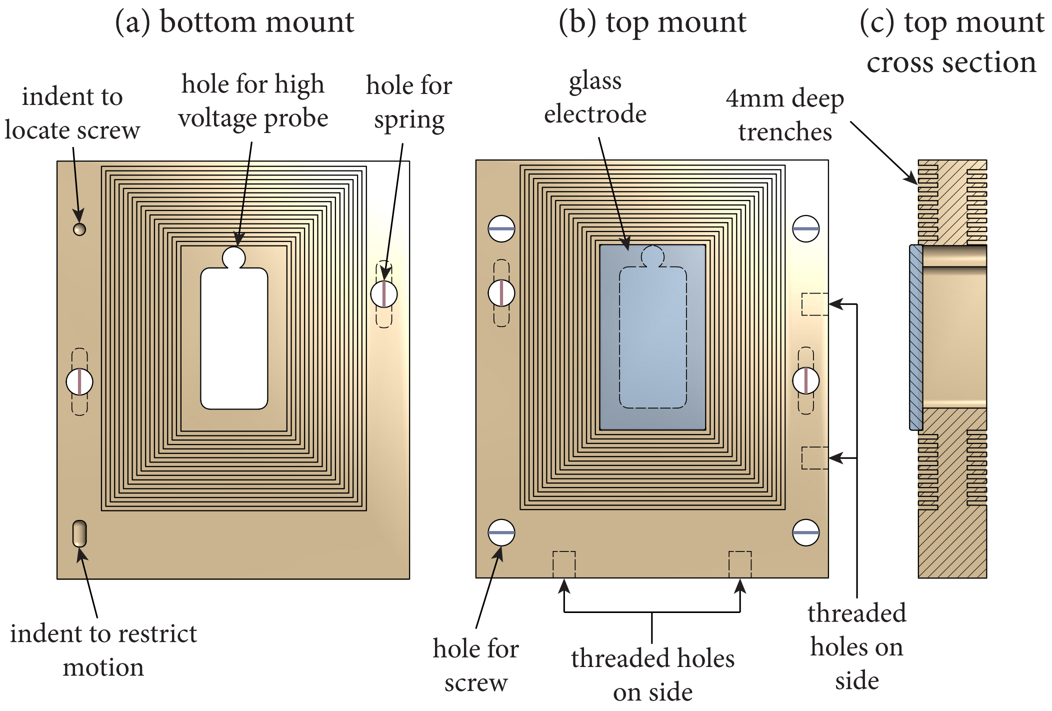

FIGURE 4.5: Inner surfaces of the (a) bottom electrode mount and (b) top electrode mount. In (c) a cross-sectional view of the top mount is shown. The horizontal blue lines indicate the holes through which screws are placed, whilst the vertical purple lines show where springs are positioned.

To discourage surface currents from flowing, a series of 4 mm deep trenches have been positioned around each glass plate. These increase the path length between the two electrodes, and have been cut into the inner and outer surfaces of both the top and bottom mounts. Electrical contact is made by positioning a high voltage probe in the small hole that sits just above the central cut out. In order to attach the electrode mount to the vacuum chamber, two pairs of threaded holes have been drilled into the bottom and right hand sides of the top plate, as shown in (b). Looking at the bottom plate, two indents can be seen on its inner surface. These are used to accommodate the ball tips of the adjustment screws. Specifically, the circular indent in the top left hand corner is used to locate the top screw, whilst the elongated channel in the bottom left hand corner restricts the horizontal motion of the bottom screw. The third screw is able to move freely, thus allowing the correct pivoting motion to be achieved. This type of setup is known as a Kelvin clamp. Figure 4.6(a) shows a photograph of the fully assembled mount, and (b) shows a side view of the mount. Here the glass electrodes have been attached to the mount by using EpoTex H74 UHV compatible epoxy, which was left to cure overnight in an oven at 80 °C.

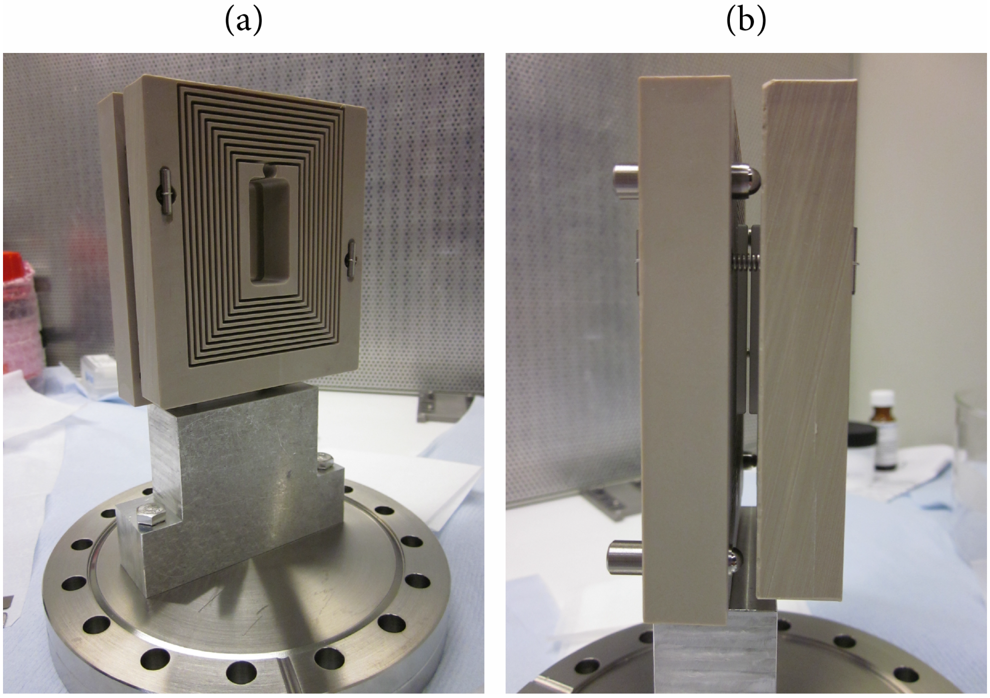

Figure 4.6: Photographs of the assembled electrode mount. In (a) the mount is attached to the vacuum flange ready to be placed in the test chamber. In (b) a side view of the mount is shown.

As the electrodes will be subjected to a large force, it is important to check that they are able to withstand this without breaking. The deflection of each plate can be determined by solving the Euler Bernoulli equation [146]. Figure 4.7 depicts the situation being modelled. Here the top plate is held in place at both ends but is free to move over the unsupported length L. Rather than look at the deflection of the top and bottom plates individually, we instead assume that the bottom plate is fixed along its entire length. By doubling the expected deflection we can then find the total displacement of the plates. The position along the electrode is labelled by x, the initial distance between the plates is given by d, the electrode deflection is $w(x)$ and both the top and bottom plates have a width in the y direction of W, and a thickness, t. Initially the force that acts on the top plate is uniform. However as the electrode deflects, the force will increase as the gap spacing decreases, thus causing the plate to deform further. As a result the force is a function of the deflection which is in turn a function of position x. Here we denote the force per unit length by $F_z(x)$.

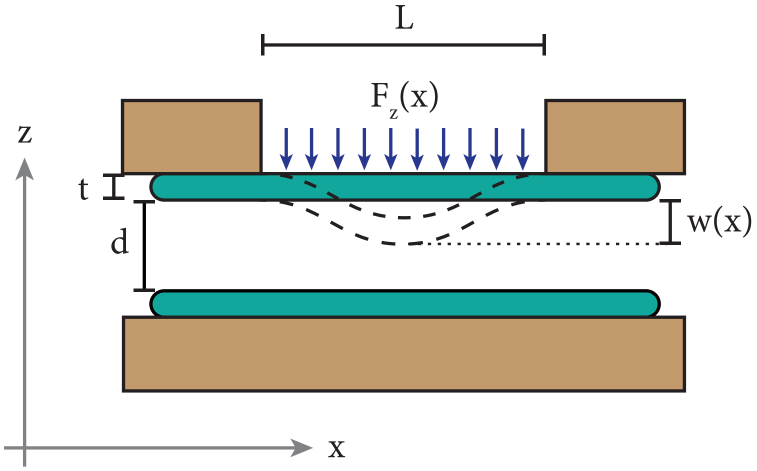

FIGURE 4.7: Model used to calculate the expected deflection of the electrode when an electric field is applied. One plate is fixed along its whole length whilst the other is fixed at both ends and is free to move in the centre. The top plate has a width of W in the y direction, a thickness t and an unsupported length L. The gap spacing is d, the deflection of the plate is labelled $w(x)$, and the force per unit length is $F_z(x)$.

Given this situation the Euler Bernoulli equation becomes

$$Y_M I \frac{d^4 w(x)}{dx^4} = F_z(x) = \frac{\epsilon_0 L W V^2}{2(d - 2w(x))^2}, \tag{4.9}$$

where Y_M is the Young's modulus of the electrode material, $I = \int\int_A z^2 dydz = t^3 W/12$ is the moment of inertia of the area, and V is the potential difference between the electrodes. To obtain the expression on the right hand side, equation (4.6) has been used. This equation is then solved subject to the boundary conditions for an electrode fixed at both ends, which are $w(0) = w(L) = 0$ and $\frac{dw(0)}{dx} = \frac{dw(L)}{dx} = 0$. For our electrodes $L = 32\,\mathrm{mm}$, $W = 24\,\mathrm{mm}$, $t = 3\,\mathrm{mm}$ and $Y_M = 72\,\mathrm{GPa}$ [147]. Note that here we are ignoring the fact that the plate is actually supported along some parts of its 24 mm width. As a result the calculated deflection will be an overestimate of the actual value. From this we find that the maximum deflection of the plates is 24 nm when a 1 MV/cm electric field is applied. This corresponds to an angle of $1.5\,\mu$rad. As the deflection is small, we conclude that the glass electrodes can easily withstand the applied force without breaking. It is worth noting that fringe fields at the ends of the plates can result in forces parallel to the plate surface. These forces are small compared to the forces that act in the direction normal to the plate surface. Nevertheless, they could potentially distort the plates, or the mounts that hold them. These effects have not yet been investigated.

4.3 Testing the ITO electrodes

As it is important to ensure that the angle between the electrodes is as small as possible, we have decided to use interferometric techniques to align the plates. This section begins by describing the setup that was used to measure and reduce the angle between the electrodes. In order to prevent damage of the delicate electrode surface, contact with the plates should be avoided. Therefore this section also describes the optical methods that were used to measure the separation of the electrodes. Next, the equipment used during the high voltage test is described, and finally the results of these tests, which were carried out using ITO coated glass electrodes, are presented.

4.3.1 Measuring the parallelism and separation of the electrodes

Before carrying out high voltage tests, the plate alignment was optimised and the gap spacing was measured. Figure 4.8 shows the setup that was used in order to reduce the angle between the electrodes. First the beam from a diode laser was expanded and collimated. The electrode mount was then positioned in the path of the laser beam, and angled so that the reflected light could be imaged on to a screen. This produced four spots on the screen, each one corresponding to light reflected from one of the four electrode surfaces. By using the adjustment screws the plate separation was reduced, causing the two central spots to overlap and form an interference pattern.

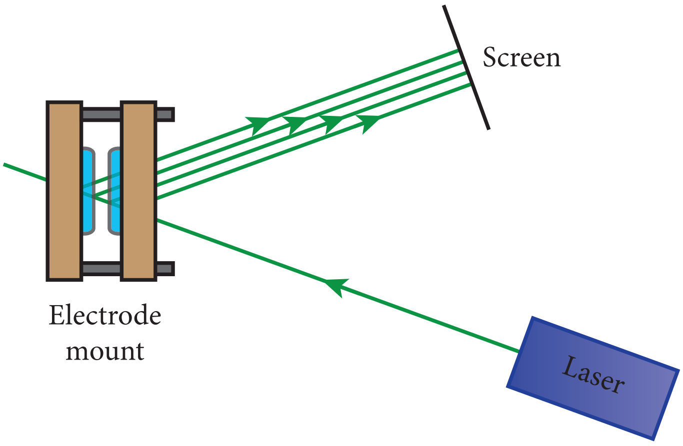

FIGURE 4.8: Setup used to reduce the angle between the electrodes.

If the light source is not well collimated we would expect perfectly parallel plates to produce circular fringes. This is because the rays within the beam will have different angles of incidence, which introduces a path length difference between the light rays, and results in the formation of fringes. If the plates are tilted, the centre of the circular fringes will move towards the edge of the interference pattern, thus producing curved fringes. For a very large tilt these will become straight line fringes. However, if the light source is collimated, then perfectly parallel plates will produce a single interference fringe that covers the entire overlap region of the beams. This is because all of the light rays have the same angle of incidence, so the path length difference between the interfering beams is dependent only on the separation of the electrodes. This means that if the distance between the electrodes were to be scanned, the interference pattern would alternate between light and dark. Tilted plates would then produce a series of straight line fringes, with each fringe corresponding to an increase in the path length of $\lambda/2$. Therefore if N fringes are present over the length of the interference pattern x, the change in the gap spacing, Δl, must be equal to $\Delta l = N\lambda/2$. The angle between the plates ϕ can then be written as

$$\phi = \frac{\Delta l}{x} = \frac{N\lambda}{2x}. \tag{4.10}$$

In order to observe any fringes, N must be at least two. For our setup, x is equal to the region of overlap between the two central spots, which was approximately 10 mm. Therefore the smallest angle that can be measured between the plates is 67 μrad, which is just below our 0.1 mrad upper limit. In practice we found that circular fringes were formed, thus indicating that the laser beam was not perfectly collimated. Given that two circular fringes were visible, and that the radius of the interference pattern was 5 mm, we conclude that the angle between the electrodes is 0.13 mrad at most. Although this is higher than our upper limit, it is still much better than can usually be achieved through machining of the electrode surface, and with more careful collimation of the beam, this angle could be reduced even further.

In order to measure the plate separation, ideally the setup shown in figure 4.8 would again be used. For this to work the diameter of the collimated laser beam would have to be reduced, so that the two central spots no longer overlap. The four reflected spots would then be imaged onto a camera, and the distance between them would be measured. As the plate thickness is already known, the distance between each spot in the image could be calibrated, thus allowing the plate separation to be determined. It was not possible to use this method for the ITO coated electrodes as the beams reflected from the front and back surfaces of a single plate were not parallel. This indicates that the plates are wedged, and means that the distances in the image cannot be calibrated.

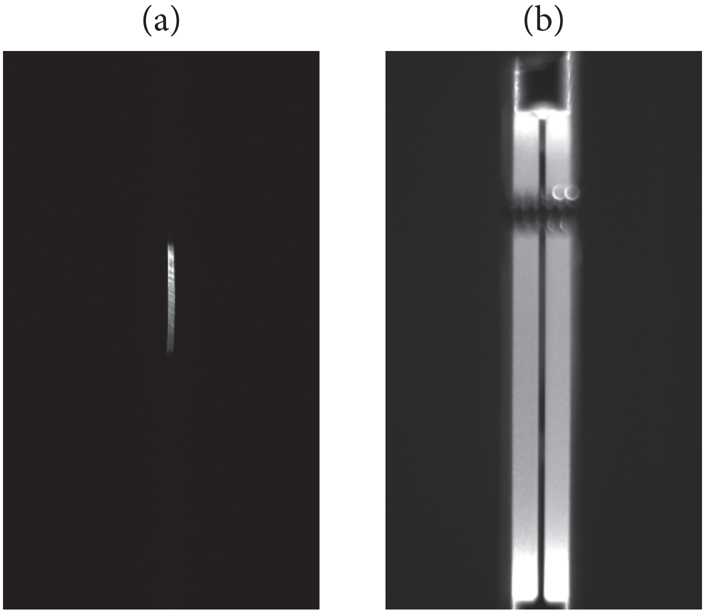

Figure 4.9: Photographs of the electrodes that were used to determine the separation of the plates. In (a) a collimated laser beam is directed between the electrodes onto the camera. In (b) a torch is used to illuminate the glass plates.

Therefore the plate separation was instead determined by taking an image of the electrode gap directly and comparing it to an image of a pair of vernier calipers set to a known distance. Figure 4.9 shows two images of the same electrode gap. In (a) a collimated laser beam is directed through the electrode gap and onto the camera, whilst in (b) a torch is positioned at the top of the image and is used to illuminate the glass plates. From these two images the plate separation was measured to be 0.62 ± 0.05 mm and 0.59 ± 0.05 mm respectively. The quoted errors represent the uncertainty in determining where the edge of the plate is, and so are relatively large. As a result the two values agree within errors, and produce a mean gap spacing of 0.605 mm.

4.3.2 High voltage setup

In order to test the ITO electrodes a separate vacuum chamber was constructed. This consisted of a $4\,1/2''$ four way cross with two DN40CF flanges welded at the junction. The electrode mount was inserted into the bottom flange of the four way cross, the high voltage probes were connected to the two horizontal flanges and a viewport was attached to the top flange. To allow images of the plates to be obtained during testing, an AVT Marlin F-033B CCD camera was positioned above the viewport. The smaller flanges were used to attach an additional viewport and a 65 litre/second turbo pump (Leybold TurboVac TW 70H). This was backed by a diaphragm pump (Leybold DiVac 2.5VT). To monitor the pressure, a Pirani gauge was used. Due to its low measurement range of 5×10^{-4} mbar to 1000 mbar, it was not possible to determine the exact pressure in the chamber, however it was expected to be somewhere in the region of 10^{-7} mbar.

In order to make electrical contact to the plates, a 30 kV feedthrough (Caburn FHV30-1S-C40) was pushed onto the back of each electrode. The two electrodes were each connected in series with an ammeter and a high voltage power supply. The ammeters are designed to measure currents in the nanoamp to microamp range, whilst floating at high voltage. The full details of the design can be found in [148]. The signals from the ammeters were recorded by a computer using a simple LabView program to allow real time current measurements for both electrodes to be made simultaneously. To supply the high voltage, two Spellman SL600 supplies were used. They have fixed and opposing polarities and can produce voltages of up to ±30 kV at a current of 20 mA. Given the 0.605 mm separation of the ITO electrodes, this enables us to produce a maximum electric field of 0.99 MV/cm.

4.3.3 Testing and results

During the electric field tests, voltage was applied symmetrically to the electrodes. This means that the voltage on one electrode was increased by a variable amount until current spikes were measured by the ammeters. At this point the voltage was held constant, allowing the current spikes to dissipate. Next the voltage of the second electrode was increased by the same amount. After another pause, the voltage of the first electrode was increased further. This process was repeated until a large, persistent current was measured, thus signifying breakdown of the electrodes. When this occurred the voltage was recorded, and the value of the electric field at breakdown was determined.

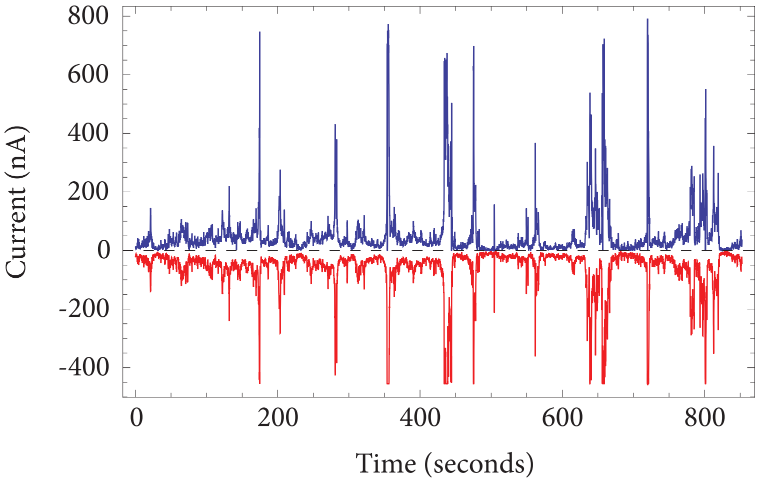

Figure 4.10: Example of the current spikes that were seen during the high voltage test. These data sets were obtained using stainless steel electrodes held at a voltage of ±2.5 kV, which equates to an electric field of 0.1 MV/cm. The blue and red lines represent the currents measured by the two ammeters.

Figure 4.10 shows an example of the current spikes that were seen during the experiment[1]. Here the blue and red lines represent the currents that were measured by the two ammeters. From this we can see that each discharge event creates a spike in the current of a few hundred nanoamps. Additionally as each current spike in the blue data is matched by a current spike of opposite sign in the red data, the current flow must be between the two electrodes, rather than to ground. It was found that after the voltage was increased the current spikes became more frequent. However if the applied voltage was low and was held constant, the spikes would eventually die away. This behaviour is typical of current conditioning, where the surface quality of the electrode improves due to the occurrence of micro-discharges. As higher voltages were reached this behaviour ceased. Instead the current spikes became more frequent and would not dissipate when a particular voltage was maintained.

---

[1] These data sets were actually taken using the stainless steel electrodes which are described in the following section, however the general behaviour of the ITO electrodes was the same.

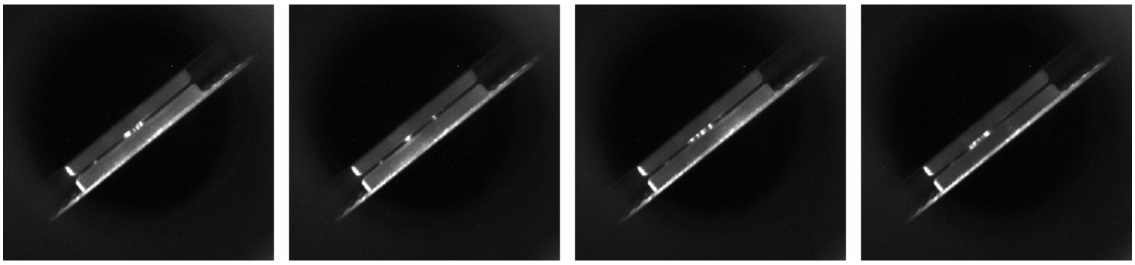

FIGURE 4.11: Photographs of sparks between the electrodes. The two diagonal rectangles are the 24 mm sides of the glass electrodes.

Images of the electrodes show that as the applied voltage increases, intermittent sparks begin to appear between the plates. In figure 4.11 a small selection of photographs show these sparking events. Here the electrodes are imaged through the top viewport of the vacuum chamber and are illuminated by a torch through the side viewport. The 24 mm sides of the glass electrodes appear in the images as two diagonal rectangles. From these photographs we can see that sparks often occur simultaneously at a variety of positions. However towards the end of testing, the sparks were mostly confined to the central region of the electrodes. At breakdown the two electrodes were held at ±6 kV. Given the measured gap spacing, this equates to an electric field of just under 0.2 MV/cm, which is well below our 1 MV/cm target.

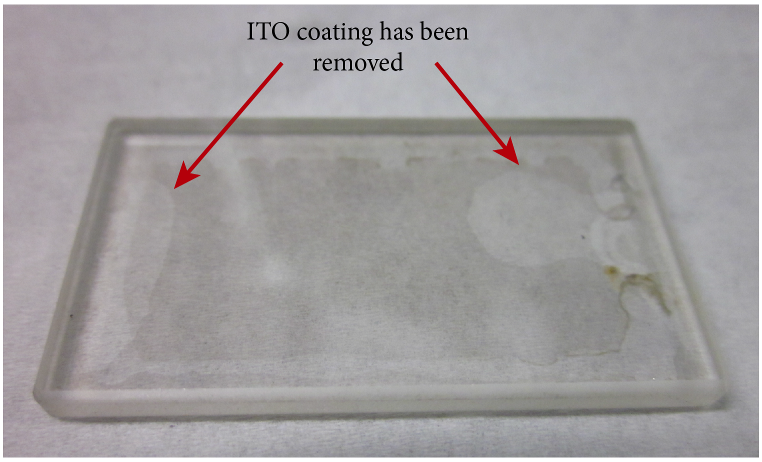

FIGURE 4.12: Photograph of one of the glass electrodes after testing. Two patches of the ITO coating have come away from the front surface of the plate.

In order to determine the cause of breakdown, the electrode surface was examined. Figure 4.12 shows a photograph of one of the plates after it was removed from the electrode mount. Just visible in the image is a border that runs around the entire electrode. Here some of the ITO coating has come away from the back of the plate. This damage was caused by removing the plate from the mount, thus indicating that the weakest point in the structure is between the ITO coating and the glass substrate. In addition to this there are two patches on the front of the electrode where the coating has been stripped away. These lie roughly in the centre of the plate, thus indicating that the sparks in figure 4.11 were caused by removal of the ITO coating.

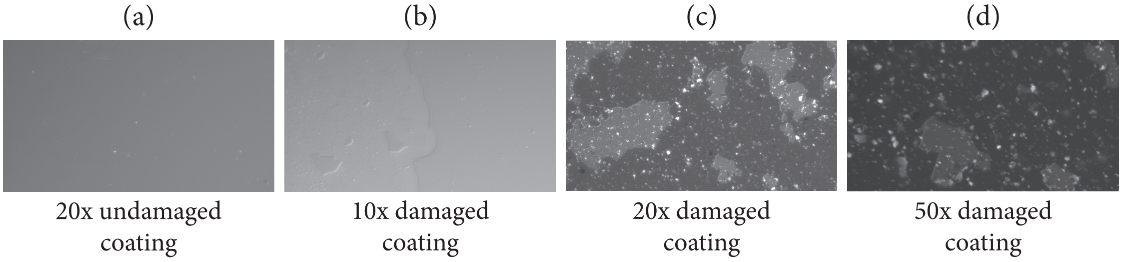

FIGURE 4.13: Images of the ITO coated glass electrodes after testing, obtained using an optical microscope. In (a) an undamaged region is shown at 20× magnification. In (b), (c) and (d) an area which has sustained damage is shown using 10×, 20× and 50× magnification respectively.

In figure 4.13 magnified images of the electrode surface are shown. These were obtained using an optical microscope. In (a) an undamaged section of the coating can be seen. This shows that even at 20× magnification the surface looks smooth and has few defects. In (b), (c) and (d) an area that has sustained damage is imaged using different levels of magnification. These images show that large sections of the coating have been ripped away from the glass surface. In addition to this the area is littered with debris from the damaged coating. This indicates that once part of the coating has been removed, the surface quality quickly deteriorates, ultimately leading to more damage in that particular region. Without knowing what the surface quality was like before testing it is not possible to determine what causes the initial removal of the ITO. However it is most likely produced by small imperfections in the coating, or by pieces of dirt that are trapped beneath the coating being ripped out by the force of the electric field.

These results show that ITO coated glass electrodes, set up in this particular geometry, are not capable of producing the large electric fields that we require. Therefore we decided to replace them with metal electrodes, as it should be possible to reach much higher fields. Of course, the main disadvantage of this is that interferometric techniques can no longer be used to determine the angle between the plates. Therefore a different method of alignment is needed. However before tackling this problem it is important to verify that metal electrodes can indeed produce the large electric fields that we require.

4.4 Stainless steel electrodes

In order to produce the highest electric field possible, it is important to make sure that the electrode surface is very smooth. Rather than try to manufacture this ourselves, we instead bought super-polished pure metal mirrors from Valley Design. One of these is shown in figure 4.14. These circular stainless steel mirrors have a diameter of 25.4 mm, a thickness of 6.35 mm and a mean surface roughness, R_a, approaching 0.5 nm. Valley Design also produce super-polished mirrors made from other metals, such as molybdenum and copper. This is useful because it allows the performance of other electrode materials to be investigated in the future.

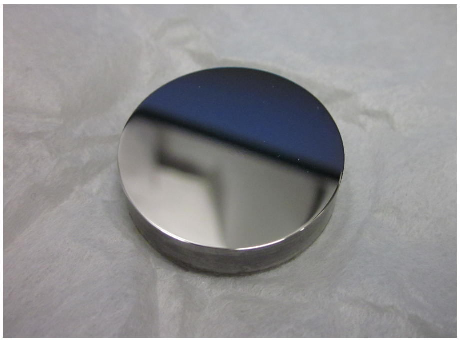

FIGURE 4.14: Photograph of a super-polished stainless steel electrode.

Instead of making a new mount, recesses were cut into the existing ITO mounts in order to accommodate the stainless steel electrodes. The plates were then glued into position and a feeler gauge was used to set the gap spacing at 0.5 mm. The electrodes were placed inside the high voltage test chamber, and using the same method as before, the breakdown voltage was determined. In this case breakdown occurred when the two electrodes were held at ±9.5 kV. This equates to an electric field of 0.38 MV/cm, which is almost twice as high as the field produced by the ITO electrodes. Although this is still relatively low compared to our ultimate target, it is approaching the 0.54 MV/cm field value at which a shape resonance is predicted for lithium [69].

Figure 4.15 shows a photograph of an electrode after testing. Here we can see that the surface is covered in a large number of fine scratches. These were most likely caused by the plates coming into contact with the feeler gauge that was used during the alignment procedure. Due to the extent of the damage we expect the performance of the plates to have been affected. Therefore with more careful treatment of the electrode surface, it should be possible to reach even higher field strengths.

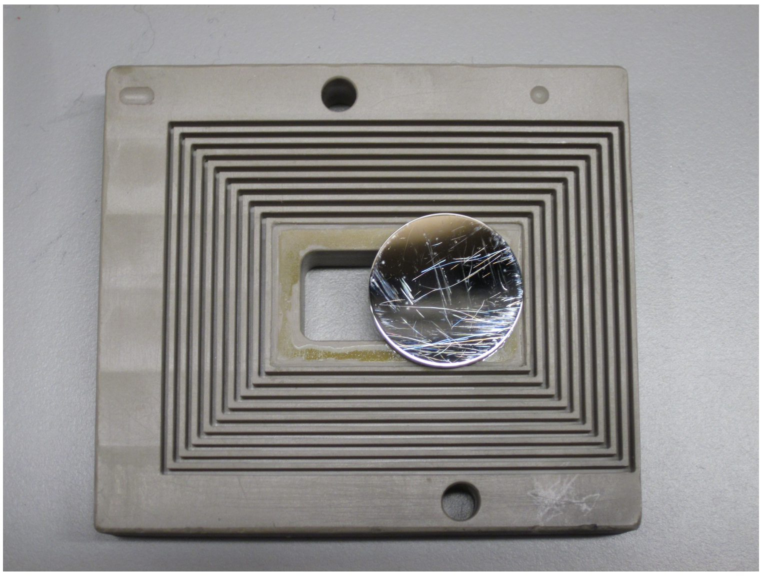

FIGURE 4.15: Photograph of a stainless steel electrode in the PEEK electrode mount, after high voltage testing has been carried out. A large number of fine scratches can be seen on the surface of the electrode.

4.5 Outlook

In order to accommodate the stainless steel plates, the electrode mount has recently been redesigned by Devin Dunseith. Overall, the design is essentially the same as that used for the ITO electrodes, as it utilises three screws to vary the angle between the plates. However a number of important changes have been made so that the stainless steel electrodes can be aligned without relying on interferometric techniques. The first major change is that the new mount will be made from Macor, which is a machineable glass ceramic. By using Macor it is possible to make the inner surface of each mount parallel to within at least 25 μm. Therefore by ensuring that the distance between the mounts is constant everywhere, they can be positioned roughly parallel to each other. This means that the electrodes will also be approximately parallel, provided the plates lie flat against the mount after being glued into position. As this alignment technique does not require direct contact with the surface of the electrode, damage should be prevented, thus allowing higher electric fields to be produced.

It is clear that by using this method of alignment, the angle between the electrodes will almost certainly be larger than 0.1 mrad. As we require the angle to be well below 0.1 mrad, two piezo actuators have been incorporated into the design of the electrode mount. This means that once the plates are under vacuum, the atoms can be used to determine whether the electrodes are parallel, and adjustments to the angle can be made accordingly. The low voltage piezo actuators (Piezomechanik FPSt 150/5/20) consist of a piezo stack mounted within a metal casing. They have a length of 20 mm, a maximum stroke of 27 μm, and a casing that is threaded on the outside. This means that we can replace two of the three adjustment screws with these piezo actuators. Coarse alignment of the plates is then achieved by rotating the actuator, whilst fine adjustments of the tilt can be made by applying voltage to the piezo stack. It is worth noting that since optical access to the electrode is no longer required, the mounts do not have a large hole in the centre. As a result the steel electrodes will be fully supported over their entire area.

By making these modifications to the design of the electrode mount, it should be possible to study the atoms under high electric fields in the near future. Once the electrodes have been installed into the science chamber, and atoms have been successfully positioned between the electrodes, initial measurements will involve recording the line shape as the applied electric field is varied. In accordance with the results of [149], the position of the $F = 2$ to $F' = 3$ resonance should shift to higher frequencies. By modelling the expected line shape, using a method similar to that described in section 3.2.4, it should be possible to verify the size of the applied electric field. Provided the electrodes are able to produce the high fields that are required, the presence of the predicted shape resonance can then be investigated, and eventually an ultracold dipolar gas can be created.

4.6 Chapter summary

As one of our experimental aims is to study lithium atoms under electric fields of up to 1 MV/cm, we have developed a setup that should be capable of producing fields that approach this value. Calculations have shown that when the maximum field is applied, the electrodes will experience a 45 N force. In addition to this, if a sufficient magnetic field gradient is to be maintained, the angle between the electrodes must be well below 0.1 mrad. In response to these design constraints we have developed an electrode mount that allows the angle between the plates to be varied. By choosing to use ITO coated glass electrodes we were able to employ interferometric techniques to measure the angle between the plates. This angle was found to be 0.13 mrad. To avoid damage of the electrode surface, optical methods were used to measure the gap spacing, which was found to be 0.605 mm. From high voltage tests the breakdown field of these electrodes was measured to be just under 0.2 MV/cm. By visually inspecting the electrode surface after testing it was found that large areas of the thin film coating had been removed, thus indicating that these electrodes cannot be used to produce the large electric fields that we ultimately require.

As a result, these plates were replaced with super-polished stainless steel electrodes. The performance of these electrodes was substantially better as the breakdown field was found to be 0.38 MV/cm. After testing we discovered that the electrode surface was covered in a number of fine scratches. These are thought to have been caused by contact with the feeler gauge that was used during the alignment procedure. As this is likely to have marred the performance of the electrodes, it is thought higher electric fields can be generated with more careful treatment of the electrode surface. The main disadvantage of these metal electrodes is that interferometric techniques can no longer be used to measure the angle between the plates. Therefore a different method of alignment is required. In response to this, the electrode mount has recently been redesigned to incorporate piezo actuators. This will allow the tilt of the electrodes to be adjusted whilst under vacuum, thus enabling us to use the atoms to determine the parallelism of the plates. Currently this new electrode mount is being built. Once constructed and tested it will be placed inside the science chamber, allowing us to investigate atoms under high electric fields in the near future.

Chapter 5

Conclusions

This chapter summarises the work described in this thesis, and outlines the steps that must be taken in the future if an ultracold dipolar gas is to be realised.

5.1 Summary

The aim of our experiment is to create an ultracold dipolar gas. To achieve this, we plan to use two distinct methods. Either we sympathetically cool polar molecules using lithium atoms as a refrigerant, or we electrically polarise the atoms by using a large electric field, thus inducing dipolar interactions. In both cases a source of ultracold lithium is required. This thesis has described the work that has been carried out to cool, trap and transport such a cloud. It also details the setup that has been developed in order to generate the large electric fields that are required to electrically polarise the atoms.

In order to form an ultracold cloud of atoms, first lithium is heated in an oven to a temperature of approximately 790 K. The atoms leave the oven through a small aperture, thus creating an effusive beam. Next they are decelerated to a velocity of approximately 50 m/s by using a decreasing field Zeeman slower and are subsequently loaded into a MOT. By optimising the oven temperature, magnetic field gradient, MOT beam powers and detunings, we were able to trap up to 2.3×10^8 atoms with an initial temperature of $\sim 1.3\,\mathrm{mK}$ and a density of approximately 9×10^9 atoms/cm^3. To further cool and compress the cloud, we have implemented a compressed MOT (CMOT) phase. By varying the magnetic field gradient, the laser beam powers and detunings during the CMOT phase, we were able to reduce the temperature of the cloud to $\sim 0.75\,\mathrm{mK}$.

As both the sympathetic cooling, and high electric field experiments will be carried out in the science chamber, the atoms must be transported to this chamber. Before this can be done, the atoms need to be transferred from the MOT to the magnetic trap. By using internally water cooled trapping coils we are able to form both the MOT and magnetic trap using the same coil pair. As high field gradients led to a loss of atoms during the CMOT phase, the magnetic trap has an axial field gradient of $60\,\mathrm{G/cm}$. It is worth noting that this is well below the maximum steady state field gradient of $137\,\mathrm{G/cm}$ that our system is capable of producing. By ramping down the MOT beam intensity and then switching the beams off, we are able to transfer approximately 23% of the MOT atoms into the magnetic trap. The lifetime of the trap was found to be $\tau_{\mathrm{MC}} = 1.53 \pm 0.01\,\mathrm{s}$ in the MOT chamber.

After the atoms have been transported, it is important that we are able to reliably image them. Therefore images of the cloud were taken after release from the magnetic trap. These highlighted the fact that atoms were disappearing from the images. In order to determine the source of this problem, line shape measurements were carried out at a variety of times after release from the MOT and CMOT. These results were compared to the predicted line shape, and from this we concluded that a time and position dependent magnetic field was present. This was attributed to eddy currents that persist in the chamber after the coils have been switched off. As it was not possible to remove this magnetic field, the transport procedure was tested by returning atoms to the MOT chamber and imaging them in the recaptured MOT.

In order to transport the magnetically trapped atoms, the trapping coils are physically moved from the MOT chamber to the science chamber by using a motorised translation stage. Preliminary tests of the transport procedure indicated that a large fraction of atoms were lost at the entrance of the connecting tube. To minimise this loss, the cloud position was optimised. This resulted in a final transport efficiency of $\eta = 41\%$. Having successfully demonstrated transport, we were able to measure the magnetic trap lifetime in the science chamber. Due to the low background gas pressure in this chamber, the lifetime was found to be $\tau_{\mathrm{SC}} = 18.5 \pm 0.7\,\mathrm{s}$. In the future this will be particularly useful for sympathetic cooling experiments, as the atoms and molecules will have more time to reach thermal equilibrium. Given our current transport efficiency, we expect approximately 7% of the MOT atoms, that is around 1.7×10^7 atoms, to be successfully transported to the science chamber. This should allow us to directly image the cloud in the science chamber, provided a suitable imaging system has been installed. As measurements indicate that atoms are still lost as they enter the connecting tube, the transport efficiency could be further improved by reducing the size of the cloud through an additional cooling stage, such as evaporative cooling.

To electrically polarise the lithium atoms, electric fields of up to 1 MV/cm are required. Generating such a large field is generally quite challenging. However, we have developed a setup that should be capable of producing fields that approach this value. Calculations have shown that if a 1 MV/cm electric field is generated, the electrodes will have to withstand a 45 N force. Additionally, if a trapping potential is to be maintained, the angle between the plates must be smaller than 0.1 mrad. In response to these design constraints we have developed an electrode mount that allows the tilt of the plates to be adjusted. By using ITO coated glass electrodes, we were able to utilise interferometric techniques to determine the angle between the plates. This angle was found to be 0.13 mrad. As contact with the delicate electrode surface can lead to damage, which tends to reduce the voltage at breakdown, optical methods were used to measure the separation of the electrodes. This produced a value of 0.605 mm for the gap spacing. High voltage tests were then performed, and the breakdown field was found to be just under 0.2 MV/cm. A visual inspection of the plates after testing uncovered the fact that large portions of the ITO coating had been removed. The initial removal of the ITO is likely to be caused by small imperfections in the coating, or by dirt trapped underneath the coating that is subsequently ripped out by the force of the electric field. As a result it is difficult to prevent damage from occurring. Therefore we conclude that ITO coated glass electrodes, in this particular geometry, are not capable of producing the large electric fields that we ultimately require.

In light of this, these plates were replaced with super-polished stainless steel electrodes. These performed much better under high voltage tests, producing a breakdown field of 0.38 MV/cm. However after testing it was found that the electrode surface had again suffered damage. This time a number of fine scratches were visible. These were most likely created by the plates coming into contact with a feeler gauge that was used during alignment. As this is likely to have had an adverse effect on the performance of the plates, with more careful treatment of the electrode surface, it should be possible to reach higher electric fields. In order to align these metal electrodes, interferometric techniques can no longer be employed. As a result the electrode mount has recently been redesigned to incorporate piezo actuators. This will allow the angle between the plates to be adjusted whilst under vacuum, thus enabling us to use the atoms themselves to measure the parallelism of the electrodes. With this improved mount design, and by using superpolished stainless steel electrodes, it should be possible to reach the high fields necessary to electrically polarise the lithium atoms.

Several aspects of the work detailed in this thesis are novel. The first of these is the design of the apparatus itself. As the atoms must eventually be transported into a microwave trap, a number of design constraints are imposed. By specifically constructing apparatus that meets these constraints, we have produced a novel experimental setup. Additionally this thesis describes the first demonstration of atomic transportation of lithium-7 using a motorised translation stage. The detailed modelling of the effect of magnetic fields on atomic spectra is also novel and by utilising this we have been able to use measured spectra to give information about how stray magnetic fields are changing in time. Lastly the comparison of the high field capabilities of ITO coated glass plates and stainless steel electrodes is also novel, as is the mounting arrangement of the plates themselves.

5.2 Outlook

The next steps that must be taken in order to create an ultracold dipolar gas are reasonably well defined. As atomic transport has been successfully demonstrated, it should now be possible to image the cloud in the science chamber. To obtain good quality photographs, an imaging system as described in section 2.4.2 must be installed. Once this is in place, further optimisation of the transport procedure will be straightforward, as the transport efficiency can be measured directly. One way in which the transport efficiency could be improved is by using evaporative cooling to decrease the size of the cloud, thereby reducing atom loss at the entrance of the connecting tube. Additionally some improvement might also be achieved through more careful adjustment of the horizontal cloud position. Another way in which more atoms could be transported to the science chamber is by optically pumping the MOT atoms into the $F = 2$, $M_F = 2$ state. This will increase the fraction of atoms that are successfully loaded into the magnetic trap, and will result in a larger sample of atoms in the science chamber, even if the transport efficiency remains the same. Also the lithium oven has recently been replaced and we expect this to give much larger atom numbers in the MOT.

Once the new electrode mount has been built, the super-polished stainless steel electrodes will be glued into position, roughly aligned and then placed inside the science chamber. In order to do this, as there is only one gate valve which separates the lithium oven from the rest of the setup, the majority of the vacuum system will have to be let up to atmosphere. Therefore, at this point, it will be incredibly useful to directly measure the magnetic field produced at the atom cloud position after the trapping coils switch off. This will enable us to verify the conclusions presented in section 3.2 and will perhaps allow a magnetic field cancellation system to be installed. By repeating this measurement at a number of different positions, it will be possible to map out the magnetic field profile along the entire transport path. This information will be particularly useful when the cloud is eventually imaged in the science chamber.

With the electrodes positioned inside the science chamber, high field testing can begin. First the atoms will be positioned between the electrodes, thus allowing the parallelism of the plates to be determined. In particular the atoms will be attracted to regions of high electric field. Therefore by monitoring the position of the atom cloud, it will be possible to reduce the angle between the plates, eventually making them completely parallel. After the electrodes have been aligned, line shape measurements will be taken for increasing electric field. By modelling the line shape and comparing it to these measurements, it should be possible to verify the size of the applied field. Once this has been completed, the presence of the shape resonance predicted at 0.54 MV/cm for lithium atoms in the $F = 2$, $M_F = 2$ state can be investigated. If higher fields can be reached, an electrically polarised gas can be generated, and dipolar interactions will become increasingly apparent. This dipolar gas can then be used to explore many interesting phenomena, such as quantum phase transitions.

In order to sympathetically cool polar molecules, in addition to ultracold atoms, a molecular source and molecular trap are also needed. To date, much progress has been made towards fulfilling these requirements. For example, molecular sources of both SrF and CaF have already been developed in our laboratory and direct laser cooling has been demonstrated for both these species. In addition to this, a UHV compatible version of the microwave trap is currently under construction. Once built, it will be placed into the science chamber where preliminary tests will involve trapping lithium atoms. Provided these tests are successful, the molecular source will then be combined with the atomic setup, thus making it possible to investigate sympathetic cooling of either SrF or CaF molecules, using lithium atoms as a refrigerant.

Bibliography

[1] M. H. Anderson, J. R. Ensher, M. R. Matthews, C. E. Wieman, and E. A. Cornell. Observation of Bose-Einstein Condensation in a Dilute Atomic Vapor. *Science*, 269(5221):198–201, 1995. URL `http://www.sciencemag.org/content/269/5221/198.abstract`.

[2] C. C. Bradley, C. A. Sackett, J. J. Tollett, and R. G. Hulet. Evidence of Bose-Einstein Condensation in an Atomic Gas with Attractive Interactions. *Phys. Rev. Lett.*, 75:1687–1690, 1995. URL `http://link.aps.org/doi/10.1103/PhysRevLett.75.1687`.

[3] K. B. Davis, M.-O. Mewes, M. R. Andrews, N. J. van Druten, D. S. Durfee, D. M. Kurn, and W. Ketterle. Bose-Einstein Condensation in a Gas of Sodium Atoms. *Phys. Rev. Lett.*, 75:3969–3973, 1995. URL `http://link.aps.org/doi/10.1103/PhysRevLett.75.3969`.

[4] C. C. Bradley, C. A. Sackett, and R. G. Hulet. Bose-Einstein Condensation of Lithium: Observation of Limited Condensate Number. *Phys. Rev. Lett.*, 78:985–989, 1997. URL `http://link.aps.org/doi/10.1103/PhysRevLett.78.985`.

[5] J. M. Gerton, D. Strekalov, I. Prodan, and R. G. Hulet. Direct observation of growth and collapse of a Bose-Einstein condensate with attractive interactions. *Nature*, 408:692–695, 2000. URL `http://www.nature.com/nature/journal/v408/n6813/abs/408692a0.html`.

[6] E. A. Donley, N. R. Claussen, S. L. Cornish, J. L. Roberts, E. A. Cornell, and C. E. Wieman. Dynamics of collapsing and exploding Bose-Einstein condensates. *Nature*, 412:295–299, 2001. URL `http://www.nature.com/nature/journal/v412/n6844/abs/412295a0.html`.

[7] T. Lahaye, C. Menotti, L. Santos, M. Lewenstein, and T. Pfau. The physics of dipolar bosonic quantum gases. *Rep. Prog. Phys.*, 72(12):126401, 2009. URL `http://stacks.iop.org/0034-4885/72/i=12/a=126401`.

[8] K. Glaum, A. Pelster, H. Kleinert, and T. Pfau. Critical Temperature of Weakly Interacting Dipolar Condensates. *Phys. Rev. Lett.*, 98:080407, 2007. URL `http://link.aps.org/doi/10.1103/PhysRevLett.98.080407`.

[9] K. Glaum and A. Pelster. Bose-Einstein condensation temperature of dipolar gas in anisotropic harmonic trap. *Phys. Rev. A*, 76:023604, 2007. URL `http://link.aps.org/doi/10.1103/PhysRevA.76.023604`.

[10] M. A. Baranov. Theoretical progress in many-body physics with ultracold dipolar gases. *Phys. Rep.*, 464(3):71 – 111, 2008. URL `http://www.sciencedirect.com/science/article/pii/S0370157308001385`.

[11] L. Santos, G. V. Shlyapnikov, P. Zoller, and M. Lewenstein. Bose-Einstein Condensation in Trapped Dipolar Gases. *Phys. Rev. Lett.*, 85:1791–1794, 2000. URL `http://link.aps.org/doi/10.1103/PhysRevLett.85.1791`.

[12] L. Santos, G. V. Shlyapnikov, P. Zoller, and M. Lewenstein. Erratum: Bose-Einstein Condensation in Trapped Dipolar Gases [Phys. Rev. Lett. 85, 1791 (2000)]. *Phys. Rev. Lett.*, 88:139904, 2002. URL `http://link.aps.org/doi/10.1103/PhysRevLett.88.139904`.

[13] S. Giovanazzi, A. Görlitz, and T. Pfau. Tuning the Dipolar Interaction in Quantum Gases. *Phys. Rev. Lett.*, 89:130401, 2002. URL `http://link.aps.org/doi/10.1103/PhysRevLett.89.130401`.

[14] M. Greiner, O. Mandel, T. Esslinger, T. W. Hänsch, and I. Bloch. Quantum phase transition from a superfluid to a Mott insulator in a gas of ultracold atoms. *Nature*, 415:39–44, 2002. URL `http://www.nature.com/nature/journal/v415/n6867/abs/415039a.html`.

[15] K. Góral, L. Santos, and M. Lewenstein. Quantum Phases of Dipolar Bosons in Optical Lattices. *Phys. Rev. Lett.*, 88:170406, 2002. URL `http://link.aps.org/doi/10.1103/PhysRevLett.88.170406`.

[16] L. D. Carr, D. DeMille, R. V. Krems, and J. Ye. Cold and ultracold molecules: science, technology and applications. *New J. Phys.*, 11(5):055049, 2009. URL `http://stacks.iop.org/1367-2630/11/i=5/a=055049`.

[17] D. Hanneke, S. Fogwell, and G. Gabrielse. New Measurement of the Electron Magnetic Moment and the Fine Structure Constant. *Phys. Rev. Lett.*, 100:120801, 2008. URL `http://link.aps.org/doi/10.1103/PhysRevLett.100.120801`.

[18] J. J. Hudson, D. M. Kara, I. J. Smallman, B. E. Sauer, M. R. Tarbutt, and E. A. Hinds. Improved measurement of the shape of the electron. *Nature*, 473:493–496, 2011. URL `http://www.nature.com/nature/journal/v473/n7348/full/nature10104.html`.

[19] M. R. Tarbutt, B. E. Sauer, J. J. Hudson, and E. A. Hinds. Design for a fountain of YbF molecules to measure the electron's electric dipole moment. *New J. Phys.*, 15(5):053034, 2013. URL `http://stacks.iop.org/1367-2630/15/i=5/a=053034`.

[20] The ACME Collaboration, J. Baron, W. C. Campbell, D. DeMille, J. M. Doyle, G. Gabrielse, Y. V. Gurevich, P. W. Hess, N. R. Hutzler, E. Kirilov, I. Kozyryev, B. R. O'Leary, C. D. Panda, M. F. Parsons, E. S. Petrik, B. Spaun, A. C. Vutha, and A. D. West. Order of Magnitude Smaller Limit on the Electric Dipole Moment of the Electron. *Science*, 343(6168):269–272, 2014. URL `http://www.sciencemag.org/content/343/6168/269.abstract`.

[21] S. Truppe, R. J. Hendricks, S. K. Tokunaga, H. J. Lewandowski, M. G. Kozlov, C. Henkel, E. A. Hinds, and M. R. Tarbutt. A search for varying fundamental constants using hertz-level frequency measurements of cold CH molecules. *Nat. Commun.*, 4:2600, 2013. URL `http://www.nature.com/ncomms/2013/131015/ncomms3600/full/ncomms3600.html`.

[22] T. Rosenband, D. B. Hume, P. O. Schmidt, C. W. Chou, A. Brusch, L. Lorini, W. H. Oskay, R. E. Drullinger, T. M. Fortier, J. E. Stalnaker, S. A. Diddams, W. C. Swann, N. R. Newbury, W. M. Itano, D. J. Wineland, and J. C. Bergquist. Frequency Ratio of Al^+ and Hg^+ Single-Ion Optical Clocks; Metrology at the 17th Decimal Place. *Science*, 319(5871):1808–1812, 2008. URL `http://www.sciencemag.org/content/319/5871/1808.abstract`.

[23] S. Blatt, A. D. Ludlow, G. K. Campbell, J. W. Thomsen, T. Zelevinsky, M. M. Boyd, J. Ye, X. Baillard, M. Fouché, R. Le Targat, A. Brusch, P. Lemonde, M. Takamoto, F.-L. Hong, H. Katori, and V. V. Flambaum. New Limits on Coupling of Fundamental Constants to Gravity Using ^{87}Sr Optical Lattice Clocks. *Phys. Rev. Lett.*, 100:140801, 2008. URL `http://link.aps.org/doi/10.1103/PhysRevLett.100.140801`.

[24] J. M. Hutson and P. Soldán. Molecular collisions in ultracold atomic gases. *Int. Rev. Phys. Chem.*, 26(1):1–28, 2007. URL `http://dx.doi.org/10.1080/01442350601084562`.

[25] R. V. Krems. Cold controlled chemistry. *Phys. Chem. Chem. Phys.*, 10:4079–4092, 2008. URL `http://dx.doi.org/10.1039/B802322K`.

[26] D. DeMille. Quantum Computation with Trapped Polar Molecules. *Phys. Rev. Lett.*, 88:067901, 2002. URL `http://link.aps.org/doi/10.1103/PhysRevLett.88.067901`.

[27] A. André, D. DeMille, J. M. Doyle, M. D. Lukin, S. E. Maxwell, P. Rabl, R. J. Schoelkopf, and P. Zoller. A coherent all-electrical interface between polar molecules and mesoscopic superconducting resonators. *Nature Physics*, 2:636–642, 2006. URL `http://www.nature.com/nphys/journal/v2/n9/full/nphys386.html`.

[28] A. Griesmaier, J. Werner, S. Hensler, J. Stuhler, and T. Pfau. Bose-Einstein Condensation of Chromium. *Phys. Rev. Lett.*, 94:160401, 2005. URL `http://link.aps.org/doi/10.1103/PhysRevLett.94.160401`.

[29] J. Stuhler, A. Griesmaier, T. Koch, M. Fattori, T. Pfau, S. Giovanazzi, P. Pedri, and L. Santos. Observation of Dipole-Dipole Interaction in a Degenerate Quantum Gas. *Phys. Rev. Lett.*, 95:150406, 2005. URL `http://link.aps.org/doi/10.1103/PhysRevLett.95.150406`.

[30] J. Metz, T. Lahaye, B. Fröhlich, A. Griesmaier, T. Pfau, H. Saito, Y. Kawaguchi, and M. Ueda. Coherent collapses of dipolar Bose-Einstein condensates for different trap geometries. *New J. Phys.*, 11(5):055032, 2009. URL `http://stacks.iop.org/1367-2630/11/i=5/a=055032`.

[31] S. Müller, J. Billy, E. A. L. Henn, H. Kadau, A. Griesmaier, M. Jona-Lasinio, L. Santos, and T. Pfau. Stability of a dipolar Bose-Einstein condensate in a one-dimensional lattice. *Phys. Rev. A*, 84:053601, 2011. URL `http://link.aps.org/doi/10.1103/PhysRevA.84.053601`.

[32] K. Aikawa, A. Frisch, M. Mark, S. Baier, A. Rietzler, R. Grimm, and F. Ferlaino. Bose-Einstein Condensation of Erbium. *Phys. Rev. Lett.*, 108:210401, 2012. URL `http://link.aps.org/doi/10.1103/PhysRevLett.108.210401`.

[33] M. Lu, N. Q. Burdick, S. H. Youn, and B. L. Lev. Strongly Dipolar Bose-Einstein Condensate of Dysprosium. *Phys. Rev. Lett.*, 107:190401, 2011. URL `http://link.aps.org/doi/10.1103/PhysRevLett.107.190401`.

[34] J. R. Bochinski, E. R. Hudson, H. J. Lewandowski, G. Meijer, and J. Ye. Phase Space Manipulation of Cold Free Radical OH Molecules. *Phys. Rev. Lett.*, 91:243001, 2003. URL `http://link.aps.org/doi/10.1103/PhysRevLett.91.243001`.

[35] H. L. Bethlem, F. M. H. Crompvoets, R. T. Jongma, S. Y. T. van de Meerakker, and G. Meijer. Deceleration and trapping of ammonia using time-varying electric fields. *Phys. Rev. A*, 65:053416, 2002. URL `http://link.aps.org/doi/10.1103/PhysRevA.65.053416`.

[36] S. K. Tokunaga, J. M. Dyne, E. A. Hinds, and M. R. Tarbutt. Stark deceleration of lithium hydride molecules. *New J. Phys.*, 11(5):055038, 2009. URL `http://stacks.iop.org/1367-2630/11/i=5/a=055038`.

[37] E. Narevicius, A. Libson, C. G. Parthey, I. Chavez, J. Narevicius, U. Even, and M. G. Raizen. Stopping supersonic oxygen with a series of pulsed electromagnetic coils: A molecular coilgun. *Phys. Rev. A*, 77:051401, 2008. URL `http://link.aps.org/doi/10.1103/PhysRevA.77.051401`.

[38] S. Y. T. van de Meerakker, P. H. M. Smeets, N. Vanhaecke, R. T. Jongma, and G. Meijer. Deceleration and Electrostatic Trapping of OH Radicals. *Phys. Rev. Lett.*, 94:023004, 2005. URL `http://link.aps.org/doi/10.1103/PhysRevLett.94.023004`.

[39] J. van Veldhoven, H. L. Bethlem, and G. Meijer. ac Electric Trap for Ground-State Molecules. *Phys. Rev. Lett.*, 94:083001, 2005. URL `http://link.aps.org/doi/10.1103/PhysRevLett.94.083001`.

[40] J. D. Weinstein, R. deCarvalho, T. Guillet, B. Friedrich, and J. M. Doyle. Magnetic trapping of calcium monohydride molecules at millikelvin temperatures. *Nature*, 395:148–150, 1998. URL `http://www.nature.com/nature/journal/v395/n6698/abs/395148a0.html`.

[41] S. M. Skoff, R. J. Hendricks, C. D. J. Sinclair, J. J. Hudson, D. M. Segal, B. E. Sauer, E. A. Hinds, and M. R. Tarbutt. Diffusion, thermalization, and optical pumping of YbF molecules in a cold buffer-gas cell. *Phys. Rev. A*, 83:023418, 2011. URL `http://link.aps.org/doi/10.1103/PhysRevA.83.023418`.

[42] C. J. Myatt, E. A. Burt, R. W. Ghrist, E. A. Cornell, and C. E. Wieman. Production of Two Overlapping Bose-Einstein Condensates by Sympathetic Cooling. *Phys. Rev. Lett.*, 78:586–589, 1997. URL `http://link.aps.org/doi/10.1103/PhysRevLett.78.586`.

[43] A. G. Truscott, K. E. Strecker, W. I. McAlexander, G. B. Partridge, and R. G. Hulet. Observation of Fermi Pressure in a Gas of Trapped Atoms. *Science*, 291 (5513):2570–2572, 2001. URL `http://www.sciencemag.org/content/291/5513/2570.abstract`.

[44] G. Modugno, G. Ferrari, G. Roati, R. J. Brecha, A. Simoni, and M. Inguscio. Bose-Einstein Condensation of Potassium Atoms by Sympathetic Cooling. *Science*, 294 (5545):1320–1322, 2001. URL `http://www.sciencemag.org/content/294/5545/1320.abstract`.

[45] D. J. Larson, J. C. Bergquist, J. J. Bollinger, W. M. Itano, and D. J. Wineland. Sympathetic cooling of trapped ions: A laser-cooled two-species nonneutral ion plasma. *Phys. Rev. Lett.*, 57:70–73, 1986. URL `http://link.aps.org/doi/10.1103/PhysRevLett.57.70`.

[46] M. Drewsen, A. Mortensen, R. Martinussen, P. Staanum, and J. L. Sørensen. Nondestructive Identification of Cold and Extremely Localized Single Molecular Ions. *Phys. Rev. Lett.*, 93:243201, 2004. URL `http://link.aps.org/doi/10.1103/PhysRevLett.93.243201`.

[47] M. D. Di Rosa. Laser-cooling molecules. *Eur. Phys. J. D*, 31(2):395–402, 2004. URL `http://dx.doi.org/10.1140/epjd/e2004-00167-2`.

[48] E. S. Shuman, J. F. Barry, and D. DeMille. Laser cooling of a diatomic molecule. *Nature*, 467:820–823, 2010. URL `http://www.nature.com/nature/journal/v467/n7317/full/nature09443.html`.

[49] V. Zhelyazkova, A. Cournol, T. E. Wall, A. Matsushima, J. J. Hudson, E. A. Hinds, M. R. Tarbutt, and B. E. Sauer. Laser cooling and slowing of CaF molecules. *Phys. Rev. A*, 89:053416, 2014. URL `http://link.aps.org/doi/10.1103/PhysRevA.89.053416`.

[50] M. T. Hummon, M. Yeo, B. K. Stuhl, A. L. Collopy, Y. Xia, and J. Ye. 2D Magneto-Optical Trapping of Diatomic Molecules. *Phys. Rev. Lett.*, 110:143001, 2013. URL `http://link.aps.org/doi/10.1103/PhysRevLett.110.143001`.

[51] K. M. Jones, E. Tiesinga, P. D. Lett, and P. S. Julienne. Ultracold photoassociation spectroscopy: Long-range molecules and atomic scattering. *Rev. Mod. Phys.*, 78:483–535, 2006. URL `http://link.aps.org/doi/10.1103/RevModPhys.78.483`.

[52] C. Chin, R. Grimm, P. Julienne, and E. Tiesinga. Feshbach resonances in ultracold gases. *Rev. Mod. Phys.*, 82:1225–1286, 2010. URL `http://link.aps.org/doi/10.1103/RevModPhys.82.1225`.

[53] K. Bergmann, H. Theuer, and B. W. Shore. Coherent population transfer among quantum states of atoms and molecules. *Rev. Mod. Phys.*, 70:1003–1025, 1998. URL `http://link.aps.org/doi/10.1103/RevModPhys.70.1003`.

[54] K.-K. Ni, S. Ospelkaus, M. H. G. de Miranda, A. Pe'er, B. Neyenhuis, J. J. Zirbel, S. Kotochigova, P. S. Julienne, D. S. Jin, and J. Ye. A High Phase-Space-Density Gas of Polar Molecules. *Science*, 322(5899):231–235, 2008. URL `http://www.sciencemag.org/content/322/5899/231.abstract`.

[55] K. Aikawa, D. Akamatsu, M. Hayashi, K. Oasa, J. Kobayashi, P. Naidon, T. Kishimoto, M. Ueda, and S. Inouye. Coherent Transfer of Photoassociated Molecules into the Rovibrational Ground State. *Phys. Rev. Lett.*, 105:203001, 2010. URL `http://link.aps.org/doi/10.1103/PhysRevLett.105.203001`.

[56] F. Lang, K. Winkler, C. Strauss, R. Grimm, and J. Hecker Denschlag. Ultracold Triplet Molecules in the Rovibrational Ground State. *Phys. Rev. Lett.*, 101:133005, 2008. URL `http://link.aps.org/doi/10.1103/PhysRevLett.101.133005`.

[57] K. Honda, Y. Takahashi, T. Kuwamoto, M. Fujimoto, K. Toyoda, K. Ishikawa, and T. Yabuzaki. Magneto-optical trapping of Yb atoms and a limit on the branching ratio of the $^1P_1$ state. *Phys. Rev. A*, 59:R934–R937, 1999. URL `http://link.aps.org/doi/10.1103/PhysRevA.59.R934`.

[58] M. L. González-Martínez and J. M. Hutson. Ultracold Hydrogen Atoms: A Versatile Coolant to Produce Ultracold Molecules. *Phys. Rev. Lett.*, 111:203004, 2013. URL `http://link.aps.org/doi/10.1103/PhysRevLett.111.203004`.

[59] M. Lara, J. L. Bohn, D. Potter, P. Soldán, and J. M. Hutson. Ultracold Rb-OH Collisions and Prospects for Sympathetic Cooling. *Phys. Rev. Lett.*, 97:183201, 2006. URL `http://link.aps.org/doi/10.1103/PhysRevLett.97.183201`.

[60] S. K. Tokunaga, W. Skomorowski, P. S. Żuchowski, R. Moszynski, J. M. Hutson, E. A. Hinds, and M. R. Tarbutt. Prospects for sympathetic cooling of molecules in electrostatic, ac and microwave traps. *Eur. Phys. J. D*, 65:141–149, 2011. URL `http://dx.doi.org/10.1140/epjd/e2011-10719-x`.

[61] L. P. Parazzoli, N. J. Fitch, P. S. Żuchowski, J. M. Hutson, and H. J. Lewandowski. Large Effects of Electric Fields on Atom-Molecule Collisions at Millikelvin Temperatures. *Phys. Rev. Lett.*, 106:193201, 2011. URL `http://link.aps.org/doi/10.1103/PhysRevLett.106.193201`.

[62] D. DeMille, D. R. Glenn, and J. Petricka. Microwave traps for cold polar molecules. *Eur. Phys. J. D*, 31:375–384, 2004. URL `http://dx.doi.org/10.1140/epjd/e2004-00163-6`.

[63] S. Truppe. *New Physics with Cold Molecules: Precise Microwave Spectroscopy of CH and the Development of a Microwave Trap.* PhD thesis, Imperial College London, 2013.

[64] D. P. Dunseith, S. Truppe, R. J. Hendricks, B. E. Sauer, E. A. Hinds, and M. R. Tarbutt. A high quality, efficiently coupled microwave cavity for trapping cold molecules. arXiv:1409.2859v1, 2014.

[65] E. R. I. Abraham, W. I. McAlexander, J. M. Gerton, R. G. Hulet, R. Côté, and A. Dalgarno. Triplet s-wave resonance in ^{6}Li collisions and scattering lengths of ^{6}Li and ^{7}Li. *Phys. Rev. A*, 55:R3299–R3302, May 1997. doi: 10.1103/PhysRevA.55.R3299. URL `http://link.aps.org/doi/10.1103/PhysRevA.55.R3299`.

[66] A. Griesmaier, J. Stuhler, T. Koch, M. Fattori, T. Pfau, and S. Giovanazzi. Comparing Contact and Dipolar Interactions in a Bose-Einstein Condensate. *Phys. Rev. Lett.*, 97:250402, 2006. URL `http://link.aps.org/doi/10.1103/PhysRevLett.97.250402`.

[67] R. W. Molof, H. L. Schwartz, T. M. Miller, and B. Bederson. Measurements of electric dipole polarizabilities of the alkali-metal atoms and the metastable noble-gas atoms. *Phys. Rev. A*, 10:1131–1140, 1974. URL `http://link.aps.org/doi/10.1103/PhysRevA.10.1131`.

[68] S. K. Tokunaga. *Production and Stark deceleration of lithium hydride molecules.* PhD thesis, Imperial College London, 2009.

[69] M. Marinescu and L. You. Controlling Atom-Atom Interaction at Ultralow Temperatures by dc Electric Fields. *Phys. Rev. Lett.*, 81:4596–4599, 1998. URL `http://link.aps.org/doi/10.1103/PhysRevLett.81.4596`.

[70] T. W. Hänsch and A. L. Schawlow. Cooling of gases by laser radiation. *Opt. Commun.*, 13(1):68–69, 1975. URL `http://www.sciencedirect.com/science/article/pii/0030401875901595`.

[71] D. J. Wineland and H. Dehmelt. Proposed 10^{14} Δ $\nu < \nu$ laser fluorescence spectroscopy on Tl^{+} mono-ion oscillator. *Bull. Am. Phys. Soc.*, 20:637, 1975.

[72] A. Ashkin. Trapping of Atoms by Resonance Radiation Pressure. *Phys. Rev. Lett.*, 40:729–732, 1978. URL `http://link.aps.org/doi/10.1103/PhysRevLett.40.729`.

[73] W. D. Phillips and H. Metcalf. Laser Deceleration of an Atomic Beam. *Phys. Rev. Lett.*, 48:596–599, 1982. URL `http://link.aps.org/doi/10.1103/PhysRevLett.48.596`.

[74] A. S. Bell, J. Stuhler, S. Locher, S. Hensler, J. Mlynek, and T. Pfau. A magneto-optical trap for chromium with population repumping via intercombination lines. *Europhys. Lett.*, 45(2):156, 1999. URL `http://stacks.iop.org/0295-5075/45/i=2/a=156`.

[75] J. J. McClelland and J. L. Hanssen. Laser Cooling without Repumping: A Magneto-Optical Trap for Erbium Atoms. *Phys. Rev. Lett.*, 96:143005, 2006. URL `http://link.aps.org/doi/10.1103/PhysRevLett.96.143005`.

[76] H. J. Metcalf and P. van der Straten. *Laser Cooling and Trapping.* Springer-Verlag New York, 1999.

[77] E. L. Raab, M. Prentiss, A. Cable, S. Chu, and D. E. Pritchard. Trapping of Neutral Sodium Atoms with Radiation Pressure. *Phys. Rev. Lett.*, 59:2631–2634, 1987. URL `http://link.aps.org/doi/10.1103/PhysRevLett.59.2631`.

[78] U. Schünemann, H. Engler, M. Zielonkowski, M. Weidemüller, and R. Grimm. Magneto-optic trapping of lithium using semiconductor lasers. *Opt. Commun.*, 158 (1-6):263–272, 1998. URL `http://www.sciencedirect.com/science/article/pii/S0030401898005173`.

[79] D. W. Sesko, T. G. Walker, and C. E. Wieman. Behavior of neutral atoms in a spontaneous force trap. *J. Opt. Soc. Am. B*, 8(5):946–958, 1991. URL `http://josab.osa.org/abstract.cfm?URI=josab-8-5-946`.

[80] C. G. Townsend, N. H. Edwards, C. J. Cooper, K. P. Zetie, C. J. Foot, A. M. Steane, P. Szriftgiser, H. Perrin, and J. Dalibard. Phase-space density in the magneto-optical trap. *Phys. Rev. A*, 52:1423–1440, 1995. URL `http://link.aps.org/doi/10.1103/PhysRevA.52.1423`.

[81] A. M. Steane, M. Chowdhury, and C. J. Foot. Radiation force in the magneto-optical trap. *J. Opt. Soc. Am. B*, 9(12):2142–2158, 1992. URL `http://josab.osa.org/abstract.cfm?URI=josab-9-12-2142`.

[82] C. Gabbanini, A. Evangelista, S. Gozzini, A. Lucchesini, A. Fioretti, J. H. Müller, M. Colla, and E. Arimondo. Scaling laws in magneto-optical traps. *Europhys. Lett.*, 37(4):251–256, 1997. URL `http://dx.doi.org/10.1209/epl/i1997-00139-0`.

[83] W. Ketterle, K. B. Davis, M. A. Joffe, A. Martin, and D. E. Pritchard. High densities of cold atoms in a *dark* spontaneous-force optical trap. *Phys. Rev. Lett.*, 70:2253–2256, 1993. URL `http://link.aps.org/doi/10.1103/PhysRevLett.70.2253`.

[84] J. Weiner, V. S. Bagnato, S. Zilio, and P. S. Julienne. Experiments and theory in cold and ultracold collisions. *Rev. Mod. Phys.*, 71:1–85, 1999. URL `http://link.aps.org/doi/10.1103/RevModPhys.71.1`.

[85] W. Petrich, M. H. Anderson, J. R. Ensher, and E. A. Cornell. Behavior of atoms in a compressed magneto-optical trap. *J. Opt. Soc. Am. B*, 11(8):1332–1335, 1994. URL `http://josab.osa.org/abstract.cfm?URI=josab-11-8-1332`.

[86] A. Höpe, D. Haubrich, G. Müller, W. G. Kaenders, and D. Meschede. Neutral Cesium Atoms in Strong Magnetic-Quadrupole Fields at Sub-Doppler Temperatures. *Europhys. Lett.*, 22(9):669, 1993. URL `http://stacks.iop.org/0295-5075/22/i=9/a=006`.

[87] P. M. Duarte, R. A. Hart, J. M. Hitchcock, T. A. Corcovilos, T.-L. Yang, A. Reed, and R. G. Hulet. All-optical production of a lithium quantum gas using narrow-line laser cooling. *Phys. Rev. A*, 84:061406, 2011. URL `http://link.aps.org/doi/10.1103/PhysRevA.84.061406`.

[88] S. Chu, L. Hollberg, J. E. Bjorkholm, A. Cable, and A. Ashkin. Three-dimensional viscous confinement and cooling of atoms by resonance radiation pressure. *Phys. Rev. Lett.*, 55:48–51, 1985. URL `http://link.aps.org/doi/10.1103/PhysRevLett.55.48`.

[89] D. Sesko, C. G. Fan, and C. E. Wieman. Production of a cold atomic vapor using diode-laser cooling. *J. Opt. Soc. Am. B*, 5(6):1225–1227, 1988. URL `http://josab.osa.org/abstract.cfm?URI=josab-5-6-1225`.

[90] P. D. Lett, R. N. Watts, C. I. Westbrook, W. D. Phillips, P. L. Gould, and H. J. Metcalf. Observation of Atoms Laser Cooled below the Doppler Limit. *Phys. Rev. Lett.*, 61:169–172, 1988. URL `http://link.aps.org/doi/10.1103/PhysRevLett.61.169`.

[91] Y. Shevy, D. S. Weiss, P. J. Ungar, and S. Chu. Bimodal speed distributions in laser-cooled atoms. *Phys. Rev. Lett.*, 62:1118–1121, 1989. URL `http://link.aps.org/doi/10.1103/PhysRevLett.62.1118`.

[92] J. Dalibard and C. Cohen-Tannoudji. Laser cooling below the Doppler limit by polarization gradients: simple theoretical models. *J. Opt. Soc. Am. B*, 6(11):2023–2045, 1989. URL `http://josab.osa.org/abstract.cfm?URI=josab-6-11-2023`.

[93] Z. Lin, K. Shimizu, M. Zhan, F. Shimizu, and H. Takuma. Laser Cooling and Trapping of Li. *Jpn. J. Appl. Phys.*, 30(7B):L1324, 1991. URL `http://stacks.iop.org/1347-4065/30/i=7B/a=L1324`.

[94] M. Mudrich, S. Kraft, K. Singer, R. Grimm, A. Mosk, and M. Weidemüller. Sympathetic Cooling with Two Atomic Species in an Optical Trap. *Phys. Rev. Lett.*, 88:253001, 2002. URL `http://link.aps.org/doi/10.1103/PhysRevLett.88.253001`.

[95] A. T. Grier, I. Ferrier-Barbut, B. S. Rem, M. Delehaye, L. Khaykovich, F. Chevy, and C. Salomon. Λ-enhanced sub-Doppler cooling of lithium atoms in D_1 gray molasses. *Phys. Rev. A*, 87:063411, 2013. URL `http://link.aps.org/doi/10.1103/PhysRevA.87.063411`.

[96] W. Li, G. B. Partridge, Y. A. Liao, and R. G. Hulet. Polarized Atomic Fermi Gases. *Int. J. Mod. Phys. B*, 23(15):3195–3204, 2009. URL `http://www.worldscientific.com/doi/abs/10.1142/S0217979209053151`.

[97] S. Nascimbène, N. Navon, K. J. Jiang, F. Chevy, and C. Salomon. Exploring the thermodynamics of a universal fermi gas. *Nature*, 463:1057–1060, 2010. URL `http://www.nature.com/nature/journal/v463/n7284/abs/nature08814.html`.

[98] Z. Hadzibabic, S. Gupta, C. A. Stan, C. H. Schunck, M. W. Zwierlein, K. Dieckmann, and W. Ketterle. Fiftyfold Improvement in the Number of Quantum Degenerate Fermionic Atoms. *Phys. Rev. Lett.*, 91:160401, 2003. URL `http://link.aps.org/doi/10.1103/PhysRevLett.91.160401`.

[99] M.-S. Heo, T. T. Wang, C. A. Christensen, T. M. Rvachov, D. A. Cotta, J.-H. Choi, Y.-R. Lee, and W. Ketterle. Formation of ultracold fermionic NaLi Feshbach molecules. *Phys. Rev. A*, 86:021602, 2012. URL `http://link.aps.org/doi/10.1103/PhysRevA.86.021602`.

[100] A.-C. Voigt, M. Taglieber, L. Costa, T. Aoki, W. Wieser, T. W. Hänsch, and K. Dieckmann. Ultracold Heteronuclear Fermi-Fermi Molecules. *Phys. Rev. Lett.*, 102:020405, 2009. URL `http://link.aps.org/doi/10.1103/PhysRevLett.102.020405`.

[101] B. DeMarco and D. S. Jin. Onset of Fermi Degeneracy in a Trapped Atomic Gas. *Science*, 285(5434):1703–1706, 1999. URL `http://www.sciencemag.org/content/285/5434/1703.abstract`.

[102] F. Schreck, L. Khaykovich, K. L. Corwin, G. Ferrari, T. Bourdel, J. Cubizolles, and C. Salomon. Quasipure Bose-Einstein Condensate Immersed in a Fermi Sea. *Phys. Rev. Lett.*, 87:080403, 2001. URL `http://link.aps.org/doi/10.1103/PhysRevLett.87.080403`.

[103] J. A. Dean. *Lange's handbook of chemistry.* McGraw-Hill, Inc., New York, fifteenth edition, 1999.

[104] M.-O. Mewes, G. Ferrari, F. Schreck, A. Sinatra, and C. Salomon. Simultaneous magneto-optical trapping of two lithium isotopes. *Phys. Rev. A*, 61:011403, 1999. URL `http://link.aps.org/doi/10.1103/PhysRevA.61.011403`.

[105] J. O. Stack. *An Ultra-Cold Lithium Source for Investigating Cold Dipolar Gases.* PhD thesis, Imperial College London, 2010.

[106] W. Demtröder. *Laser Spectroscopy.* Springer-Verlag, New York, 1999.

[107] M. Greiner, I. Bloch, T. W. Hänsch, and T. Esslinger. Magnetic transport of trapped cold atoms over a large distance. *Phys. Rev. A*, 63:031401, 2001. URL `http://link.aps.org/doi/10.1103/PhysRevA.63.031401`.

[108] H. J. Lewandowski, D. M. Harber, D. L. Whitaker, and E. A. Cornell. Simplified System for Creating a Bose-Einstein Condensate. *J. Low Temp. Phys.*, 132(5-6):309–367, 2003. URL `http://dx.doi.org/10.1023/A%3A1024800600621`.

[109] S. Händel, A. L. Marchant, T. P. Wiles, S. A. Hopkins, and S. L. Cornish. Magnetic transport apparatus for the production of ultracold atomic gases in the vicinity of a dielectric surface. *Rev. Sci. Instrum.*, 83(1):013105, 2012. URL `http://scitation.aip.org/content/aip/journal/rsi/83/1/10.1063/1.3676161`.

[110] H. D. Young and R. A. Freedman. *Sears and Zemansky's University physics with modern physics.* Addison Wesley, San Franciso, eleventh edition, 2004.

[111] R. A. Nyman, G. Varoquaux, B. Villier, D. Sacchet, F. Moron, Y. Le Coq, A. Aspect, and P. Bouyer. Tapered-amplified antireflection-coated laser diodes for potassium

and rubidium atomic-physics experiments. *Rev. Sci. Instrum.*, 77(3):033105, 2006. URL `http://scitation.aip.org/content/aip/journal/rsi/77/3/10.1063/1.2186809`.

[112] W. Ketterle, D. S. Durfee, and D. M. Stamper-Kurn. Making, probing and understanding Bose-Einstein condensates. *P. Int. Sch. Phys.*, cond-mat(5):90, 1999. URL `http://arxiv.org/abs/cond-mat/9904034`.

[113] R. S. Longhurst. *Geometrical and physical optics.* Longman, New York, third edition, 1973.

[114] G. Brooker. *Modern classical optics.* Oxford University Press, Oxford, 2003.

[115] N. W. M. Ritchie, E. R. I. Abraham, Y. Y. Xiao, C. C. Bradley, R. G. Hulet, and P. S. Julienne. Trap-loss collisions of ultracold lithium atoms. *Phys. Rev. A*, 51: R890–R893, 1995. URL `http://link.aps.org/doi/10.1103/PhysRevA.51.R890`.

[116] K. Lindquist, M. Stephens, and C. Wieman. Experimental and theoretical study of the vapor-cell Zeeman optical trap. *Phys. Rev. A*, 46:4082–4090, 1992. URL `http://link.aps.org/doi/10.1103/PhysRevA.46.4082`.

[117] M. R. Tarbutt, J. J. Hudson, B. E. Sauer, and E. A. Hinds. Preparation and manipulation of molecules for fundamental physics tests. In R. Krems, B. Friedrich, and W. C. Stwalley, editors, *Cold Molecules: Theory, Experiment, Applications*, chapter 15. CRC Press, Cleveland, 2009. doi: arXiv:0803.0967.

[118] G. J. Van Wylen and R. E. Sonntag. *Fundamentals of classical thermodynamics.* John Wiley & sons, New York, third edition, 1985.

[119] N. F. Ramsey. *Molecular beams.* Oxford University Press, London, 1956.

[120] W. H. Wing. On neutral particle trapping in quasistatic electromagnetic fields. *Prog. Quant. Electron.*, 8(3-4):181 – 199, 1984. URL `http://www.sciencedirect.com/science/article/pii/0079672784900120`.

[121] W. Petrich, M. H. Anderson, J. R. Ensher, and E. A. Cornell. Stable, Tightly Confining Magnetic Trap for Evaporative Cooling of Neutral Atoms. *Phys. Rev. Lett.*, 74:3352–3355, 1995. URL `http://link.aps.org/doi/10.1103/PhysRevLett.74.3352`.

[122] Y.-J. Lin, A. R. Perry, R. L. Compton, I. B. Spielman, and J. V. Porto. Rapid production of ^{87}Rb Bose-Einstein condensates in a combined magnetic and optical potential. *Phys. Rev. A*, 79:063631, 2009. URL `http://link.aps.org/doi/10.1103/PhysRevA.79.063631`.

[123] R. Dubessy, K. Merloti, L. Longchambon, P.-E. Pottie, T. Liennard, A. Perrin, V. Lorent, and H. Perrin. Rubidium-87 Bose-Einstein condensate in an optically plugged quadrupole trap. *Phys. Rev. A*, 85:013643, 2012. URL `http://link.aps.org/doi/10.1103/PhysRevA.85.013643`.

[124] M.-S. Heo, J.-Y. Choi, and Y.-I. Shin. Fast production of large ^{23}Na Bose-Einstein condensates in an optically plugged magnetic quadrupole trap. *Phys. Rev. A*, 83:013622, 2011. URL `http://link.aps.org/doi/10.1103/PhysRevA.83.013622`.

[125] D. E. Pritchard. Cooling Neutral Atoms in a Magnetic Trap for Precision Spectroscopy. *Phys. Rev. Lett.*, 51:1336–1339, 1983. URL `http://link.aps.org/doi/10.1103/PhysRevLett.51.1336`.

[126] C. Cohen-Tannoudji, B. Diu, and F. Laloë. *Quantum Mechanics*, volume 2. John Wiley & Sons., Singapore, 2005.

[127] G. Breit and I. I. Rabi. Measurement of Nuclear Spin. *Phys. Rev.*, 38:2082–2083, 1931. URL `http://link.aps.org/doi/10.1103/PhysRev.38.2082.2`.

[128] R. H. Fowler and L. Nordheim. Electron Emission in Intense Electric Fields. *Proc. R. Soc. Lond. A*, 119(781):173–181, 1928. URL `http://rspa.royalsocietypublishing.org/content/119/781/173.short`.

[129] L. Nordheim. Zur Theorie der thermischen Emission und der Reflexion von Elektronen an Metallen. *Z. Phys.*, 46(11-12):833–855, 1928. URL `http://dx.doi.org/10.1007/BF01391020`.

[130] N. A. Surplice and R. J. D'Arcy. Reduction in the work function of stainless steel by electric fields. *J. Phys. F: Met. Phys.*, 2(1):L8, 1972. URL `http://stacks.iop.org/0305-4608/2/i=1/a=003`.

[131] W. P. Dyke and J. K. Trolan. Field Emission: Large Current Densities, Space Charge, and the Vacuum Arc. *Phys. Rev.*, 89:799–808, 1953. URL `http://link.aps.org/doi/10.1103/PhysRev.89.799`.

[132] D. Alpert, D. A. Lee, E. M. Lyman, and H. E. Tomaschke. Initiation of Electrical Breakdown in Ultrahigh Vacuum. *J. Vac. Sci. Technol.*, 1(2):35–50, 1964. URL `http://scitation.aip.org/content/avs/journal/jvst/1/2/10.1116/1.1491722`.

[133] F. M. Charbonnier, C. J. Bennette, and L. W. Swanson. Electrical Breakdown between Metal Electrodes in High Vacuum. I. Theory. *J. Appl. Phys.*, 38(2):627–633, 1967. URL `http://scitation.aip.org/content/aip/journal/jap/38/2/10.1063/1.1709385`.

[134] C. J. Bennette, L. W. Swanson, and F. M. Charbonnier. Electrical Breakdown between Metal Electrodes in High Vacuum. II. Experimental. *J. Appl. Phys.*, 38 (2):634–640, 1967. URL `http://scitation.aip.org/content/aip/journal/jap/38/2/10.1063/1.1709386`.

[135] D. W. Williams and W. T. Williams. Effect of electrode surface finish on electrical breakdown in vacuum. *J. Phys. D: Appl. Phys.*, 5(10):1845, 1972. URL `http://stacks.iop.org/0022-3727/5/i=10/a=314`.

[136] R. V. Latham. *High votlage vacuum insulation: The physical basis.* Academic Press Inc., London, 1981.

[137] D. Alpert, D. Lee, E. M. Lyman, and H. E. Tomaschke. Effect of Gas Pressure on Electrical Breakdown and Field Emission. *J. Appl. Phys.*, 38(2):880–881, 1967. URL `http://scitation.aip.org/content/aip/journal/jap/38/2/10.1063/1.1709429`.

[138] G. P. Beukema. Effects of clumps and ion bombardment on electrical breakdown in vacuum. *J. Phys. D: Appl. Phys.*, 7(12):1740, 1974. URL `http://stacks.iop.org/0022-3727/7/i=12/a=319`.

[139] S. Bajic, A. M. Abbot, and R. V. Latham. The influence of gap voltage temperature and gas species on the gas conditioning of HV electrodes. *Electrical Insulation, IEEE Transactions on*, 24(6):891–896, 1989. URL `http://ieeexplore.ieee.org/stamp/stamp.jsp?arnumber=46306`.

[140] R. Hackam and G. R. G. Raju. Electrical breakdown of a point-plane gap in high vacuum and with variation of pressure in the range $10^{-7} - 10^{-2}$ Torr of air, nitrogen, helium, sulphur hexafluoride, and argon. *J. Appl. Phys.*, 45(11):4784–4794,

1974. URL `http://scitation.aip.org/content/aip/journal/jap/45/11/10.1063/1.1663136`.

[141] G. P. Beukema. Electrical breakdown properties of stainless steel and titanium electrodes in ultra-high vacuum. *Physica B+C*, 103(2-3):397–411, 1981. URL `http://www.sciencedirect.com/science/article/pii/0378436381901479`.

[142] D. K. Davies and M. A. Biondi. Vacuum Electrical Breakdown between Plane-Parallel Copper Electrodes. *J. Appl. Phys.*, 37(8):2969–2977, 1966. URL `http://scitation.aip.org/content/aip/journal/jap/37/8/10.1063/1.1703148`.

[143] J. He, M. Lu, X. Zhou, J. R. Cao, K. L. Wang, L. S. Liao, Z. B. Deng, X. M. Ding, X. Y. Hou, and S. T. Lee. Damage study of ITO under high electric field. *Thin Solid Films*, 363(1-2):240 – 243, 2000. URL `http://www.sciencedirect.com/science/article/pii/S0040609099010664`.

[144] R. Schinzinger and P. A. A. Laura. *Conformal mapping methods and applications.* Dover Publications, New York, 2003.

[145] K. F. Riley, M. P. Hobson, and S. J. Bence. *Mathematical methods for physics and engineering.* Cambridge University Press, New York, third edition, 2006.

[146] J. M. Gere and B. J. Goodno. *Mechanics of materials.* Cengage Learning, Stamford, eighth edition, 2013.

[147] N. P. Bansal and R. H. Doremus. *Handbook of Glass Properties.* Academic Press Inc., London, 1986.

[148] B. E. Sauer, D. M. Kara, J. J. Hudson, M. R. Tarbutt, and E. A. Hinds. A robust floating nanoammeter. *Rev. Sci. Instrum.*, 79(12):126102, 2008. URL `http://scitation.aip.org/content/aip/journal/rsi/79/12/10.1063/1.3036985`.

[149] L. Windholz, M. Musso, G. Zerza, and H. Jäger. Precise Stark-effect investigations of the lithium D_1 and D_2 lines. *Phys. Rev. A*, 46:5812–5818, 1992. URL `http://link.aps.org/doi/10.1103/PhysRevA.46.5812`.